Structure and Composition of the Protein Corona in Animal Cells

DISSERTATION

zur Erlangung des akademischen Grades
doctor rerum naturalium
(Dr. rer. nat.)
im Fach Chemie
eingereicht an der
Mathematisch-Naturwissenschaftlichen Fakultät
der Humboldt-Universität zu Berlin
von

M.Sc. Gergő Péter Szekeres

Präsidentin der Humboldt-Universität zu Berlin
Prof. Dr.-Ing. Dr. Sabine Kunst
Dekan der Mathematisch-Naturwissenschaftlichen Fakultät
Prof. Dr. Elmar Kulke

Gutachter/innen:
1. Prof. Dr. Janina Kneipp
2. Prof. Dr. Maria Montes-Bayón
3. Prof. Dr. Jörg Bettmer

Tag der mündlichen Prüfung: 26.11.2019

Abstract

The characterization of the protein-nanoparticle interactions in complex biomolecular systems such as a living cell is vital for pharmaceutical, medical, and environmental research fields. In such an environment, biomolecules, mostly proteins readily adsorb on the surface of nanoparticles, and a complex equilibrium between thermodynamic and kinetic effects will determine the composition and behavior of the as-formed protein layer, called the protein corona. Due to the increasing exposure to nanoparticles, it is important to broaden our knowledge on the protein-nanoparticle surface interactions, and the composition and evolution of the corona.

This thesis focuses on the characterization of the protein corona in living cells combining surface-enhanced Raman scattering (SERS), sodium dodecyl sulfate-polyacrylamide gel electrophoresis (SDS-PAGE) and high-performance liquid chromatography coupled electrospray ionization mass spectrometry (HPLC-ESI-Q-TOF-MS), and cryo soft X-ray nanotomography (XRT). First, nanoparticle-protein interactions were studied in solutions of model proteins. Due to the proposed sample preparation, the experiments yielded comparable SERS data to those of live cells without the interference of added chemicals. The results indicate different protein-nanoparticle interactions at different protein concentrations and suggest that the high SERS enhancement in living cells is due to the additional positioning of the intracellular aggregates rather than just the crowded biomolecular environment. The comparison of the SERS spectra of similar proteins revealed their different interactions with the nanoparticles, which allowed for the determination of specific binding segments in the protein structure. Spectral signatures indicating protein cleavage were identified in the SERS spectra, which revealed the presence of protein fragments in the intracellular hard protein corona, that is, the layer of proteins strongly interacting with the nanoparticles' surface. An analytical method combining SDS-PAGE and HPLC-ESI-Q-TOF-MS was developed to study the composition of the unaltered hard protein corona formed in cells. The hard corona proteome, the cellular ultrastructure revealed by XRT, and the intracellular nanoparticle-protein interactions probed by SERS provide more comprehensive knowledge about the cellular processing of citrate-stabilized gold nanoparticles in different animal cell lines.

The combination of these analytical methods reveals the uptake mechanism, processing, accumulation site, molecular environment, and the induced cellular responses of internalized gold nanoparticles. This thesis provides information about the structure and composition of the protein corona, the nanoparticle-protein surface interactions, and the impact of nanoparticles on the cellular ultrastructure. The work validates the use of SERS in the analysis of the protein corona in the solution of model proteins and in living cells, and presents a suitable method for the analysis of the unaltered hard protein corona formed in living cells. These analytical advancements have further implications for the more comprehensive study of the protein corona formed *in vivo*.

Zusammenfassung

Die Charakterisierung der Protein-Nanopartikel-Wechselwirkungen in komplexen biomolekularen Systemen wie einer lebenden Zelle ist für die pharmazeutische, medizinische und umweltbezogene Forschung von entscheidender Bedeutung. In einer solchen Umgebung bestimmen Biomoleküle, meist Proteine, die leicht an der Oberfläche von Nanopartikeln adsorbieren sowie ein komplexes Gleichgewicht zwischen thermodynamischen und kinetischen Effekten die Zusammensetzung und das Verhalten der so gebildeten Proteinschicht, die als Proteinkorona bezeichnet wird. Aufgrund der zunehmenden Exposition gegenüber Nanopartikeln ist es wichtig, unser Wissen über die Wechselwirkungen zwischen Proteinen und der Nanopartikeloberfläche sowie über die Zusammensetzung und Entwicklung der Korona zu erweitern.

Diese Dissertation befasst sich mit der Charakterisierung der Proteinkorona in lebenden Zellen, dafür werden oberflächenverstärkte Raman-Streuung (SERS), Natriumdodecylsulfat-Polyacrylamid-Gelelektrophorese (SDS-PAGE) und Hochleistungs-Flüssigchromatographie-gekoppelter Elektrospray-Ionisations-Massenspektrometrie (HPLC-ESI-Q-TOF-MS) und Cryo-Soft-Röntgen-Nanotomographie (XRT) kombiniert. Zunächst wurden Nanopartikel-Protein-Wechselwirkungen in Lösungen von Modellproteinen untersucht. Aufgrund der vorgeschlagenen Probenvorbereitung ergaben diese Experimente vergleichbare SERS-Daten wie bei der Betrachtung lebender Zellen ohne die Beeinflussung durch zugesetzte Chemikalien. Die Ergebnisse weisen auf unterschiedliche Protein-Nanopartikel-Wechselwirkungen bei unterschiedlichen Proteinkonzentrationen hin und legen nahe, dass die hohe SERS-Verstärkung in lebenden Zellen eher auf die zusätzliche Positionierung der intrazellulären Aggregate als nur auf die überfüllte biomolekulare Umgebung zurückzuführen ist. Der Vergleich der SERS-Spektren ähnlicher Proteine enthüllte unterschiedliche Wechselwirkungen mit den Nanopartikeln, die die Bestimmung spezifischer Bindungssegmente in der Proteinstruktur ermöglichten. Spektrale Signaturen, die auf eine Proteinspaltung hinweisen, wurden in den SERS-Spektren identifiziert, die das Vorhandensein von Proteinfragmenten in der intrazellulären Hartproteinkorona, d.h. der Schicht von Proteinen, die stark mit der

Oberfläche der Nanopartikel wechselwirken, zeigten. Eine analytische Methode, die SDS-PAGE und HPLC-ESI-Q-TOF-MS kombiniert, wurde entwickelt, um die Zusammensetzung der in Zellen gebildeten unveränderten Hartproteinkorona zu untersuchen. Das Hartkorona-Proteom, die durch XRT aufgedeckte zelluläre Ultrastruktur und die durch SERS untersuchten intrazellulären Nanopartikel-Protein-Wechselwirkungen liefern ein umfassenderes Wissen über die zelluläre Verarbeitung von Zitrat-stabilisierten Goldnanopartikeln in verschiedenen tierischen Zelllinien. Die Kombination dieser Analysemethoden enthüllt den Aufnahmemechanismus, die Prozessierung, die Akkumulationsstelle, die molekulare Umgebung und die induzierten zellulären Reaktionen von internalisierten Goldnanopartikeln. Diese Arbeit liefert Informationen über die Struktur und Zusammensetzung der Proteinkorona, die Wechselwirkungen zwischen Nanopartikeln und Proteinoberflächen sowie den Einfluss von Nanopartikeln auf die zelluläre Ultrastruktur. Die Arbeit validiert die Verwendung von SERS bei der Analyse der Proteinkorona in der Lösung von Modellproteinen und in lebenden Zellen und präsentiert eine geeignete Methode zur Analyse der in lebenden Zellen gebildeten unveränderten Hartproteinkorona. Diese Fortschritte haben weitere Implikationen für die umfassendere Analyse der *in vivo* gebildeten Proteinkorona.

Acknowledgements

These nearly three years of PhD filled up my life with endless joy and countless adventures, which would not have been the same – or would not have even existed – without some wonderful people, whom I owe my eternal gratitude.

I would like to express my deepest appreciation and gratitude to my PhD supervisors, Prof. Dr. Janina Kneipp, Prof. Dr. Maria Montes-Bayón, and Prof. Dr. Jörg Bettmer for their guidance and endless professional and personal support. First of all, I would like to thank Prof. Dr. Janina Kneipp for welcoming me into her group from the beginning, and for the amazing, deep, and honest scientific discussions, which led me to write this thesis. Without her support and encouraging personality, these years would have felt much longer and been much less fruitful. I am indebted to Prof. Dr. Maria Montes-Bayón and Prof. Dr. Jörg Bettmer, who were willing to do anything to arrange even the nearly impossible if that was what I needed during my short time spent in Oviedo. With their support, I believe that I managed to do more than seven months worth of research there. I am convinced, therefore, that I have had the best PhD supervisors one could ask for, and I could not be happier about the outcome of our work together.

My special thanks go to Dr. Stephan Werner, Dr. Peter Guttmann, Dr. Nerea Fernández-Iglesias, and all the wonderful scientists with whom I had the chance to collaborate during my PhD project.

I owe a debt of gratitude to the incredible Barbara Franke and the SALSA administration, especially to Dr. Virginia Merck, Katharina Schultens, Stefanie Sellon, and Pablo Lores Lareo. Without their help and guidance in organization and bureaucracy my time in Berlin and during my scientific trips would have been very difficult.

I would like to thank the members of the Kneipp Group and the Mass Spectrometry and Biomedical Analysis Group for their support, the great discussions, and the friendly atmosphere even on the hardest days. I am grateful for the amazing company of Dr. Vesna Zivanovic and Dr. Cecilia Spedalieri during BESSY shifts, with whom those twelve hours on several consecutive days, even in night shifts, felt a bit shorter. I would like to thank Dr. Daniela Drescher for her help and patience when I kept asking questions about the tomograms and their reconstruction. I thank all the people who made time for me and gave their wonderful insight on my PhD thesis.

I would like to express my deepest appreciation to Prof. Klára Hernádi, Dr. Krisztina Schrantz, and Dr. Zsuzsanna Heiner, who showed me guidance in the ever-expanding maze of academia, and always reminded me of my motivation when the scientific life became trickier.

I am grateful for my friends in Berlin and Oviedo, Zsuzsanna, Márk, Sabrina, Vesna, Tom, Cecilia, Fani, Maki, Steve, Sinem, Nerea, Jeni, Rober, Silvia, Annika, Marichu, Dani, Xavi, Mario, and Alejandro, and everyone else who made me feel welcome wherever I went, for providing me with an extended family away from home. Their tolerance on rainy days and especially on rainy Mondays meant the world to me.

I would have never been able to start a PhD in Berlin, if it were not for my teachers, Márta and Károly, who saw it in me and convinced me that the life of a scientist is the only one in which my curiosity can be at least a bit tamed, for which I am grateful.

My deepest gratitude goes to the Bagázs and Adél, Niki, Tomi, Zita, and all my oldest and dearest friends, who managed to free my mind even at times when I never believed it to be possible. I am especially grateful for the love and support of Döme, Eri, Gergő, Krisztián, Tündi, and Zsuzsi, who have been better friends than it is humanly possible. I must express my warmest appreciation to Christian, who provided amazing support and patience in times when they were most needed.

Last but not least, my greatest appreciation go to my family. I owe a debt of gratitude for the unconditional love, support, and sacrifice of my parents, Piroska and József, to guide me and provide for me in life and in my education. Without the love of my sister, Katinka, and her appreciation of nature, I do not think I would have ever become a scientist, for which I am eternally grateful. The wisdom of my grandmother and the long phone calls always reminded me of where I come from, and wherever I am in the world, the love of these people will always make me feel that I belong. Therefore, I would like to dedicate this work to my beloved family, who are better people than I could have ever wished for.

Thank you. Köszönöm.

"Az élet viharaival szemben olyan légy, mint a madár, amely, ha a fát kivágják alóla, nem a mélybe zuhan, hanem a magasba száll."

— Br. Eötvös József

Table of Contents

Chapter 1

Introduction

Humans are emergently exposed to nanoparticles on a daily basis [1, 2]. Contact with nanoparticles can be based on intentional and unintentional exposure [2, 3]. Most of the time, intentional exposure results from therapeutic treatment due to the administration of nanopharmaceuticals [4-6], photothermal therapy [7, 8], or diagnostic procedures [9-11]. Unintentional exposure can come from natural sources such as volcano eruptions, dust storms, or forest fires, while there is an increasing amount of nanoparticles that enter our environment originating from industrial sources [2]. The interaction of nanoparticles with biological matter ranging from single cells to functioning organisms results in the biological surface functionalization with proteins and with other biomolecules to a lesser extent [12-14]. In most of the studies, the adsorbed protein layer on the surface of the nanoparticles termed the 'protein corona' is concluded to bear the greatest influence on the induced effects in the biological systems. In such complex biomolecular systems, the smaller, more abundant proteins adsorb first. These proteins often have a low surface affinity, and they continuously exchange for proteins with higher surface affinity [15-17]. Eventually, a protein-nanoparticle bioconjugate evolves, where the nanoparticle forms the core that is continuously in contact with the hard corona, *i.e.,* the layer of adsorbed proteins with high surface affinity. Other proteins may interact with the hard corona forming a second layer of adsorbed proteins, called the soft corona. The new biological identity of the nanoparticles as a result of the adsorbed protein corona influences the

residence time of nanoparticles in the organism based on the induced processing mechanisms, and it can lead the nanoparticles to accumulation sites [12-14]. Both the residence time and the accumulation of nanoparticles are of high interest in past and current research projects since they are key determining factors in therapeutic or diagnostic efficiency and in studies investigating the cytotoxicity of nanoparticles [14, 18-20].

The protein corona development, its evolution, and the surface interactions between the proteins and the nanoparticles is still an essential topic of on-going research [4, 14, 18, 21]. The protein corona can be analyzed in different systems depending on the focus of the study. Generally, the mixture of pure proteins and well-characterized nanoparticles is studied to understand the on-going surface interactions [22-28]. Serum albumins are among the most studied proteins in their interaction with nanoparticles [22-26, 29-31] due to the possibility of intravenous administration of nanoparticles. Despite the well-characterized and relatively simple systems, there are still controversies about the surface processes responsible for the adsorption [22-25]. Biological fluids, such as blood serum or cell lysate are brought into contact with nanoparticles, which facilitates the observation of the time-resolved evolution of the protein corona [32] and to understand the dependency of the corona composition on nanoparticle characteristics, such as size [33]. While the studies in biological fluids yield valuable information about the surface interactions and the qualitative and quantitative composition of the protein corona, the current knowledge of the protein corona composition in a live biological environment, such as cells or tissues, is incomplete. Therefore, to elucidate the intracellular composition of the protein corona, new experimental approaches have to be exploited. This thesis aims to reveal important aspects of the so-far unknown intracellular development of the hard protein corona and, by studying the surface processes, provide a concept for the intracellular processing of nanoparticles at the level of proteins and their side chains.

For this aim, modern proteomics [13, 19, 34] combined with state-of-the-art mass spectrometric techniques [35-38], as well as the advances in vibrational spectroscopy, especially those of surface-enhanced Raman scattering (SERS) [39-42] provide promising new pathways to observe nanoparticle-protein interactions both *in situ* and *in vitro*. SERS signals report in great detail about the local biochemical environment of the

plasmonic nanoparticles as a result of its high sensitivity and selectivity [43, 44]. The intracellular processing of the plasmonic nanoparticles, yielding nanoparticle aggregates, allows for the large SERS enhancements observed, while the spatially distributed signals can be constructed into maps of nanoparticle-protein interactions in live cells. The main goal of this thesis is to combine SERS with the *ex situ* mass spectrometric analysis of the protein corona composition, which can provide crucial information about the development of the protein corona inside living cells. In particular, SERS will be used to probe nanoparticle-protein interactions in the solutions of pure proteins, protein mixtures, and in live cells. The latter will be elucidated by the combined SERS and mass spectrometric analysis of the intracellularly formed protein corona, augmented with the monitoring of induced ultrastructural changes by cryo soft X-ray nanotomography (XRT).

In this work, nanoparticle-protein interactions are discussed in the solutions of model proteins based on SERS data. The acquired knowledge on the spectral features of such interactions allows for the more in-depth interpretation of the SERS spectra of complex systems, such as in live cells. The mass spectrometric analysis of the isolated hard protein corona provides information on the interacting proteins. The SERS and mass spectrometric data combined with XRT reveal details about the intracellular protein corona.

Chapter 2

Background and state-of-the-art

2.1. Brief description of protein molecules

Proteins are large molecules (macromolecules) that serve a great variety of functions in living organisms. In 2017, a publication about the Cell Atlas Project discussed the monitoring of over 12,000 different kinds of proteins in the subcellular proteome [45]. Their high abundance and essential functions, including DNA replication, signaling, and catalysis of metabolic processes result in their research by a plethora of frontier scientific fields, such as biophysics, biochemistry, and bioinformatics.

A simple protein molecule consists of a chain of amino acids held together by peptide bonds. Their native folding is driven by thermodynamics, that is, the three-dimensional structure in which the protein remains intact and preserves its function. The native folding is stabilized by intramolecular and intermolecular processes based on hydrophobic, electrostatic, and van der Waals interactions, and it is further stabilized by hydrogen bonds, and covalent bonds in disulfide bonds [46].

The structure of a protein molecule can be described at four different levels. The primary structure is the sequence of amino acids bound together by peptide bonds. The secondary structure describes the three-dimensional organization of the intramolecular polypeptide segments and consists of well-characterized elements, such as the α-helix or the β-sheet.

The secondary structural elements can group into domains, which are separated three-dimensional structures inside the protein molecule with their own function. The co-organization of the secondary structural elements that do not form a domain is called the supersecondary structure, while the three-dimensional organization of different protein domains is called the tertiary structure. When a protein molecule consists of more than one chain, or it is in complex with other molecules, the structure that describes the three-dimensional organization of the whole protein complex is called the quaternary structure [46].

2.2. The interaction of proteins with macroscopic surfaces

Protein molecules are generally built up by the different combinations of twenty standard amino acids, which have well-distinguished chemical characteristics. Therefore, aliphatic, aromatic, hydrophilic, and charged side chains are all expected to interact differently with a surface of specific characteristics.

In an aqueous environment, the folding of a protein results in a hydrophobic core and a hydrophilic surface [46, 47]. The diversity of the different amino acids and the structure of the different protein molecules results in distinct interactions with a solid surface, which can be typical for only a short segment of the whole protein chain. It is important to learn about the behavior of specific proteins, and that of proteins in general, when they come in contact with surfaces possessing different characteristics.

The use of implants and different prosthetics justifies the importance of studying the interaction of proteins with flat surfaces since implants are continuously exposed to proteins once they are incorporated into the body. Understanding such interactions is also of great importance to facilitate surface functionalization, which prevents the recognition of the implant as a foreign body. The study of protein adsorption on solid surfaces dates back to the early 1900s [48, 49]. Then, in 1962, Leo Vroman published new findings of the different adsorption properties of proteins on hydrophobic and hydrophilic surfaces [50], which turned out to be pioneering in the field, and the results are still used to interpret protein adsorption kinetics [15].

Most proteins readily adsorb on different surfaces due to their amphiphilic nature [51]. In a complex protein solution, a dynamic equilibrium is set between the association and

dissociation of different protein species, which determines their affinity to the surface [16, 18, 50, 52]. The equilibrium simultaneously depends on the rate constants of association (k_{on}) and dissociation (k_{off}). Proteins with a higher concentration and stronger diffusion, as are generally small protein species, possess a high k_{on} constant, while the k_{off} constant is larger for those whose binding energy to the surface is low [16, 18, 50, 52]. This means that when a complex protein solution comes in contact with a solid surface, first the smaller, more concentrated proteins will adsorb on the surface, which then gradually exchange for the larger proteins with higher surface affinity [16, 18, 50, 52]. This process is known as the Vroman effect.

However, the surface affinity does not only depend on the physicochemical characteristics of the native protein structure. When proteins adsorb on a solid surface, their structure can undergo conformational changes [15, 53-55]. Such changes can significantly enhance the binding energy, which results in the irreversibility of both the adsorption and the unfolding of the protein [15, 53-55]. These conformational changes have been shown to account for the adsorption mechanism as well, resulting in a two-step adsorption process in the case of, *e.g.,* fibrinogen [53].

2.3. The protein corona of nanoparticles

In this thesis, the interaction of proteins with nanoparticles and the resulting protein corona will be analyzed. The protein corona can be defined as the adsorbed layers of proteins on the surface of nanoparticles. While the proteins in the innermost layer interact preferentially with the surface of the nanoparticle, the rest of the proteins interact with each other. Based on the Vroman effect discussed in the previous section, in blood serum and other complex protein solutions, the surface of the nanoparticles is first covered with proteins that show higher diffusion and are present at higher concentrations, which gradually exchange to proteins that have a higher affinity to the surface [16, 18, 50, 52]. The different layers of the protein corona are referred to as “hard corona” and “soft corona”, but their definition in the literature is still ambiguous. In this dissertation, the innermost layer formed by proteins that strongly interact with the surface of the nanoparticle will be referred to as the “hard corona”, while the rest of the multi-layer protein coverage will be discussed under the name of “soft corona”. The qualitative

analysis of the hard corona proteome is presented in Chapters 7 and 9, which sheds light on the adsorption and exchange of the different corona proteins in the culture medium and inside the cell.

The emerging use of nanotechnology in pharmaceutical and industrial applications demands the detailed study of nanoparticle-biosystem interactions. Due to their high concentration and great variety of functions, the investigation of protein-nanoparticle interactions is of high interest. While most effects responsible for protein adsorption and competition on solid surfaces are applicable for the surface of nanoparticles as well, major differences can arise from their small size and surface curvature. The small size of nanoparticles results in an asymmetrical force field rendering higher energy levels for the surface atoms [56-58]. Such high surface energy is thermodynamically unfavorable and the processes that lower the surface energy are prioritized. The adsorption of proteins on the surface of the nanoparticles reduces the surface energy by the net change in the Gibbs free energy originating from the protein binding [56-58], which makes the interaction energetically favorable. Therefore, it is expected that in a complex protein solution, the surface of nanoparticles will always be covered with proteins, unless it is functionalized to repel them [59].

The conformational changes observed in the case of adsorption on macroscopic solid surfaces can take place during the nanoparticle-protein interactions as well, although, they strongly depend on the surface characteristics of the nanoparticles. Individual particles with a larger diameter and, therefore, smaller surface curvature were shown to cause more severe conformational changes due to the larger surface provided for interactions [60]. It has been shown that an oligopeptide on thiolated gold nanoparticles could change its primarily α-helical structure into β-sheets [61], while in another study, β-sheets were found to change into α-helices upon adsorption [62]. The conformational changes of proteins often result in changes in their function, thus, they must be addressed in every experiment aiming at revealing nanoparticle-protein interactions.

The literature focusing on nanoparticle-protein interactions usually describes experiments either in pure protein solutions [22, 23, 25, 63] or highly complex solutions with hundreds to thousands of protein species, such as blood sera or cell lysates [34, 35, 64-66]. The former systems are adequate to determine the surface interactions, but they inform less

about binding kinetics, contrary to the latter, which describe the adsorption and competition in a complex solution but often lose the information about exact surface interactions.

There have been debates in the literature about the interaction of citrate-stabilized gold nanoparticles and proteins. Brewer and colleagues showed that bovine serum albumin adsorbs on the surface of nanoparticles by interacting purely with the citrate layer and they proposed the indirect protein-nanoparticle interaction based on electrostatic effects while rejecting the possibility of the exchange of surface-adsorbed citrate ions [25]. Some studies have proposed the same electrostatic interactions as well [24, 63], while others proposed the direct protein-nanoparticle interactions due to the exchanged citrate ions on the surface [22, 63]. Further studies are needed to identify the nature of surface interactions since it has implications for the corona formation, stability, and the extent of protein denaturation in the corona.

The studies of the composition and evolution of the protein corona have also yielded controversial results. Some of them propose that the composition of the corona changes dynamically over time [12, 67-69], while a nowadays often considered concept is that the protein corona forms rapidly and only the quantitative ratio of the proteins changes [32]. However, this latter, widely accepted theory can only stand its ground in a homogeneous protein solution, because the intracellular processing of nanoparticles and their direction to digestive cellular compartments are expected to significantly alter the corona composition. In this thesis, the interactions of proteins with citrate-stabilized gold nanospheres of uniform size will be studied by surface-enhanced Raman scattering (SERS) in the solutions of pure proteins and in protein mixtures (Chapters 5, 6, and 8).

Even though nowadays nanoparticles can be engineered with different shapes, sizes, and surface functionalization, in a complex protein solution, their behavior can strongly differ from the expected due to the adsorption of the protein corona [12, 18]. This new surface functionalization by the adsorbed proteins, also known as the “biological identity” [12], determines the path of the nanoparticles in the biomolecular system, the residence time, and the site and extent of accumulation [70-73]. In other words, this new layer is what the cell “sees” [19]. Previous studies have shown that the presence of the protein corona can reduce the cellular stress caused by the nanoparticles and their inherent cytotoxicity [73],

while others suggest an increment in the adverse effects of the nanoparticles [74] based on the interaction of the protein corona with the biomolecular environment. However, knowing only the composition of the *in vitro* protein corona does not guarantee the suitable prediction of the *in situ* effects of the nanoparticles [75], as in living cells, each cellular compartment where the nanoparticles can reside has their own chemical environment, which can strongly influence the corona composition. Therefore, to characterize the protein corona formed *in situ*, new analytical methods have to be developed.

2.4. Cellular uptake and processing of the nanoparticles

Nanoparticles must pass through the cell membrane in order to reach the intracellular space. The uptake of nanoparticles has been proposed to be based on passive and active processes as well. Passive uptake is the passive diffusion of the nanoparticles through the cell membrane, which is observed mostly for small nanoparticles and generally results in severe cytotoxic effects since the nanoparticles directly interact with the proteins in the cytosol [76-78]. It is more probable that nanoparticles penetrate the cell membrane *via* active processes, which can be receptor-mediated, such as clathrin- or caveolin-mediated endocytosis, or receptor-independent endocytosis. The activated uptake mechanism strongly depends on the characteristics of the nanoparticles and the type of cells interacting.

The size of the nanoparticles is one of their most deterministic traits. Since clathrin-mediated endocytosis, a primary pathway for nanoparticle internalization, mostly generates small, up to ~100-200 nm vesicles [79-81], larger particles or aggregates enter based on other processes. These larger particles, depending on the cell line with which they interact, can be engulfed by either phagocytosis [33, 82, 83] or macropinocytosis [84]. Macrophages, such as J774 cells favor the nanoparticle uptake *via* phagocytosis [33, 82, 83], while other cell lines activate clathrin-mediated or clathrin-independent pathways for the same purpose [84]. It is important to clarify that while macropinocytosis is common among epithelial cell lines, some of them, *e.g.,* A549 cells do not prioritize the uptake of extracellular substances based on that mechanism [84]. Therefore, when evaluating the composition and evolution of the protein corona, the uptake mechanisms

must be carefully considered, because they can result in vastly different nanoparticle-cell membrane interactions.

Nanoparticle properties other than size can also play an essential role in uptake efficiency. Chithrani and Chan showed that cells internalized spherical nanoparticles more readily than nanorods [85], while similar comparisons were made between nanorods and nanocylinders [86], and between nanorods, nanostars, and nanotriangles [87] as well. These studies allow for the conclusion that besides size, particle shape is also a determining factor in their internalization. The influence of nanoparticle surface charge on the uptake was also investigated, and it was found that differently charged nanoparticles penetrate the cell membrane in a different manner, positively charged particles being internalized more rapidly in general [86, 88, 89]. Nanoparticles are engineered for specific purposes and it can be expected that each new kind of nanoparticle will have distinct interactions with different cell lines.

Even though the cell-nanoparticle interactions can differ, which results in distinct uptake mechanisms, eventually most mechanisms lead to a specific stage of the endolysosomal processing of the internalized materials. Since 30 nm citrate-stabilized gold nanoparticles are often internalized by clathrin-mediated endocytosis [90, 91], the stages of the endolysosomal processing will be introduced based on the example of clathrin-mediated endocytosis.

Clathrin-mediated endocytosis is a receptor-mediated pathway, where the cargo (in this case, the nanoparticles) can interact with different kinds of receptors to initiate the clathrin coat assembly on the intracellular side of the membrane. Once the cargo binds to an adequate receptor on the cell membrane, a multitude of proteins is activated and transported to the cell membrane in a specific order, among them, clathrin [92]. Once the clathrin coat (in complex with many other proteins) is complete, actin filaments polymerize on the coating, and with the help of BAR domain proteins, the invagination and subsequent constriction and scission are initiated [92]. After the scission of the clathrin-coated vesicle, proteins, such as chaperons, disassemble the endocytic machinery, removing the clathrin coat of the vesicle [92]. The complete internalization process takes up to ~120 s [92].

After the disassembly of the endocytic machinery, the vesicle with the nanoparticles fuses with an early endosome. These endosomes accept cargo not only from clathrin-mediated endocytosis but many other uptake routes as well [93]. During the endosomal maturation, the early endosomes are matured into late endosomes, which, after undergoing drastic structural and molecular changes, fuse with lysosomes [93] forming the endolysosome. After the processing of the endolysosomal content, the product can either be used by the cell or it can be exocytosed.

Exocytosis is a process by which cells excrete unnecessary substances, such as denatured proteins and damaged DNA, but it has been found to have an essential role in intercellular communication as well [94-96]. This process was shown to eliminate intracellular gold nanoparticles [85]. In the cellular compartments targeted for extracellular cargo release, nanoparticles can interact with protein molecules and organelles with which they would not interact otherwise [96, 97]. Therefore, finding signs of such interactions in the intracellular protein corona can inform about the fate of the nanoparticles.

2.5. SERS of biomolecules and cells

In this thesis, nanoparticle-protein interactions are elucidated by SERS in protein-nanoparticle aggregates formed in solutions and in living cells. When the frequency of the incident photon matches the frequency of the surface plasmon, that is, the collective oscillation of the free electrons, an enhancement of the excitation field and of the Raman scattered field is observed, the latter is known as SERS.

Raman scattering is the inelastic scattering of photons as a result of exciting molecules to higher energy levels. The effect was first predicted by the Austrian theoretical physicist, Adolf Smekal in 1923 [98]. In 1928, the inelastic light scattering was experimentally proved by the Indian scientists C. V. Raman and K. S. Krishnan in liquids [99, 100], and in independent experiments by G. Landsberg and L. Mandelstam in the Soviet Union, who demonstrated the same effect in crystals [101]. Raman received the Nobel prize in Physics in 1930 “for his work on the scattering of light and for the discovery of the effect named after him”.

When a photon interacts with a molecule and scattering takes place, in most cases, the energy of the photon remains unchanged, *i.e.,* elastic scattering takes place, also known

as Rayleigh scattering (Figure 2.1). In the case of inelastic light scattering, the incident photon can interact with molecules at lower energy states, and the scattered photon will lose energy as a result of exciting the molecule to a higher energy state. This process is known as the Stokes scattering (Figure 2.1). When the incident photon interacts with molecules at higher energy states, it is possible that after the interaction, the scattered photon gains energy as a result of the interacting molecule returning to a lower energy state, which phenomenon is known as anti-Stokes scattering (Figure 2.1). The absolute changes in the photon energies are the same for both the Stokes and anti-Stokes effects for a given molecular vibration, and the difference in the photon energy is characteristic to the vibration. As a general rule, a molecular vibrational mode is Raman active if the vibration changes the polarizability of the molecule. Therefore, the collected spectrum will contain information about the vibrational modes present in the molecule, which makes it possible to identify the molecule, characterize its structure, and the interactions in complex mixtures of molecules. A biological sample typically represents such a complex mixture. A special case of Raman scattering is called resonance Raman scattering, which occurs when the energy of the incident photon matches the energy of an electronic transition in the molecule (Figure 2.1). This resonance condition can result in highly enhanced signals allowing for the detection of analytes at low concentrations, while the excited electronic transition can provide further structural details about the molecule.

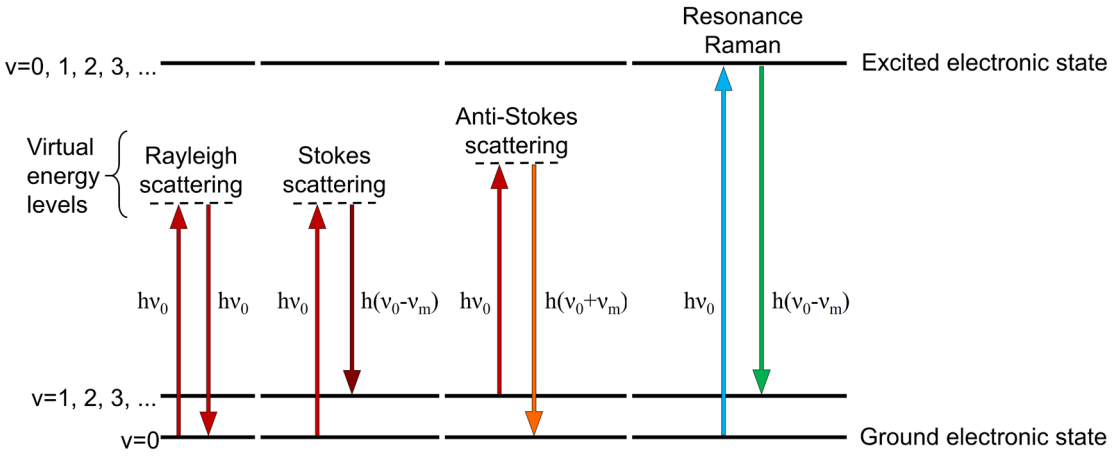

Figure 2.1. The Jablonski representation of the Rayleigh scattering, Stokes scattering, anti-Stokes scattering, and resonance Raman scattering. ν_0 and ν_m refer to the frequencies of the incident photon and the molecular vibration, respectively.

The spectra resulting from Stokes and anti-Stokes scattering are symmetrical to each other, though, the intensity of anti-Stokes scattering is considerably lower due to the larger quantity of molecules residing at lower energy states at room temperature as a result of the Boltzmann distribution. Therefore, in this thesis, all the presented Raman and SERS spectra correspond to Stokes scattering.

Due to the selection rules of Raman spectroscopy, spectrum acquisition is possible in aqueous media, making it optimal for many biochemical and biomedical analyses. Even though Raman experiments can be performed at a wide range of wavelengths, near-IR lasers are often favored in the study of biological samples to avoid photodegradation. After the discovery of the Raman effect, studies of biologically relevant molecules [102, 103] opened up the path for the Raman study of proteins, which has become an important alternative to FTIR for the determination of the protein structures in solution [104-106]. In particular, resonance Raman scattering has been extensively used to elucidate the structure of protein molecules [107-109]. Since then, Raman spectroscopy has become an essential tool in analyzing the biochemistry of cells [110-112]. Regardless of its advantages and sensitivity, Raman spectroscopy is not widely used in biological applications due to its small cross-section [113]; however, its beneficial characteristics, such as the narrow linewidth and the compatibility with aqueous samples, can be exploited by means of SERS.

The probing of molecules in the close proximity of plasmonic surfaces can yield highly enhanced Raman signals, in a process known as SERS [43, 114-118]. In 1974, Fleischmann and colleagues first published their findings that intense Raman spectra of a pyridine thin film were acquired, which, due to technical limitations, was not possible at that time [114]. They found that the Raman spectra could be collected from the surface of a roughened silver electrode, which they attributed to the increased surface area of the electrode [114]. They also found that the changes in the Raman spectra obtained from the pyridine film were the result of changes in the surface orientation of pyridine molecules; therefore, in the first SERS experiments, the advantages of SERS have already been demonstrated: its high sensitivity and selectivity. However, at that time, the reason for the high signal enhancement remained unknown.

In their study published in 1977, Jeanmaire and Van Duyne [119] postulated that the high Raman signal is the result of an electric field enhancement, which also allowed for the discussion of the surface orientation of adsorbed nitrogenous aromatic species. In the same year, Albrecht and Creighton also published their findings on the high signal enhancement observed in the Raman signal of pyridine adsorbed on a roughened silver electrode [116]. They found no correlation between the signal intensity and the increased surface area of the silver electrode, and they suggested that the signal enhancement must be based on some surface effect. Based on a study by Philpott [120] describing that surface plasmons may induce resonance Raman effect, they suggested that the underlying cause for the observed signal enhancement of ~10^5 might be the result of the interaction of the incident photons with surface plasmons as well. In 1978, Moskovits used nanoparticles to induce SERS, proving that the signal enhancement is most probably attributed to nanosized structures rather than surface effects [117, 121].

When the frequency of the incident photon matches the frequency of collectively oscillating electrons in a metallic nanoparticle, *e.g.,* gold and silver, localized surface plasmon resonance (LSPR) is observed. The molecule in the proximity of such nanostructures is exposed to the electromagnetic field of the LSPR-induced dipole superposed with that of the incident light. As a result, an enhancement of the excitation field and the Raman scattered field is observed. Two enhancement mechanisms contribute to the SERS signal. A larger contribution derives from the electromagnetic enhancement that is observed when Raman scattering occurs in the high local field of plasmonic nanoparticles. At a smaller extent, a so-called chemical enhancement can also take place, when the molecule interacts with the plasmonic surface resulting in larger cross-sections. The chemical enhancement can be the result of different processes, e.g., charge-transfer [122, 123]. Formula (1) accounts for both enhancement mechanisms in the description of the SERS signal *(P^{SERS})*:

$$P^{\mathrm{SERS}}(\nu_S) = N'\sigma^{R}_{\mathrm{ads}}|A(\nu_L)|^2\,|A(\nu_S)|^2\,I(\nu_L) \qquad (1)$$

where *$A(\nu_S)$* and *$A(\nu_L)$* are the enhancements of the Raman scattered field and the excitation field, *N'* is the number of probed molecules, σ^{R}_{ads} is the higher Raman cross-section due to the chemical enhancement, and *$I(\nu_L)$* is the excitation intensity [121]. Even though the molecule does not necessarily have to interact with the plasmonic surface to

yield SERS spectra enhanced by the electromagnetic effect, the magnitude of enhancement strongly depends on the distance of the molecule from the surface:

$$A(\nu) = \frac{E_M(\nu)}{E_0(\nu)} \sim \frac{\varepsilon - \varepsilon_0}{\varepsilon + 2\varepsilon_0}\left(\frac{r}{r+d}\right)^3 \quad (2)$$

where E_M is the superposition of the excitation field E_0 and the field of the LSPR-induced dipole, ε is the dielectric constant of the plasmonic nanoparticle, ε_0 is the dielectric constant of the surrounding medium, r is the radius of the nanoparticle, and d is the distance between the molecule and the surface of the nanoparticle [121]. From (1) and (2) it can be deduced that the electromagnetic enhancement dramatically decreases with the distance by ~ $(1/d)^{12}$ [121].

When plasmonic nanoparticles cluster together, a higher enhancement can be observed due to plasmon coupling [124], which has been shown to reach enhancements of up to 10^{14} [125]. However, the field distribution in nanoparticle clusters is not homogeneous, and the highest enhancements can be observed in the so-called "hot spots" based on finite-difference time-domain (FDTD) calculations, as shown in Figure 2.2A as well. Due to the size of hot spots, when large molecules, *e.g.,* proteins are probed (Figure 2.2B), the very high local field enhancement allows to report about small segments of the proteins [121, 126]. There has been a myriad of studies targeting protein-nanoparticle interactions in *in vitro* solutions, most of them relying on the induced pre-aggregation of plasmonic nanoparticles [127-129] or other means of aggregate formation [26, 130]. Even though nanoparticle aggregation facilitates the collection of SERS spectra with good enhancement, it is essential to evaluate the influence of introducing chemicals to facilitate the aggregation process both on the system and the SERS data as well [131-133]. In this thesis, gold nanoparticles are aggregated by the protein molecules of interest (Chapters 5, 6, and 8) or due to their active processing by the biomolecules in cells (Chapters 8 and 9), which allows for the elucidation of the nanoparticle-protein interactions in an unaltered chemical environment. Gold nanoparticles were chosen in all experiments instead of silver, because in the case of excitation at 785 nm, the dielectric function of gold nanoparticles was shown to result in higher signal enhancement [134, 135].

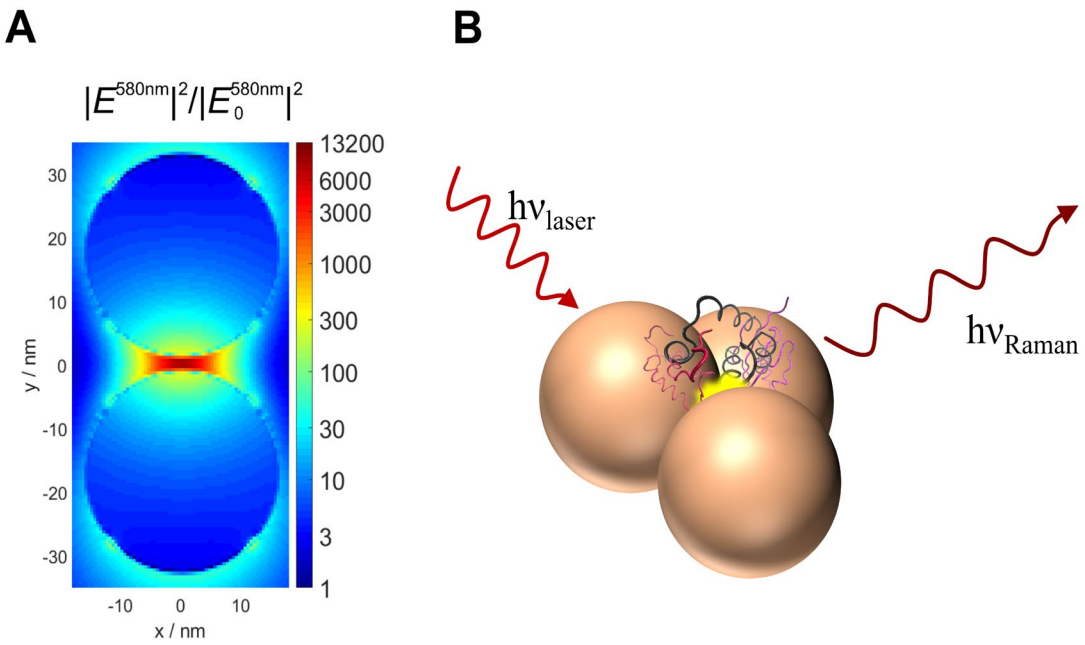

Figure 2.2. Illustration of a hot spot in a gold nanosphere dimer based on FDTD calculations [136] (A). Schematic representation of a SERS experiment with proteins in a nanoaggregate (B). PDB IDs: 4V6X [137], 1USS [138], 1IJE [139].

Even though the hot spots theoretically allow for the probing of small segments of adsorbed proteins, in a probed volume usually there are several hot spots, and therefore, the obtained SERS signal is the combination of all the probed vibrations in all the probed hot spots. Since the nanoparticle aggregates continuously move and change in solution, it is difficult to interpret the acquired SERS data. The variation of protein SERS spectra can be reduced by the immobilization of the SERS-active nanostructures [28, 140], though, it limits their applicability in biological samples. Multivariate analysis can be used to extract information about datasets with intrinsic SERS spectra [141-144]. Principal component analysis is often used in the analysis of SERS data [141-143] and is now implemented in many commercial softwares. Recently, random-forest analysis has been demonstrated in the interpretation of live cell SERS data, which made it possible to identify the spectral features of changes in the biomolecular environment of the nanoparticles due to the administration of tricyclic antidepressants [144].

Since living cells process nanoparticles and often form intracellular aggregates, feeding plasmonic nanoparticles to the cells can result in SERS-active nanostructures producing SERS signals that are characteristic to their local biochemical environment [42, 145, 146]. Often, reporter molecules are used to monitor specific cellular properties. It was

demonstrated previously that *para*-mercaptobenzoic acid (*p*MBA) can report about the pH of the local environment of *p*MBA-functionalized nanoparticles in SERS experiments [11, 147, 148]. In another study, gold nanorods were functionalized with 4-mercaptophenylboronic ester, which helped in the quantitation of H_2O_2, a major reactive oxygen species [149]. However, reporter molecules and other modifications of the plasmonic nanoparticles are not necessary to acquire SERS data from living cells. The changes in cellular chemistry due to induced mechanisms such as apoptosis were observed in living cancer cells [150]. In other live cell SERS experiments, it was possible to show the time-dependent location of the intracellular gold nanoparticles [151], which informs about the pathways involved in the re-localization of the nanoparticle. The functionalization of the nanoparticles allows for their use in diagnostics. It was shown that the squamous cell carcinoma antigen in cervical cancer can be identified by SERS with an antigen-functionalized immunoassay [152]. Plasmonic nanoparticles can also be used in photothermal therapy, where the degradation of the tumor tissue can be induced, while the changes in the biomolecular environment can be followed [153].

It is expected that different nanoparticles interact in distinct ways with the intracellular environment. Au-magnetite and Ag-magnetite composite nanoparticles were shown to have different surface interactions and, therefore, different proteins may interact with these nanoparticles inside the cell than with pure gold and silver nanoparticles [154]. However, SERS-active gold nanoparticles can also be generated inside the cells due to the reductive environments present in many intracellular compartments [155]. The results showed that the localization and surface interactions of the *in situ* generated gold nanoparticles significantly depend on the cell incubation conditions [155].

SERS has proven to be useful in monitoring the changes in organelles, *e.g.,* in mitochondria [156]. Signatures of parasitic infection were also identified, which implies that SERS has high potential in diagnostic applications [157]. *Leishmania*-infected cells were incubated with gold nanoparticles, which revealed the specific changes in the biomolecular environment around the nanoparticles in the proximity of the parasite [157]. The pharmaceutical implications of SERS were demonstrated by Zivanovic and colleagues, showing the intracellular effects of tricyclic antidepressants on eukaryotic cells [144]. Moreover, the suitability of SERS to monitor changes in three-dimensional

spherical cell cultures was also shown, and the cellular responses to external stimuli could be identified based on the acquired data [143].

The specific information acquired from live cell SERS experiments about the local environment of the nanoparticles and the on-going surface processes can be combined with results from complementary analytical techniques such as elemental analysis by mass spectrometry. Laser ablation inductively coupled plasma mass spectrometry (LA-ICP-MS) mapping experiments combined with SERS mapping data revealed the number of gold nanoparticles in the cells and their biomolecular environment, which allowed for the conclusion that a significant portion of intracellular gold nanoparticles does not form SERS-active aggregates [145, 154, 155, 158]. While inductively coupled plasma mass spectrometry provides an elemental distribution map of a sample, mass spectrometry can be combined with soft ionization techniques, which allow to determine the biomolecular composition of a sample. In this thesis, electrospray ionization (ESI) will be coupled with tandem-MS to determine the composition of the hard corona proteome.

2.6. Mass spectrometric analysis of the protein corona composition

In order to have a more comprehensive understanding of the processing of nanoparticles in the intracellular environment, the composition of the protein corona must be analyzed. For this purpose, mass spectrometric approaches can be used.

Mass spectrometry is based on the analysis of ionized species. The ion sources are adapted to the analytical approach: in elemental analysis, hard ionization, *e.g.,* an inductively coupled plasma ion source is used. When the composition of larger molecules is in the focus of the study, soft ionization is applied, *e.g.,* by an electrospray ion source (ESI), which is introduced in more detail below. The ionized species are separated in a mass analyzer based on their mass-to-charge ratio. There is a variety of mass analyzers that apply either an electric field, a magnetic field, or their combination in a static or dynamic manner. Based on the dynamics of charged particles in an electromagnetic field [159, 160], the mass-to-charge ratio (m/Q) determines the motion of the ion, and the ion can be identified once its initial conditions are known. In most cases, instead of the m/Q ratio, the dimensionless m/z ratio is used to characterize an ion, where z is the elementary charge number of the ion proportional to the charge of a proton [159, 160].

For proteins and peptides, soft ionization techniques are used, *e.g.,* matrix-assisted laser ionization/desorption (MALDI) or ESI. These ionization techniques prevent the sensitive biomolecule chains from fragmentation. In this thesis, ESI was used to convert the peptides separated by liquid chromatography from liquid phase into charged species in the gas phase. In ESI, ionization occurs when a solution passes through a needle with high voltage (4-5 kV) compared to a counter electrode [160]. If the solution is an electrolyte, it receives a positive or negative net charge and transforms into a fine charged mist at the end of the needle. A flow of dry gas passing in the opposite direction allows for the evaporation of the solvent in the droplets, and as a result of the identically charged ions getting close to each other, the arising Coulombic repulsive forces aid the formation of much smaller droplets. This process repeats itself until the charged ions become completely solvent-free, which eventually flow into the mass analyzer.

The instrument used in this thesis work was an impact II UHR-Qq-TOF-MS (ultrahigh-resolution double-quadrupole time-of-flight mass spectrometer). In this tandem-MS instrument, there are two quadrupoles (Qq) and a time-of-flight mass analyzer (TOF). Quadrupoles consist of four parallel metal rods positioned symmetrically, and each pair of opposing rods is electrically connected. In the first quadrupole, a radio-frequency voltage with a DC offset is applied to the pairs of rods, resulting in an electric field that destabilizes the trajectories of most ions and only allows a specific m/z range to pass through the analyzer [160]. The second quadrupole acts as a collision cell, where only radio-frequency voltage is applied with no m/z filtering, and the ions colliding with the applied inert gas flow (*e.g.,* N_2) undergo fragmentation [160]. The fragments are then analyzed by the TOF mass analyzer, where a known electric field is applied to accelerate ions, resulting in the same kinetic energy for ions with identical charge [160]. Therefore, the velocity of identically charged ions, and their time-of-flight, solely depends on their mass, heavier ions reaching the detectors later than the lighter ions.

A tandem-MS experiment of a mixture of peptides can yield large datasets, which are difficult to evaluate manually. Nowadays, tandem-MS data can be analyzed by readily available commercial softwares specialized to the analytes of interest. In this thesis, commercially available softwares and open databases were used to identify peptides and determine the corresponding protein species, as described in Chapters 7 and 9.

Most of the studies of the protein corona found in the literature begin with isolating the nanoparticle-protein bioconjugates, which is generally followed by the electrophoretic analysis of the corona constituents. The purification of the bioconjugates is often based on centrifugation, including differential centrifugation [36] and the use of a sucrose cushion [35], while the proteins are generally identified eventually with the help of mass spectrometry [32, 35, 36, 161, 162].

The formation of the protein corona is extensively studied in *in vitro* solutions. Tenzer and colleagues demonstrated that the size of the nanoparticles was the most deterministic trait of nanoparticles in the formation of the protein corona [163]. The group further discussed that the protein corona forms rapidly once the nanoparticle is introduced into the biomolecular system, and the building proteins do not change over time, only their relative concentration to each other [32]. The quantitative analysis of the protein corona is difficult due to the extensive purification of the nanoparticle-protein bioconjugates, but attempts have been made for the protein enumeration, for example, based on the average number of sulfur atoms in proteins with ICP-MS [35].

The proteomic analysis of the adsorbed proteins on nanoparticles in cell lysates can help approximate the expected interactions in live cells. It was found that in such an *in vitro* environment, different proteins interacted with the nanoparticles from those expected based on the surface functionalization of nanoparticles, and the adsorption of several immunoproteins can reflect on the biocompatibility of the used nanoparticles [37]. These results support that the engineered surface properties only influence the protein adsorption up to a certain extent, as discussed earlier. The possibilities of the therapeutic application of gold nanoparticles were demonstrated in experiments where cancer-specific proteins were found enriched in the protein corona even without the active processing of cells [34, 38].

Regardless of the extensive studies of the protein corona composition in different protein solutions, the intracellular formation of the protein corona is still poorly understood. Interestingly, the proteome of the cellular compartments in which internalized particles reside has been investigated for decades now [82, 83], but the protein corona formed inside the cells has still not been directly analyzed. The exchange of fluorescently labeled proteins was observed on the surface of intracellular nanoparticles, and the total intensity

of fluorescence informed about both the residence time of the nanoparticles in the cells and the cleavage of the serum proteins [69]. The intracellular protein corona composition was evaluated in rainbow trout gill cells, and with differential centrifugation, the protein corona complex was recovered, containing both hard and soft corona proteins [36]. Despite the significant advances in understanding the intracellular protein corona formation, these results yielded a list of proteins that may or may not interact directly with the nanoparticles' surface as a cellular response to their presence, and therefore, further studies are required for the analysis of the hard protein corona formed inside cells.

2.7. Cryo soft X-ray nanotomography in the studies of the cellular ultrastructure

SERS and mass spectrometric results corresponding to the protein corona can be complemented with ultrastructural information about the cells. Cryo soft X-ray nanotomography (XRT) provides three-dimensional information of vitrified cells, preserving them in their quasi-native state [164].

One of the biggest advantages of XRT is that cells can be vitrified in aqueous solutions, such as buffers used to maintain physiological conditions. This is allowed by the wavelength range of the X-ray radiation used in the experiments being typically in the so-called water window range of 2.34-4.38 nm, where water is completely transparent, while biomolecules absorb the light at different extents. With advances in the resolution of XRT, a pixel resolution below 10 nm was achieved [164], making it possible to locate intracellular nanoparticles and providing sufficient details about the state of the organelles.

Due to the generally high X-ray absorption of metallic nanoparticles, they can easily be identified in the intracellular compartments, and at the same time, they serve as fiducial markers in the reconstruction of the tomographic data. With the detailed analysis of the resulting data, it is not only possible to evaluate the cellular ultrastructure, but conclusions on the biomolecular processing of the internalized nanoparticles can also be drawn [39, 144, 165-168]. Drescher and colleagues showed based on XRT data combined with SERS experiments that silver nanoparticles form ring-shaped structures inside 3T3 cells, which can be related to the formation of a specific biomolecule corona [39]. The intracellular nanoparticle aggregation can also yield information about the effects of the nanoparticles:

the aggregate morphologies can be recovered after the virtual segmentation of the tomograms, which informs about the processes responsible for the aggregate formation inside cells [167, 168].

The overall ultrastructural changes yield crucial information about the state of the cells. Even the smallest change can be followed due to the well-characterized ultrastructural features of unaltered cells [169] if it is above the resolution limit of the microscope. For example, changes in lipid accumulation were found after treating eukaryotic cells with antidepressants, which could be concluded from the slightly higher absorption of the cellular compartments with the gold nanoparticles inside [144].

Chapter 3

Goals and contents of the thesis

The goals of this thesis are to reveal the governing interactions in gold nanoparticle-protein agglomerates and to elucidate properties of the hard protein corona formed in live cells by means of surface-enhanced Raman scattering (SERS), proteomics with mass spectrometry, and cryo soft X-ray nanotomography (XRT). Protein-nanoparticle interactions will be probed by SERS in *in vitro* solutions of pure proteins and of protein mixtures, respectively, to learn about the protein-nanoparticle interactions in aggregates. As a result of the variety of interacting molecules inside cells, the collected live cell SERS data are highly complex. By correlating live cell SERS data with those from protein-nanoparticle interactions, the contribution of proteins to the live cell SERS spectra can be discussed more in details. The live cell SERS data will be combined with the *ex situ* mass spectrometric analysis of the hard protein corona, which allows for the interpretation of the biomolecular environment of intracellular nanoparticles. A concept for the cellular processing of gold nanoparticles will be provided on the basis of the combined SERS and mass spectrometric data augmented with ultrastructural information of the cells revealed by XRT.

This thesis consists of ten chapters. The used chemicals, sample preparations, and experimental parameters are presented in Chapter 4. The results of this PhD work and their detailed discussion are described in Chapters 5 to 9, while Chapter 10 provides a summary of the thesis and the scientific outlook.

In Chapter 5, a refined sample preparation approach is proposed, and the results of SERS experiments in protein solutions with varying concentrations and in a DNA solution are shown. The data suggest that the proposed sample preparation approach is suitable for the SERS study of nanoparticle-biomolecule interactions without the interference of additional chemicals, and the high signal enhancement in live cell SERS experiments is due to the proper positioning of the intracellular aggregates rather than the crowded biomolecular environment only. The comparison of the SERS data acquired from the solutions of two highly similar proteins, bovine serum albumin and human serum albumin, is shown in Chapter 6. The results reveal specific protein-nanoparticle interactions, and binding sites were identified in the structure of human serum albumin during its interaction with gold nanoparticles. The data shown in Chapters 5 and 6 infer that SERS can be used for the more comprehensive analysis of protein-nanoparticle interactions in complex biomolecular systems. In Chapter 7, an analytical approach is provided for the extraction, purification, and analysis of the hard protein corona of gold nanoparticles formed inside cells. Chapter 8 details the comparison of SERS data acquired from live J774 cells and from their isolated cytoplasm. In combination with the data of enzymatically cleaved bovine serum albumin, the strong interaction of intracellularly cleaved proteins with the gold nanoparticle surface is revealed, while the spectral features of enzymatic cleavage, as well as different secondary structural elements, are discussed. In Chapter 9, the combination of the mass spectrometric analysis of the hard corona proteome, XRT experiments on vitrified cells, and live cell SERS data provides an in-depth discussion of the processing of gold nanoparticles in different cell lines and the formation of the hard protein corona, while concluding on the protein-nanoparticle surface interactions.

Chapter 4

Materials and methods

4.1. Materials

Gold(III) chloride trihydrate, McCoy's Modified 5A medium, bovine serum albumin (BSA), human serum albumin (HSA), bovine trypsin, Triton X-100, glacial acetic acid, N,N'-methylenebisacrylamide, tris(hydroxymethyl)aminomethane (Tris), 35% aqueous formaldehyde solution, sucrose, sodium dodecyl sulfate (SDS), ammonium persulfate (APS), ammonium hydrogencarbonate, bromophenol blue, glycerol, tetramethylenediamine (TEMED), Coomassie Brilliant Blue R-250, and ethylenediaminetetraacetic acid were purchased from Sigma-Aldrich (Steinheim, Germany). XTT cell proliferation assay kit was purchased from Caymanchem (Hamburg, Germany). NE-PER™ Nuclear and Cytoplasmic Extraction kit was purchased from Thermo Scientific (Brunswick, Germany). Acrylamide was purchased from Bio-Rad Laboratories (Madrid, Spain). Trisodium citrate dihydrate was purchased from Chemsolute (Renningen, Germany). 2-propanol and β-mercaptoethanol were purchased from Merck (Darmstadt, Germany). HPLC-grade acetonitrile, PageRuler™ Plus Prestained Protein Ladder, and HPLC-grade methanol were purchased from Fisher (Geel, Belgium). J774 macrophage cells from *Mus musculus*, 3T3 fibroblast cells from *Mus musculus*, A549 lung carcinoma cells from *Homo sapiens* were purchased from DSMZ

(Braunschweig, Germany). HCT-116 colorectal carcinoma cells and MCF-7 breast carcinoma cells from *Homo sapiens* were purchased from LGC Standards (Wesel, Germany). Dulbecco's Modified Eagle Medium (DMEM), fetal bovine serum (FBS), trypsin/EDTA solution, phosphate buffered saline (PBS), and ZellShield^{TM} were purchased from Biochrom (Berlin, Germany). 90% and 70% ethanol were purchased from VWR Chemicals (Fontenay-sous-Bois, France). Milli-Q water was used in all experiments.

4.2. Preparation of gold nanoparticles

~30 nm citrate-stabilized gold nanoparticles were used in every experiment throughout the whole project. In each experiment, where the comparison of two or more data sets was a key element, the same aliquot of gold nanoparticles was used to facilitate the data interpretation.

Gold(III) chloride trihydrate and trisodium citrate dihydrate were used for gold nanoparticle synthesis by the recipe described in [170]. Prior to the synthesis, a 500 mL three-neck round bottom flask was cleaned with *aqua regia*. 200 mL of Milli-Q water was measured into the flask, a glass tube with a cooling coil inside was attached to the flask, then 300 µL of 0.25 M aqueous gold(III) chloride solution was pipetted into the flask. The solution in the flask was continuously stirred, and a water bath was placed beneath the flask to heat the system up to ~85 °C. The system was covered with an aluminum foil to protect it from direct light. 40 mg trisodium citrate dihydrate was dissolved in 4 mL Milli-Q water, and this solution was quickly transferred into the flask with the gold(III) chloride solution when the temperature reached 85 °C. After 35 min, the stirring was switched off, the water bath was removed, and the system was let to cool down to room temperature. The resulting clear, red colloid was transferred into a glass bottle, which was kept from direct light.

The nominal nanoparticle concentration was 0.4 nM, which was calculated based on the diameter distribution of 155 gold nanoparticles (32±7 nm) by the following formula:

$$c_{\mathrm{AuNP}} = \frac{n_{\mathrm{Au}} \times M_{\mathrm{Au}}}{\rho_{\mathrm{Au}} \times \frac{4}{3}\pi \mathrm{r}^3 \times V_{\mathrm{tot}} \times N_A} \qquad (3)$$

where c_{AuNP} is the nominal gold nanoparticle concentration, n_{Au} is the amount of gold added for the synthesis in moles, M_{Au} is the molar mass of gold in g/mol, ρ_{Au} is the density of gold in g/cm^3, r is the averaged radius of gold nanoparticles in cm, V_{tot} is the total volume of the synthesis mixture in L, and N_A is the Avogadro constant. The final pH of the synthesis product was 4.54.

The synthesis protocol described by Lee and Meisel in 1982 was chosen to synthesize gold nanoparticles as the resulting ~30 nm average size (compare with Figure 4.1) and the 0.4 nM nominal stock concentration are reportedly adequate for the SERS investigation of biologically relevant molecules with a signal enhancement of 10^8 [171] and living cells as well [40, 42].

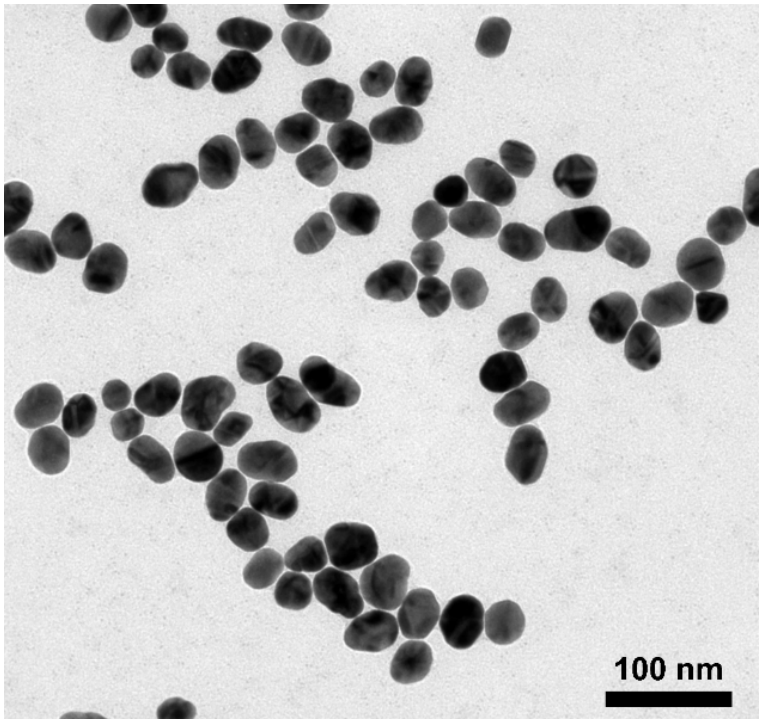

Figure 4.1. 30 nm citrate stabilized gold nanoparticles synthesized based on the protocol described by Lee and Meisel [170].

4.3. Cell cultivation of different cell lines

Two-dimensional cell lines were used in several experiments, such as live cell SERS mapping, the study of the intracellularly formed hard protein corona, the extraction of cytoplasm, and the extraction of DNA.

J774 macrophage cells and 3T3 fibroblast cells from *Mus musculus*, and A549 lung carcinoma, HCT-116 colorectal carcinoma, and MCF-7 breast cancer cells from *Homo sapiens* were cultivated identically, with minor changes in the passaging of J774. In most cases, cells were cultivated in Dulbecco's Modified Eagle Medium supplemented with 10 vol% FBS (further referred to as DMEM-FBS), and if not stated otherwise, the phrase "culture medium" refers to this mixture. In some cases, McCoy's Modified 5A Medium was supplemented with 10 vol% of FBS (further referred to as McCoy-FBS) and was used as culture medium for the cultivation of HCT-116 and A549 cells.

4.3.1. Passaging of the cell culture

The cells were cultured under standard cultivating conditions at 37 °C in humid air with 5% CO_2 as described in ref. [145]. Prior to passaging cells, the working bench with laminar airflow was sterilized with UV light for 15 min, followed by the sterilization of every used surface with 70% ethanol. The health of the cell cultures was observed under a light microscope. Then, the culture medium was exchanged for 8-10 mL PBS without calcium- and magnesium ions to carefully rinse the adherent cells and remove detached cells and the remaining culture medium. The PBS was removed, and 1-2 mL trypsin-EDTA solution was added to the cell flask. The detaching cells were observed with a light microscope, and then the cell culture flask was placed back to the incubator (37 °C, 5% CO_2) for 8-12 min depending on the confluence of the adherent cell layer. After the incubation time, the trypsinization was terminated by the addition of 4-5 mL of the cell culture medium, due to the excess of serum proteins compared to the amount of trypsin. The cell suspension was collected into a 10 mL conical centrifuge tube, and it was centrifuged for 10 min at 4 °C and 1500 rpm. The supernatant was then exchanged for 5 mL of fresh culture medium, and the cell pellet was carefully resuspended. ~300,000 cells were transferred into a new cell culture flask with fresh culture medium. The second and third cycles of passaging were done with a culture medium supplemented with 1% of the antibiotic ZellShield™.

In the case of J774 cells, the trypsinization step was omitted, and after the addition of PBS (with calcium- and magnesium ions), the cells were detached from the bottom of the flask with a microbiological scraper.

4.3.2. Cell sample preparation for SERS mapping

After the passaging of cells, 30,000-60,000 cells were transferred onto a sterilized microscopy glass slide, which was previously placed into a well of a 6-well plate with 2 mL of culture medium. After at least 24 h, the culture medium was removed, 900 µL of the chosen cell culture medium was mixed with 100 µL of the gold nanoparticles, and it was pipetted into the well that contained the glass slide with the adherent cells. After the chosen incubation time of 1.5 h or 24 h, the culture medium and the gold nanoparticles were removed, and the sample was carefully rinsed with PBS three times. Then, the sample was transferred to the Raman microscope for SERS experiments in PBS. The corresponding samples are discussed in Chapters 8 and 9.

4.3.3. Cell sample preparation for the extraction of the hard protein corona

After the passaging of the cells, ~100,000 cells were transferred into a 25 cm^2 cell culture flask with 5 mL DMEM-FBS culture medium. After at least 24 h, the culture medium was exchanged for the mixture of 4.5 mL of the culture medium and 500 µL of the gold nanoparticles, and the cells were left to be incubated with the gold nanoparticles for 1.5 h, 3 h, 6 h, or 24 h. The corresponding samples are discussed in Chapters 7 and 9.

4.3.4. Cell sample preparation for DNA or cytoplasm extraction

After passaging the cells, ~100,000 cells were transferred into a cell culture flask with 5 mL of the chosen culture medium, and the cells were left to grow in an incubator (37 °C, 5% CO_2) until the adherent cell layer reached a confluence of ~90%. The corresponding samples are discussed in Chapters 5 and 8.

4.4. Instrumentation and experimental parameters of normal Raman and SERS experiments with protein solutions

The specifications of SERS experiments on protein solutions were described in refs. [171, 172]. Normal Raman experiments were performed as control experiments prior to protein SERS, which served both as the basis of band comparison to understand nanoparticle-

protein interactions [171, 172] and as a reference of signal intensity to estimate signal enhancement [171].

Normal Raman and SERS spectra were measured with a microspectroscopic setup containing a single-stage spectrograph equipped with a liquid-nitrogen-cooled charge-coupled device detector. Excitation of the Raman scattering was done in 180° backscattering geometry through a 60× immersion objective (Olympus, Germany) using a wavelength of 785 nm with a laser intensity of 5.7×10^5 W/cm^2.

Spectra were collected from the ~10 fL focal volume created in droplets of 50 µL sample solution without (normal Raman) or with gold nanoparticles (SERS) on CaF_2 slides. The acquisition times per spectrum varied between 1 s and 120 s depending on the sample.

In the SERS experiments of proteins, the excitation light was focused on randomly chosen microscopic nanoparticle-protein aggregates, and approximately 100 SERS spectra were collected, except for the sample simulating intracellular protein concentrations where the nanoparticle-protein aggregate formation was not observed.

4.5. Studies of the SERS signal dependency on protein concentration

The results corresponding to this section are discussed in Chapter 5.

4.5.1. Normal Raman experiments at intracellular protein concentration

For the normal Raman experiments aiming at simulating the crowded biomolecular environment in cells [171], the bovine serum albumin (BSA) concentration was chosen to be in the range of intracellular protein concentration values (based on data from previous work, this range corresponds to a concentration interval of 0.02-0.55 g/mL for BSA) [173]. 0.5 g of BSA was dissolved in 1 mL Milli-Q water. The resulting solution was highly viscous. 50 µL of this solution was transferred to a CaF_2 slide, and Raman spectra were collected from the droplet with an acquisition time of 10 s.

4.5.2. SERS experiments on BSA solutions at different concentrations

In the SERS experiments aiming at investigating the effect of protein concentration on the SERS signal, mixtures of gold nanoparticles and BSA were prepared at different gold nanoparticle : BSA molar ratios [171]. The final nominal concentration of gold nanoparticles in the SERS experiments was estimated to be in the range of 0.3-0.4 nM.

In the first experiment, to simulate the crowded intracellular environment of internalized gold nanoparticles, a sample with a gold nanoparticle : BSA ratio of $1:10^7$ was prepared by mixing 50 µL 0.5 g/mL protein solution with 100 µL gold nanoparticles, corresponding to a three-fold dilution of the initial solution of 0.5 g/mL, and yielding a final protein concentration in the range of intracellular protein concentration (0.15 g/mL) [173]. The SERS spectra were collected immediately after sample preparation with an acquisition time of 5 s.

In the second experiment, a sample with a gold nanoparticle : BSA molar ratio of 1:40000 was prepared by adding 5 µL of 0.01 g/mL BSA solution to 50 µL of gold nanoparticles (final BSA concentration of ~15 µM). In the light microscope, micrometer-sized protein-nanoparticle agglomerates were observed. Focusing on the bottom of the droplet, where the precipitated aggregates had settled, SERS spectra were collected with an acquisition time of 1 s immediately after sample preparation.

In the third experiment, the 0.01 g/mL BSA solution was diluted 10^5-fold, and 5 µL of this BSA solution was added to 50 µL of the gold nanoparticles to obtain samples with a protein concentration of ~150 pM, corresponding to a molar gold nanoparticle : BSA ratio of 2.5:1. The samples were incubated for 90 min before SERS spectra were measured focusing on the settled aggregates, with an acquisition time of 1 s.

4.6. Experiments with bovine serium albumin and human serum albumin

Normal Raman and SERS experiments were performed to differentiate between BSA and human serum albumin (HSA). The results corresponding to this section are discussed in Chapter 6.

4.6.1. Sample preparation for normal Raman experiments on albumins

In the comparative study of BSA and HSA [172], normal Raman spectra were collected from their respective solutions with a concentration of 0.1 g/mL (corresponding to a concentration of 1.5 mM), which is comparable with the total protein level of blood serum [174, 175]. In these experiments, 50 µL of the protein solutions were respectively transferred onto a CaF_2 slide, and normal Raman spectra were collected with an acquisition time of 120 s.

4.6.2. Sample preparation for SERS experiments on albumins

For the comparative SERS studies of BSA and HSA, 150 µM solutions were prepared. 0.01 g BSA and 0.01 g HSA were respectively dissolved in 1 mL Milli-Q water. 5 µL of the respective protein solution was added to 50 µL of the gold nanoparticles, then 50 µL of this mixture was transferred to a CaF_2 slide, and SERS experiments were performed with an acquisition time of 1 s as described above.

4.7. Sample preparation for SERS studies of DNA

For the DNA extraction from 3T3 cells, the culture medium was removed from a cell flask containing an adherent cell layer with ~90% confluence, and the cells were rinsed with PBS. After detaching the cells from the bottom of the flask by trypsin-EDTA solution, the collected cell suspension was centrifuged (4 °C, 14,000 rpm), which resulted in a cell pellet. This pellet was resuspended in 100 µL water, and full cell lysis was performed by repeating the cycle of freezing in liquid nitrogen and thawing in a 37 °C water bath four times. The sample was centrifuged, the supernatant was transferred to a new Eppendorf® tube, and the sediment with the cell debris was discarded. Ice-cold 70% ethanol was added to the supernatant for the precipitation of DNA, and the sample was then centrifuged. After discarding the supernatant, the remaining DNA pellet was resuspended in pure ethanol and centrifuged once more to make sure that all the proteins were removed. Following the centrifugation, the supernatant was discarded, the DNA pellet was dried, then dissolved in 1 mL Milli-Q water. 5 µL of this solution was added to 50 µL of gold nanoparticles, consistent with SERS experiments on protein solutions. 50 µL of the sample was transferred onto a CaF_2 slide, and SERS spectra were collected

identically to the SERS experiments on protein solutions with an acquisition time of 1 s. The corresponding results are discussed in Chapter 5.

4.8. Sample preparation for SERS studies of enzymatic cleavage

The results corresponding to this section are discussed in Chapter 8.

4.8.1. Control SERS experiments of BSA and trypsin

SERS experiments of BSA and trypsin were performed to collect comparative data of the pure proteins. 0.01 g/mL BSA and 0.0035 g/mL bovine trypsin solutions were respectively prepared to reach the identical protein concentration of 150 µM. Due to the self-digestion of trypsin, the solution was always prepared immediately before the experiments. 50 µL of the gold nanoparticles were mixed with 5 µL BSA or trypsin solution, respectively. 50 µL of the protein-nanoparticle mixture was transferred onto a CaF_2 slide, and SERS spectra were collected with an acquisition time of 1 s immediately after sample preparation.

4.8.2. Sample preparation for studies of BSA trypsinization

SERS spectra of the digestion of BSA by bovine trypsin were collected from the same aggregate of the same sample as the SERS spectra of the pure BSA solution to ensure the best basis of comparison. First, 50 µL of gold nanoparticles were mixed with 5 µL of 0.01 g/mL BSA solution, which resulted in the formation of microscopic aggregates. 50 µL of this sample was transferred onto a CaF_2 slide, and the focus was set on a settled aggregate, and 100 SERS spectra were collected. Then, while making sure from the live feed of the light microscope that the aggregate remained steady, 5 µL of the 0.0035 g/mL bovine trypsin solution was added to the sample. After waiting 1 min for the trypsinization of BSA, 100 SERS spectra were collected from the same sample position. After the spectrum collection, it was observed that the size of the settled aggregates decreased while their number increased, allowing for the conclusion that the trypsinization of BSA was successful.

4.9. Extraction and SERS experiments of the J774 cytoplasm

To understand the interactions and the environment of gold nanoparticles in the different cellular compartments in which they are localized, SERS studies on the extracted cytoplasm were performed.

J774 macrophage cells were cultured as described above, then NE-PER™ Nuclear and Cytoplasmic Extraction kit was used to break the cell walls and isolate the cytoplasmic fraction. After the extraction, the sample was diluted to double volume with Milli-Q water to lower the signal contribution of non-specific interactions between the nanoparticles and the detergent molecules. 5 µL of the diluted cytoplasmic extract was mixed with 50 µL of gold nanoparticles. Then, the sample was incubated for 90 min to be comparable with live cell SERS data, then 50 µL of it was transferred onto a CaF_2 plate, and SERS spectra were collected identical to the SERS studies of protein solutions with 1 s acquisition time.

The SERS spectra of the chemicals used in the extraction of the cytoplasm (CER I, CER II, and the NER agents) were also collected and compared with the SERS spectra of the isolated cytoplasm. It was observed that these chemicals did not contribute significantly to the SERS spectra of the isolated cytoplasm. The corresponding results are discussed in Chapter 8.

4.10. Live cell SERS mapping

The microscopy glass slides were placed on a CaF_2 slide and the SERS spectra were collected in the same microspectroscopic setup as described in Section 4.4. The experiments were performed in PBS, which proved to be sufficient to keep the cells intact for the length of the SERS experiments of ~1.5 h. Healthy cells were chosen, and SERS spectra were collected through a 60× water immersion objective (Olympus, Germany) in a virtually marked rectangular area with 1 µm step sizes, with an excitation wavelength of 785 nm, an acquisition time of 1 s, and a laser intensity of 2.3×10^5 W/cm^2. The lower laser intensity was chosen for the live cell SERS mapping than for the SERS experiments on protein solutions to make sure the cells remain intact throughout the whole SERS

mapping experiment. The results of such live cell SERS experiments are discussed in Chapters 8 and 9.

4.11. Data pre-processing and analysis

4.11.1. Pre-processing of the data

All spectra were de-spiked and frequency-calibrated using a spectrum of the 1:1 mixture of acetonitrile and toluene. To avoid the influence of the intensity and the background fluctuation of SERS spectra, further data treatment before averaging and principal component analysis (PCA) was applied. First, the spectra were background corrected based on an asymmetric least squares algorithm (ASLS) [176]. After the background correction, the spectra were vectornormalized, which means that first, the spectra were mean-centered, then divided by the square root of the sum of the squared mean-centered intensities [177].

4.11.2. Principal component analysis

After pre-processing, the PCA of the spectra was performed in MatLab in the spectral range of 400 cm^{-1} to 1800 cm^{-1}. First, the spectra were interpolated and smoothed based on the Savitzky-Golay algorithm [178], then the first derivatives of the spectra were calculated, and PCA was performed. PCA results of SERS spectra are discussed in Chapters 6 and 8.

4.11.3. Calculation of band occurrences

Since the datasets always consisted of at least 100 SERS spectra, which, due to the characteristics of SERS, often showed different spectral profiles, one of the most essential data analysis approach of this work was the analysis of the abundance of bands in whole datasets, that is, band occurrences. Band occurrences in whole SERS datasets are discussed in Chapters 8 and 9.

First, the pre-processed spectra were interpolated, and an empty spectrum was also chosen as reference. Integrals of the spectra were calculated by a moving integral window of ±10 cm^{-1} around the central wavenumber, with 5 cm^{-1} central wavenumber steps. The as-

calculated integrals at every central wavenumber were compared to the average of the resulting integrals of the empty spectrum. If the calculated integral at a central wavenumber exceeded the threshold of five times the average of the integrals calculated from the empty spectrum, which, after the ASLS background correction referred to the average integral of the standard deviation of the noise, the script registered that the chosen spectrum exhibits a band at the given central wavenumber. This comparison was performed in each spectrum at every central wavenumber, and the results were summed up into a dataset of the band occurrences in the whole dataset. In these data, the co-occurrence of chosen bands could also be analyzed, which provided a more comprehensive insight into the nanoparticle-protein interactions.

There are some important considerations regarding the band occurrence graphs. The width of a peak corresponds to the probability of finding the same vibration at given distances from the local maximum, *i.e.,* to band shifts, rather than the width of the original band. Furthermore, the integrals were calculated in the 1800 cm^{-1} – 400 cm^{-1} spectral region with 5 cm^{-1} step sizes. The positions of the local maxima in the band occurrence curves were assigned based on the band positions in the average spectra, when the deviation from the calculated maximum was less than 4 cm^{-1}. This was consistent with the spectral resolution of the collected SERS data, calculated to be 3-4 cm^{-1} over the whole spectral range. When the difference between the wavenumber of a band in the average spectrum and that in the calculated relative band occurrence curve was more than 4 cm^{-1}, the calculated local maximum was discussed separately in the text.

4.12. Structural comparison of BSA and HSA

To understand the protein-nanoparticle interactions based on the SERS data of BSA and HSA, their protein sequences and structural data also had to be compared to shed light on any difference in their primary, secondary, or tertiary structure (see in Chapter 6). The data were obtained from PDB – Protein Data Bank [179], with the PDB IDs 4OR0 [180] and 5ID7 [181] for BSA and HSA, respectively. The protein data were loaded into VMD – Visual Molecular Dynamics [182], which was used to visualize the different segments or the chosen residues in the three-dimensional protein structures.

4.13. UV-vis absorbance experiments

Gold nanoparticles and the samples containing a BSA solution-nanoparticle mixture with a molar gold nanoparticle : BSA ratio of 1:40000, and of 2.5:1, respectively, were measured in a quartz cuvette, and spectra were acquired with a Jasco V-670 spectrometer in the wavelength range of 300-1000 nm. The corresponding results are discussed in Chapter 5.

4.14. Brownian motion of the gold nanoparticles in the protein solutions

The displacement of the nanoparticles in a solution is discussed in Chapter 5, and it can be described as

$$< r^2 > = \frac{2k_B T}{3\pi\eta\alpha} t \tag{4}$$

where $<r^2>$ is the time-averaged two-dimensional displacement of the particle, k_B is the Boltzmann constant, T is the temperature, t is the time, η is the dynamic viscosity, and α is the particle radius [183]. The viscosity of BSA solutions changes exponentially with the concentration:

$$\eta = \eta_0 \, e^{\frac{[\eta]c}{1-\frac{k}{v}[\eta]c}} \tag{5}$$

where η is the dynamic viscosity, η_0 is the viscosity of the solvent, $[\eta]$ is the intrinsic viscosity in mL/g, k is the self-crowding factor, v is the Simha shape parameter, and c is the BSA concentration in g/mL [184]. The viscosity of the SERS sample for the different gold nanoparticle : BSA ratios was estimated by substituting η_0 with 0.8 cP (approximate viscosity of the nanoparticle colloid [185]), $[\eta]$ with 3.8 mL/g (at pH=4.54) [186], and the k/v ratio with 0.45, as determined by Yadav *et al.* [184].

4.15. Soft cell lysis and extraction of hard corona proteins

MCF-7 and J774 cells were cultured and incubated with gold nanoparticles for the extraction of the hard corona proteins as described in Section 4.3.3. The incubation times varied depending on the purpose of the experiment; Since MCF-7 internalized gold

nanoparticles very slowly in preliminary experiments, only 24 h incubations were performed on this cell line, while J774, which showed fast nanoparticle uptake in previous studies, were incubated with gold nanoparticles for 1.5 h, 3 h, 6 h, or 24 h. Each cell culture sample underwent soft lysis after the incubation time was over. An aliquot of 150 µL of lysis buffer (150 mmol L^{-1} NaCl, 1 mmol L^{-1} ethylenediaminetetraacetic acid, 20 mmol L^{-1} tris(hydroxymethyl)aminomethane, < 1% (v/v) Triton X-100) was added to a 25 cm^2 cell culture flask with a cell culture of 75-90% confluence determined by light microscopy, and after keeping the flask on ice for 10 min, 850 µL PBS (with the original 1× concentration) was added to the lysate and transferred to an Eppendorf tube. The lysates were stored on ice during the short time (~5 min) between the lysis and the corona protein purification to lower the probability of protein desorption from the surface of the nanoparticles due to the concentration changes during the lysis. The nanoparticle-protein bioconjugates were separated from the cell debris by centrifugation following a purification protocol previously described [35, 187]; The lysates were centrifuged (10,000×g, 5 min, 4°C) to collect the cell debris in the sediment, then they were ultrasonicated for 1 min to free the bioconjugates trapped in the debris. After waiting for 15 min for the debris to sediment again, the supernatant containing the cytoplasm and the protein-nanoparticle bioconjugates was transferred to a new Eppendorf® tube, and the cell debris was discarded. Non-bound proteins and those that only weakly interact with the hard corona were removed with the help of a sucrose cushion (18,000×g, 30 min, 4°C) with a sucrose concentration of 0.7 M. The supernatant with the sucrose above the sediment of the nanoparticle-protein bioconjugates was exchanged for PBS, the sediment was resuspended, and the sample was centrifuged again (18,000×g, 5 min, 4 °C). This purification step was repeated three times, in the last cycle, a 10-fold dilution of PBS was used to reduce the interference of dissolved salts in the separation [188]. After the last centrifugation step, the supernatant was carefully removed, and its volume was reduced to 50-100 µL, and the samples were kept at 4 °C until further analysis.

4.16. Sample preparation for the time-resolved study of the hard corona composition

J774 mouse macrophage cells were incubated with gold nanoparticles for 1.5 h, 3 h, 6 h, and 24 h, ranging from the formation of early endosomes until over the total cell cycle of

J774 cells, which is reported to be ~19 h [189]. After the incubation, the cell cultures underwent soft cell lysis, and the hard corona proteins were purified as described later in Section 4.18. The results of these experiments are discussed in Chapter 7.

4.17. Sodium dodecyl sulfate-polyacrylamide gel electrophoresis

Sodium dodecyl sulfate-polyacrylamide gel electrophoresis (SDS-PAGE) was performed to separate the hard corona proteins based on their molecular masses and facilitate their identification in subsequent mass spectrometric experiments. Each incubation condition was investigated in at least two parallel samples. Denaturing SDS-PAGE experiments were performed based on the protocol described in refs. [35, 190].

Polyacrylamide gels were hand-cast with a total acrylamide concentration of 12%, which allowed for the resolution of low-mass protein species as well. The necessary solutions for gel casting, sample pre-treatment, electrophoresis, gel fixing, and gel staining are detailed below.

30% acryl-bisacrylamide solution

29 g acrylamide and 1 g of N,N'-methylenebisacrylamide were dissolved in 60 mL Milli-Q water. To facilitate the dissolution of the chemicals, the container was kept in a 37 °C water bath. After the dissolution was complete, the volume was adjusted to 100 mL with Milli-Q water, and the solution was stored at 4 °C protected from light. The measuring of the acrylamide and N,N'-methylenebisacrylamide and their dissolution in Milli-Q water were performed with high caution using laboratory gloves and face masks, due to the health hazards of acrylamide.

0.5 M Tris-HCl (pH 6.8)

6.06 g of tris(hydroxymethyl)aminomethane (Tris) was dissolved in 100 mL Milli-Q water, and the pH was adjusted to 6.8 with droplets of ~37% HCl solution using a pH-meter.

1.5 M Tris-HCl (pH 8.8)

18.17 g of Tris was dissolved in 100 mL milli-Q water, and the pH was adjusted to 8.8 with droplets of ~37% HCl solution using a pH-meter.

10% SDS

1 g of sodium dodecyl sulfate (SDS) was dissolved in 10 mL Milli-Q water.

10% APS

100 mg ammonium persulfate (APS) was dissolved in 1 mL Milli-Q water. This solution was always prepared immediately before use.

Running buffer

3 g of Tris, 14.4 g of glycine, and 1 g of SDS were dissolved in 1 L of Milli-Q water with a final pH of 8.3.

Sample buffer

First, 100 mg bromophenol blue was dissolved in 10 mL Milli-Q water to prepare a 1% solution. Then, 1.25 mL of the 0.5 M Tris-HCl (pH 6.8) solution, 2 mL of the 10% SDS solution, 2.5 mL of glycerol, and 100 µL of the 1% bromophenol blue solution were mixed, and the volume was adjusted to 10 mL with Milli-Q water. The solution was divided into 0.950 mL aliquots, which were stored at -20 °C. Prior to use, an aliquot was thawed at room temperature, and 50 µL of β-mercaptoethanol was added before mixing with the sample.

Fixing solutions

The electrophoretic gels were fixed with two different fixing solutions based on their further use. The electrophoretic gels prepared for analysis by mass spectrometry were fixed with acetic acid and methanol because this method enables the extraction of peptide segments after in-gel digestion [35, 190, 191]. Some low-mass protein molecules, especially those with a basic pI, tend to be more challenging to be precipitated with the acidic solution [192]. In such cases, where preventing the elution of low-mass polypeptides was necessary, the fixation of protein molecules in the gel was facilitated by formaldehyde, which resulted in the chemical cross-linking of proteins in the gel [192,

193]. Even though the fixation based on the chemical cross-linking is favored to retain a higher amount of protein molecules, due to the occurring chemical modifications, this fixation method is not advised for the further mass spectrometric analysis of the proteins [194].

For the acetic acidic fixation, 200 mL methanol, 50 mL glacial acetic acid, and 250 mL Milli-Q water were mixed, and the solution was stored at room temperature.

The fixing solution with formaldehyde was prepared by mixing 50 mL ~36% formaldehyde, 90 mL ethanol, and 220 mL Milli-Q water, then stored at room temperature.

Coomassie blue staining solution

2.5 g Coomassie Brilliant Blue R-250 were dissolved in a mixture of 450 mL methanol, 100 mL glacial acetic acid, and 450 mL Milli-Q water. The solution was stirred until the dye completely dissolved, then filtered and stored at room temperature.

De-staining solution

To remove the excess of Coomassie blue dye, a de-staining solution was prepared by mixing 450 mL methanol, 100 mL glacial acetic acid, and 450 mL Milli-Q water. The solution was stored at room temperature.

Hand-casting polyacrylamide gels

Polyacrylamide gels were hand-cast in a Mini-PROTEAN® Tetra Handcast System (Bio-Rad Laboratories, Madrid, Spain). A schematic illustration of the assembled gels is shown in Figure 4.2. The first step after assembling the hand-casting system was to prepare a sealing gel layer at the bottom of the cast to prevent the gel from leaking out. The sealing gel was mixed according to a running gel with 12% acrylamide to avoid insufficient resolution due to differences in the running- and sealing gels. 3.3 mL Milli-Q water, 4.0 mL 30% acryl-bisacrylamide solution, 2.5 mL 1.5 M Tris-HCl (pH 8.8) solution, and 100 µL 10% SDS solutions were mixed, and the resulting solution was aliquoted into 500 µL samples. Prior to use, 10 µL APS and 1 µL TEMED were added to a 500 µL aliquot, the solution was thoroughly homogenized, and 450 µL of it was rapidly pipetted to the bottom of the gel cast. ~2 mL of 2-propanol was spread on top of the sealing gel

before the polymerization to remove air bubbles from the surface and to keep the homogeneity of the gel. The sealing gel polymerized in less than 2 min, the 2-propanol was removed, the surface of the sealing gel was rinsed with Milli-Q water, and the excess of water was removed with the help of a clean paper towel.

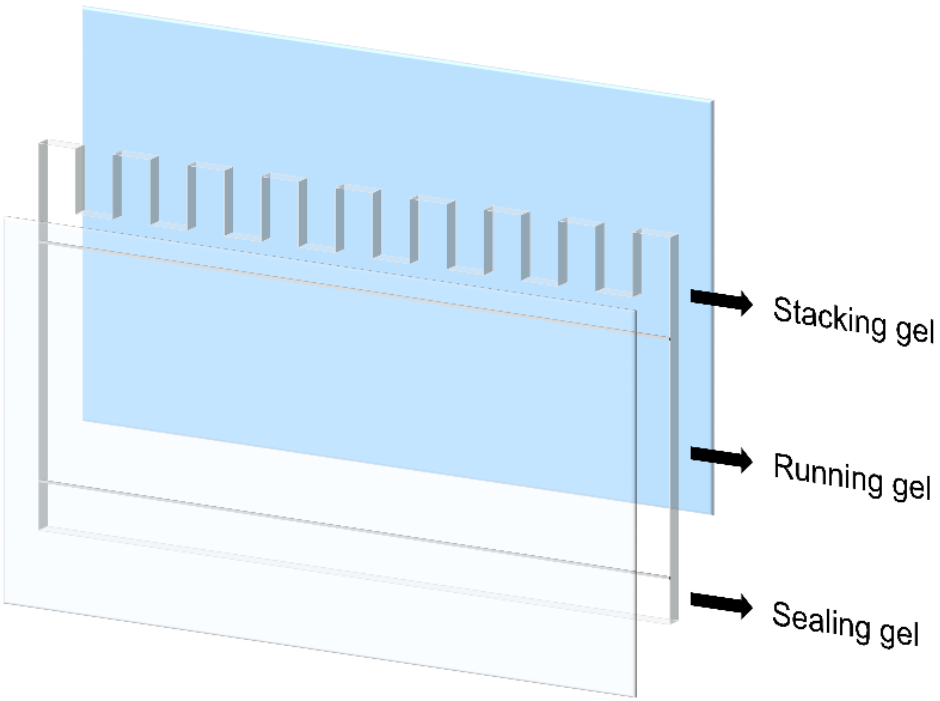

Figure 4.2. Schematic illustration of the different layers of the hand-cast gels.

As a result of using a sealing gel layer, the length of the running gel was shortened, which resulted in a decreased resolution of protein bands in the gel. Therefore, a higher acrylamide concentration was used to reduce the pore sizes in the gel, which increased the resolution of the protein bands. The running gel with ~16% acrylamide content for two gels was prepared by mixing 2.0 mL Milli-Q water, 5.3 mL 30% acryl-bisacrylamide solution, 2.5 mL 1.5 M Tris-HCl (pH 8.8) solution, 100 µL 10% SDS solution, 100 µL 10% APS solution, and 8 µL TEMED. The solution was carefully homogenized to avoid bubble formation, and it was divided between two gel casts. The casts were filled with the running gel up to a level that was previously determined to be 5 mm below the stacking gel comb to ensure the proper assembly of the gels. 2-propanol was poured over the gels in the casts to remove the bubbles on the surface of the gel, and the gels were left

to polymerize for an hour. After the running gels were polymerized, the 2-propanol was removed, the surface of the gels was carefully rinsed with Milli-Q water, and the excess of water was removed with a clean paper towel.

The stacking gel for two gels was prepared by mixing 3 mL Milli-Q water, 660 µL 30% acryl-bisacrylamide solution, 1.26 mL 0.5 M Tris-HCl (pH 6.8) solution, 50 µL 10% SDS, 50 µL 10% APS, and 5 µL TEMED. The solution was carefully homogenized while avoiding bubble formation, and it was poured over the running gels. A stacking gel comb was inserted into both casts prior to the polymerization of the stacking gel to form the pockets for the protein samples. The gels were kept still for an hour to ensure a complete, homogeneous gel polymerization. After the gels were assembled, the protein samples were prepared for SDS-PAGE.

The previously extracted corona proteins were mixed with the sample buffer containing β-mercaptoethanol in 1:1 ratio resulting in a complete sample volume of 40 µL and kept in a hot water bath at 95 °C for 5 min. Then, the stacking gel combs were removed, 20 µL of the samples with the denatured proteins were respectively loaded into separate gel pockets, and electrophoretic separation was performed by applying 120 V for 60 min on the gels in a Mini-PROTEAN Tetra Cell (Bio-Rad Laboratories, Madrid, Spain) filled up with the running buffer. Each gel was additionally loaded with 8 µL of PageRuler™ Plus Prestained Protein Ladder to mark protein masses in the 10-250 kDa range, and a control sample containing 20 µL sample buffer with 20 µL Milli-Q water, treated identically to the corona protein samples, to make sure the sample buffer and the gels were exempt of protein contamination prior to the separation.

After the 60 min of electrophoresis, the gels were collected and carefully rinsed with Milli-Q water. The stacking gel was separated from the running gel, and it was discarded. Then, the running gels were carefully transferred into a container filled with the chosen fixing solution and agitated for 30 min or 60 min in the case of fixing with acetic acid or formaldehyde, respectively. After the gel fixation, the fixing solution was exchanged for Coomassie blue staining solution, and the gels were stained for ~1.5 h. After staining, the Coomassie blue solution was exchanged for the de-staining solution. The de-staining solution had to be exchanged 3-6 times until the protein bands were visible in the gel.

After the successful de-staining of the gels, they were stored in 20% ethanol at 4 °C until further use. The results of SDS-PAGE experiments are discussed in Chapters 7 and 9.

4.18. In-gel protein digestion and peptide extraction

For the HPLC-ESI-Q-TOF-MS analysis of the hard corona proteins, the proteins in the polyacrylamide gels had to be cleaved, and the resulting peptides were extracted.

The gel segments of interest were carefully excised with a surgical scalpel and were transferred into separate, pre-labeled Eppendorf® tubes. This step was crucial in the mass spectrometric analysis, because the information of the approximate molecular mass was preserved, and the noise of the mass spectra was reduced by excluding the gel segments without visibly stained protein bands. The in-gel digestion and the peptide extraction protocols are detailed below for one Eppendorf® tube, which was generally used for every sample.

To de-stain the protein bands, 1 mL of 25 mM NH_4HCO_3 was added to the Eppendorf® tube, which was then kept in a 25 °C water bath for 30 min. Afterward, the solution was exchanged for the mixture of 500 µL acetonitrile and 500 µL 25 mM NH_4HCO_3, and the Eppendorf® tube was placed back into the 25 °C water bath for 30 min. These two steps were repeated 3-5 times until the protein bands were completely de-stained.

Following the de-staining, the excised gel segment was cut into small, ~1-4 mm^2 pieces, which were placed into a new, pre-labeled Eppendorf® tube corresponding to the initially excised gel segment. The gel slices were kept in 50 µL of acetonitrile for 10 min to remove the water from the gel, then the supernatant was discarded, and the Eppendorf® tube was placed into an Eppendorf Concentrator 5301 centrifugal evaporator operated at 30 °C until the gel slices were completely dried. 100 µg mass spectrometry grade porcine trypsin were dissolved in 25 µL of the provided trypsin buffer, and 975 µL of 25 mM NH_4HCO_3 were mixed with the trypsin solution. The volume of this trypsin-NH_4HCO_3 solution added to the dried gel slices was determined to be enough to cover all the gel slices in the Eppendorf tube, which was then placed in a 37 °C water bath and was kept there overnight. The Eppendorf tube was then transferred to a -80 °C freezer to stop the in-gel trypsinization and was kept there for at least 1 h. After thawing the sample, the supernatant was transferred to a new Eppendorf® tube designated to collect the extracted,

dissolved peptides. 50 µL acetonitrile was added to the Eppendorf® tube with the gel slices, which was kept in the water bath at 37 °C for 30 min, followed by 15 min ultrasonication; then, the supernatant was transferred to the Eppendorf® tube with the extracted, dissolved peptides. This step was repeated with adding 50 µL of 5% formic acid, then once again with 50 µL acetonitrile. After transferring the acetonitrile supernatant to the Eppendorf® tube with the extracted, dissolved peptides, the gel slices were discarded, and the solvents from the Eppendorf® tube with the extracted peptides were completely evaporated in the rotary evaporator operating at 30 °C for 24 h. The dried samples were kept at -150 °C in a freezer until further analysis.

4.19. Experimental details of the HPLC-ESI-Q-TOF-MS analyses

The dried, extracted peptides were dissolved in 12 µL of the aqueous solution of 2% acetonitrile and 0.1% formic acid and were ultrasonicated for 15 min.

Gradient HPLC separation by an UltiMate 3000 instrument (Thermo Scientific) was performed in a Europa Peptide 120 C18 reverse phase column with 5 µm silica particles, 0.21 mm internal diameter and 15 cm length (Teknokroma, Spain). The gradient was set by changing the initial mobile phase composition of the aqueous solution of 2% acetonitrile and 0.1% formic acid to 95% acetonitrile and 0.1% formic acid over the course of 90 min with a flow rate of 0.2 mL/min. After the HPLC separation, the peptides were transported into the mass spectrometer with ESI. The applied operation parameters of ESI are shown in Table 4.1. The ESI-Q-TOF-MS analysis was performed with an impact II instrument (Bruker) with a spectrum collection rate set to 2.00 Hz in the m/z range of 100-2200. Each precursor ion was subject to fragmentation when detected at least five times and was excluded and released after appearing in three spectra and after 30 s, respectively. The mass spectrometric analysis of the hard corona proteins in combination with MASCOT data analysis (see Section 4.20) are discussed in Chapters 7 and 9.

Table 4.1. The ESI parameters used in the HPLC-ESI-Q-TOF-MS experiments.

ESI parameters	
Endplate offset:	500 V, 51 nA
Capillary:	4500 V, 178 nA
Nebulizer pressure:	186.16 kPa (27 psi)
Dry gas flow:	5 L/min
Dry temperature:	200 °C

4.20. MASCOT data analysis

4.20.1. Parameters of the analysis

After the mass spectrometric experiments, the compounds were automatically searched for in the mass spectra by Bruker's Compass software, and the resulting data were exported for protein identification. MS/MS ions search was performed in the exported data by Matrix Science's MASCOT [195]. The parameters set in MASCOT are shown in Table 4.2.

The proteomes of *Homo sapiens* and *Mus musculus* are well investigated, therefore the SwissProt database could be used for peptide identification. The results were narrowed down to mammalian proteins, and trypsin was chosen as the enzyme, since it was used for the in-gel digestion of proteins. The 1+ charged peptides were excluded from the data, and ESI-QUAD-TOF was chosen as the instrument used in the analyses. The rest of the parameters were left on their default values.

Table 4.2. Set parameters in the MASCOT analysis of the MS/MS data.

MASCOT parameters	
Databases:	Contaminants (AA), SwissProt
Taxonomy:	Mammalia (mammals)
Enzyme:	Trypsin
Allowed number of missed cleavages:	1
Quantitation:	None
Fixed modifications:	N/A
Variable modifications:	N/A
Peptide tolerance:	± 1.2 Da
#^{13}C:	0
MS/MS tolerance:	± 0.6 Da, monoisotopic
Peptide charge:	2+, 3+ and 4+
Data format:	Mascot generic
Instrument:	ESI-QUAD-TOF
Decoy:	—
Precursor:	N/A
Error tolerant:	—
Report top:	AUTO hits

4.20.2. Significance of the results

The MS/MS ion search of MASCOT offers the interpretation of significance in the form of scores in the results. The score is determined by the MASCOT system to be

$$score = -10 \times \log(P) \tag{6}$$

where *P* is the calculated probability that the match found between the experimental data and the chosen database, in this case, SwissProt, is a random event [195, 196]. When the score of a peptide exceeds the threshold set by MASCOT, it is said that the peptide match reached the identity threshold. However, in datasets with higher noise, the peptides may never reach the identity threshold; therefore, the server analyzes the distribution of the

probability scores, and determines a lower score threshold, too, which is called homology threshold [195, 196]. The scores assigned to the peptide ions also depend on the database used to identify the peptides, resulting in further ambiguity of the distinction of real hits and random events. The protein scores are determined based on the individual ion scores identified as fragments of the same protein [195, 196]. Therefore, in this work, the default significance value was used, set to $p<0.05$ by the MASCOT server, and identified proteins with a score of 40, determined to be the threshold of identity or extensive homology by the MASCOT server, were considered to be identified. Furthermore, common contaminants, such as keratins, were excluded from the discussion.

4.21. Cryo soft X-ray tomography

A549 and HCT-116 cells were respectively grown as a monolayer on a Formvar-coated circular gold grid (Quantifoil® R 2/2 of Au G200F1 finder grids from Quantifoil Micro Tools, Jena, Germany) for cryo soft X-ray tomography (XRT). The gold grids were placed in separate Petri dishes with 2 mL DMEM-FBS or McCoy-FBS. ~40,000 cells were pipetted on top of the grid, and the samples were incubated under standard cell culture conditions (37 °C, 5% CO_2) for at least 24 h. After the growth period, the grids were studied under a light microscope to make sure that the cells attached to their grids sufficiently. Subsequently, the culture medium was exchanged for the mixture of 900 µL of the corresponding culture medium and 100 µL of non-aggregated gold nanoparticles or 100 µL of gold nanoparticles pre-aggregated with 10 µL of 1 M NaCl solution. The samples were incubated for 24 hours under standard cell culture conditions (37 °C, 5% CO_2). After 24 h, the culture medium was discarded, and the samples were carefully rinsed with PBS three times prior to vitrification. The excess of PBS was removed from the surface of the grids by blotting with a clean filter paper, and the samples were plunge-frozen in liquid ethane.

The XRT data were collected with an X-ray microscope equipped with a cryo stage and a 25 nm zone plate objective, which allowed for the resolution of individual gold nanoparticles with a pixel size corresponding to ~9.8 nm. The tilt series were recorded in the range of -60° to +60° with 1° increments, resulting in datasets of up to 121°. The tilt series were reconstructed into tomograms by Etomo (IMOD© 4.9.0. by the Regents of the

University of Colorado, 1994-2017) based on a manually seeded fiducial model with ~15 fiducial markers selected in each tilt series. XRT results are discussed in Chapter 9.

The XRT experiments were conducted in collaboration with the research group of Prof. Gerd Schneider at BESSY II of the Helmholz-Zentrum Berlin für Materialien und Energie at the U41-XM beamline.

4.22. Cell viability tests

The changes in cell viability as a result of their incubation with gold nanoparticles were studied with an XTT cell proliferation assay kit. The samples were analyzed with a Multimode Plate Reader, Victor X5 (Perkin-Elmer, Berlin, Germany) operating in absorbance mode. A549 and HCT-116 cells were cultured in clear, flat bottom Greiner-type 96-well plates. Based on experience, HCT-116 cells grew slower in DMEM-based medium than in McCoy's Modified 5A-based medium; therefore ~5000 cells and ~2,500 cells were pipetted into each well in the experiments with DMEM-FBS and McCoy-FBS, respectively. A549 cells showed comparable growth in both media, and ~2,000 cells were transferred into each well in the XTT experiments. At least four sample replicates were studied for each incubation condition. Pure gold nanoparticles, pure culture media, and the 1:10 mixture of the nanoparticles and the culture media were analyzed as control samples. Each control was analyzed with and without the XTT assay to determine whether the background signal from the pristine samples contributes significantly to the absolute absorbance. The following samples were prepared for the cell viability studies: (i) cells without nanoparticles (positive control); (ii) cells incubated with the 1:10 mixture of non-aggregated gold nanoparticles and the respective culture medium; (iii) cells incubated with the 1:10 mixture of pre-aggregated gold nanoparticles and the respective culture medium; (iv) cells incubated with Triton X-100 (negative control); and (v) cells incubated with the 1:10 mixture of non-aggregated gold nanoparticles and the respective culture medium, then with Triton X-100 (negative control). The incubation with gold nanoparticles was started at least 24 h after seeding the cells into the 96-well plate. Every sample was prepared in two series: one with and one without XTT assay to make sure the absorbance of the pure sample was negligible in the analysis. These experiments were

performed with both cell lines in both culture media, respectively, and the results are presented in Chapter 9.

Chapter 5

SERS probing of proteins in gold nanoparticle agglomerates

This chapter was published as part of a manuscript in *G. P. Szekeres, J. Kneipp, Frontiers in Chemistry, 7:30, 2019*, and it is reproduced here with permission.

Since its discovery, SERS has been emergently used to study biomolecular systems. The sensitivity and high surface selectivity allow for the precise investigation of the interactions between the biomolecules and the nanoparticles' surface. This makes SERS a suitable option to study the interactions in the protein corona, which could contribute to the development of nanopharmaceuticals. Even though there have been some studies on simple solutions of nucleic acids [197, 198] and proteins [26, 27, 65, 199], collecting SERS spectra with high signal-to-noise ratio from the solutions of biomolecules, especially proteins, still poses a major challenge. The SERS study of protein solutions often requires the physical or chemical modification of the protein-nanoparticle systems in the form of nanoparticle pre-aggregation [27, 127, 129, 200-202] since single particles are known to provide very low SERS enhancement [44, 203], the re-structuring [130] or immobilization of the SERS substrates [28, 140], optical tweezing [26], or the use of specially tailored substrates [204]. While these approaches provide good signal

enhancement, valuable information about the formation of the protein corona on nanoparticles can be lost due to the altered substrates. However, SERS experiments yielding data with high signal-to-noise ratio have been routinely performed on complex biological samples ranging from living cells [42, 153, 157, 205, 206] to micro-animals [207, 208] and tissues in mammals [5, 209, 210]. There are some major differences between the SERS experiments with protein solutions and those with complex biological samples, which can result in successful data collection in cells and tissues but also prevent the sufficient data acquisition from protein solutions. Even though single nanoparticles are internalized by the cells, they are often processed further by their biomolecular environment and form aggregates that yield high SERS enhancement [145]. These intracellular protein-nanoparticle agglomerates are located in different intracellular compartments, generally in a crowded biomolecular environment, meaning that the protein concentration around internalized nanoparticles is higher than in general *in vitro* solutions [173, 211]. Another difference is that although proteins facilitate the formation of nanoparticle aggregates both in cells and *in vitro* [26, 212-214], the aggregates move around freely in solutions due to Brownian motion [183], while they are steadily positioned inside the cells throughout the data collection [39, 151].

In this chapter, an alternative sample preparation approach will be presented for the SERS analysis of proteins. Samples with different BSA : gold nanoparticle ratios will be prepared to shed light on how the protein concentration affects the aggregation. Additional experiments with a DNA sample extracted from 3T3 cells will be performed to demonstrate the general applicability of the sample preparation approach for studying nanoparticle-biomolecule interactions in general.

5.1. Normal Raman and SERS experiments at different BSA concentrations

For normal Raman and SERS experiments, BSA solutions with different concentrations were prepared as described in Section 4.5. The normal Raman experiments were performed on a sample with 0.5 g/mL BSA concentration that corresponds to that of the crowded environment inside a cell [173]. In the SERS experiments, the same amount of citrate stabilized gold nanoparticles (corresponding to a final nominal gold nanoparticle concentration of 0.3-0.4 nM) was added to BSA solutions with different concentrations

to reach final gold nanoparticle : BSA molar ratios of 1:10^7, 1:40000 and 2.5:1, respectively. To obtain the ratio of 1:10^7, the original BSA solution was diluted threefold, maintaining the similarity to the protein concentration in a cell. A representative Raman spectrum of BSA in solution and SERS spectra of the different samples are shown in Figure 5.1.

The normal Raman spectrum (Figure 5.1, bottom) and the SERS spectrum of the sample with the gold nanoparticle : BSA molar ratio of 1:10^7 are very similar both in band positions (Tables 5.1 and 5.2) and signal-to-noise ratio. The normal Raman spectrum is in good accordance with previous data [104]. The spectrum of the sample with the gold nanoparticle : BSA ratio of 1:10^7 (Figure 5.1, green trace) shows some altered band positions and minimal enhancement of up to a factor of ~6 for some of the bands, *e.g.,* the phenylalanine ring breathing mode at ~1004 cm^{-1}, and indicates that most of the signal is a normal Raman signal. This is in agreement with the fact that only a tiny fraction of BSA molecules in the focal volume can interact with the nanoparticles (approximately 100 BSA molecules/nanoparticle) [63], and that the absolute protein concentration of 0.15 g/mL is high enough to yield a normal Raman signal. The enhancement of approximately one order of magnitude indicates that those nanoparticles that contribute to the SERS signal do so by acting as individual nanostructures and cannot form aggregates [44].

When the protein concentration is decreased to a gold nanoparticle : BSA molar ratio of 1:40000, while maintaining the concentration of gold nanoparticles, the formation of nanoparticle aggregates is observed in the Raman microscope. The signals in the spectrum increase drastically, and new bands appear. The vibrations at 838 cm^{-1}, 895 cm^{-1}, 1252 cm^{-1}, 1458 cm^{-1}, 1504 cm^{-1}, and 1526 cm^{-1}, which are the same as in the normal Raman spectrum of BSA (marked in bold in Table 5.2; see comparison in Table 5.1) show very high relative intensities. Some, *e.g.,* the vibration of tryptophan at 895 cm^{-1}, known from the normal Raman spectrum (cf. Figure 5.1, bottom, and ref. [104]) are absent from other SERS spectra [26, 215], including most of those shown here (Figure 5.1).

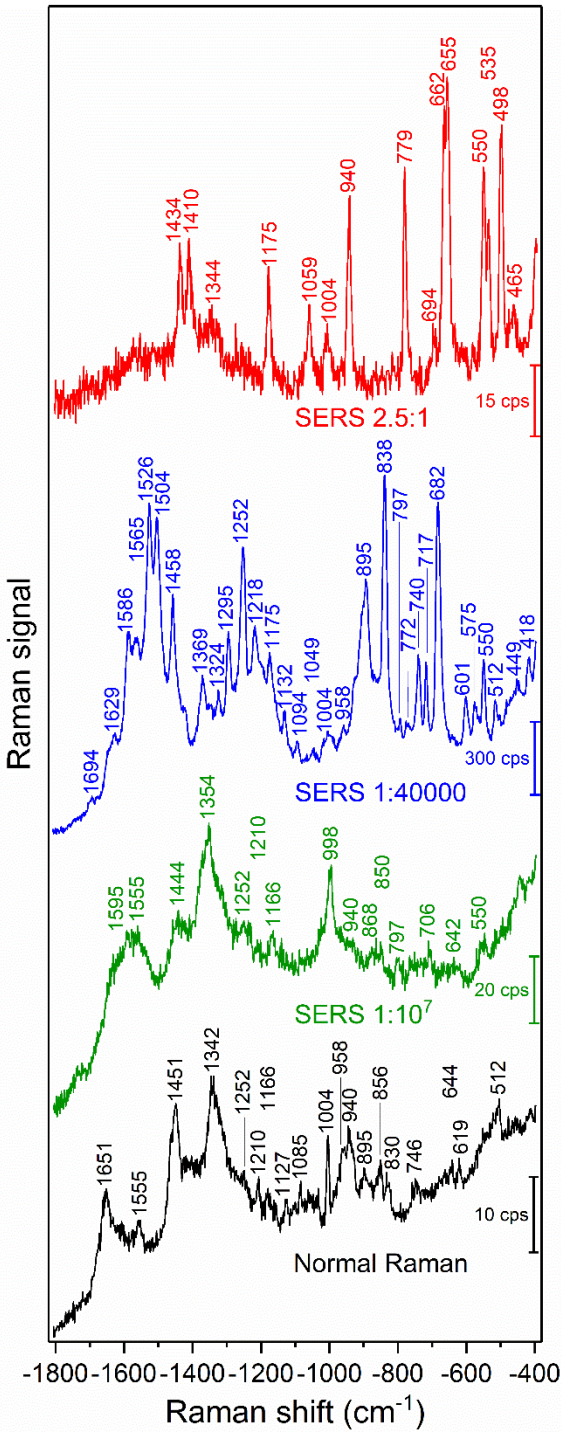

Figure 5.1. SERS spectra of BSA with gold nanoparticles with different gold nanoparticle : BSA molar ratios as indicated in the graph. Excitation wavelength: 785 nm, excitation intensity 5.7×10^5 W/cm^2, acquisition time per spectrum: 5 s for normal Raman, 1 s for SERS spectra.

Table 5.1. Raman shift values and tentative band assignments of the normal Raman spectrum of BSA solution. Abbreviations: *δ* deformation, *br* breathing, *ν* stretching, *symm* symmetric. The band assignments were based on refs. [40, 104-106, 215-219].

Raman shift (cm^{-1})	Tentative assignment
1651	Amide I
1555	Trp
1451	$\delta(CH_2/CH_3)$
1336	δ(C-H)
1210	Tyr, Phe
1127	C-N
1085	C-N
1004	R br
958	Trp, Val
940	$\delta(C\text{-}C\text{-}N)_{symm}$, α-helical skeletal
895	Trp
856	Tyr
830	Tyr
746	Trp, ν(C-S)
644	Tyr, ν(C-S)
619	Tyr, ν(C-S)
512	ν(S-S)

Based on the assignments of the bands in the spectrum (Table 5.2), it was concluded that an interaction of the protein with the nanoparticles' surface takes place in such a way that both the peptide backbone and the aromatic side chains of BSA are in the proximity of the nanoparticle surface. The signals of the aromatic side chains can suggest the unfolding of the protein since these side chains are rarely present on the surface of BSA, as indicated by its crystallographic data (Figure 5.2A) [180]. However, the bands at 512 cm^{-1}, 550 cm^{-1}, and 575 cm^{-1}, assigned to S-S stretching vibrations of disulfide bonds formed by cysteine, indicate that at least parts of the native structure remain intact. The bands at 1252 cm^{-1}, 1295 cm^{-1}, 1504 cm^{-1}, 1526 cm^{-1}, 1565 cm^{-1}, 1629 cm^{-1}, and 1694 cm^{-1} can be assigned to some components of the amide III, amide II, and amide I bands, respectively, which indicate the interaction of nanoparticles with the peptide backbone. This also points to a more intact, folded protein chain, where specific side chain-nanoparticle interactions are less likely to take place.

Table 5.2. Raman shift values and tentative band assignments of the SERS. Abbreviations: *sciss* scissoring, *δ* deformation, *v* stretching, *bend* bending, *R* benzene ring, *r* pyrrole ring. Bands appearing in the normal Raman spectrum of BSA solution are marked bold. The band assignments were based on refs. [40, 104-106, 215-219].

Raman shift (cm^{-1})	Tentative assignment	Raman shift (cm^{-1})	Tentative assignment
1694	Amide I	**998;1004**	R breathing
1629	Amino acids	**958**	ν(N-$C_α$-C) skeletal
1595	Phe, Tyr: ν(R), ν (COO^-)asymm, OH mode	**940**	δ(C-C-N)symm, α-helical skeletal
1586	δ(R), ν(R)	**895**	Trp
1577	Trp, NH_2 sciss, ν(R,r)	868	Tyr
1565	Amide II	850	Tyr: R breathing
1555	Trp: ν(R), ν(r), amide II	**838**	Tyr
1526	δ(NH_3^+)Lys, amide II	**797**	ν(C-H), δ(-N-H)
1504	Amide II, ν(R,r) Trp, ν(C-H)	772;779	Trp, δ(-C-H)
1458	δ(C-H), δ(CH_2/CH_3)	**740**	Trp, ν(C-S)
1444	δ(C-H) of CH_2	**717**	ν(C-S), Trp
1434	δ(CH_2)	**706**	ν(C-S), δ(COO^-)
1425	δ(CH_2)Cys	694	C-C, C-O bend
1410	δ(CH_3), ν(COO^-)	682	δ(-C-H)
1369	δ(CH_3)symm	655;**662**	ν(C-S), Tyr
1354	γ(CH_2)	**642**	ν(C-S)
1344	γ(CH_2,CH_3), Trp(Cα-H)	601	δ(COO^-)
1324	δ(C-H), δ(CH_2/CH_3)	575	ν(S-S)
1295	Amide III, C-H, C-C	550	ν(S-S)
1252	Amide III	535	δ(N-H), ν(S-S), δ(skeletal)
1210; 1218	Tyr, Phe, ν(C-C)	**512**	ν(S-S)
1175	Tyr, ν(-C-N)	**498**	ν(S-S)
1166	Tyr	465	ν(C-S)
1132	ν(-C-N), Pro	**449**	ν(C-S)
1094	ν(C-C),ν(C-N), H(r) bend	**418**	Trp
1049;1059	ν(-C-N), Phe		

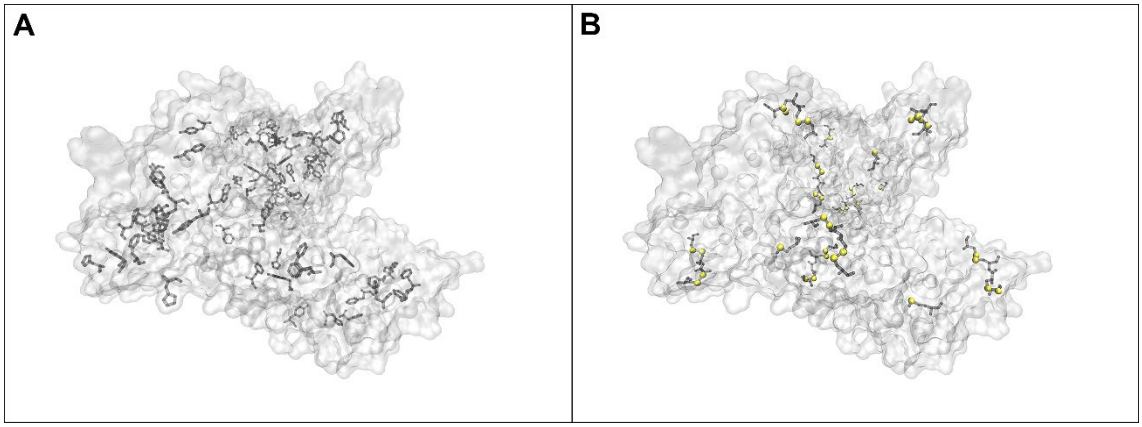

Figure 5.2. Location of the aromatic side chains in BSA (A), and the location of cysteine and methionine residues in the structure of BSA [180, 182]. Sulfur atoms are marked with yellow spheres.

At ~150 pM (10^{-8} g/mL) BSA concentration, corresponding to a gold nanoparticle : BSA ratio of 2.5:1, the surface of the nanoparticles cannot be covered entirely by BSA molecules. In this case, the aggregation, observed in the dark field of the Raman microscope by eye, must be based on the bridging of individual nanoparticles by a protein molecule [214]. Comparing the SERS spectrum (Figure 5.1, red trace) to those of the other samples, an increment in the relative intensities of the bands at 498 cm^{-1}, 550 cm^{-1}, 655 cm^{-1}, and 662 cm^{-1} is observed in spite of a lower overall intensity, all of which correspond to C-S and S-S vibrations. The crystal structure of BSA indicates that cysteine and methionine side chains are not exposed on the surface of the molecule (Figure 5.2B) [180]; therefore, the interaction of sulfuric residues with the gold nanoparticle surface would require unfolding of the native structure of BSA.

Different from the sample with the gold nanoparticle : BSA ratio of 1:40000 (Figure 5.1, blue trace), no amide bands are present in this spectrum, which suggests a more unfolded structure, where specific side chain interactions become more preferred than peptide backbone interactions. This is in agreement with the expected aggregation process since a protein molecule must undergo conformational changes while binding to two different nanoparticles at the same time. Nevertheless, while the unfolding of the native structure is observed at this concentration, the presence of S-S vibrations, *e.g.,* at 550 cm^{-1} indicates that the native folding is not entirely disrupted.

5.2. UV-vis absorbance experiments of the nanoparticle-BSA agglomerates

UV-vis experiments were performed to learn about the aggregation state of the gold nanoparticles in the samples mixed with BSA. Figure 5.3 shows the UV-vis absorbance spectra of the samples at the nanoparticle : BSA molar ratios of 1:40000 and 2.5:1, and a spectrum of the nanoparticles without BSA.

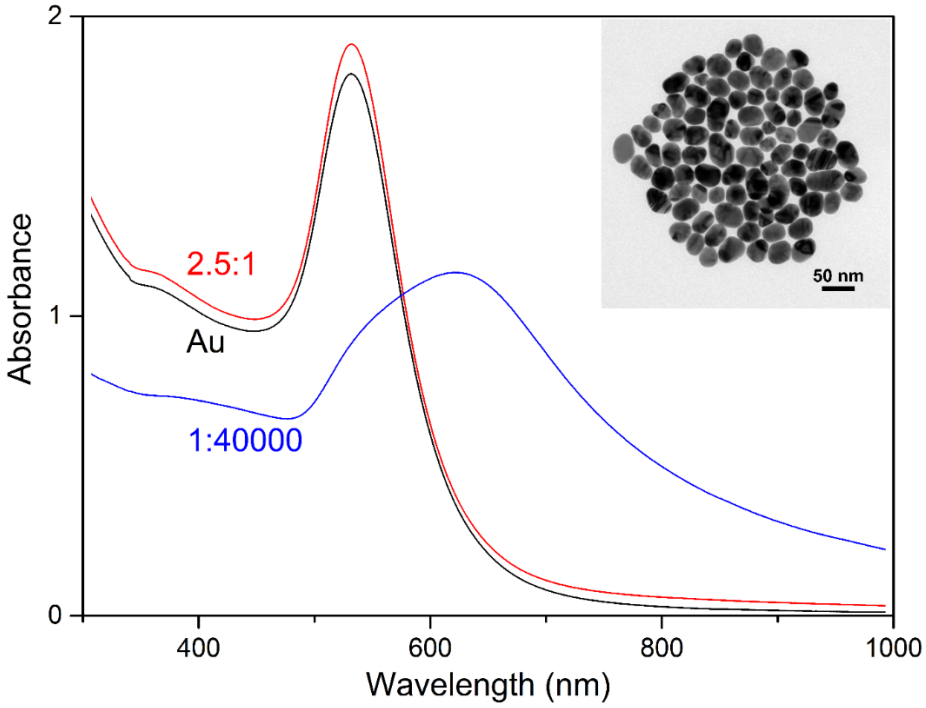

Figure 5.3. Absorbance spectra of the gold nanoparticles (Au) and the mixture of BSA with the gold nanoparticles at the nanoparticle : BSA molar ratios of 2.5:1 and 1:40000. The inset shows a TEM micrograph of the gold nanoparticles.

The results of the sample without BSA show an absorbance maximum at 532 nm, the single, relatively narrow peak suggests relatively high monodispersity of spherical nanoparticles. This was confirmed by transmission electron microscopy (TEM), which indicates a nanoparticle diameter distribution of 32±7 nm (inset in Figure 5.3). Upon addition of BSA to the gold nanoparticles to yield a ratio of 40000 BSA molecules per nanoparticle, aggregates of the nanoparticles form, as indicated by the extension of the plasmon band, with a shift of its maximum to 618 nm. This observation is in accord with data from other albumin-containing samples [39], where the change in plasmonic properties of these gold nanoparticles was also connected to aggregate formation. Protein

molecules are known to aggregate nanoparticles in specific concentration ranges *via* depletion, bridging, or by reducing the surface charge during adsorption [213, 214].

In the sample containing gold nanoparticles and BSA molecules at a ratio of 2.5, the differences between the spectra are relatively small (compare red and black traces in Figure 5.3), but the dark field view in the microscope indicates the presence of small gold nanoaggregates as well. This is in accord with the SERS spectra indicating an interaction of the protein with the nanoparticles and supports a bridging interaction of protein molecules that can connect several individual nanoparticles. As discussed previously, the formation of such small aggregates has a smaller effect on the bulk absorbance spectrum and can lead to an underestimation of electromagnetic SERS enhancement [44] using a quantitative relation to the absorbance spectra [220]. However, the substantial increase in SERS enhancement that is brought about by the formation of such aggregates clearly evidences their presence, albeit often in small numbers, in SERS experiments [43, 44, 136].

5.3. Estimation of the SERS enhancement of nanoparticle-protein agglomerates

Different from well-defined molecular systems and their interaction and coverage of gold surfaces [44, 221], the number of BSA molecules participating in the SERS enhancement is difficult to estimate in the agglomerates here. As indicated by the overall signals in the spectra in Figure 5.1, the enhancement by the gold nanoaggregates, whose formation is induced by BSA varies for different protein concentration, is in agreement with the concentration-dependent interaction of the protein with the gold nanoparticles [214]. This will result in a different portion of nanoparticles present in aggregates, as well as a different aggregate morphology. The latter, specifically the variation of inter-particle distance and the combination of not-ideally spherical nanoparticles, was recently shown to have a strong influence on the local field enhancement of gold nanostructures for excitation in the near-infrared [136] and is expected to play a major role in the different overall enhancement observed here as well.

Despite the strong influence of the BSA molecule on the optical properties of the gold nanoparticle aggregates, rendering protein quantification impossible. However, a comparison of overall SERS signals is interesting regarding the ability to probe protein

composition and interaction in cells, where such aggregates are formed from individual gold nanoparticles when they meet with the real biological environment. Comparing the normal Raman signals (Figure 5.1, black trace) of a 7.5 mM BSA solution with the SERS spectrum obtained at a BSA concentration of ~150 pM (Figure 5.1, red trace), an enhancement of ~10^8 was estimated.

5.4. Brownian motion and viscosity at intracellular protein concentrations

It is important to consider that all samples for the SERS experiments (Figure 5.1) consist of citrate stabilized gold nanoparticles and BSA, and the highest BSA concentration resulted in the lowest signal intensities, rather than in a saturated overall intensity as would be expected due to a limited available surface of the SERS substrate [44]. This observation is in agreement with recent discussions [214] that nanoparticle aggregation hardly occurs when the protein concentration is much higher than the concentration needed to form a monolayer on each particle. This is the case in the sample with a gold nanoparticle : BSA molar ratio of 1:10^7. In a protein-nanoparticle system, the governing transport process of the particles is diffusion by Brownian motion, which depends on the dynamic viscosity η of the system as well. The η of the SERS sample with the gold nanoparticle : BSA ratio of 1:40000 was estimated to be 0.803 cP, while the SERS sample with the gold nanoparticle : BSA ratio of 1:10^7 exhibits a η of 1.94 cP. Displacement of the nanoparticles also depends on the particle radius that significantly changes upon the adsorption of additional protein layers. It can be concluded that the slower Brownian motion and the increased minimum inter-particle spacing due to multilayer protein adsorption contribute significantly to the absence of aggregate formation and therefore to the weaker SERS enhancements at higher protein concentrations. As the result of estimating the number of nanoparticles taken up by a typical cell [158], and the number of typical-size gold nanoaggregates [39] that would fit in a focal volume, the number of particles appear to be very similar. Since the most concentrated sample approximates the cellular protein concentration, the observed high SERS signals from live cells [42, 157] must be related to differences in the intracellular inhomogeneity of protein concentrations and to active transport processes. These effects, individually or together, can facilitate the formation and positioning of aggregates in cellular compartments. Therefore, the

combination of these phenomena can contribute to the SERS signal enhancement experienced in live cell SERS mapping.

5.5. Demonstration of applicability: SERS experiments with DNA

To show the application of gold nanoparticles and direct SERS probing in other biomolecular solutions, DNA extracted from 3T3 fibroblast cells was used. A representative SERS spectrum of the DNA solution is shown in Figure 5.4.

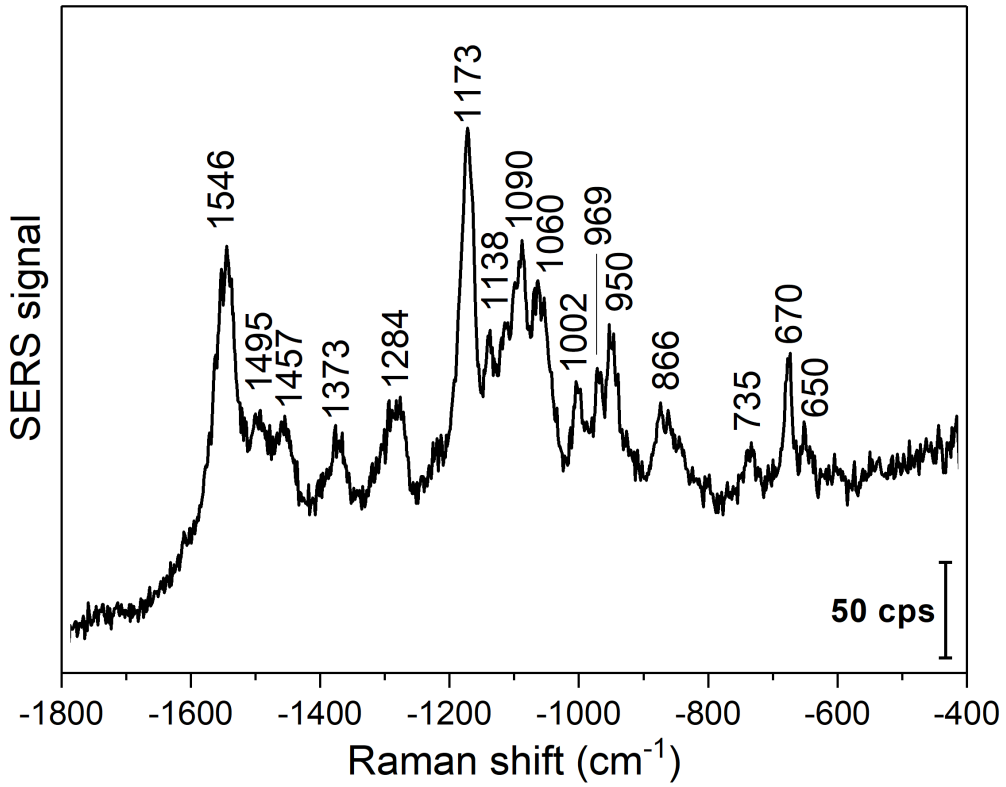

Figure 5.4. Representative SERS spectrum of 3T3 DNA in the presence of gold nanoparticles. Excitation wavelength: 785 nm, excitation intensity 5.7×10^5 W/cm^2, acquisition time per spectrum: 1 s.

The SERS experiments were conducted at ~pH 4.5, which can destabilize the DNA duplexes by titrating the polar groups in the nucleobases [222]. High relative intensities of the vibrations at 1090 cm^{-1} assigned to PO_2^- symmetric oxygen stretching [106, 223], at 1173 cm^{-1}, corresponding to base external C-N vibrations [224], and at 1546 cm^{-1} from NH_2 scissoring in adenine, N3-C4-C5 stretching in cytosine, and C-N stretching, NH_2 scissoring, and N1-H bending in guanine [218] are observed. The lower relative intensity

of the deoxyribonucleoside and backbone vibrations (Figure 5.4 and Table 5.3) and the appearance of the 797 cm^{-1} band in the spectra indicate the destabilization of the double helix [224], as well as the proximity and possible interaction of the nucleobases and the gold nanoparticle surface. Due to the short experiment times, the depurination in the DNA strands can be excluded, which was reported to occur at low pH only after several hours [225]. The spectrum obtained with purified DNA (Figure 5.4) suggests that biomolecule-nanoparticle interactions other than those of proteins can be studied, and further supports that structural information about the state of the biomolecules can be obtained.

Table 5.3. Raman shift values and tentative band assignments of the SERS spectrum of 3T3 DNA. Tentative band assignments are based on refs. [106, 218, 223, 224, 226]. *dA* deoxyadenosine, *dC* deoxycytidine, *dT* deoxythymidine, ν stretching.

Raman shift (cm^{-1})	Tentative assignment
1546	A, C, G
1495	A
1457	A, G, T
1373	dA, dC, dT
1284	T
1173	base external C-N stretch
1138	A
1090	$\nu(PO_2^-)$
1060	G
1002	A, C
969	A, G
950	G
866	G
797	sugar-phosphate symmetric stretch
735	A
670	dT
650	dC, backbone

5.6. Summary

In this chapter, a refined sample preparation approach was presented for the SERS analysis of proteins and other biomolecules. The main advantages of this approach are the general applicability among biomacromolecules, the high SERS enhancement, and the lack of need for additional chemicals for the aggregation or fixation of the substrate.

Therefore, SERS spectra of biomolecules can be obtained in a setting that resembles the application of individual, non-aggregated gold nanoparticles in a complex biosystem such as a living cell. SERS spectra were measured in solutions of the protein BSA over a wide range of concentrations in the presence of gold nanoparticles. Aggregates of the gold nanoparticles were formed by their interaction with the protein molecules. As indicated by the SERS spectra, the BSA molecules undergo a partial structural change, which strongly depends on the protein concentration. Specifically, at a low gold nanoparticle : protein molar ratio, the significant unfolding of the protein could be observed, in agreement with the expected aggregation mechanism at low concentrations, that is, flocculation *via* bridging. Apart from qualitative changes in the spectra, the varied interaction of the proteins with the gold nanoparticles modifies aggregate morphology, which yields a great variation in SERS enhancement. The highest enhancement factor, approximately 10^8, was estimated in the case of the sample with a gold nanoparticle : BSA ratio of 2.5:1.

When protein concentrations in the solutions approximate cellular protein concentrations, the high viscosity and the multilayer protein adsorption on the surface of the nanoparticles hinders the formation of nanoaggregates that can provide high SERS enhancement. This was attributed to decreased Brownian motion and an increased inter-particle distance as a result of multi-layer protein adsorption. These results show that the high SERS signals in live cells are the consequence of the active processing of gold nanoparticles, resulting in the additional positioning and the formation of intracellular aggregates apart from the crowded environment inside a cell alone.

Chapter 6

Different binding sites of serum albumins in the protein corona of gold nanoparticles

This chapter was part of a manuscript published in *G. P. Szekeres, J. Kneipp, Analyst, 143, 6061-6068, 2018,* and it was reproduced by permission of the Royal Society of Chemistry.

One of the many possibilities of being in contact with nanoparticles is the intravenous administration of nanopharmaceuticals, which has become the focus of the search for alternative drug delivery of anti-cancer agents [227]. When the nanoparticles enter the bloodstream, proteins will rapidly adsorb on their surface [13, 33, 201, 228]. The Vroman effect dictates that first, the most abundant proteins will interact with the nanoparticles [17], which in this case means the interaction with human serum albumin (HSA).

There have been contradictory discussions of how citrate-stabilized gold nanoparticles interact with serum albumins. Several previous studies state that the exchange of citrate

ions to protein residues is possible, and therefore the protein molecules directly interact with the surface of gold nanoparticles [22, 63], while others complement the hypothesis or counter-propose that proteins only interact with the adsorbed citrate layer on the surface [24, 25, 63].

In this chapter, the power of SERS will be demonstrated to determine the interaction of gold nanoparticles and two different serum albumins: BSA and HSA, respectively. The two proteins exhibit a sequence overlap of 77.5%, which makes it difficult to distinguish them, but due to the high surface selectivity of SERS, attempts will be made to identify the influence of the moderately different primary structures.

6.1. Normal Raman experiments of BSA and HSA

Raman spectroscopy has been extensively used to study proteins, since the different side chains, structural elements, and protein-protein interactions facilitate the distinction of proteins [104, 105, 229, 230]. To study the possible differences in the interactions of BSA and HSA with gold nanoparticles, it was essential to analyze their normal Raman spectra first to learn whether spectral differences arise even in bulk in normal Raman experiments. Figure 6.1 shows the normal Raman spectra of BSA and HSA in 0.05 g/mL aqueous solutions. Tentative assignments are presented in Table 6.1.

As it can be seen in Figure 6.1, the differentiation between the two highly similar protein molecules (with a sequence overlap of 77.5%) proves to be difficult only based on normal Raman data collected from their solutions. However, due to the high surface selectivity of SERS, there is a distinct possibility that the SERS study of the adsorption of BSA and HSA on citrate-stabilized gold nanoparticles could yield valuable information about possible differences in their interactions with gold nanoparticles as a result of the small difference in their primary structures.

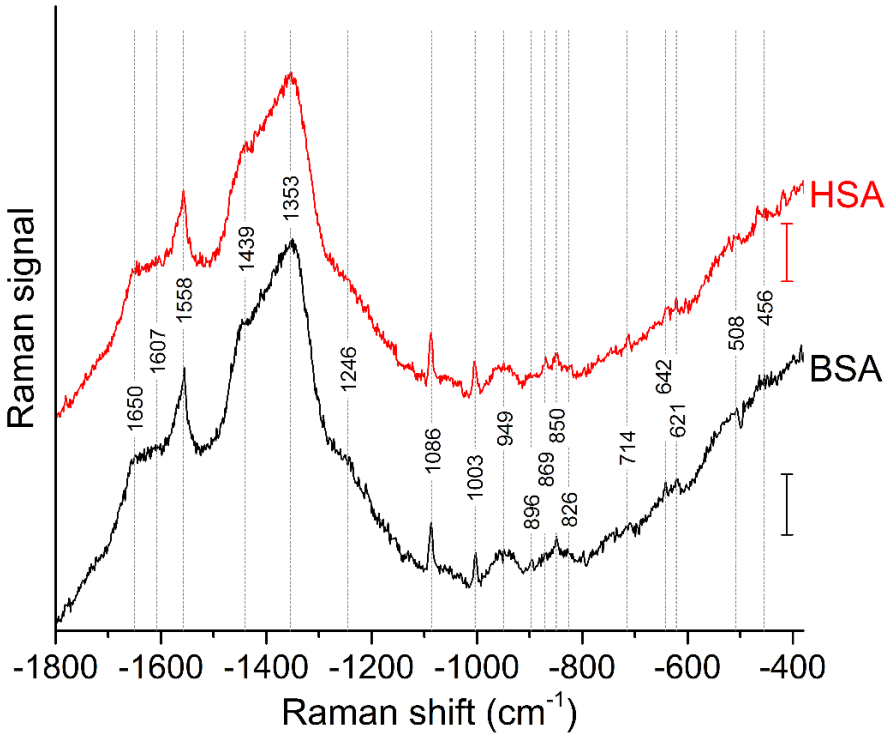

Figure 6.1. Normal Raman spectra of the 0.05 g/mL solutions of BSA and HSA, respectively. The identical band positions are marked with dashed vertical lines. The scale bars on the right correspond to 300 counts. Excitation wavelength: 785 nm, laser intensity: 5.7×10^5 W/cm^2, acquisition time: 120 s.

Table 6.1. Tentative assignments of the normal Raman spectra of BSA and HSA presented in Figure 6.1. The assignments were based on ref. [104, 105, 219].

Raman shift (cm^{-1})	Tentative assignments
1650	Amide I
1607	Phe
1558	Trp
1439	C-H deformation
1353	Trp, C_α-H deformation
1246	Amide III
1086	C-N deformation
1003	Phe+Trp ring breathing
949	Trp, Val
896	Trp
869	Tyr
850	Tyr
826	Tyr
714	Trp
642	Tyr
621	Tyr, C-S stretching
508	S-S stretching
456	Trp ring deformation

6.2. Average and single SERS spectra of BSA and HSA

The SERS spectra of BSA and HSA were collected under identical experimental conditions. After the 0.01 g/mL protein solutions were respectively mixed with the gold nanoparticles in 1:10 volume ratio, the sample pH was ~4.5 for both proteins. At this pH, both BSA and HSA possess a net positive surface charge, given their respective pI's of 5.60 and 5.67 calculated using the 'Compute pI/Mw tool' of ExPASy Bioinformatics Resource Portal [231]. At this pH, BSA was shown to remain in its native folded structure [232], and due to their high structural similarity, it is expected that major pH-induced changes in the folding of HSA also do not occur. The samples were respectively transferred onto a CaF_2 slide, and SERS spectra were recorded as described in Sections 4.4 and 4.6.

Figure 6.2 shows the averages of ~100 background corrected and vectornormalized BSA and HSA SERS spectra obtained with gold nanoparticles in solution. Table 6.2 provides the assignments of important bands in the spectra. In accordance with previous work [199, 233, 234], the spectra are dominated by amide II and amide III vibrations [104, 216] at 1559 cm^{-1} and ~1250 cm^{-1}, respectively, and by the bands assigned to vibrations of aromatic amino acid side chains that have high Raman cross-sections, such as their ring vibrations at ~680 cm^{-1}, ~840 cm^{-1}, ~860 cm^{-1}, or ~890 cm^{-1} [105, 219].

The presence of the stretching vibrations of S-S bonds, at 523 cm^{-1} and 533 cm^{-1} [105] in HSA and BSA, respectively, suggests that the protein molecules maintain their disulfide bridges as important elements of their secondary structure upon interaction with the nanoparticle surface. This is different from the interaction of other proteins with the surface of silver nanoparticles, where cleavage of disulfide bonds is possible [39, 235].

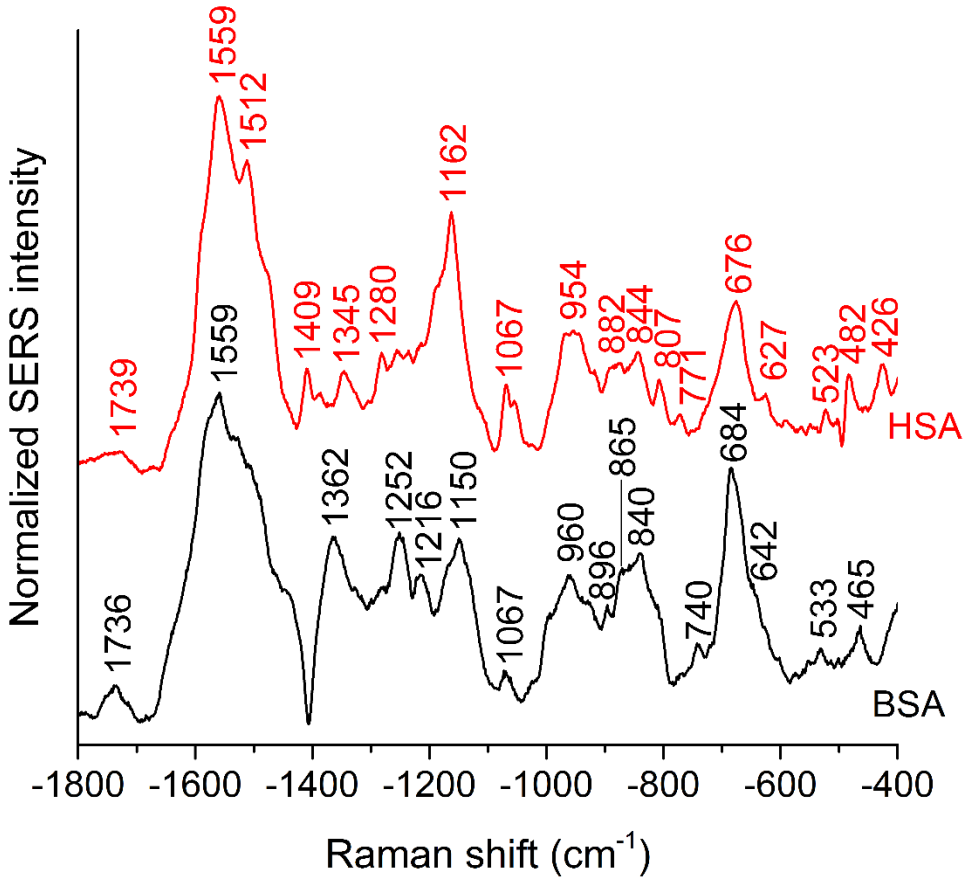

Figure 6.2. Averages of ~100 BSA and ~100 HSA SERS spectra obtained with citrate-stabilized gold nanoparticles. Excitation wavelength: 785 nm, acquisition time: 1 s, excitation intensity of 5.7×10^5 W/cm^2. The spectra were stacked for clarity.

The average spectra show differences in the bands 865 cm^{-1}, 840 cm^{-1}, and 642 cm^{-1} assigned to different vibrations of tyrosine (see Table 6.2). Contrary to normal Raman experiments in bulk, the confinement of SERS to the immediate proximity to the nanoparticle enables the probing of those parts of the protein that interact with the surface [26-28, 233, 234]. When the primary structures of BSA and HSA are compared, it can be observed that BSA has two more tyrosine residues at the positions 155-156 than HSA [180, 181], which could potentially account for the slight spectral differences. This could be facilitated by their location in the three-dimensional protein structure: as observed in the crystallographic data of BSA [180], the two tyrosine residues at positions 155 and 156 are partially revealed on the surface of the molecule with the aromatic functional group pointing away from the protein structure. Residues closer to the protein-nanoparticle interface are expected to contribute more to the SERS signal than residues hidden in the folded structure.

Even though vectornormalization prevents the average spectra from being dominated by a few high-intensity individual spectra, and those bands that frequently occur in the individual spectra are present in the average spectra, some band shifts and bands that occur rarely or have low intensity may disappear upon averaging. Therefore, it is useful to analyze individual spectra, and also their variation (see Figure 6.3 and Figure 6.5 below). In Figure 6.3, representative BSA and HSA single spectra from the data sets are shown, the respective band assignments are also given in Table 6.2.

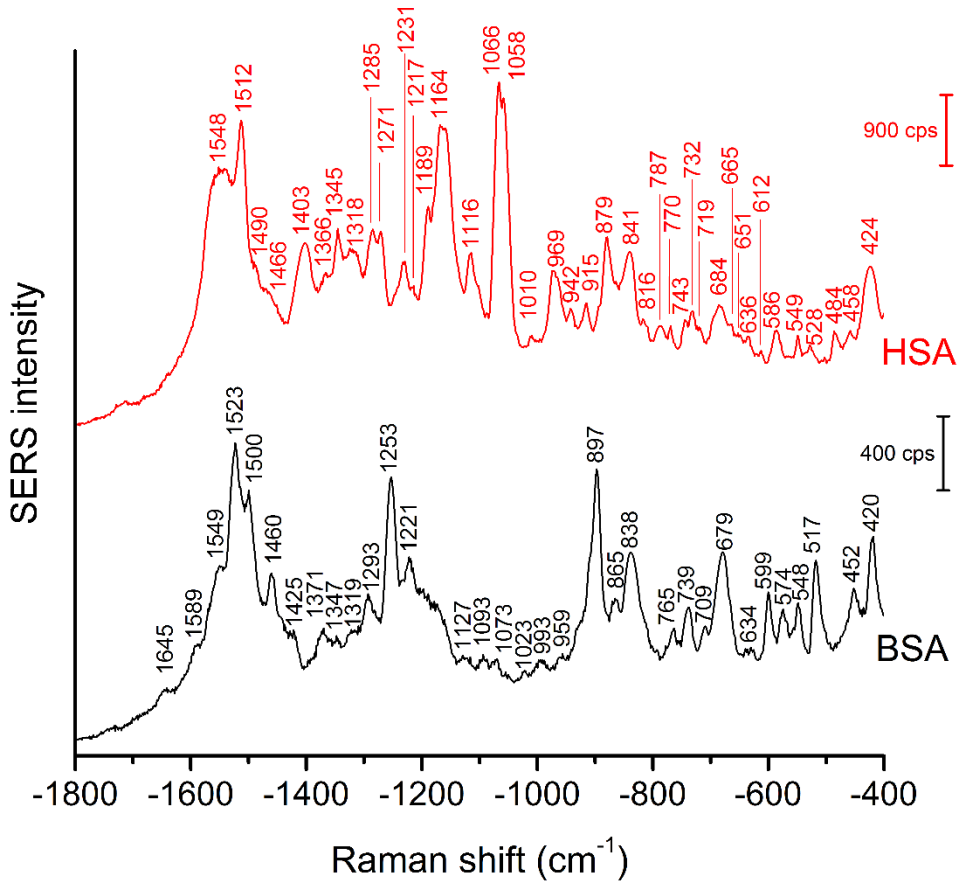

Figure 6.3. Representative single SERS spectra of BSA and HSA obtained with citrate-stabilized gold nanoparticles. Excitation wavelength: 785 nm, excitation intensity: 5.7×10^5 W/cm^2, acquisition time: 1 s. The spectra are stacked for clarity.

Table 6.2. Tentative assignments of the bands in the SERS spectra of BSA and HSA shown in Figures 6.2 and 6.3, based on refs.[40, 104-106, 215-219]. Abbreviations: *ν* stretching, *δ* deformation, *br* breathing, *symm* symmetric, *wag* wagging, *sciss* scissoring, *bend* bending, *rock* rocking, *tor* torsion, *R* benzene ring, *r* pyrrole ring.

Raman bands (cm^{-1})		Assignments	Raman bands (cm^{-1})		Assignments
BSA	**HSA**		**BSA**	**HSA**	
1736	1739	ν(C=O)		942	ν(C-C)
1645		Amide I		915	Glu, Ile, Thr, Lys: ν(C-C)
1589		ν(R)	897		R
1550	1550	Amide II, Trp: ν(R, r)		879	H(R,r) sciss, N-H bend
1523		Lys: $\delta(NH_3^+)$	865		Tyr, δ(C-CH) R
	1512	NH2 bend, ν(R)	838	841	$\nu(C_\alpha$-N, C-C), Tyr
1500		ν(R, r)		816	Ser: $\delta(COO^-)$
	1490	C-H bend, δ(N-H)		807	δ(R)
1460	1466	C^β bend, $\delta(CH_2, CH_3)$		787	δ(C-H)
1425		ν(C-N-H(r))	765	770	Trp: $br(indole)_{symm}$, δ(CH)
	1406	$\nu(COO^-)_{symm}$	740	743	δ(CH), ν(C-S), Trp
1370	1366	$\delta(CH_3)$		732	$\delta(COO^-)$, ν(C-S)
1345	1345	CH_2 sciss, $\delta(CH_3)$, ν(C-C), CH_2 rock	709	719	ν(C-S)
1319	1319	CH_2 wag	684	684	δ(C-H), δ(R), δ(COO-)
1290	1290	Amide III, $\delta(CH_2$, $CH_3)$, CH bend		665	ν(C-S)
	1271	Amide III, $\delta(CH_2, CH_3)$		651	ν(C-S)
1253		Amide III, $\delta(CH_2, CH_3)$	642		Tyr
1221	1231	Trp+Phe: δ(R)	634	636	Tyr: δ(R, CH), ν(C-S)
1216	1217	Tyr+Phe: ν(R)		612	δ(R, C-H)
	1189	Tyr+Phe	599		δ(R)
	1170	ν(C-N)		586	δ(R, C-C)
1150		ν(C-N)	574		δ(R,r), N-H(r) bend
1127	1116	ν(C-N, C-C)	548	549	Trp: $C\text{-}COO^-$ asymm bend
1093		ν(C-C)	533	528	δ(N-H), ν(S-S)
1070	1070	$\nu(C_\alpha$-N, $C\text{-}CH_2)$, NH_2 bend, ν(C-O)	517		ν(S-S)
	1058	$\nu(C_\alpha$-N, $C\text{-}CH_2)$, NH_2 bend		484	R tor/bend, NH_2 wag
1023		ν(C-N), NH_2 bend	465	458	Trp: δ(R, r)
993	1010	Phe+Tyr: br(R)	452		ν(C-S)
959	963	Trp, Val, H(R) twist, ν(C-C)	420	424	Trp

The BSA spectrum shows pronounced signals of the $-NH_3^+$ deformation vibration of lysine residues at 1523 cm^{-1} [215], of the amide III band at 1253 cm^{-1} [104], of a ring

vibration of tryptophan at 897 cm^{-1} [105], and of the C-C and/or C_α-N stretching vibration at 838 cm^{-1} [219]. Interestingly, the band of lysine [215] is not pronounced in the normal Raman spectrum of BSA reported, *e.g.,* in refs.[104, 199] (Figure 6.1 and Table 6.1). Nevertheless, its strong contribution to the SERS spectrum despite its small Raman cross-section suggests that the lysine residues must be in very close proximity to the gold surface. A direct lysine-citrate interaction has been discussed in previous work using other approaches [24, 25, 28, 63, 236], and the SERS spectra of BSA support the hypothesis that binding takes place by such an electrostatic interaction [24, 25, 28, 63, 236]. The strong amide III band at 1253 cm^{-1} and the band at 838 cm^{-1} assigned to vibrations of both the protein backbone and tyrosine in the BSA SERS spectrum suggest that the peptide backbone must be very close to the nanoparticle surface as well. Interestingly, the usually very strong ring vibration of phenylalanine and tryptophan at 1004 cm^{-1} [104] does not appear in the spectrum, excluding the proximity of aromatic side chains to the nanoparticle surface. Since the nonpolar amino acid side chains are mostly located inside the folded structure [180, 182], hidden from the hydrophilic environment, the absence of the 1004 cm^{-1} band suggests that the probed BSA molecules preserved their secondary structure in so far as these residues do not become exposed.

In addition, the single SERS spectrum of HSA (Figure 6.3) displays selective enhancement of bands that are not particularly prominent in the normal Raman spectrum of the molecule (Figure 6.1 and Table 6.1) [237, 238]. Examples are the pronounced signals at 1550 cm^{-1} of the ring stretching of tryptophan [219] or the deformation vibrations of the -NH_2 group at 1512 cm^{-1}, at 1058 cm^{-1}, as well as at 1070 cm^{-1} [219]. The latter two bands also contain contributions from vibrations of C_α-N and C-CH_2 bonds in the peptide backbone, in accord with a distinct signal of the C-N stretching band at 1170 cm^{-1} [104]. The enhancement of the SERS signals from the -NH_2 groups and of the protein backbone indicate the proximity of the basic amino acid residues and of the peptide backbone, respectively, to the nanoparticle. The basic NH_2 groups can be expected to interact with citrate ions in an acid-base equilibrium more than with the net positive surface of the bare nanoparticles [239] that can be revealed after the desorption of citrate ions since upon their protonation, -NH_3^+ groups would be electrostatically repelled from the positively charged bare gold surface. Therefore, it can be concluded that just like the BSA spectrum, also the HSA spectrum suggests the interaction of the

protein based on the electrostatic binding hypothesis [22, 24, 25, 63]. In the complete datasets of BSA and HSA, the 1523 cm^{-1} band appears in 80 and 62, and the 1512 cm^{-1} band appears in 74 and 56 spectra, respectively. This means that the interaction with the surface lysine groups has a substantial contribution to the whole dataset, which indicates the general proximity of the $-NH_3^+$ and $-NH_2$ groups to the nanoparticles' surface. The schematic illustration of the interaction of lysine residues on the surface of HSA and the citrate layer of the nanoparticles is shown in Figure 6.4.

As seen in the case of the SERS spectra of BSA, the 1004 cm^{-1} band is absent, which suggests that the native structure of the adsorbed HSA molecules is at least partially intact. There are several bands in both the BSA and HSA SERS spectra assigned to aromatic and aliphatic vibrations (Table 6.2), indicating their proximity to the nanoparticle surface, which could also point toward a hydrophobic interaction with the nanoparticles.

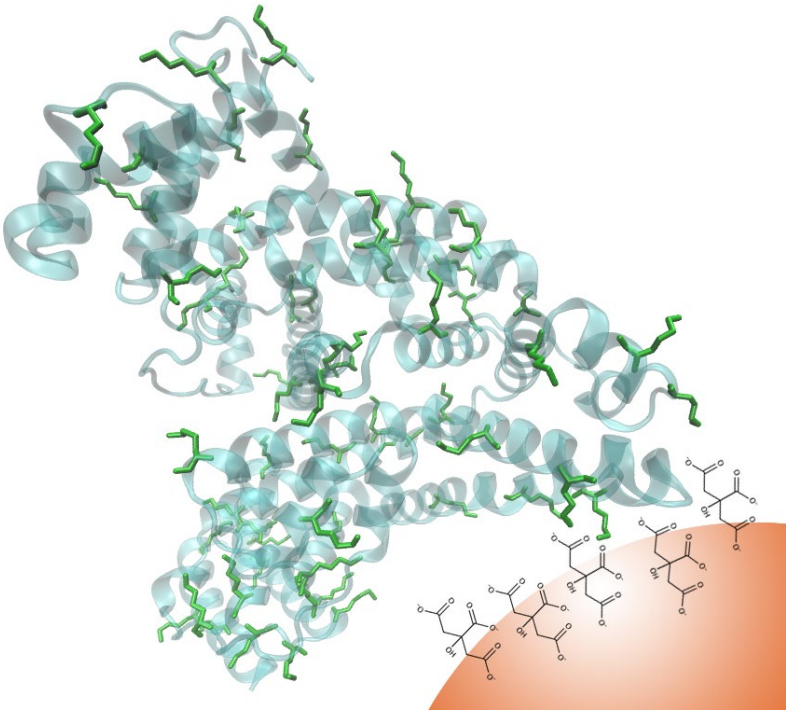

Figure 6.4. Schematic representation of the expected interaction between the citrate layer on the gold nanoparticle surface and the lysine residues of HSA (marked with green).

6.3. Principal component analysis of the SERS data of BSA and HSA

In order to take into account the molecular information from many gold nanostructures and molecules without averaging effects, all individual spectra of the data sets were analyzed in principal component analysis (PCA). The results of PCA are presented in Figure 6.5.

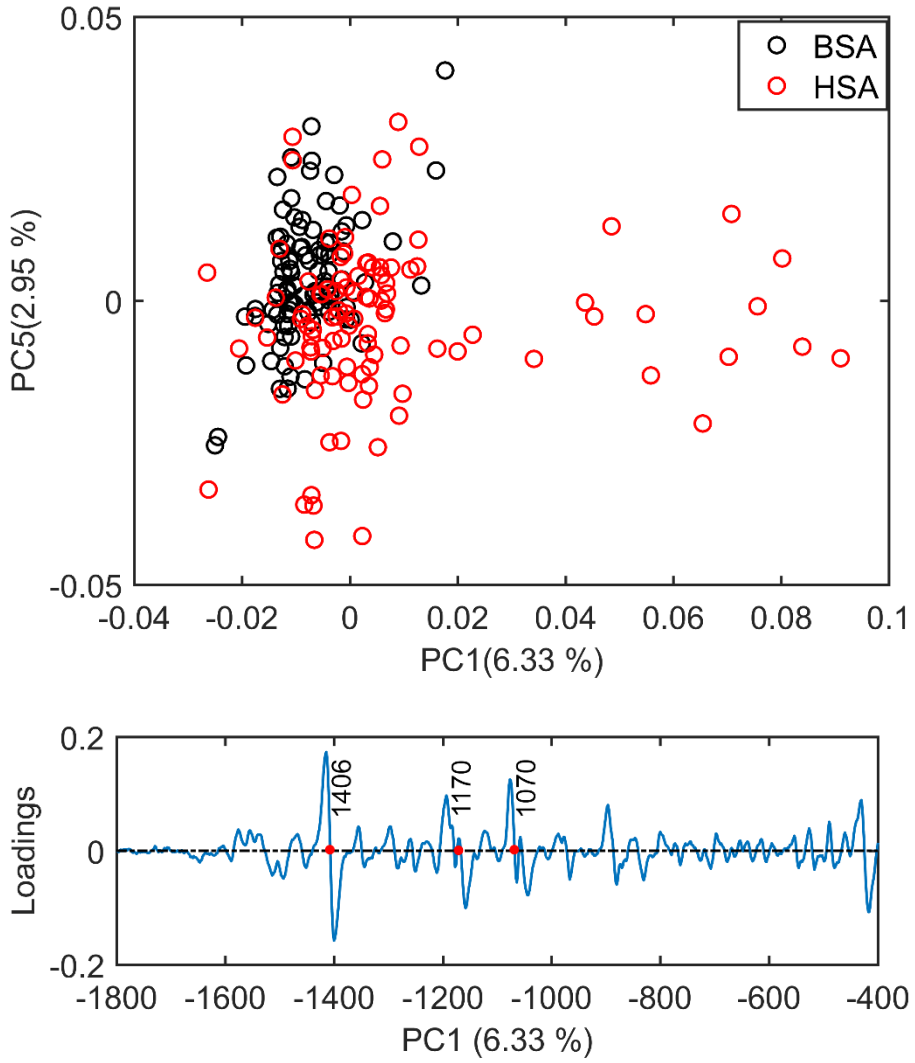

Figure 6.5. Scores plot of the first and second principal component obtained in a PCA using the 400 cm^{-1} – 1800 cm^{-1} spectral range of vectornormalized first derivatives of BSA and HSA SERS spectra (top) and loadings of the first PC (bottom). The dots mark the bands at 1406 cm^{-1} and 1170 cm^{-1} of the symmetric COO^- stretching and C-N stretching vibrations [215, 219], and at 1070 cm^{-1} of the C-O and/or C-C, NH_2, and C-N stretching vibrations [219, 240].

Figure 6.5 (top graph) shows the scores plot of the first two principal components (PC) as the result of a PCA using all individual spectra of HSA and BSA in the spectral range

of 400 cm^{-1} to 1800 cm^{-1} as input. As is visible from the scores of the first PC, the spectra of HSA show a greater variation than those of BSA (compare black and red symbols in Figure 6.5 top). The loading values of PC1 displayed in Figure 6.5 (bottom graph), which account for 6.33% of the variation in the datasets, suggest that the variance in the band at 1406 cm^{-1}, which can be assigned to the COO^- symmetric stretching [219, 240], has the strongest influence on this separation. Furthermore, variances are observed for the band at 1070 cm^{-1}, assigned to stretching vibrations of C-O and/or C-C, NH_2, and C-N groups, and the C-N stretching mode at 1170 cm^{-1} [215, 219]. The abundance of these bands in the BSA and HSA spectra is presented in Figure 6.6.

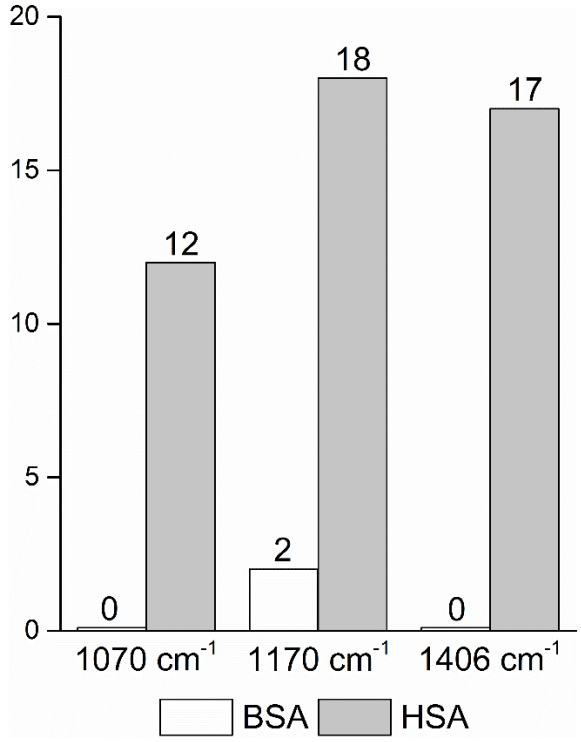

Figure 6.6. The abundance of the vibrational bands at 1070 cm^{-1} of the C-O and/or C-C, NH_2, and C-N stretching modes[219, 240], and at 1170 cm^{-1} and 1406 cm^{-1} of the C-N and the symmetric COO^- stretching vibrations[215, 219] in the BSA and HSA dataset, respectively.

Only two out of the 100 BSA spectra contain the band at 1170 cm^{-1}. In contrast, the 1070 cm^{-1}, 1170 cm^{-1}, and 1406 cm^{-1} bands are mostly present in the HSA spectra. There, the three bands appear mostly together, or the 1406 cm^{-1} vibration appears together with either the 1170 cm^{-1} or the 1070 cm^{-1} vibrations. Therefore, the analysis of the whole plethora of different individual spectra suggests that in some cases, specific for HSA,

different surface interactions take place than the citrate-lysine electrostatic interaction [22, 24, 25, 63].

In order to understand the potential interaction based on the SERS data, they are discussed in the context of the protein primary structure here. The two proteins HSA and BSA are very similar: a comparison of the two sequences showed approximately 77.5% sequence overlap. Since both the citrate layer and the pristine gold nanoparticle surface possess a negative and a positive net charge, respectively, protein molecules are expected to interact with the nanoparticles primarily *via* their charged side chains. In BSA, there are 40 aspartic acid, 59 glutamic acid, 17 histidine, 59 lysine, and 23 arginine residues, while in HSA there are 36 aspartic acid, 62 glutamic acid, 16 histidine, 59 lysine, and 24 arginine side chains. Even though the side chain of histidine is only weakly acidic, it participates in acid-base interactions, since the nitrogen atoms in its ring can act as proton shuttle depending on protonation [241]. Therefore, the fast transport of protons between side chains is facilitated, and an acidic or a basic residue in the proximity of histidine is more likely charged.

Figure 6.7 shows that the aspartic acid and glutamic acid residues in BSA and HSA (99 and 98 in total in each protein, respectively) are distributed homogeneously along the protein chains.

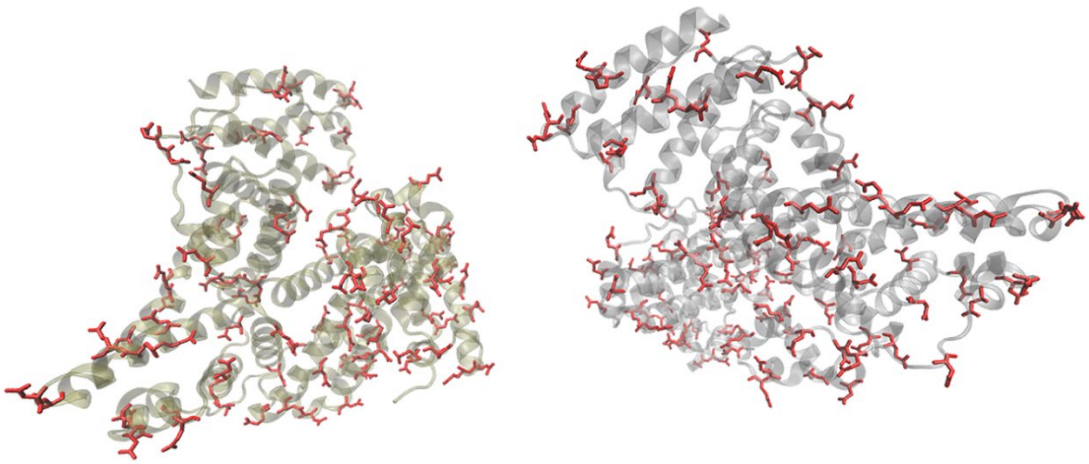

Figure 6.7. Distribution of acidic residues in BSA (left) and HSA (right), based on refs. [180] and [181], respectively. Protein data were visualized by VMD [182].

The protonation state of these amino acid side chains can be altered by their neighboring residues since the pH of the local microenvironment can be very different from the global

pH. Here, especially those neighbors that possess basic characteristics exert influence, since they can facilitate the deprotonation of the acidic residues in proximity. Table 6.3 shows the list of neighboring groups of each aspartic acid and glutamic acid residue in both BSA and HSA, and the distribution of the basic lysine and arginine residues, as well as of histidine are marked. The data indicate that in BSA, there are 12 and 15 lysine and one and five arginine residues neighboring aspartic acid and glutamic acid residues, respectively (Table 6.3). There are three histidine residues following a glutamic acid residue (Table 6.3). In contrast, in HSA, there are eight lysine, three arginine, and two histidine residues next to aspartic acid residues, and 11 lysine, four arginine, and two histidine residues next to glutamic acid residues (Table 6.3). In total, BSA contains six more amino acids that facilitate the deprotonation of their neighboring aspartic acid or glutamic acid.

The pH of the sample was around 4.5, close to the isoelectric points of BSA [25] and HSA [242]; therefore, a deprotonating effect could influence the protonation state of -COOH groups nearby. Considering an interaction with the citrate ions, a deprotonated $–COO^-$ group would be repelled electrostatically from them, as they also carry negative charges. This would result in an overall lower affinity of BSA than that of HSA in case the interaction would take place with the citrate layer via -COOH groups on the surface. The symmetric COO^- stretching vibration in the spectrum of HSA at 1406 cm^{-1} (compare Figure 6.3) indicates that the -COOH groups in the protein must be deprotonated; thus, the attractive electrostatic interaction between the $–COO^-$ and the negatively charged citrate layer can be precluded based on the SERS spectra. Since the acidity constants of the aspartic acid and glutamic acid side chains (2.23×10^{-4} and 5.62×10^{-5}, respectively [243]) are close to the first and second acidity constants of citrate ions (7.08×10^{-4} and 1.70×10^{-5}, respectively[244]), a dynamic protonation-deprotonation equilibrium can establish between the aspartic acid and glutamic acid side chains and the citrate ions of any degree of deprotonation. A fully protonated citric acid can re-protonate the deprotonated aspartic acid or glutamic acid side chain. As a consequence, $-COO^-$ groups can be in the proximity of the citrate layer, as is indicated in the spectra in the form of a signal of the symmetric $–COO^-$ stretching vibration.

Table 6.3 Neighboring side chains of the acidic residues (green), in the proteins BSA[180] and HSA[181], sorted from N- to C-termini. Basic residues are marked with red, and histidine with purple.

BSA									HSA								
—	Asp	Thr	Ser	Glu	Ile	Asp	Glu	Pro	—	Asp	Ala	Ser	Glu	Val	Val	Glu	Glu
Lys	Asp	Leu	Gly	Glu	Glu	Phe	Glu	Lys	Lys	Asp	Leu	Gly	Glu	Glu	Glu	Glu	Pro
Phe	Asp	Glu	Glu	Glu	His	Gly	Glu	Tyr	Glu	Asp	His	Glu	Glu	Asn	Cys	Glu	Leu
Ala	Asp	Glu	Asp	Glu	His	Val	Glu	Val	Ala	Asp	Glu	Phe	Glu	Asp	Phe	Glu	Gln
Gly	Asp	Glu	Asn	Glu	Leu	Pro	Glu	Ser	Cys	Asp	Lys	Asn	Glu	Val	Gly	Glu	Tyr
Gly	Asp	Met	Thr	Glu	Phe	Ser	Glu	Arg	Gly	Asp	Lys	Thr	Glu	Phe	Val	Glu	Val
Ala	Asp	Cys	Asp	Glu	Ser	Thr	Glu	Asp	Ala	Asp	Cys	Asp	Glu	Ser	Pro	Glu	Ala
Lys	Asp	Asp	Cys	Glu	Lys	His	Glu	Lys	Lys	Asp	Asp	Ala	Glu	Asn	Ala	Glu	Asp
Asp	Asp	Ser	Asp	Glu	Leu	Ser	Glu	Lys	Asp	Asp	Asn	Arg	Glu	Thr	His	Glu	Lys
Pro	Asp	Leu	Arg	Glu	Thr	Thr	Glu	Ser	Val	Asp	Val	Gly	Glu	Met	Thr	Glu	Ser
Pro	Asp	Pro	Cys	Glu	Lys	Asp	Glu	Thr	His	Asp	Asn	Gln	Glu	Pro	Leu	Glu	Val
Cys	Asp	Glu	Gln	Glu	Pro	Asp	Glu	Lys	Ala	Asp	Lys	Pro	Glu	Arg	Asp	Glu	Thr
Ala	Asp	Glu	Pro	Glu	Arg	Thr	Glu	Lys	Leu	Asp	Glu	Asn	Glu	Cys	Lys	Glu	Phe
Glu	Asp	Lys	Asn	Glu	Cys	Val	Glu	Leu	Arg	Asp	Glu	Pro	Glu	Val	Ala	Glu	Thr
Thr	Asp	Leu	Asp	Glu	Phe	Thr	Glu	Glu	Thr	Asp	Leu	Asn	Glu	Glu	Ser	Glu	Lys
Gly	Asp	Leu	Asp	Glu	Lys	Glu	Glu	Gln	Gly	Asp	Leu	Glu	Glu	Thr	Lys	Glu	Arg
Ala	Asp	Asp	Tyr	Glu	Ile	Met	Glu	Asn	Ala	Asp	Asp	Tyr	Glu	Ile	Val	Glu	Leu
Asp	Asp	Arg	Pro	Glu	Leu	Lys	Glu	Ala	Asp	Asp	Arg	Pro	Glu	Leu	Lys	Glu	Gln
Ala	Asp	Leu	Gln	Glu	Cys	Val	Glu	Gly	Ala	Asp	Leu	Thr	Glu	Cys	Val	Glu	Lys
Cys	Asp	Asn	Ala	Glu	Asp				Gln	Asp	Ser	Asp	Glu	Leu	Lys	Glu	Thr
Gln	Asp	Thr	Ile	Glu	Thr				Asn	Asp	Glu	Asp	Glu	Gly	Ala	Glu	Glu
Cys	Asp	Lys	Arg	Glu	Lys				Ala	Asp	Leu	Gly	Glu	Arg	Glu	Glu	Gly
Lys	Asp	Ala	Gly	Glu	Arg				Ala	Asp	Phe	Ala	Glu	Phe			
Ala	Asp	Phe	Ala	Glu	Phe				Lys	Asp	Val	Ala	Glu	Val			
Glu	Asp	Lys	Val	Glu	Val				Lys	Asp	Val	Thr	Glu	Cys			
Lys	Asp	Val	Lys	Glu	Cys				Pro	Asp	Tyr	Leu	Glu	Cys			
Lys	Asp	Ala	Leu	Glu	Cys				Ala	Asp	Pro	Cys	Glu	Asn			
Lys	Asp	Asp	Lys	Glu	Cys				Phe	Asp	Glu	Lys	Glu	Cys			
Asp	Asp	Pro	Leu	Glu	Lys				Glu	Asp	Tyr	Cys	Glu	Lys			
Phe	Asp	Lys	Ala	Glu	Val				Ser	Asp	Arg	Leu	Glu	Lys			
Val	Asp	Glu	Val	Glu	Lys				Val	Asp	Glu	Ala	Glu	Val			
Cys	Asp	Gln	Pro	Glu	Asn				Ala	Asp	Ile	Val	Glu	Asn			
Glu	Asp	Tyr	Ala	Glu	Asp				Met	Asp	Asp	Asp	Glu	Met			
Pro	Asp	Glu	Gln	Glu	Ala				Asp	Asp	Phe	Val	Glu	Ser			
Phe	Asp	Glu	Tyr	Glu	Tyr				Ala	Asp	Asp	Ala	Glu	Ala			
Ala	Asp	Ile	Pro	Glu	Tyr				Asp	Asp	Lys	Tyr	Glu	Tyr			
Pro	Asp	Thr	Lys	Glu	Tyr							Tyr	Glu	Thr			
Val	Asp	Lys	Tyr	Glu	Ala							Leu	Glu	Lys			
Ala	Asp	Asp	Leu	Glu	Glu							His	Glu	Cys			
Asp	Asp	Lys	Glu	Glu	Cys							Asp	Glu	Phe			

The data also indicate a direct adsorption of the protein molecules to the nanoparticle surface as a consequence of the exchange of the citrate ligands by the protein molecules. The direct adsorption of protein molecules on the positively charged surface of gold nanoparticles requires negatively charged residues, namely the deprotonated $–COO^-$ groups that are observed in the spectra of HSA. Furthermore, steric restrictions are implied by the protein secondary structure. Specifically, more flexible random coil structures would be energetically favored over very much defined α-helices, since flexible segments are distorted easier, allowing for the most preferred orientation of side chains involved in specific residue-nanoparticle interactions [245]. In order to achieve the energetically most preferred site for adsorption, the amino acids inside a random coil sequence are expected to interact preferentially with the nanoparticle surface. In BSA, no acidic side chain was found in a completely random-coiled structure, without having neighbors with basic residues that could be repelled by the net positive surface charge of the gold nanoparticles [180, 182]. In contrast, in HSA two such segments can be identified: ...-Val_{293}-Glu_{294}-Asn_{295}-Asp_{296}-Glu_{297}-Met_{298}-... and ...-Leu_{491}-Glu_{492}-Val_{493}-..., both of which contain acidic residues. The flexibility of the segments was verified by modeling of protein structure flexibility, calculating the root-mean square fluctuations of the residues by CABS-flex 2.0 [246] for the entire HSA chain, which suggests that the identified segments are indeed not rigid (Figure 6.8).

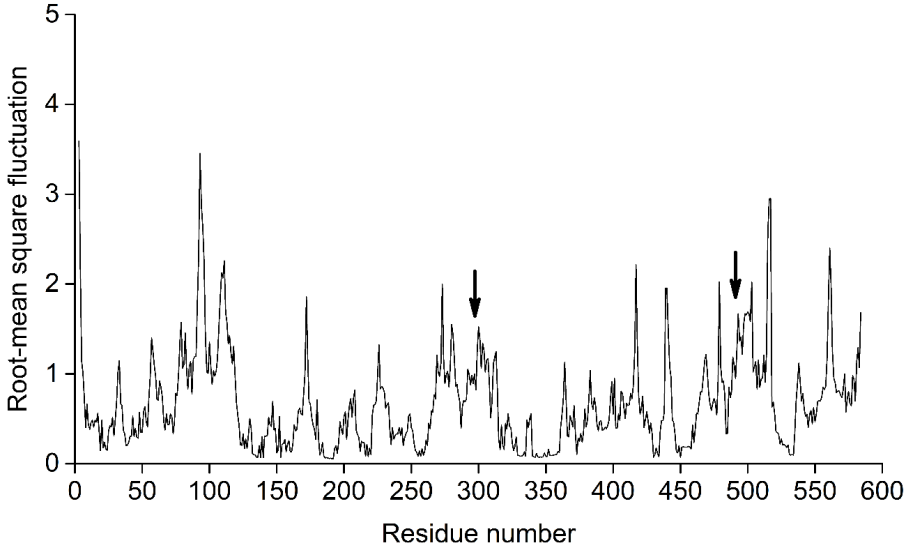

Figure 6.8. Root-mean square fluctuation calculation results for the HSA chain obtained in a simulation with CABS-flex 2.0. The position of the ...-Val_{293}-Glu_{294}-Asn_{295}-Asp_{296}-Glu_{297}-Met_{298}-... and ...-Leu_{491}-Glu_{492}-Val_{493}-... segments are marked with arrows.

The analysis of band co-occurrences revealed that the bands at 1070 cm^{-1}, 1170 cm^{-1}, and 1406 cm^{-1} are present together in several spectra, in about half of the spectra displaying the 1406 cm^{-1} band. In accord with this, the ...-Val_{293}-Glu_{294}-Asn_{295}-Asp_{296}-Glu_{297}-Met_{298}-... segment contains three free -COOH groups, which are expected to adsorb on the positively charged surface of gold nanoparticles in the deprotonated form. The Asn_{295} residue between the Glu_{294} and Asp_{296}, carries an amide functional group, which can contribute to both the 1070 cm^{-1} and the 1170 cm^{-1} signal as well. The simultaneous appearance of these three bands in one spectrum (see, *e.g.,* Figure 6.3, top spectrum) suggests the interaction of the ...-Val_{293}-Glu_{294}-Asn_{295}-Asp_{296}-Glu_{297}-Met_{298}-... segment with the surface of the nanoparticles. This interaction is illustrated in Figure 6.9. The ... Leu_{491}-Glu_{492}-Val_{493}-... segment, where Glu_{492} has neighbors with only CH_x (with x of 1, 2 or 3) groups, can only contribute to the 1406 cm^{-1} band; therefore the sole appearance of this band can be explained by the adsorption of this segment when considering the direct interaction with the nanoparticle surface.

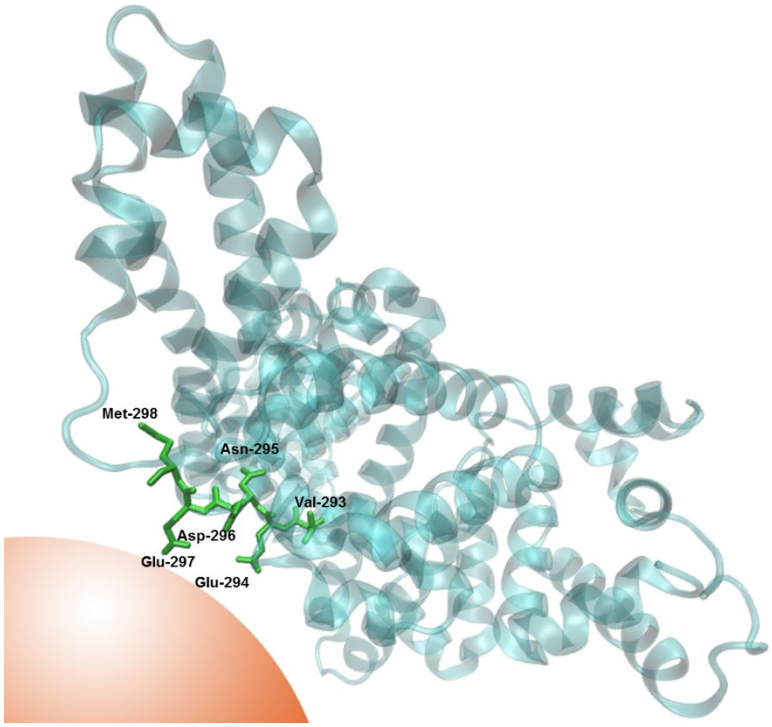

Figure 6.9. Schematic illustration of the expected interaction between the ...-Val_{293}-Glu_{294}-Asn_{295}-Asp_{296}-Glu_{297}-Met_{298}-... segment of HSA and the gold nanoparticle surface.

6.4. Summary

In this chapter, the interaction of BSA and HSA with gold nanoparticles was elucidated. Due to the high similarity of the two proteins, their normal Raman spectra are nearly identical and therefore, the differentiation between the two proteins solely based on their normal Raman data is difficult. Regardless the significant overlap between the primary structures of the two proteins, which could cause nearly identical interactions with the gold nanoparticles, distinct spectral features were observed in the SERS datasets of the two proteins interacting with gold nanoparticles. The SERS data indicate that the electrostatic binding of the proteins to the citrate layer without ligand exchange is possible both for BSA and HSA *via* lysine residues, supporting data obtained by other methods [24, 25, 28, 63, 236]. However, different from BSA, a portion of the HSA spectra clearly indicate different interactions as well, which were revealed by PCA. The band at 1406 cm^{-1} assigned to the symmetric stretching vibration of the $–COO^–$ functional group appears in 17 SERS spectra in the dataset of HSA. Considering the interaction with the citrate ions on the surface of the gold nanoparticles and the local microenvironment of acidic residues in HSA, it was found that a protonation-deprotonation equilibrium can arise between the citrate ions and the carboxyl groups of aspartic acid and glutamic acid residues. Moreover, the band at 1406 cm^{-1} often co-occurred with the bands at 1070 cm^{-1} and 1170 cm^{-1} assigned to C-O and/or C-C, NH_2, and C-N groups, and a C-N stretching mode. After combining this information with the crystallographic data of HSA and root-mean square fluctuation calculations revealing the flexibility of the protein chain, the direct binding of HSA to the nanoparticle surface *via* the ...-Val_{293}-Glu_{294}-Asn_{295}-Asp_{296}-Glu_{297}-Met_{298}-... and ...-Leu_{491}-Glu_{492}-Val_{493}-... segments was proposed, which results in the exchange of citrate ions. In addition to this particular structural information, the results indicate that in single protein systems the high selectivity and sensitivity of SERS are very beneficial for obtaining vibrational information, and the differentiation between two nearly identical proteins is possible. This further underpins the critical role of surface-enhanced optical spectroscopies in the characterization of nano-bio-interactions and for future probing of the biomolecular corona *in situ* and *in vivo*.

Chapter 7

Mass spectrometric analysis of the hard protein corona formed in living cells

This chapter was part of a manuscript published in *G. P. Szekeres et al., Journal of Proteomics, 212, 103582, 2020,* and it is reproduced here with permission of Elsevier.

Besides the protein-nanoparticle surface interactions, which were analyzed in Chapter 5 and Chapter 6, the molecular composition of the hard protein corona has a deterministic effect on the fate of the nanoparticle inside the cell, as well as its interactions with its biomolecular environment. The evolution of the protein corona formed on a nanoparticle is a complex process, which already starts when the nanoparticles are introduced into the culture medium. In the culture medium, serum proteins (which were added to the primary medium as protein supplementation) adsorb on the surface of the nanoparticle, forming a primary corona. The longer the nanoparticle resides in the culture medium, the stronger the protein-nanoparticle interactions will be due to the exchange of the most abundant proteins in the solution to the proteins with higher affinity [17]. This primary protein corona formed before the cellular internalization of the nanoparticles can alter the

cytotoxicity of the nanoparticles [58, 73, 247], and the new, "biological identity" of the nanoparticles, that is, their changed behavior in biological samples (*e.g.,* in living cells) due to the adsorbed protein layer*,* will determine the fate of the nanoparticle and its effects inside the cell [20]. In other words, the protein corona is the first point of interaction between the cell and the protein-nanoparticle bioconjugates, that is, what the cell "sees" [19]. However, this primary corona immediately starts to exchange upon contact with the cells due to the higher affinity of some intracellular proteins [17, 69]. The continuously developing protein corona will evolve into a less dynamic layer during the cellular processing of the nanoparticle, which is called the hard protein corona. Therefore, in light of our current knowledge of nanoparticle-protein bioconjugates, studying the nature of the hard protein corona is vital for the understanding of the effects of nanomaterials and for the development of nanopharmaceuticals. Most studies focus on the composition of the protein corona in complex protein solutions *in vitro* such as in blood serum [13, 19, 35, 39, 75, 161, 187, 248] or cell lysate [34, 37, 38]. Therefore, the understanding of the hard protein corona processing and its composition in living systems is, so far, poor, generally relying on indirect experiments, *e.g.,* the overall analysis of the protein corona complex [36] or the study of the exchange of labeled proteins on the surface of the nanoparticles [69, 190].

In this chapter, an attempt to assess the composition of the unaltered hard protein corona formed in living cells is presented, which so far could not be found in the state-of-the art literature. The results forms the basis of direct correlation with the datasets of complementary analytical methods, such as SERS.

7.1. Brief description of the analysis approach

The combination of soft cell lysis, hard corona purification through a sucrose cushion, SDS-PAGE, in-gel protein digestion followed by peptide extraction, and HPLC-ESI-Q-TOF-MS was used to determine the composition of the hard protein corona formed on internalized gold nanoparticles in living cells. Figure 7.1 schematically displays the entire protocol used here to analyze the hard protein corona in living cells. The corresponding experimental steps are described in details in Sections 4.15-4.20.

After the incubation of cells, the cell- and organelle membranes were ruptured by soft cell lysis, and the hard corona-nanoparticle bioconjugates were purified, as described in Section 4.15. Then, SDS-PAGE was used to separate the hard corona proteins based on their molecular mass (Section 4.17). After the SDS-PAGE, in-gel trypsinization was performed to cleave the proteins inside the polyacrylamide gel and to facilitate the extraction of the resulting peptides (Section 4.18). Then, the extracted peptides could be analyzed with HPLC-ESI-Q-TOF-MS (Section 4.19), and the data were evaluated by MASCOT (Section 4.20).

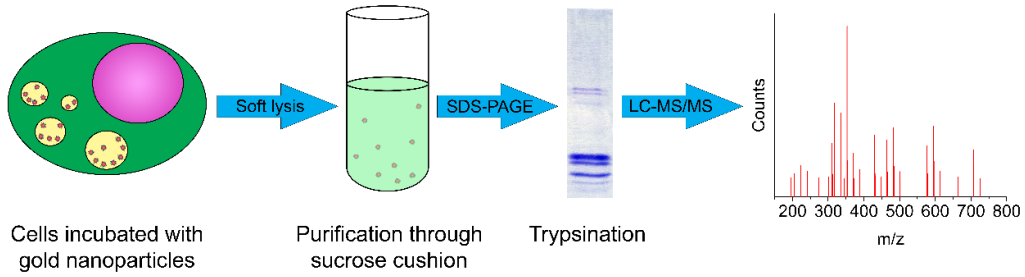

Figure 7.1. Schematic graph of the nanoparticle-hard corona bioconjugate extraction, purification, and analysis.

7.2. The composition of the hard protein corona formed in MCF-7 cells

Due to their small size and easily tailored surface characteristics, nanoparticles emerged into the focus of the research for the formulation of new pharmaceuticals. One of the most promising fields of the application of nanopharmaceuticals is cancer diagnostics and treatment [249, 250]. Based on the cancer statistics of 2018, breast cancer was the second most common type of cancer in both sexes, and the leading cancer type in women, claiming over 600,000 lives worldwide. MCF-7 is an immortal cell line that derives of human breast carcinoma, which was chosen to model the proteome of the hard corona formed on internalized gold nanoparticles in breast cancer cells.

Figure 7.2 shows the representative electropherogram of the corona proteins extracted from MCF-7 cells. After the electrophoresis, gels were fixed with the aqueous solution of 10% acetic acid and 50% ethanol to allow for the subsequent extraction of proteins from the gel. It can be seen that the electropherogram contains a large number of different

proteins in the 10-250 kDa molecular weight regime, with a higher protein concentration in the ~10-20 kDa, ~25-30 kDa, ~40-60 kDa, and ~65-90 kDa regions.

Seven gel segments were excised (Figure 7.2, M1-M7) for the mass spectrometric identification of proteins in the extracted hard protein corona, from which the fragmented proteins were extracted after in-gel tryptic digestion (see experimental details in Section 4.18 and in ref. [35]). With the excision of gel segments and their separate analysis, the identified proteins could be better controlled for false hits, based on the molecular weight range assigned to the sample.

For protein identification, reversed-phase HPLC was coupled with ESI-Q-TOF-MS. The experimental specifications were described in details in Section 4.19. After the HPLC-ESI-Q-TOF-MS analysis, the results were evaluated by MASCOT [195] (see search parameters in Section 4.20).

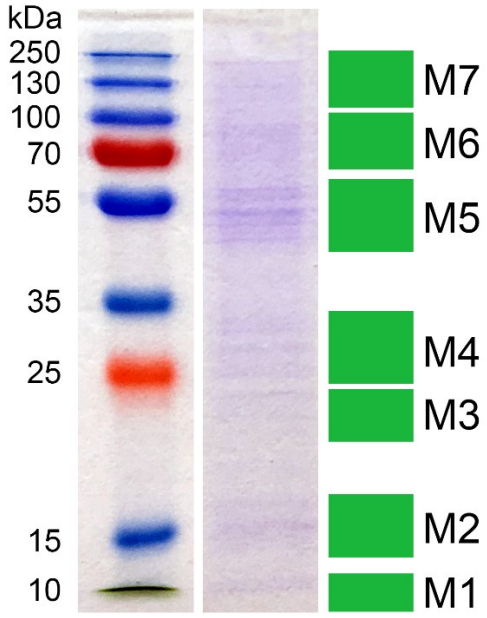

Figure 7.2. Protein corona profile of nanoparticle-protein bioconjugates extracted from MCF-7 cells after 24 h incubation. The numbers on the left represent the molecular mass of the corresponding band in the protein ladder in kDa next to them, while the green rectangles (M1-7) indicate the excised gel segments for HPLC-ESI-Q-TOF-MS analysis.

108 proteins with identity or extensive homology (markers of significant hits, see detailed description in Section 4.20.2) were found in the hard protein corona extracted from MCF-7 as shown in Table S7.1, out of which 102 originate from human cells and 6 from

bovine blood serum. The MASCOT analysis yields a plethora of information, including those that do not directly help the understanding of the hard protein corona. Therefore, only the accession numbers, names, the number of recovered residues in the protein fragments compared to the length of total chains, MASCOT scores, and the molecular mass of the identified proteins were displayed here after careful data analysis. Porcine trypsin used for the in-gel digestion and common contaminants were excluded from the summary of identified proteins. The excised bands with intense color contained high amounts of bovine hemoglobin (M1, M2), histones (M1, M2), and ribosomal proteins (M2-M5), among others. To find connection between the identified proteins, the data were analyzed by DAVID (Database for Annotation, Visualization and Integrated Discovery, https://david.ncifcrf.gov); 36 ribosome-related, 10 nucleus-related, 3 translation elongation-related, 3 helicase-related, 7 GTP binding-related, 5 nucleosome-related, 3 LEM domain-related, and 3 clathrin-mediated endocytosis-related proteins were found in the protein ontology analysis. DAVID calculates an approximate protein enrichment in the samples, which is an indicator of the ratio of specific proteins in the sample compared to the natural composition of the cells. Based on the calculated enrichment scores, ribosome-related and nucleus-related proteins were significantly enriched in the protein corona. 30 nm citrate-stabilized gold nanoparticles generally reside outside of the cell nucleus in cellular compartments connected to the endolysosomal pathway [42, 90]. A possible explanation of the enrichment of these proteins in the hard corona is the co-localization of nanoparticles with damaged organelles (*e.g.,* ribosomes) and proteins in vesicles destined to be transported into the extracellular matrix.

The hard protein corona of gold nanoparticles internalized by MCF-7 cells was analyzed after an incubation time of 24 h. It has been shown that cells interact with nanoparticles on much shorter time scales as well, resulting in different intracellular aggregate morphologies indicating different processing of the nanoparticles [168]. Nanoparticles processed for shorter times can exhibit different corona compositions based on the extent of primary corona protein exchange [69]. Therefore, it was essential to study the hard protein corona composition after different incubation times to gain information about its possible evolution.

7.3. Time-resolved analysis of the hard protein corona composition

To investigate the composition of the hard protein corona and its possible changes over time, shorter incubation times also had to be studied, for which, MCF-7 cells exhibited a less efficient nanoparticle uptake than necessary to exceed detection limits after short incubation periods. Therefore, J774 macrophage cells were chosen for the time-resolved experiments, since the biological function of macrophages requires an increased rate of nanoparticle uptake of extracellular matter, which has been proved in previous studies with fluorescence-labeled polystyrene nanoparticles [251] and with intracellular particle enumeration in cryo soft X-ray tomograms after 3 h [168].

In the experiments aiming at studying the evolution of the hard protein corona over time, J774 mouse macrophage cells were incubated with gold nanoparticles for 1.5 h, 3 h, 6 h, and 24 h. The resulting electropherograms of the proteins are shown in Figure 7.3. The gels were fixed with the aqueous solution of 5% formaldehyde and 25% ethanol to cross-link the low-mass peptide species, thus preventing their release from the gel.

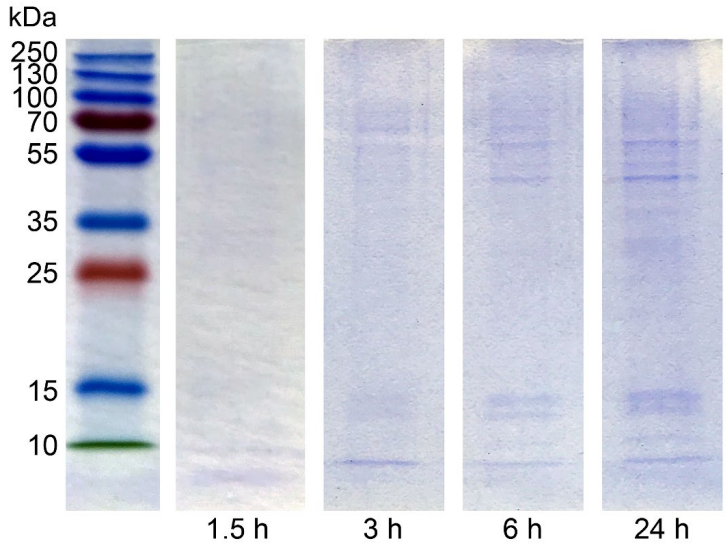

Figure 7.3. SDS-PAGE of parallel samples of the hard corona proteins extracted from J774 cells after 1.5 h, 3 h, 6 h, and 24 h incubation.

The color intensity of the bands in the electropherograms increased with the incubation time, proportional to the increased gold nanoparticle uptake over time, accompanied by

the overall higher amount of extracted hard corona proteins. After comparing the electropherograms of the samples with different incubation times, no major changes could be observed in terms of appearance or disappearance of bands in the incubation time interval of 1.5-24 h. This is in agreement with previous work showing that the protein corona forms rapidly, and its composition remains unchanged over time [32].

For the mass spectrometric analysis, J774 cells were incubated with gold nanoparticles for 1.5 h, and after the hard corona purification and SDS-PAGE, the electropherograms were fixed in the aqueous solution of 10% acetic acid and 50% ethanol to facilitate the extraction of fragmented proteins after in-gel digestion. A blurry band was visible under the 10 kDa marker in the electropherograms fixed with formaldehyde, which did not show in the electropherogram fixed with acetic acid (Figure 7.4). This band denotes low-mass polypeptide species, which are washed out of the gel upon acetic acidic fixation, as it does not cross-link proteins. Since the <10 kDa band only appeared in the electropherograms fixed with a solution used to retain low-mass polypeptides as well, it can be excluded that it was an artifact.

Five gel segments were excised of the electropherogram shown in Figure 7.4 for the mass spectrometric identification of the hard corona proteins, marked with J1-J5.

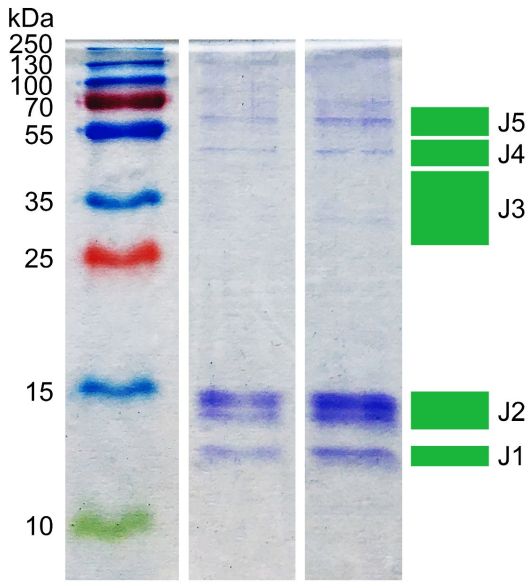

Figure 7.4. SDS-PAGE of two parallel samples of the hard corona proteins extracted from J774 cells after 1.5 h incubation. The green rectangles (J1-5) represent the excised gel segments further analyzed by HPLC-ESI-Q-TOF-MS.

It can be seen that larger gel segments were excluded from the analysis. The gel segments not displaying protein bands contain only a low amount of protein molecules, if any, which would be below the detection limit of the instruments or below the scores of identity or extensive homology in MASCOT, thus reducing the signal-to-noise ratio in the dataset.After the data analysis, 11 proteins were identified, out of which 10 originated from the J774 cells *(Mus musculus)* and one from the culture medium *(Bos taurus)*. The 11 identified hard corona proteins are presented in Table S7.2. Since inside macrophage cells, gold nanoparticles primarily reside in phagosomes [252], the results were compared with previous studies of phagosomal proteins [82, 83]. There is a considerably higher number of identified proteins in the phagosome than in the hard protein corona, while based on the data presented in this chapter it is evident that specific proteins, mostly histones, were enriched in the hard protein corona compared to the phagosome.

Similar to the hard corona proteome formed in MCF-7 cells, histones were among the more abundant proteins, and bovine hemoglobin was also found in the hard corona formed in J774 cells, while only one ribosomal protein was found above the significance threshold. Different from the proteome of phagosomes, which changes over time depending on the maturation process [82], it was observed that the hard corona proteome formed on gold nanoparticles in J774 cells remains unchanged over the course of 24 h, which is longer than the complete cell cycle of J774 cells [189]. This is contrary to the findings of Bertoli *et al.* [69], who showed based on fluorescently labeled serum proteins that the serum proteins continuously exchange on the surface of differently functionalized polystyrene nanoparticles over the course of hours after the nanoparticles were internalized by cells. There are two possible explanations for the different findings: they used different nanoparticles from those used in these experiments, and they performed SDS-PAGE on whole endolysosomes rather than only the hard protein corona. Based on those results, it was not possible to differentiate between proteins that strongly interact with the nanoparticles, those that only weakly interact, and those that do not interact at all, while the data presented in this chapter represents explicitly the hard protein corona.

It can be observed that even though, there was a 10-fold decrement in the number of identified hard corona proteins in J774 compared to that of MCF-7, histones, ribosomal proteins, cytoplasmic actin, and bovine hemoglobin were found in both hard protein coronas (Tables S7.1 and S7.2). Since the electropherograms of parallel samples (see

Figure 7.4), as well as those of the time-resolved experiments (Figure 7.3), showed high similarity, while the hard corona proteome in J774 was different from the proteome of phagosomes (compare Figures 7.3 and 7.4, and Table S7.2 with ref. [82]), it can be concluded that the hard protein corona must form based on active cellular processes and not only by random protein adsorption. As stated above, parallel hard corona samples extracted from the same cell line showed high similarity, while the hard corona proteomes of MCF-7 and J774 were different (Figures 7.2 and 7.3, Tables S7.1 and S7.2), which indicates that the hard protein corona is typical for a cell line, while major differences can be found in the hard corona proteomes extracted from different cell lines.

7.4. Summary

In this chapter, the combination of soft cell lysis, SDS-PAGE, and HPLC-ESI-Q-TOF-MS was proposed as an analytical approach to study the composition of the hard protein corona formed in living cells. MCF-7 (human breast carcinoma) and J774 (mouse macrophage) cells were incubated with gold nanoparticles, the hard corona-nanoparticle bioconjugates were extracted, and the proteins were analyzed after purification.

108 proteins were identified in the hard corona formed in MCF-7, out of which 6 derived from the bovine blood serum in the culture medium, while only 11 proteins were found in the hard corona formed in J774 cells. Despite the more complex hard corona proteome in MCF-7, the two cell lines both produced hard coronas that contained histones, ribosomal proteins, cytoplasmic actin, and bovine hemoglobin deriving from the culture medium, indicating the general enrichment of specific proteins in the hard protein coronas. The experiments on the time-dependent evolution of the hard corona formed in J774 cells revealed that the hard corona proteome of gold nanoparticles remains unchanged over the course of 24 h in J774 cells, which exceeds their complete cell cycle [189]. The results of this chapter suggest that the proteome of the hard protein corona is typical for each cell line, but major differences can be found between the hard corona proteomes formed in different cell lines. Therefore, it is probable that the hard corona of internalized nanoparticles forms based on specific intracellular processes rather than the adsorption of random proteins.

Contrary to those in the state-of-the-art literature, the analytical method presented here is capable of the qualitative analysis of the unaltered hard protein corona formed in living cells. It is expected that this approach can be easily applied for the analysis of the hard protein corona formed in more complex biological samples, such as tissues.

A line corresponding to polypeptides with <10 kDa molecular mass was found in the electropherograms fixed with formaldehyde, which was absent in the case of fixing in the solution of acetic acid and methanol. Its presence could indicate low-mass polypeptides, but the mass spectrometric identification was not possible; therefore, an alternative analytical approach was necessary for their study, which is presented in Chapter 8.

Chapter 8

Identifying spectral signatures of protein fragmentation in live cell SERS data

This chapter was part of a manuscript published in *G. P. Szekeres et al., Analytical Chemistry, 92, 8553-8560, 2020,* and it is here reproduced with permission of the American Chemical Society.

When gold nanoparticles enter a cell in incubation experiments, they are already surrounded by a primary protein corona formed in the culture medium. The environment of the gold nanoparticles can dramatically change over time due to the active processing of the internalized materials and to the endosomal maturation [82]. It has been shown previously in Chapter 5 and Chapter 6 that the applied sample preparation approach for the analysis of protein solutions is suitable to benefit from the high sensitivity and surface selectivity of SERS. The SDS-PAGE results of the time-resolved studies of the hard corona evolution in J774 cells suggest that low-mass polypeptide species, possibly fragmented proteins (see Chapter 7 and ref. [69]) are present in the protein corona. The aim of the study detailed in this chapter is to identify spectral signatures of protein fragmentation in living cells. In this chapter, the SERS spectra from live cells and from the isolated cytoplasm will be compared to identify the signs of intracellular processing

in the SERS signals. Additionally, as control data, the SERS spectra of BSA, bovine trypsin, and their mixture, where the enzymatic cleavage of BSA takes place, will be analyzed, which allow for the differentiation of the spectral signatures of protein cleavage from other changes induced by the altered matrix or the chemicals used for isolating the cytoplasm. This chapter also extends the discussion of BSA-gold nanoparticle interactions described in Chapter 6.

8.1. Comparison of the SERS data of live J774 cells and the isolated cytoplasm

The cytoplasm of J774 cells was isolated, as described in Section 4.9. The rate of the enzymatic processes in the isolated cytoplasm was expected to be severely decreased due to the much lower protein concentration resulting from the extraction method compared to intracellular protein concentrations. SERS spectra were obtained from the isolated cytoplasm of J774 macrophage cells and from live J774 cells after being incubated with 30 nm citrate-stabilized gold nanoparticles for 1.5 h (see sample preparation and SERS data collection in Sections 4.3., 4.9, and 4.10).

8.1.1. Analysis of the average spectra of live cells and the isolated cytoplasm

The average SERS spectra of the endolysosomal compartments (live cell SERS mapping) and of the isolated cytoplasm are presented in Figure 8.1. The average spectra of the endolysosomal compartments and of the isolated cytoplasm were calculated from 883 and 613 SERS spectra, respectively. The endolysosomal spectra originated from five different J774 cells with identical incubation conditions to compensate for cell-to-cell variation. The two average spectra exhibit different traits. The main differences appear in the 1580-1440 cm^{-1}, 1320-1220 cm^{-1}, 1180-1120 cm^{-1}, and the 680-460 cm^{-1} regions. The average SERS spectrum of the extracted cytoplasm shows a higher intensity in the 1580-1440 cm^{-1} and the 1320-1220 cm^{-1} regions, which include many vibrations assigned to the amide II and amide III bands [253], as shown in Table 8.1. Some spectral bands corresponding to vibrations of tryptophan at 1352 cm^{-1}, C-C and C-N stretching at 1170 cm^{-1}, 1130 cm^{-1}, and 1085 cm^{-1}, vibrations of tyrosine at 838 cm^{-1}, and C-S and S-S stretching vibrations at 670-466 cm^{-1} are more intense in the average of the endolysosomal spectra (compare black spectrum in Figure 8.1 and tentative assignments

in Table 8.1). The prominent presence of the vibrational bands of tryptophan and tyrosine and those of C-C stretching allow for the conclusion that the nonpolar residues of proteins can be exposed in the endolysosomal compartments. An increased exposure of the nonpolar side chains to the aqueous environment can result from the denaturation and fragmentation of some protein molecules, as proteins tend to fold into structures with hydrophobic cores in polar solvents [47]. The increased contribution of nonpolar residues to the SERS spectra can further indicate the interaction of the gold nanoparticles with the membrane of the compartments they reside in, which has been discussed previously [39]. Since the laser intensity was lower in the SERS data collection of live cells than in solution, it can be excluded that the denaturation of those proteins results from photothermal damage.

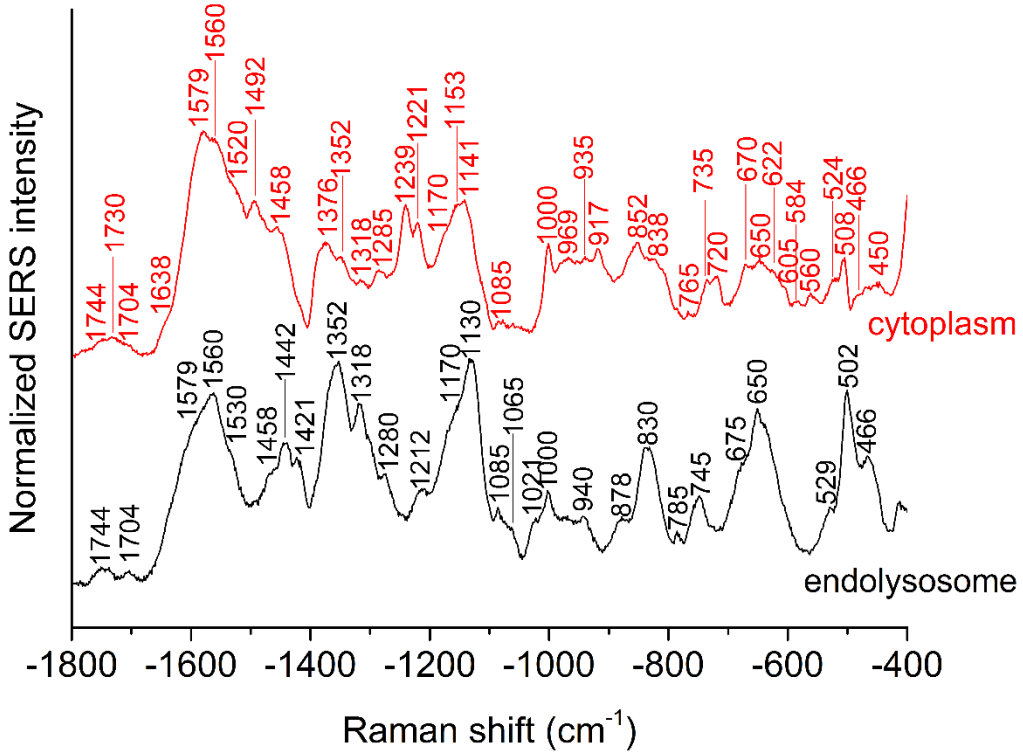

Figure 8.1. The average of 613 SERS spectra from the isolated cytoplasm (red trace) and of 883 SERS spectra from five live J774 cells (black trace). 24 h incubation, excitation wavelength: 785 nm, acquisition time: 1 s, excitation intensity: 2.3×10^5 W/cm^2 and 5.7×10^5 W/cm^2 in the endolysosomal compartments and the isolated cytoplasm, respectively.

The presence of S-S stretching vibrations in the 500-600 cm^{-1} region in the average spectra of both the endolysosomal compartments and the isolated cytoplasm indicates that

despite the suggested denaturation and fragmentation of some protein molecules, other protein chains preserve their secondary and tertiary structures at least partially (Figure 8.1 and Table 8.1). The higher intensity of the C-S and S-S stretching vibrations between 466 cm^{-1} and 675 cm^{-1} in the endolysosomal spectra (Figure 8.1 black spectrum and Table 8.1) can come from the revealed disulfide bridges during protein digestion or from proteins with a high number of sulfur bridges [254, 255]. Based on the results of Chapter 7 (see Table S7.2), the latter can be explained by the high amount of histones in the protein corona, as nucleosomes have been shown to stabilize with disulfide bonds [256] between the N-terminal cysteine of histone H4 and a cysteine in the α-helix 2 of histone H2A [257, 258].

Table 8.1. Raman shifts and their tentative assignments in Figure 8.1. *ν* stretching, *δ* deformation, *symm* symmetric, *wag* wagging, *rock* rocking, *br* breathing, *R* benzene ring, *r* pyrrole ring. Band assignments were based on refs. [40, 104, 171, 172, 215, 219, 253].

Raman shift (cm^{-1})	Tentative assignment	Raman shift (cm^{-1})	Tentative assignment
1744	ν(C=O)	1021	ν(C-O) of ribose
1730	ν(C=O)	1000	R br
1704	δ (COOH) of Asp, Glu	969	C-C wag, lipids
1638	Amide I	935	Pro, ν(C-C)
1579	ν(C-C,COO^-), Amide II	917	Pro and Val ν(C-C)
1560	Amide II, Trp, Tyr, ν(COO^-)	878	Pro and Val ν(C-C)
1520	Amide II	852	ν(Cα-N,C-C), Tyr, Phe, Pro
1492	Amide II, NH_3^+	838	$\nu(O\text{-}P\text{-}O)_{asymm}$, Tyr, Pro
1458	δ(CH_2,CH_3)	785	ν(O-P-O), C, U, T R br
1442	δ(CH_2,CH_3)	765	Trp R def, C, U, T R br
1421	A, G, CH_3CH_2 twisting	745	Trp symm br
1376	T, A, G, Trp, δ(CH_3)	735	A, ν(C-S,C-C), Pro
1352	Trp, G	720	ν(C-N,C-S), CH_2 rock, DNA, A
1318	G, δ(C-H), Amide III	675	ν(C-S), G, T
1285	Amide III, CH_2 wag, DNA/RNA	650	ν(C-S), C-C twisting of Tyr, Phe
1239	Amide III, A, RNA, $\nu(PO_2)_{asymm}$	622	Phe C-C twisting, ν(C-S)
1221	Amide III, T, A, ν(PO_2,C-N)	605	δ(COO^-), δ(R), δ(C-H)
1212	Tyr, Trp, Phe, ν(C-N), Amide III	584	δ(R), ν(S-S)
1170	C, G, Tyr C-H bend, lipids	560	Trp, ν(S-S)
1153	ν(C-C, C-N)	529	ν(S-S)
1141	ν(C-C,C-N), Pro	508	ν(S-S)
1130	ν(C-C,C-N), carbohydrate ν(C-O)	466	ν(C-S)
1085	ν(C-C,C-N)	450	ν(C-S)
1065	ν(C-C), ν(PO_2) of DNA/RNA, Pro		

8.1.2. Principal component analysis of live cell and isolated cytoplasm spectra

Principal component analysis (PCA) was performed to gain information about the differences that are characteristic of the two samples. The scores plot and the loadings of the first and second principal components (PC1 and PC2, respectively) are shown in Figure 8.2.

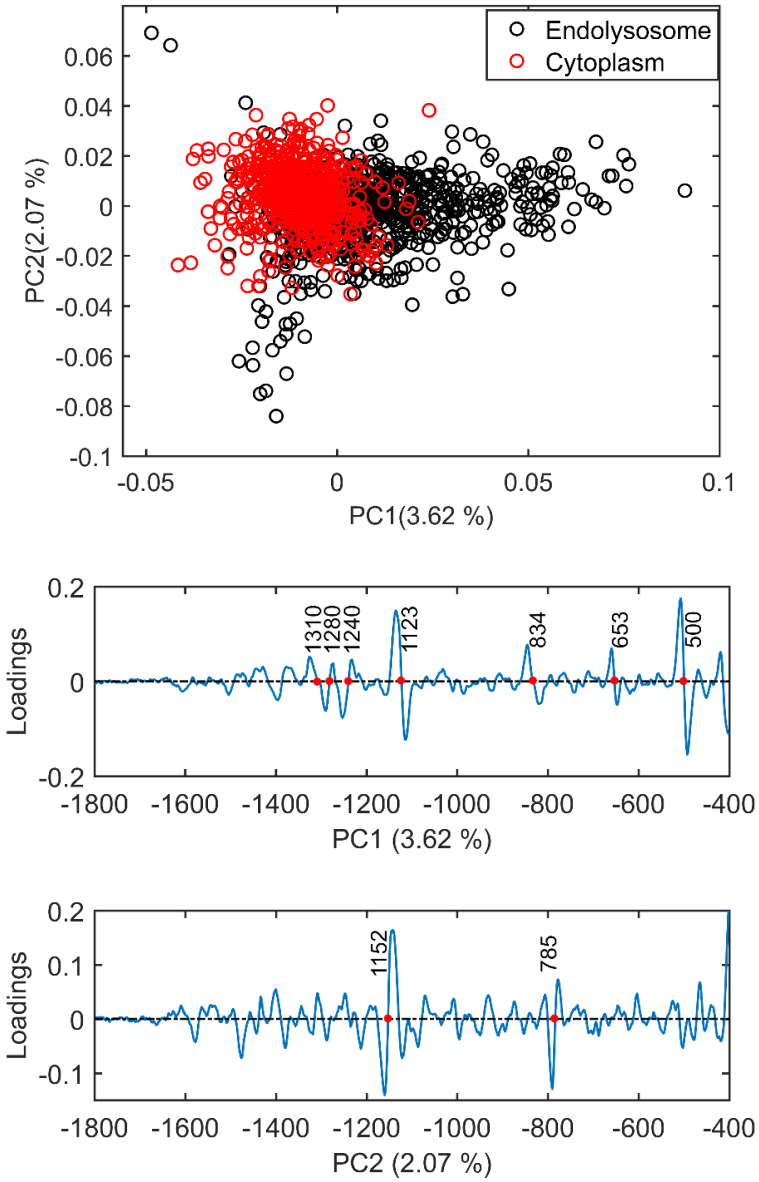

Figure 8.2. Scores plot (top) and the loadings of the first (middle) and second principal components (bottom) as results of the PCA of the SERS data of five live J774 cells (883

spectra) and the isolated J774 cytoplasm (613 spectra), incubated with gold nanoparticles for 1.5 h.

The incubation of living J774 cells was continuous during the 1.5 h incubation time, which could result in gold nanoparticles residing in intracellular compartments that are in different states of the endolysosomal pathway: some particles had just been internalized, while others had been processed for the whole incubation time. This intracellular heterogeneity is well reflected in the scores plot (Figure 8.2 top). While the SERS spectra collected from the homogeneous solution of isolated cytoplasm show low variance along PC1 and PC2, the endolysosomal spectra are spread along both principal components. As the PC1 loading shows (Figure 8.2 middle), the PCA separation of the data was based on the variances at the wavenumbers 1310 cm^{-1} assigned to vibrations of guanine, amide III, and C-H deformation; 1280 cm^{-1} assigned to vibrations of amide III, DNA, RNA, and CH_2 wagging; 1240 cm^{-1} assigned to vibrations of amide III, adenine, RNA, and PO_2 asymmetric stretching; 1123 cm^{-1} assigned to C-C and C-N stretching of proteins and C-O stretching of carbohydrates; 834 cm^{-1} assigned to vibrations of tyrosine, proline, and O-P-O asymmetric stretching; 653 cm^{-1} assigned to C-S stretching and C-C twisting vibrations of tyrosine and phenylalanine; and 500 cm^{-1} assigned to S-S stretching vibrations (for tentative assignments, see Table 8.1). The highest variances were observed in the bands at 1123 cm^{-1} and 500 cm^{-1}. It can be seen by comparing the PC1 loadings with the average spectra (Figures 8.2 middle and 8.1) that all the bands with high variance are more characteristic to the spectra collected from the endolysosomal compartments, except for the 1240 cm^{-1} band, which is more prominent in the spectra of the isolated cytoplasm. These bands were assigned to vibrations of nonpolar protein residues, which suggests a more hydrophobic environment of the gold nanoparticles. This could partially be due to their interaction with the membrane of the intracellular compartment [39], since the band at 1123 cm^{-1} can be further assigned to (phospho)lipid vibrations [144, 253], and also to the denaturation of the probed proteins in the close proximity of the gold nanoparticles. Moreover, most of the bands can be assigned to different vibrations of nucleic acids as well, which suggests their higher abundance in the close proximity of the gold nanoparticles inside the cells than in the solution of isolated cytoplasm. The loadings of the second principal component (Figure 8.2 bottom) reflect that the band at 785 cm^{-1} is more prominent in the dataset of living cells, which can be attributed to nucleic acids

(for tentative assignments, see Table 8.1). Due to the general association of nucleic acids with histones, these findings are in agreement with the mass spectrometry data of the hard protein corona presented in Chapter 7 and Tables S7.1 and S7.2, and further support that the interaction of nanoparticles with the histone molecules in the hard protein corona contributes to the high abundance of the C-S and S-S stretching vibrations in the endolysosomal spectra.

8.1.3. Band occurrences in the spectra of live cells and the isolated cytoplasm

To understand the variances in the datasets, the band occurrences were analyzed in every spectrum as described in Section 4.11.3. The results of this analysis are independent of the relative band intensities and inform of whether an interaction takes place between the nanoparticle and the given functional group or not.

In Figure 8.3, the band occurrences are shown with respect to whole datasets comprising all the spectra of all five cells and of the extracted cytoplasm, respectively. The analysis of band occurrences was described in details in Section 4.11.3. The relative band occurrence graphs are the summaries of these analyses in the whole datasets, where the peak at a chosen Raman shift refers to the number of spectra in which the band at the chosen wavenumber appeared. The band occurrences of datasets belonging together were presented in the same figure so that the occurrence of individual bands in the whole datasets could be related. Hence, the figures are graphs of relative band occurrences, where comparing the intensity of a chosen band in relevant datasets sheds light on the likeliness of the corresponding nanoparticle-biomolecule interaction in the given datasets.

In the relative band occurrence curve interpreting the SERS data of the isolated cytoplasm (Figure 8.3 red curve), so-far undetected vibrational bands appear with low relative abundance at 1340 cm^{-1} assigned to vibrations of guanine, amide III, and C-H deformation; 815 cm^{-1} assigned to vibrations of proline, tyrosine, and C-C stretching; and at 785 cm^{-1} assigned to various vibrations of nucleic acids, such as O-P-O stretching and the C6-ring breathing vibrations of cytosine, uracil, and thymine (Table 8.1). In the average spectra (Figure 8.1), these bands only appear as weak shoulders due to their low abundance in the whole dataset.

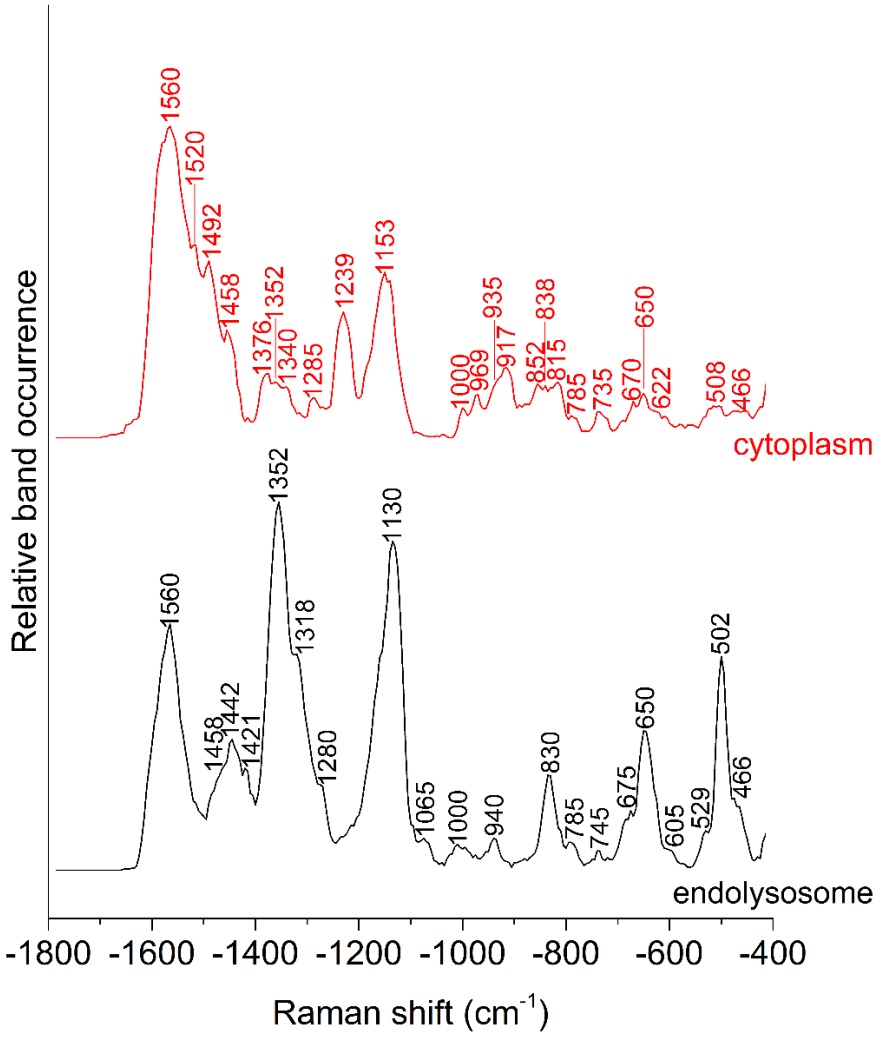

Figure 8.3. The relative band occurrences in the dataset of 613 SERS spectra from the isolated cytoplasm (red trace) and in the dataset of 883 SERS spectra from five live J774 cells (black trace).

The abundance of several bands attributed to components of the amide II vibration decreases in the endolysosomal spectra compared to the spectra of the isolated cytoplasm, *e.g.,* at 1560 cm^{-1}, 1520 cm^{-1}, 1492 cm^{-1}, and amide III bands, *e.g.,* at 1239 cm^{-1} (Figure 8.3). At the same time, bands of nonpolar group vibrations are more abundant in the endolysosomal spectra than in the spectra of the isolated cytoplasm, such as at 1352 cm^{-1} attributed to vibrations of tryptophan, 1153 cm^{-1}, 1130 cm^{-1} attributed to C-C and C-N stretching, and 830 cm^{-1} attributed to vibrations of tyrosine (Table 8.1 and Figure 8.3). Similar to the average spectra and the PCA results (Figures 8.1 and 8.2), the C-S stretching vibration at 650 cm^{-1} and the S-S stretching vibration at 502 cm^{-1} are more common in the endolysosomal spectra (Figure 8.3 black curve). The amide bands derive

from vibrations of the polypeptide backbone [105], and their loss potentially indicates the decreased number of peptide bonds, denoting the cleavage of the protein chains that interact with the gold nanoparticle. Based on these results, it can be deduced that the spectral differences were the results of protein denaturation rather than the nanoparticle-membrane interactions.

The data presented above suggest the interactions of the gold nanoparticles with protein fragments resulting from enzymatic cleavage. To support the presence of these interactions, the enzymatic digestion of bovine serum albumin (BSA) by bovine trypsin (which process is further referred to as trypsinization) was studied to model the arising differences between the interaction of gold nanoparticles with intact BSA molecules and with their digested fragments, respectively.

8.2. Comparison of the SERS datasets of BSA, trypsin, and trypsinized BSA solutions

The SERS spectra of the pure proteins were collected from gold nanoparticle agglomerates aggregated by BSA or trypsin, respectively (see Sections 4.5.1 and 4.8 for experimental details). After the BSA spectra were collected, 5 µL of the pure trypsin solution was added to the sample carefully, while observing the steadiness of the agglomerate used for the spectrum acquisition of BSA molecules previously. Acquiring SERS spectra from the same sample position before and after the addition of trypsin allowed for the collection of highly comparable data, which represented the changes that occur in the agglomerate upon digestion.

8.2.1. Average SERS spectra of BSA, trypsin, and trypsinized BSA

The average of the SERS spectra of BSA, bovine trypsin, and the trypsinized BSA are shown in Figure 8.4. The three average spectra, each calculated from ~100 representative SERS spectra, showed significant differences. It is important to see that the strongest band in the average spectrum of trypsin at 1145 cm^{-1}, corresponding to C-N and C-C stretching vibrations, only has a minor contribution to the average spectrum of trypsinized BSA (see Table 8.2 for the tentative band assignments). The strongest bands in the pure BSA average spectrum, *e.g.,* at 681 cm^{-1}, corresponding to the imidazole ring deformation in

histidine [219], have a much lower relative intensity in the average spectrum of trypsinized BSA. Several bands appear in the SERS data of trypsinized BSA that are not present in the average spectra of BSA and trypsin.

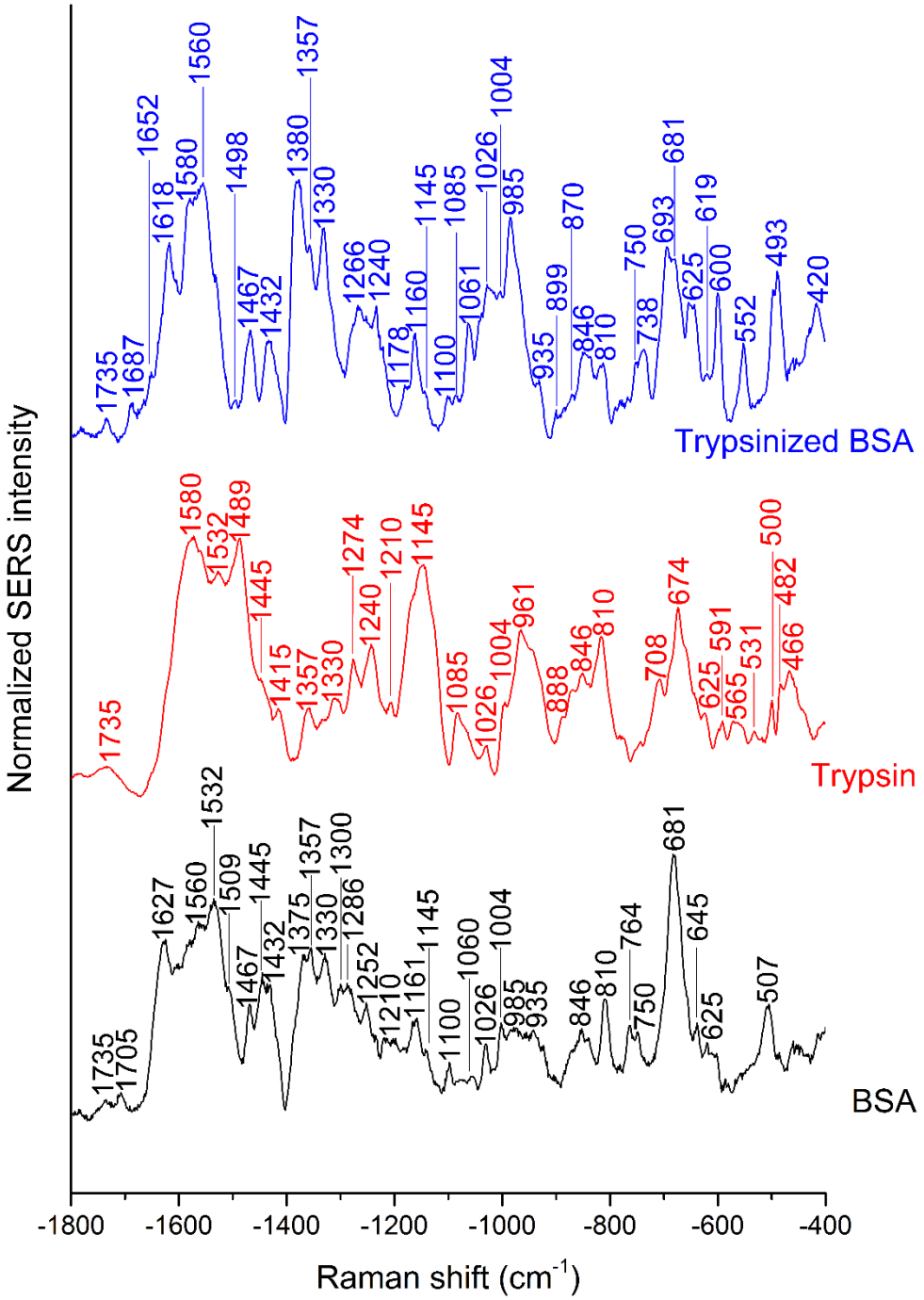

Figure 8.4. The averages of ~100 respective SERS spectra collected from BSA, trypsin, and from trypsinized BSA solutions in the presence of gold nanoparticles. The spectra are stacked for clarity. Excitation wavelength: 785 nm, acquisition time: 1 s, excitation intensity: 5.7×10^5 W/cm^2.

Table 8.2. Raman shifts and their tentative assignments in Figure 8.4. *v* stretching, *δ* deformation, *symm* symmetric, *rock* rocking, *wag* wagging, *tor* torsion, *br* breathing, *bend* bending, *R* benzene ring, *r* pyrrole ring. Band assignments were based on refs. [40, 104, 171, 172, 215, 219, 253].

Raman shift (cm^{-1})	Tentative assignment	Raman shift (cm^{-1})	Tentative assignment
1735	δ(COOH) of Asp, Glu	1060	ν(C-C), Pro
1705	δ(COOH) of Asp, Glu	1026	Phe, ν(C-C)
1687	Amide I	1004	R br
1652	Amide I	985	ν(C-C)
1627	Trp, Amide I	961	ν(C-C) of Pro and Val
1618	Tyr, Trp, Phe ν(C=C), Amide I	935	Pro, ν(C-C)
1580	ν (C-C), ν(COO^-)	899	δ(C-C), Trp
1560	Amide II, Trp, Tyr, COO^- def	888	CH_2 rock, Trp
1532	Amide II	870	Pro, Val, ν(C-C)
1509	NH_2 bend of Tyr, ν(R), Amide II	846	ν(C_α-N,C-C), Tyr, Phe, Pro
1498	ν(R, r), Amide II	810	Pro, Tyr, ν(C-C)
1489	NH_3^+, Amide II	764	Trp δ(R)
1467	δ(CH_2)	750	Trp symm br
1445	δ(CH_2,CH_3)	738	ν(C-S, C-C)
1432	δ(CH_2)	708	ν(C-S)
1415	ν(COO^-)$_{symm}$	693	ν(C-S)
1380	Trp, CH_3 def	681	δ(His imidazole ring)
1357	Trp	674	ν(C-S)
1330	R, δ(CH_2,CH_3), Amide III	645	ν(C-S), C-C twisting of Tyr, Phe
1300	Amide III, δ(CH,CH_2,CH_3)	625	Phe C-C twisting, ν(C-S)
1286	Amide III, C, C-H bend	600	δ(COO^-,R)
1274	Amide III, CH_2 wag	591	δ(R)
1266	Amide III	565	Trp, ν(S-S)
1252	Amide III	552	ν(S-S)
1240	Amide III, CH_2 wag	531	ν(S-S)
1210	Amide III	507	ν(S-S)
1178	Tyr C-H bend	500	ν(S-S)
1161	ν(C-C,C-N), Tyr	493	ν(S-S), R tor and bend
1145	ν(C-C/C-N)	482	R tor and bend
1100	Phe, ν(C-N)	466	ν(C-S)
1085	ν(C-C/C-N)	420	Trp

The spectral regions of 1380 cm^{-1} – 1350 cm^{-1}, 1070 cm^{-1} – 940 cm^{-1}, and of 610 cm^{-1} – 490 cm^{-1}, mostly corresponding to nonpolar group vibrations and C-S and S-S stretching vibrations (see Table 8.2 for tentative assignments) are more intense in the average spectrum of the trypsinized BSA than in the average spectra of the pure proteins. These

results allow for the conclusion that the BSA molecules adsorbed on the surface of gold nanoparticles did not exchange to trypsin molecules during the time of the SERS experiments (~5 min). The data show that due to the addition of trypsin, major changes have occurred in the interaction of gold nanoparticles with the BSA molecules, which can be attributed to the enzymatic digestion of the BSA molecules. This was supported by the observed changes on the micrometer-scale: after ~5 min, much smaller aggregates appeared on the surface of the CaF_2 slide, which can be interpreted as the successful digestion of BSA resulting in the agglomerates falling apart.

8.2.2. PCA analysis of the SERS spectra of BSA, trypsin, and trypsinized BSA

To further understand the differences in the three datasets, PCA analysis was performed. The scores plot and the loadings of PC1 and PC2 are shown in Figure 8.5. As the scores plot shows in Figure 8.5, the trypsin dataset is the most homogeneous, which can derive from the fact that over half of the trypsin molecule is natively folded into random coils and turns [179, 259], which has previously been shown to facilitate specific residue-nanoparticle interactions rather than non-specific adsorption [172]. The most heterogeneous dataset was the one collected from the sample with trypsinized BSA, which is possibly the result of the many possible interactions the protein fragments can have with the gold nanoparticles. It is important to observe that the intact BSA and trypsin data partially overlap, while the SERS data of the trypsinized BSA strongly separate along PC1 and PC2, the two principal components explaining the highest variance. Since the mixture originally contained the same proteins as the pure solutions of BSA and trypsin, the separation of the trypsinized BSA data from the other two datasets must be based on the new interactions resulting from the enzymatic cleavage of BSA.

The loadings of PC1 (Figure 8.5 middle) reveal that the highest variance in the three datasets can be found in the bands at 1376 cm^{-1} assigned to vibrations of tryptophan and CH_3 deformation, 1021 cm^{-1} assigned to vibrations of phenylalanine and C-C stretching, 976 cm^{-1} assigned to C-C stretching, 643 cm^{-1} assigned to C-S stretching and the C-C twisting of tyrosine and phenylalanine, 596 cm^{-1} assigned to benzene ring deformation, and 552 cm^{-1} and 490 cm^{-1} assigned to S-S stretching vibrations (Table 8.2). These bands are more abundant in the data collected from the solution of trypsinized BSA. As

discussed before, the exposure of nonpolar residues and the disulfide bridges to a polar environment suggests protein denaturation [47, 260].

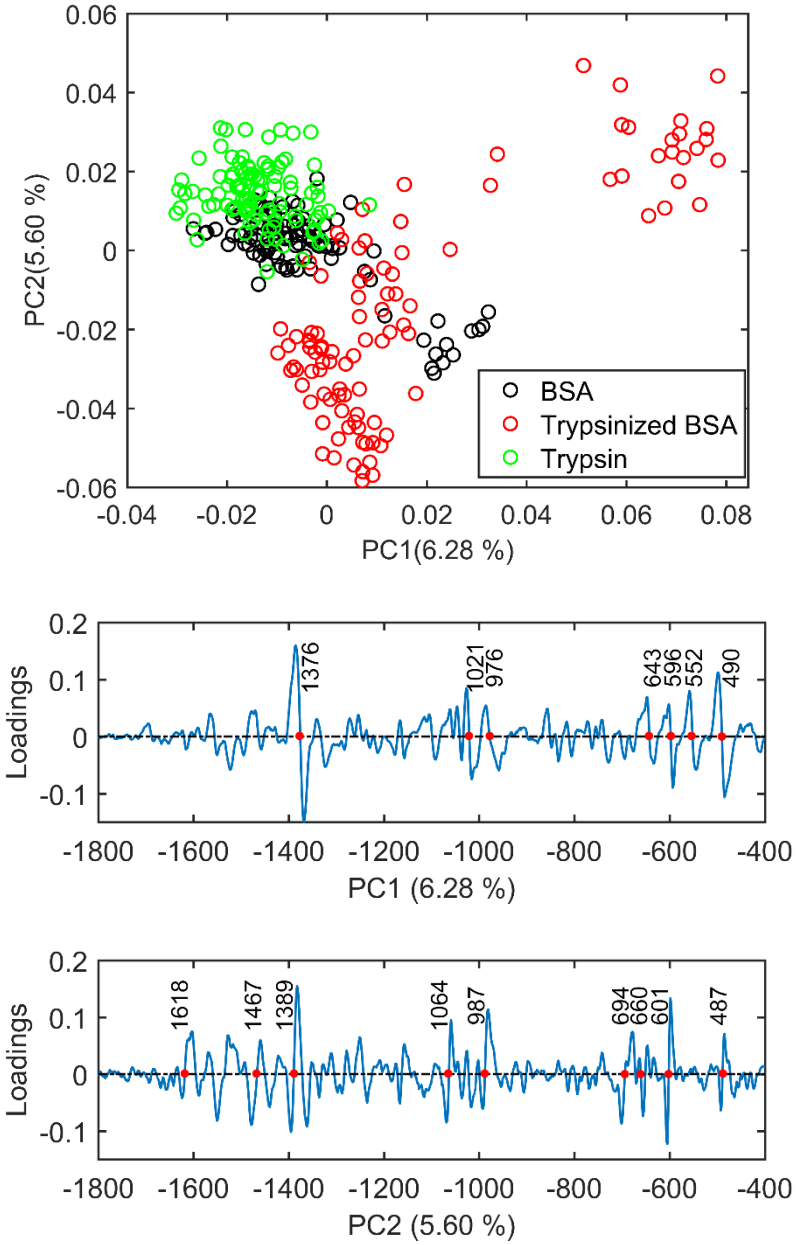

Figure 8.5. Scores plot (top) and the loadings of PC1 (middle) and PC2 (bottom) of the PCA analysis of the SERS datasets collected from BSA, trypsin, and trypsinized BSA solutions in the presence of gold nanoparticles. Each sample was represented by ~100 SERS spectra.

The loadings of PC2 (Figure 8.5 bottom) reveal further basis of the separation of the trypsinized BSA SERS data from the SERS data of pure protein solutions. The separation of the datasets along PC2 was based on the variances at the wavenumbers 1618 cm^{-1}

assigned to an amide I vibration and to the C=C stretching in tyrosine, tryptophan, and phenylalanine; 1467 cm^{-1} and 1389 cm^{-1} respectively assigned to CH_2 and CH_3 deformations; 1064 cm^{-1} assigned to vibrations of proline and C-C stretching; 987 cm^{-1} assigned to C-C stretching; 694 cm^{-1} assigned to C-S stretching; 660 cm^{-1} assigned to a C-S stretching vibration and to the C-C twisting of tyrosine and phenylalanine; 601 cm^{-1} assigned to COO^- and benzene ring deformation; and 487 cm^{-1} assigned to vibrations of S-S stretching, benzene ring torsion and bending (Table 8.2). These bands all appear more prominently in the SERS data of trypsinized BSA than in those of the pure protein solutions.

The bands at 1536 cm^{-1} assigned to an amide II vibration, 1486 cm^{-1} assigned to vibrations of NH_3^+ and amide II, and 1244 cm^{-1} assigned to an amide III vibration and CH_2 wagging were more characteristic to the datasets of the pure BSA and trypsin solutions (Table 8.2). It can be observed that the separation of SERS spectra collected in the trypsinized BSA solution was not only based on the higher abundance of nonpolar group vibrations and the C-S and S-S stretching vibrations, which suggest the denaturation of proteins in a polar environment, but also on the loss in amide II and amide III bands, similarly to the separation of the SERS spectra of the isolated cytoplasm and the endolysosomal compartments of live cells. Contrary to the biochemical environment in the endolysosomal compartments, no other processes occur in the solution of trypsinized BSA that could cause these spectral signatures. Therefore, the loss in amide bands must be the result of the fragmentation of the polypeptide backbone of proteins in cells.

8.2.3. Band occurrences in the spectra of BSA, trypsin, and trypsinated BSA

Some of the bands based on which the datasets separated do not appear in the average spectra, because even though the data were background corrected and vectornormalized, some very intense and frequently occurring bands can overpower other, less frequent or less intense bands in the average spectra. The analysis of the band occurrences can help to gain further understanding of the data.

The occurrence of spectral bands in the SERS data of BSA, trypsin, and trypsinized BSA, respectively, are shown in Figure 8.6. The 1170 cm^{-1} and 1150 cm^{-1} bands, the 955 cm^{-1}

and 920 cm^{-1} bands, and the 865 cm^{-1} and 840 cm^{-1} bands in the relative band occurrence curve of the pure BSA spectra, which show low abundance in Figure 8.6, appear as single bands in the average SERS spectrum of pure BSA at 1161 cm^{-1}, 935 cm^{-1}, and 846 cm^{-1}, respectively (see tentative assignments in Table 8.2).

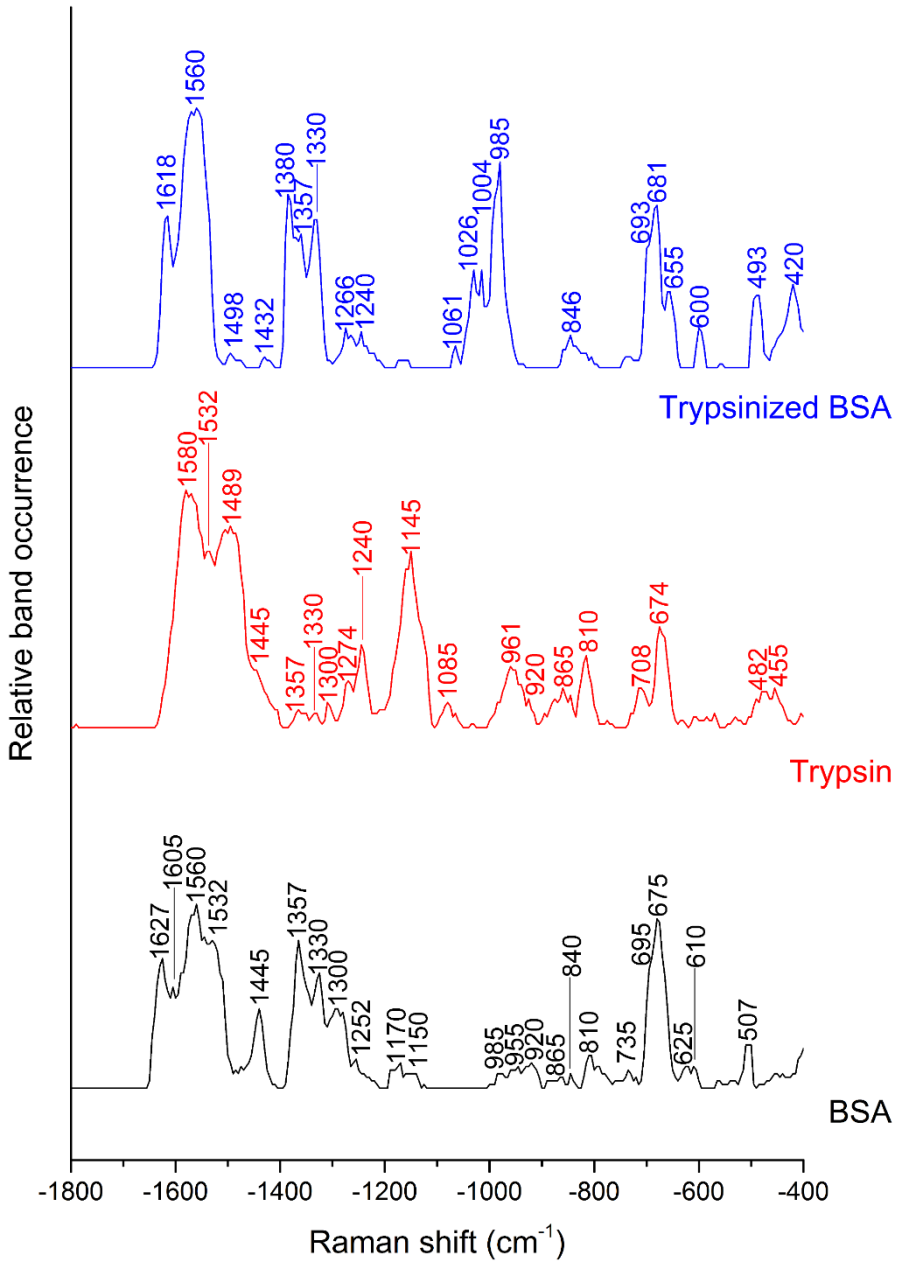

Figure 8.6. Relative band occurrence in the SERS data sets collected from the solutions of BSA, trypsin, and trypsinized BSA, respectively. Each analyzed dataset consisted of ~100 individual spectra.

The data suggest the absence of the significant exchange of BSA molecules on the surface of gold nanoparticles by trypsin, as observed in the average spectra of the three datasets

as well. This is supported, *e.g.,* by the highly abundant 1145 cm^{-1} band in the trypsin spectra, which is nearly completely absent in the spectra collected from the trypsinized BSA solution.

Nonpolar group vibrations are more abundant in the spectra of trypsinized BSA compared to the spectra of pure BSA, as seen in the bands at 1618 cm^{-1} assigned to the C=C stretching vibrations of tyrosine, tryptophan, and phenylalanine, and an amide I vibration; 1560 cm^{-1} assigned to vibrations of tryptophan, tyrosine, amide II, and COO^- deformation; 1380 cm^{-1} assigned to CH_3 bending; 1145 cm^{-1} assigned to C-C and C-N stretching vibrations; 1004 cm^{-1} assigned to a vibration of phenylalanine; 985 cm^{-1} assigned to C-C stretching; and 600 cm^{-1} assigned to COO^- and benzene ring deformations (tentative assignments were based on Table 8.2). This suggests the denaturation of BSA in the presence of trypsin [47].

This is further supported by the appearance of a new C-S stretching vibration at 655 cm^{-1} and the higher abundance of the S-S stretching vibration at 490 cm^{-1}, given the often nonpolar environment of disulfide bridges inside the protein structures [260]. The abundance of contributions by components of the amide II, *e.g.,* at 1535 cm^{-1}, and amide III bands, *e.g.,* at 1320 cm^{-1} and 1300 cm^{-1}, is reduced in the spectra of the trypsinized BSA compared to the spectra of pure BSA, which suggests that the observed denaturation of the BSA molecules is the result of protein fragmentation. These results are in accordance with the spectral signatures observed in the comparison of the cytoplasmic and endolysosomal datasets (Figure 8.3), and with the average spectra and the PCA results of the pure protein and trypsinized BSA datasets (Figures 8.4 and 8.5), which allows for the conclusion that protein fragments contribute to the SERS signal of live cells incubated with gold nanoparticles.

The different approaches of SERS data analysis presented here revealed that in the endolysosomal compartments where the internalized nanoparticles reside, protein fragments readily interact with the gold nanoparticles. As shown in Figure 7.3 in Chapter 7, after the extraction of the hard protein corona formed in J774 cells after 1.5 h incubation with gold nanoparticles, a line was found in the electropherogram of the hard corona proteins indicating low-mass peptide species. This information combined with the results from the SERS spectra presented here provides proof that gold nanoparticles

internalized by J774 cells strongly interact with protein fragments, which are constituents of the hard protein corona. Even though the combined results suggest that the protein fragments interact strongly with the gold nanoparticles, *i.e.,* they have high affinity to the gold nanoparticles' surface, the spectral features of cleaved proteins interacting with the gold nanoparticles are less abundant in the SERS spectra of the isolated cytoplasm than in those of the endolysosomal compartments. Due to the Vroman effect [17], in a complex biomolecular solution, the immediately adsorbed proteins on the gold nanoparticles' surface gradually exchange to those with the highest affinity to the surface. As protein fragments must be present in the isolated cytoplasm as well, it can be concluded that the fragments strongly interacting with the gold nanoparticles in the endolysosomal compartments are probably the products of the proteins cleaved after adsorbing on the nanoparticles' surface rather than the products of proteins cleaved prior to adsorption.

8.3. Secondary structural information in the SERS spectra of proteins

The average spectra (Figure 8.4) and the band occurrences in the SERS data of the pure BSA and trypsin solutions (Figure 8.6) further reveal important traits in the spectral region of 1320 cm^{-1} – 1200 cm^{-1}, which is the region of amide III vibrations [253]. In the amide III region, the bands at higher wavenumbers are more prominent in the spectra of BSA, while the tendency is the opposite in the case of trypsin (Figures 8.4 and 8.6). Both samples were prepared with the same molar ratios, with approximately 40,000 protein molecules for each gold nanoparticle. Therefore, the differences in the amide III bands representing the interaction of the gold nanoparticles and the protein peptide backbones probably derive from the different structural elements in the proteins.

In Figure 8.7, snapshots of the 3D structures of BSA (Figure 8.7 left) and bovine trypsin (Figure 8.7 right) can be observed. Based on the color-coding in the illustration, the differences between the two structures are well visible. The changes in the amide III spectral region in Figure 8.4 suggest different nanoparticle-peptide backbone interactions, which can be the result of different structural elements interacting with the gold nanoparticles in the probed volume. Based on the crystallography data [180, 259], the native folding of BSA contains 73% helical structure, while the rest of the protein chain

remains in random coils and turns – contrary to the folding of trypsin, which is 10% α-helical, 34% β-sheet, and 56% random coils and turns.

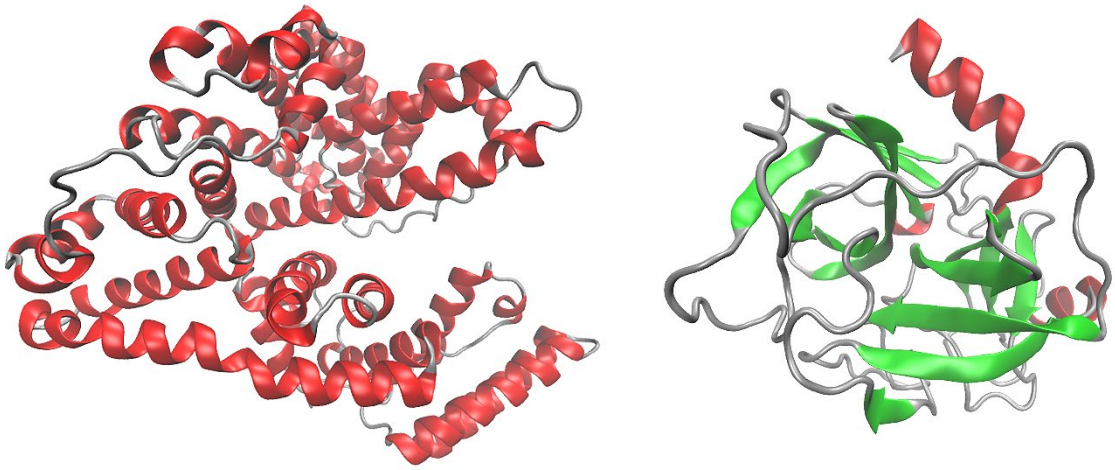

Figure 8.7. Structural comparison of BSA (left) and bovine trypsin (right) based on PDB IDs 4OR0 [179, 180] and 1S0Q [179, 259], respectively. The red segments correspond to α-helical structures, the green segments correspond to β-sheet structures, and the grey segments correspond to other structures, *e.g.,* random coils or turns. The protein molecules were visualized by VMD [182].

There have been extensive, past and recent, infrared spectroscopic (*e.g.,* [261-265]), circular dichroism spectroscopic (*e.g.,* [266-269]), and Raman spectroscopic studies (*e.g.,* [108, 109, 270-273]) of the secondary structural elements of proteins. While these methods provide plausible evidence of the different secondary structures, it is more challenging to interpret similar bands in the SERS spectra. It has been shown that the adsorption of an oligopeptide on thiolated gold nanoparticles can result in changes between α-helical structure to β-sheets [61, 62]. Since such drastic conformational changes are possible due to the adsorption of the protein molecules, the conclusions only represent the structural elements probed by SERS.

A tendency similar to that in the average spectra (Figure 8.4) can be observed in the band occurrence data (Figure 8.6). The amide III bands at 1320 cm^{-1}, 1300 cm^{-1}, and 1295 cm^{-1} are generally attributed to an α-helical structure, the band at 1250 cm^{-1} can be assigned to the amide III band of random coils, while the band at 1240 cm^{-1} in the trypsin data can originate from β-sheets [105, 253, 272]. This means that in BSA, possibly α-helical and

random coil structures were probed, while the data collected from trypsin further suggest the probing of β-sheets, which is in agreement with the previous crystallographic data of the proteins (Figure 8.7).

8.4. Summary

In this chapter, the SERS data of live J774 cells were compared to those of the isolated cytoplasm respectively incubated with gold nanoparticles for 1.5 h to gain information about the biomolecular environment in contact with the nanoparticles' surface throughout the processing of the gold nanoparticles. The average spectra, PCA, and the analysis of band occurrences were in aggreement. It was found that in the SERS spectra collected from live cells, corresponding to the environment of gold nanoparticles in the endolysosomal compartments, a higher abundance of nonpolar group vibrations can be observed, while the prominence of amide II and amide III bands decreases. It was concluded that such changes could be the results of the interaction of gold nanoparticles with fragmented proteins.

To support the conclusion, the enzymatic cleavage of BSA was studied in solution. Based on the suggested data analytical approach, secondary structural elements in the probed volume could be inferred. These results extend the discussion of the BSA-nanoparticle interactions presented in Chapter 6. The average SERS data of the pure solutions of BSA and bovine trypsin, respectively, showed significant differences between each other and the SERS spectra of the trypsinized BSA as well, which was further supported by the separation of the three datasets in PCA along the first two principal components. The separation was based on the increased presence of nonpolar group vibrations in the SERS data of the trypsinized BSA solution, while the abundance of amide II and amide III bands decreased. These differences, which are characteristic to enzymatic cleavage, strongly agree with the observed differences between the SERS datasets of live J774 cells and of the isolated cytoplasm, which allowed for the conclusion that the gold nanoparticles readily interact with protein fragments in endolysosomal compartments. Compared with the SDS-PAGE results of Chapter 7, where a band marking low-mass peptides appeared in the electropherogram of the hard corona proteins, it could be concluded that the gold nanoparticles interact directly with protein fragments. These fragments are the products

of proteolysis after, rather than prior to, the adsorption of the intact proteins on the gold nanoparticles' surface.

Chapter 9

Gold nanoparticle processing by the biomolecular environment in living cells

This chapter was published as part of a manuscript in *G. P. Szekeres et al., Nanoscale, 2020, DOI:10.1039/D0NR03581E,* and it is here reproduced with permission of the Royal Society of Chemistry.

The analysis of the protein corona formed in living cells and the monitoring of the intracellular processing of nanoparticles has proven to be a major challenge based on the state-of-the-art literature. The processing of the nanoparticles and the composition of the protein corona both depend on the incubation conditions, the surface interactions of the internalized nanoparticles, and the induced cellular response mechanisms.

As it has been shown in Chapters 5 to 8, vibrational spectroscopy and mass spectrometry provide complementary information about the proteins interacting with the gold nanoparticles in a complex biomolecular environment and about the nature of the surface interactions. The SERS mapping of live cells allows for the analysis of the nanoparticle-biomolecule interactions in single cells [39, 42, 274], which combined with elemental

analysis (*e.g.,* LA-ICP-MS) could inform about the extent of nanoparticle uptake with regards to protein-nanoparticle interactions [154]. Cryo soft X-ray nanotomography (XRT) on vitrified cells yields three-dimensional information with a resolution lower than 10 nm, allowing for the detailed investigation of metallic nanoparticles: their localization, state of aggregation, and the overall cellular ultrastructure in a quasi-native state [39, 144, 154, 168]. Previously, the combination of XRT and SERS results yielded valuable information about the interaction of the protein corona with nanoparticles in endosomes [39].

In this chapter, the findings of the previous chapters will be brought together to elucidate the live cell-nanoparticle interactions at the biomolecular level. Samples prepared under the same conditions will be used in each corresponding experiment. The interacting proteins in the hard corona will be identified by *ex situ* mass spectrometry. The interaction between the identified proteins and the nanoparticles will be probed by SERS in live cells, which assures the data collection in the native, live environment. The intracellular processing of gold nanoparticles, as well as the induced ultrastructural changes will be studied by XRT on vitrified cells, yielding three-dimensional information of cells in a quasi-native state. HCT-116 and A549 cells will be used in the experiments to compare the nanoparticle-protein interactions in different cell lines under different incubation conditions.

9.1. The hard corona proteomes of gold nanoparticles in HCT-116 and A549

After HCT-116 and A549 cells were respectively incubated with gold nanoparticles for 24 h in DMEM-FBS, the hard protein corona of the internalized gold nanoparticles was purified and analyzed by gel electrophoresis and mass spectrometry (complete methodology described in Sections 4.15-4.20 and Chapter 7). This provides direct information about the interacting proteins and cellular responses. The electropherogram of the hard corona proteins extracted from HCT-116 and A549 cells, respectively, are shown in Figure 9.1. Despite some similarities, the two hard corona profiles are majorly different (Figure 9.1 and Table S9.1). Compared to the electropherograms shown in Chapter 7, the hard corona proteome of HCT-116 appears to be similar to that of MCF-7, while the hard corona proteome of A549 is more similar to that of J774. After the mass

spectrometric analysis of the peptides extracted from the excised gel segments (marked with green rectangles in Figure 9.1), 298 and 54 proteins were identified with MASCOT [195] in the protein corona of gold nanoparticles in HCT-116 and in A549, respectively (see the lists of identified proteins in Table S9.1 and Table S9.2). As seen in Figure 9.1, only the most intense bands in the extracted hard corona proteins from A549 cells were excised for further mass spectrometric analysis, because proteins with low concentration reduced the signal-to-noise ratio of the datasets.

The hard corona proteomes were analyzed by two online tools: DAVID (Database for Annotation, Visualization and Integrated Discovery, https://david.ncifcrf.gov) and STRING [275]. DAVID was used to perform data analyses to provide a general idea of protein groups with similar functions in the case of enriched proteins in the hard corona, while STRING analyzed them only based on function, and protein enrichment was not considered.

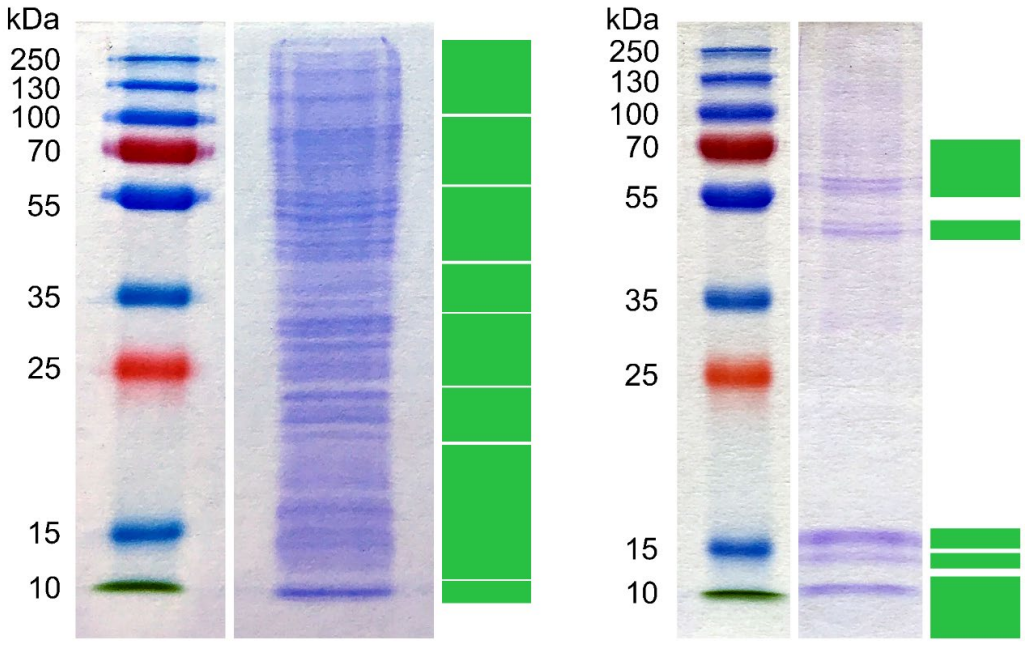

Figure 9.1. Different protein profile is observed in the protein corona of gold nanoparticles internalized by HCT-116 (left) and A549 cells (right). Green rectangles mark the excised gel segments analyzed by HPLC-ESI-Q-TOF MS.

The proteins listed in Table S9.1 and Table S9.2 were first analyzed by DAVID. In the hard corona proteome formed in HCT-116 cells, 12 clusters were assigned based on the total of 297 identified human proteins: 77 ribonucleoprotein-related, 16 translation

initiation factor-related, 5 translation regulation-related, 32 RNA-binding-related, 4 RNA transport-related, 9 protein folding-related, 5 nucleosome-related, 8 helicase-related, 6 GTP-binding-related, 10 endoplasmic reticulum-related, 14 mitochondrion-related, and 4 porin-related proteins were grouped together. The functions of the different protein clusters were based on the calculated enrichment and the known functions of the proteins clustered together. 110 proteins were not assigned to any group. The 52 human proteins in the hard corona formed in A549 were classified into 3 clusters: 9 nucleosome-related, 3 glycolysis-related, and 4 calcium ion binding-related, while 40 proteins were not classified in clusters. Furthermore, bovine proteins were found in the hard corona proteome of both cell lines: 4 in that of HCT-116 and 2 in that of A549.

The hard corona proteins extracted from live cells provide an unprecedented insight into the interactions of the gold nanoparticles from the moment of their introduction into the cell culture medium until the cell lysis. Bovine hemoglobin subunit alpha and vitronectin were found in the respective protein coronas extracted from both cell lines, and hemoglobin fetal subunit beta and a protein similar to bovine apolipoprotein B were additionally detected in the hard corona formed in HCT-116. These proteins were present in the hard corona even after 24 h of incubation, which suggests their strong interaction with gold nanoparticles. In a complex protein solution, first, the most abundant proteins interact with the surface, which then gradually exchange to proteins with higher surface affinity because of the Vroman effect [15, 17]. The concentration of bovine serum albumin, the most abundant protein in fetal bovine serum-supplemented culture media, was below the detection limit (see Section 4.20.2 for a detailed description of significance), which suggests that bovine serum albumin only participates in weak interactions with the gold nanoparticles. This is in accordance with the previous discussion of bovine serum albumin–gold nanoparticle interactions (See Chapter 6 and ref. [172]), concluding only non-specific interactions between the revealed lysine residues of bovine serum albumin and the citrate ions adsorbed on the nanoparticle's surface.

The enrichment of some proteins in the hard corona (see Tables S9.1 and S9.2) allows for further discussions of the cellular processing of the nanoparticles by the tentative assignment of protein functions. Some of the identified corona proteins such as annexins and ladinin indicate gold nanoparticle-cell membrane interactions [276, 277], and the interactions of nanoparticles with cilia (*e.g.,* cilia- and flagella-associated protein 157 in

HCT-116). Cytoplasmic actin is present in both protein corona profiles, which are responsible for the pit formation in the cell membrane during active uptake [278]. In HCT-116 cells, gold nanoparticles can be internalized by clathrin-mediated endocytosis, suggested by the presence of clathrin light chain A and clathrin heavy chain 1, as well as AP-2 complex subunit alpha-1 in the hard corona [279, 280]. After their internalization, gold nanoparticles induce different cellular response mechanisms in the two cell lines. In A549, the protein corona of gold nanoparticles contains vimentin, which is the highest scoring entry among the heavier proteins based on the algorithms in MASCOT [195] (Table S9.2). Vimentin is involved in the formation of aggresomes, which are intracellular bodies formed by the grouping of aggregated, denatured proteins that are meant to be processed further [281].

Compared to the protein profile of the hard corona formed in A549, the corona extracted from HCT-116 shows very distinct properties: 77 different ribosome-related proteins and 14 mitochondrial proteins are present. Since gold nanoparticles are most often stored in different intracellular compartments, they can only interact with ribosomes and mitochondria inside endolysosomal organelles, *e.g.,* autophagolysosomes. These organelles are crucial for the processing of damaged or unwanted intracellular materials, and they help in their ejection in the form of extracellular vesicles [97, 282]. In comparison, the DAVID analysis of the hard corona proteome of A549 yielded zero ribosomal and mitochondrial proteins, while STRING [275] analysis classified 10 proteins related to ribosomes and zero to mitochondria.

Both cell lines associate gold nanoparticles with histones (Tables S9.1 and S9.2), as seen from the color intensity of the bands corresponding to 10-15 kDa proteins in Figure 9.1. Histones can adsorb on the surface of gold nanoparticles in extracellular vesicles, most frequently in apoptotic bodies [96]. Apoptotic bodies contain intact organelles with cytoplasmic matter and, in some cases, nuclear fragments. In such extracellular vesicles, gold nanoparticles can interact with histones, ribosomes, and mitochondria as well. Moreover, 23 and 15 stress-related, and 41 and 14 apoptosis-related proteins were also identified by STRING [275] in the hard coronas extracted from HCT-116 and A549 cells, respectively, which further supports that apoptotic processes were activated in the presence of gold nanoparticles.

9.2. The ultrastructure of HCT-116 and A549 cells under different incubation conditions

Many of the above-mentioned conclusions drawn about the processing of the nanoparticles based on the hard corona proteome result in characteristic ultrastructural changes in the living cells. These ultrastructural changes induced by the internalized gold nanoparticles, as well as their intracellular accumulation sites can elucidate the cellular response mechanisms to the internalization of the gold nanoparticles. To obtain ultrastructural information, cryo soft X-ray nanotomography (XRT) experiments were performed, which yielded three-dimensional visual information about organelles and internalized gold nanoparticles in their quasi-native state preserved by vitrification.

Both cell lines were cultured in DMEM-FBS and McCoy-FBS media as well to see the possible effects of the choice of culture medium. DMEM-FBS is one of the most common cell culture media nowadays, and numerous studies use it in experiments with HCT-116 [283-285], while the distributor ATCC® suggests the use of McCoy-FBS in their cultivation. McCoy's Modified 5A medium is more supplemented than Dulbecco's Modified Eagle's Medium [286], and as a possible result of improper nutrition, HCT-116 cells grew slower in DMEM-FBS than in McCoy-FBS as observed under a light microscope. Gold nanoparticles were added to the culture medium of choice in non-aggregated and in pre-aggregated form, respectively, to elucidate the influence of pre-aggregation on the internalization and the intracellular aggregate morphology (pre-aggregation was achieved with a final NaCl concentration of 0.1 M). Since the resolution of the reconstructed tomograms is ~9.8 nm/pixel, 30 nm gold nanoparticles are visible even as single particles in the intracellular compartments. The tomograms were reconstructed in Etomo using the internalized gold nanoparticles as fiducial markers.

Tomographic slices of HCT-116 cells incubated with non-aggregated gold nanoparticles in DMEM-FBS and in McCoy-FBS, respectively, are shown in Figure 9.2. In both cell culture media, gold nanoparticles are aggregated inside the cells, which suggests that gold nanoparticles are actively processed. Since signs of clathrin-mediated endocytosis were found in the hard corona proteome (Table S9.1), which allows the uptake of only a few nanoparticles in the same vesicle, it can be concluded that the aggregate formation occurred inside the cells. Several different traits can be observed in the two tomographic

slices representing the incubation of cells in DMEM-FBS and McCoy-FBS media, respectively.

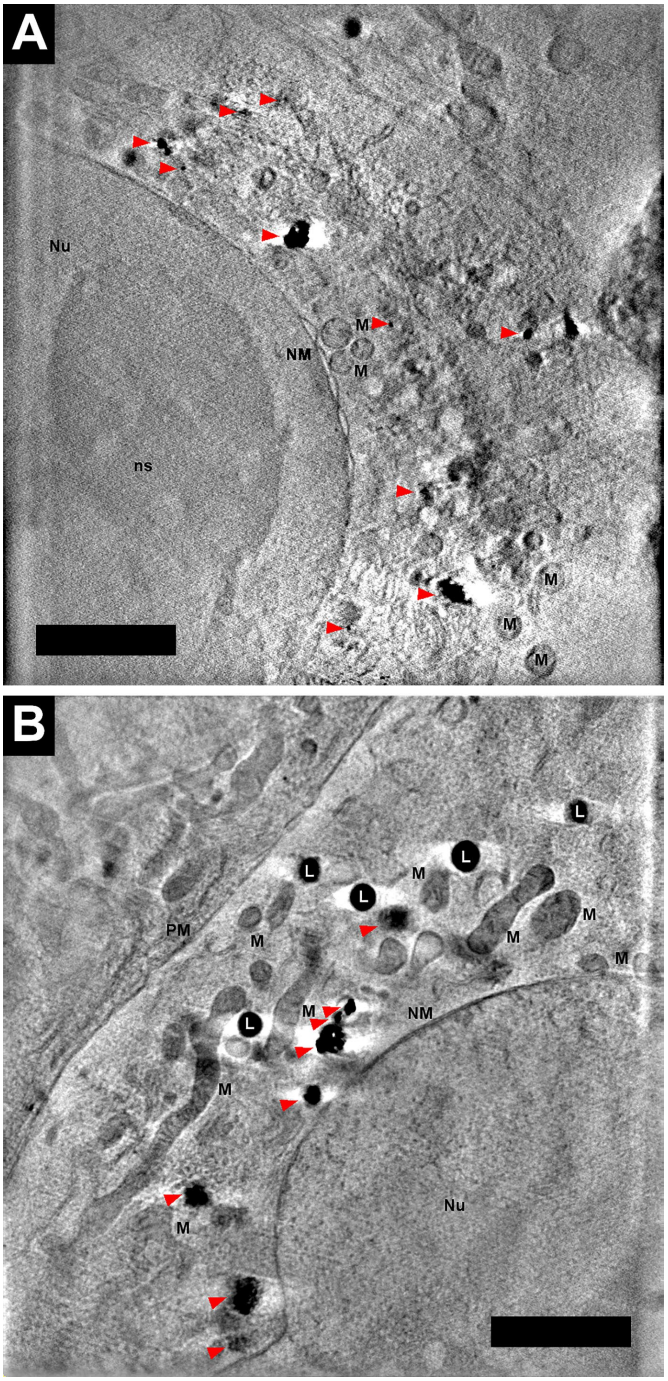

Figure 9.2. Tomographic slices of HCT-116 cells grown in DMEM-FBS (A) and McCoy-FBS (B) incubated with non-aggregated gold nanoparticles. The images are representative of 11 and 14 tomograms, respectively. Mitochondrion: M, liposome: L, plasma membrane: PM, nuclear membrane: NM, nucleus: Nu, nucleolus: ns, vesicles: V, gold nanoparticles are marked with red arrowheads. The scale bars represent 2 μm.

The increased number of small, round mitochondria suggests mitochondrial fission (Figure 9.2A), and the dilated perinuclear cisternae (Figure 9.2A) indicate that apoptosis could be initiated in HCT-116 cells cultured in DMEM-FBS [287-290] after internalizing non-aggregated gold nanoparticles. In contrast, when HCT-116 cells were grown in McCoy-FBS and incubated with non-aggregated gold nanoparticles (Figure 9.2B), longer mitochondria and intact nuclear membrane were observed. Therefore, it is possible that the use of DMEM-FBS promotes cellular stress by the improper nutrition of the HCT-116 cells: essential components of the McCoy-FBS, *e.g.,* biotin, vitamin B12, or ascorbic acid are not constituents of the DMEM-FBS medium. Furthermore, the lack of choline has been shown to promote apoptosis [291], which has a three-times lower concentration in DMEM-FBS than in McCoy-FBS. It is known that gold nanoparticles can trigger mitochondrial damage, which results in mitochondrial fission or apoptosis [282]. However, the smaller mitochondria could still be active, since the mitochondrial cristae are well contoured, suggesting that these organelles are intact. The signs of the cellular and organelle damage due to the uptake of gold nanoparticles can be more prominent in the cells cultured in DMEM-FBS as a result of the processes promoting the survival of cells being less efficient under less optimal culture conditions.

Contrary to the incubation with non-aggregated nanoparticles, HCT-116 cells show traits of cellular injury and stress in both culture media upon incubation with pre-aggregated nanoparticles (Figure 9.3). Mitochondrial fission (not seen in the figure) or hyperfusion (Figure 9.3A) can be observed in the whole tomogram due to mitochondrial damage and higher energy demand [289, 292], respectively. In the nucleus, chromatin tends to form granules (Figure 9.3), and large vacuoles with bright lumen appear in the cytoplasm (Figure 9.3B), which indicate cellular damage [293-295]. It can be excluded that the granules in the nucleus are the naturally abundant heterochromatin patches, since they are present in every living cell, yet the granules seen in Figure 9.3 are unique compared to Figure 9.2. The darkness of the granules, that is, their higher X-ray absorption relative to their surroundings means that they are tightly packed, which is a result of the possibly occurring chromatin condensation [295].

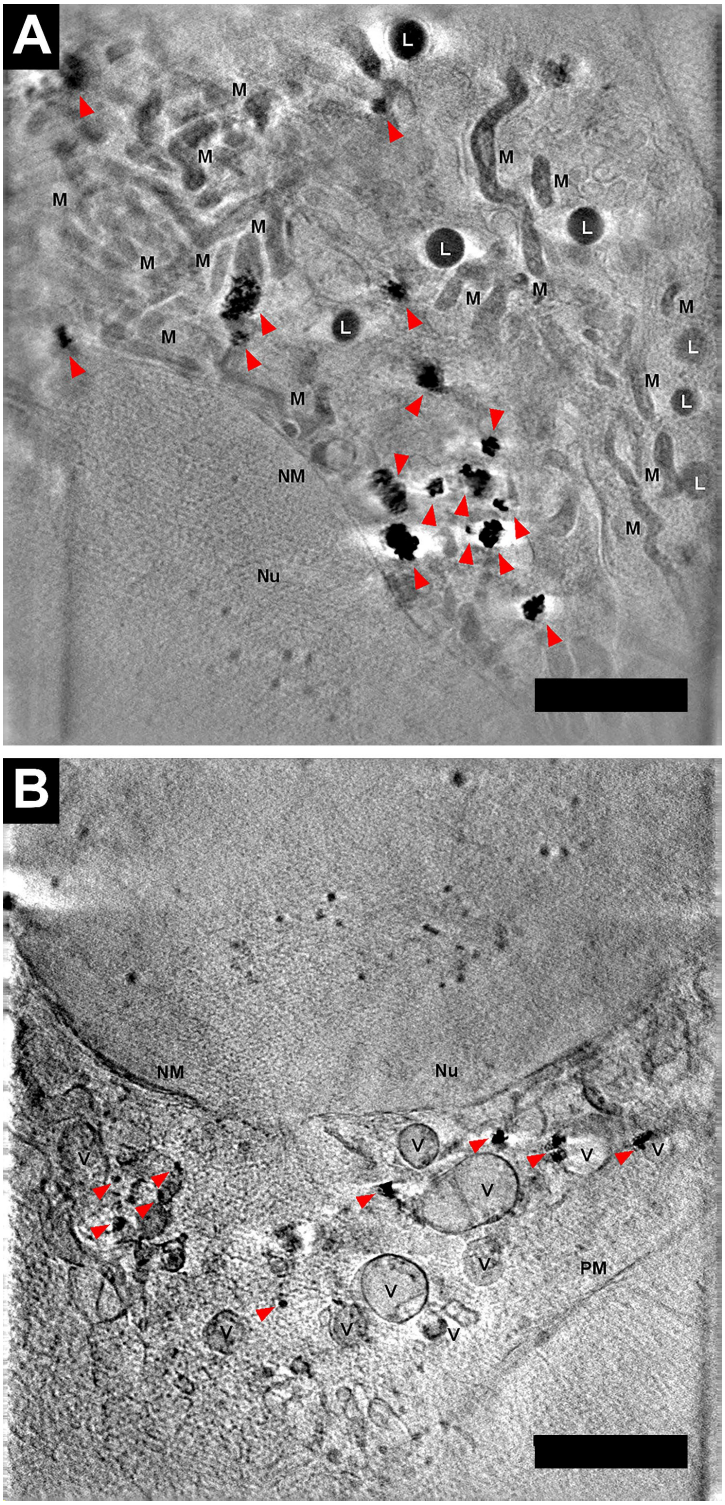
A
L
M
M
M

The virtual segmentation of the whole tomogram (Figure 9.4) corresponding to the tomographic slice in Figure 9.3B visualizes the chromatin granules (blue volumes) and the high intracellular volume occupied by the cytoplasmic vacuoles (red volumes). It has been shown that the excessive endocytosis of gold nanoparticles can induce apoptosis and autophagy [282], the latter resulting in the accumulation of large cytoplasmic vacuoles similar to those shown in Figure 9.3B. The cytoplasmic vacuoles with bright lumen can also originate from the dilation of the endoplasmic reticula [293] or other processes related to the water permeation of the cell membrane [294], which all suggest cellular injury or cell death.

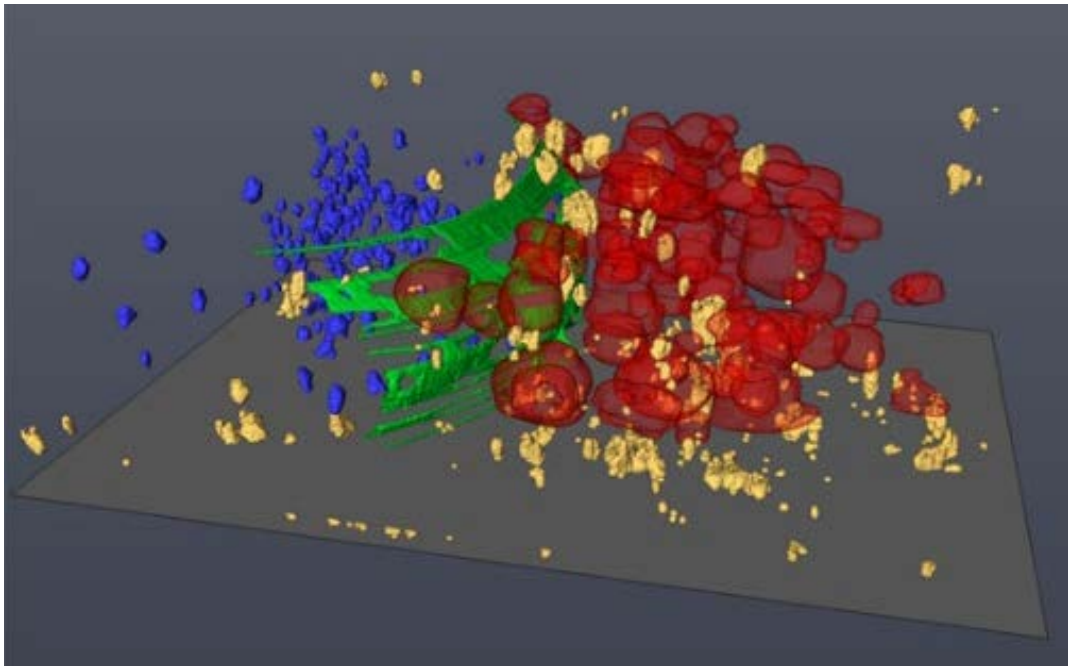

Figure 9.4. The segmentation of the tomogram represented by a tomographic slice in Figure 9.3B (HCT-116 cell, McCoy-FBS, pre-aggregated gold nanoparticles). Red volumes: vacuoles, yellow volumes: gold nanoparticles, green mesh: nuclear membrane, blue volumes: chromatin granules.

To learn whether the same ultrastructural changes can be induced in A549 as well, they were cultivated identically in both culture media like HCT-116 cells (Figures 9.5 and 9.6). The growth rates of A549 cells in the two culture media were comparable.

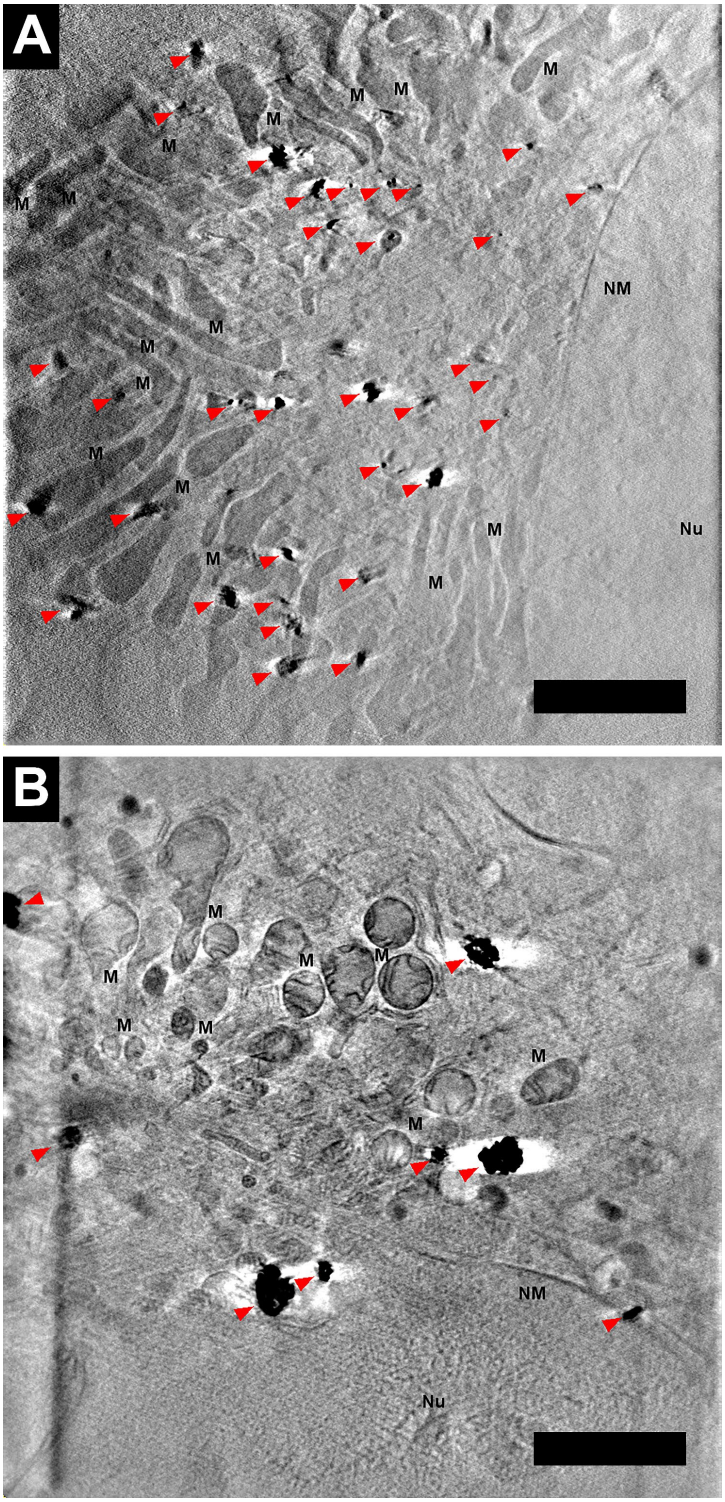

Figure 9.5. Tomographic slices of A549 cells incubated with non-aggregated (A) and pre-aggregated (B) gold nanoparticles in DMEM-FBS. The images are representative of 14 and 6 tomograms, respectively. Mitochondrion: M, liposome: L, plasma membrane: PM, nuclear membrane: NM, nucleus: Nu, vesicles: V, gold nanoparticles are marked with red arrowheads. The scale bars represent 2 μm.

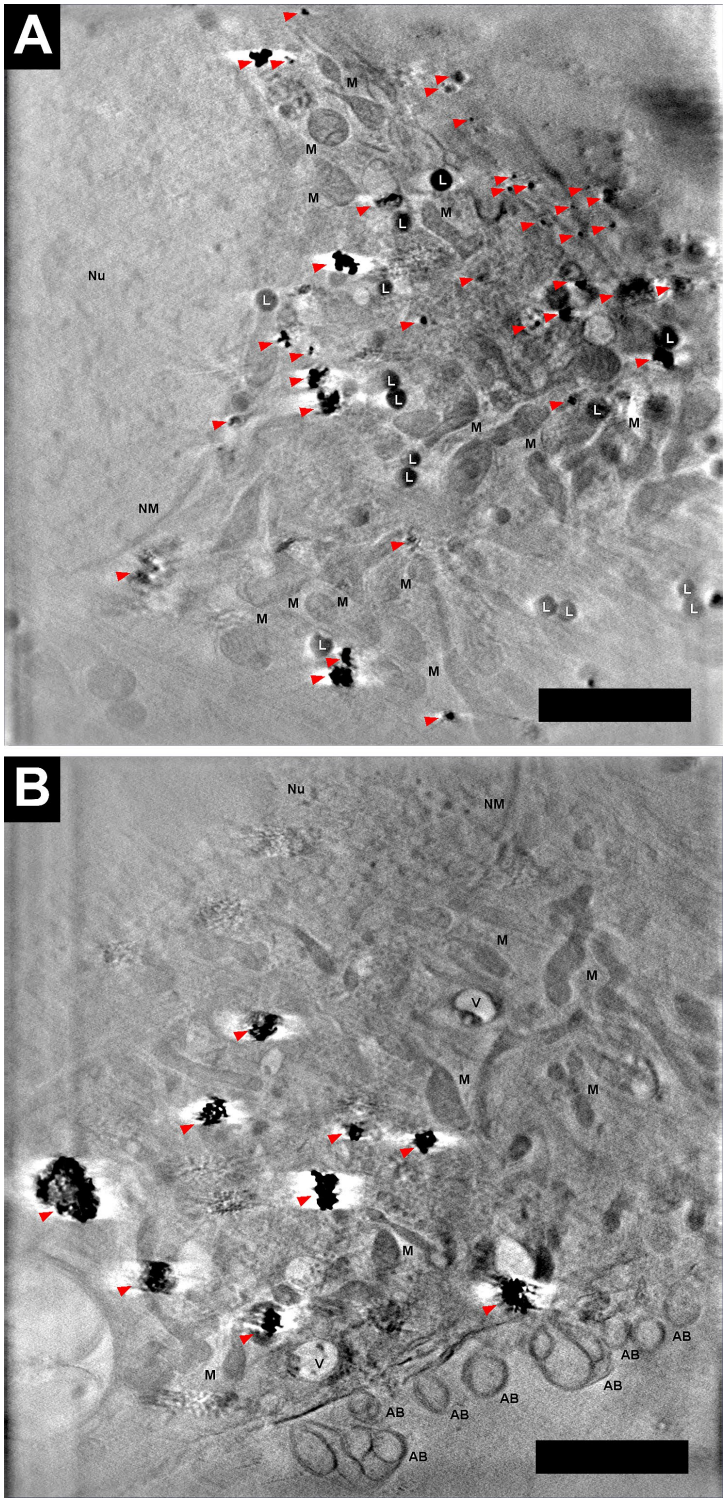

Figure 9.6. Tomographic slices of A549 cells incubated with non-aggregated (A) and pre-aggregated gold nanoparticles (B) in McCoy-FBS. The images are representative of 11 and 12 tomograms, respectively. Mitochondrion: M, liposome: L, plasma membrane: PM, nuclear membrane: NM, nucleus: Nu, vesicles: V, gold nanoparticles are marked with red arrowheads, apoptotic bodies: AB. The scale bars represent 2 µm.

The ultrastructural features of A549 cells after their incubation with non-aggregated gold nanoparticles are shown in Figure 9.5A and Figure 9.6A. In both cell culture media, A549 cells appeared healthy, though, in Figure 9.5A representing A549 cells grown in DMEM-FBS and incubated with non-aggregated gold nanoparticles, mitochondria appear to be slightly more abundant in the whole tomogram than in the cells grown in McCoy-FBS (Figure 9.6A). It can be seen that the gold nanoparticles form intracellular aggregates of a few nanoparticles. When A549 cells are incubated with pre-aggregated gold nanoparticles (Figure 9.5B in DMEM-FBS and Figure 9.6B in McCoy-FBS), the signs of cellular injury and cellular stress appear similar to those observed in HCT-116 cells (compare with Figures 9.2 and 9.3). The altered mitochondrial morphologies (rounding due to fission or long, branching structures as a result of hyperfusion [292]) infer changes in the energy production and energy demand of the cells.

Chromatin granules formed in the nucleus (Figure 9.6B) and the disruption of the nuclear membrane (Figure 9.5B and Figure 9.6B) both reveal the presence of cellular damage or cell death as discussed in the case of HCT-116. The formation of extracellular vesicles can be observed in Figure 9.6B, which are probably apoptotic bodies according to the mass spectrometric results (Table S9.2), thus exhibiting a clear sign of induced apoptosis (Figure 9.6B). It can be concluded that the XRT experiments yielded valuable information about the cellular stress and injury induced by gold nanoparticles on a single-cell level. The extent of the ultrastructural changes implying cellular injury and cell death depends both on the cell line and the chosen incubation conditions.

9.3. Intracellular aggregate properties based on tomogram segmentation

With the virtual segmentation of the tomograms, the intracellular gold nanoparticle aggregate morphologies can be revealed, which sheds light on the cellular response induced by their uptake. Gold nanoparticle aggregates were rendered in the tomograms represented in Figures 9.2-9.6 based on their high X-ray absorption, as shown in refs. [144, 168]. The tomogram segmentation and particle rendering depend strongly on the contrast of the tomographic slices, which was manually adjusted to provide the best rendering of the nanoparticles and their aggregates.

The segmented gold nanoparticle aggregates in HCT-116 and A549 cells are shown in Figure 9.7. It can be observed that the size of intracellular aggregates increased when the cells were incubated with pre-aggregated gold nanoparticles (Figure 9.7 right column) compared to the incubation with non-aggregated gold nanoparticles (Figure 9.7 left column). In HCT-116, the estimated number of total internalized nanoparticles rendered in the individual tomograms (Figures 9.2 and 9.3) changes from 10500 to 20000 and from 8500 to 9000 in DMEM-FBS and McCoy-FBS, respectively, when they were incubated with pre-aggregated gold nanoparticles instead of single particles. In A549, the numbers of intracellular gold nanoparticles in the individual tomograms (Figures 9.5 and 9.6) changed from 15000 to 33500 and from 15000 to 24500 in DMEM-FBS and in McCoy-FBS, respectively, when they were incubated with pre-aggregated gold nanoparticles instead of single particles. The overall increment in the nanoparticle uptake in both cell lines is the result of the higher number of simultaneously internalized particles in the form of aggregates compared to the case of single nanoparticle uptake. In HCT-116, the significantly higher intracellular gold nanoparticle number in DMEM-FBS can be explained by the suboptimal nutrition of cells in this medium. Since the gold nanoparticles are covered with the primary protein corona formed in the serum when they reach the cell membrane, it is possible that the cell recognizes them as a source of nutrients and thus internalizes them more readily than in McCoy-FBS where the conditions are optimal for the cells. As seen in Figures 9.5 and 9.6, the signs of cellular stress in A549 become more prominent in the case of incubation with pre-aggregated gold nanoparticles. While the numbers of rendered nanoparticles in the cells incubated with single gold nanoparticles were comparable in both culture media, they increased in DMEM-FBS by over 37% when incubated with pre-aggregated gold nanoparticles. Based on the XRT results and the corresponding numbers of intracellular gold nanoparticles, it was found that the nanoparticle uptake was higher under higher cellular stress.

It can be seen by comparing the intracellular gold nanoparticle structures after incubation with non-aggregated gold nanoparticles that a larger number of aggregates with more homogeneous size distribution are present inside A549 (Figure 9.7E and G) than in HCT-116 (Figure 9.7A and C). Since the nanoparticles were administered as single particles and not as aggregates, these figures yield important information about the intracellular processing of the nanoparticles.

In the comparison of the average number of nanoparticles per aggregate in the tomograms, systematic differences were found in the two cell lines, which further inform about the mechanisms induced by the nanoparticles.

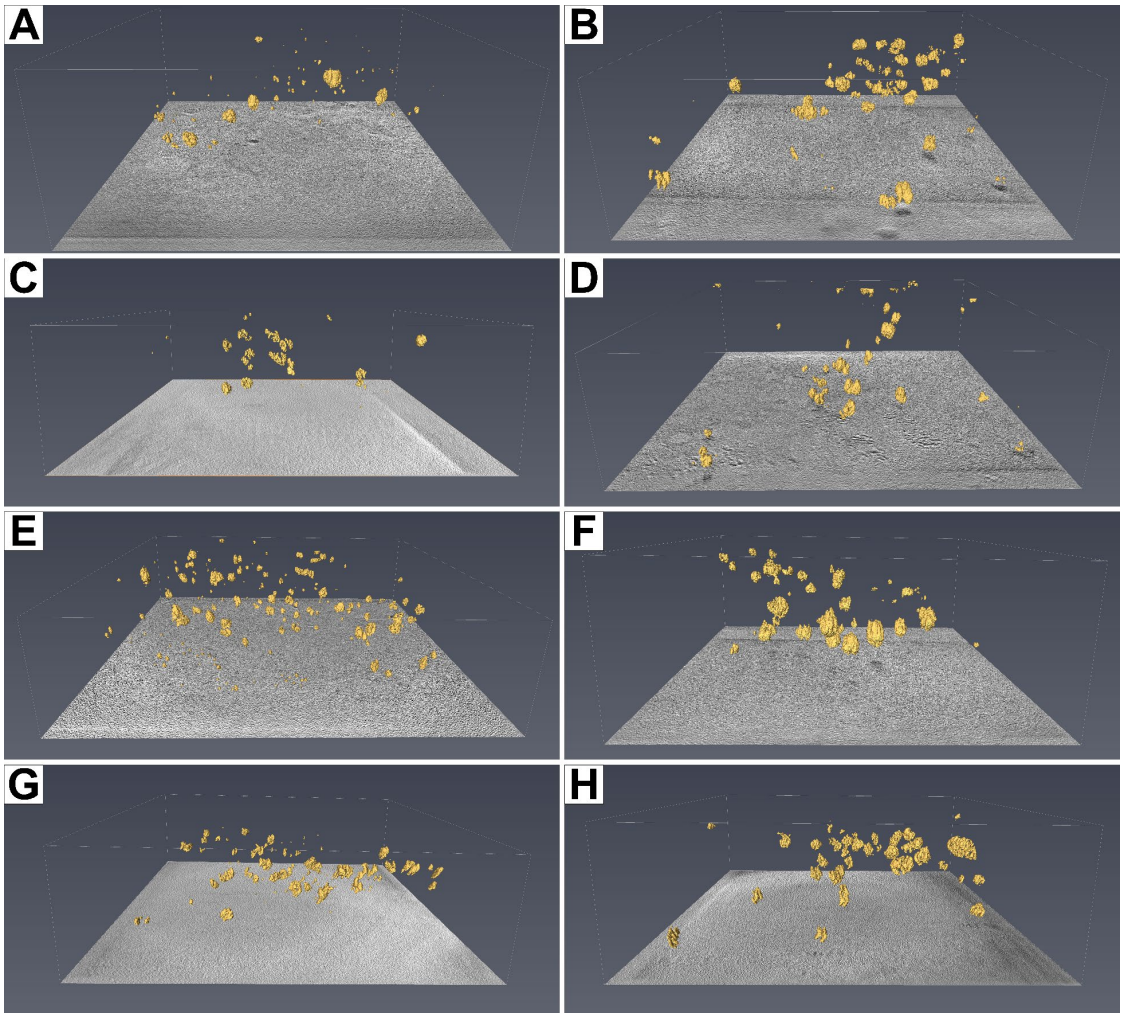

Figure 9.7. Tomographic segmentation reveals gold nanoparticle aggregates in the previously presented tomograms (Figures 9.2-9.6): HCT-116 cells grown in DMEM-FBS with non-aggregated (A) and pre-aggregated gold nanoparticles (B), HCT-116 cells grown in McCoy-FBS incubated with non-aggregated (C) and pre-aggregated gold nanoparticles (D). A549 cells grown in DMEM-FBS incubated with non-aggregated (E) and pre-aggregated gold nanoparticles (F), and A549 cells grown in McCoy-FBS incubated with non-aggregated (G) and pre-aggregated gold nanoparticles (H).

The average numbers of nanoparticles per aggregate were comparable in HCT-116, ranging from 108 to 137 (Figure 9.7 A-D) regardless of whether the particles were administered as single or pre-aggregated gold nanoparticles. In A549, more substantial differences were found: the average number of particles changed from 66 to 242

(Figure 9.7 E-F) and from 111 to 221 (Figure 9.7 G-H) in DMEM-FBS and McCoy-FBS, respectively, when the cells were incubated with pre-aggregated nanoparticles instead of single particles. Based on these numbers, HCT-116 readily processes the nanoparticles and their aggregates further after their uptake, thus resulting in comparable numbers of particles per intracellular aggregate in each sample, opposed to A549, which preserves the state of the internalized particles more. The difference between the nanoparticle processing of the two cell lines can be explained by comparing the hard corona proteomes with the intracellular aggregate morphologies. Based on the mass spectrometric results (Table S9.2), one of the most abundant proteins in the hard corona extracted from A549 is vimentin, which plays a key role in intracellular aggresome formation [281]. Aggresomes are the deposit sites of aggregated or misfolded proteins regulated by the cell. It has been known that the proteins forming the corona are what the cell "sees" [19]; however, these results indicate that A549 cells might see the nanoparticle corona as a form of aggregated proteins. The formation of a vimentin cage around the gold nanoparticles can reduce oxidative stress as it was previously shown [296]. This might explain why A549 cells with a high abundance of vimentin around the nanoparticles are more robust to the administration of gold nanoparticles than HCT-116 cells, which process the nanoparticles and their aggregates based on different mechanisms, as also indicated by the hard corona proteome (Table S9.1).

While the total number of aggregate structures increased in HCT-116 when the internalized particles were pre-aggregated (Figure 9.7 A-D), in A549 their number decreased (Figure 9.7 E-H). Based on the presence of related proteins in the hard corona, clathrin-mediated endocytosis is a possible uptake mechanism for the internalization of gold nanoparticles by HCT-116. However, clathrin-mediated endocytosis only explains the uptake of single particles or small aggregates formed by 2-6 particles [79-81]. Another mechanism has to be activated for the uptake of larger structures, *e.g.,* macropinocytosis. It has been shown by Palvai *et al.* that HCT-116 cells readily combine clathrin-mediated endocytosis with macropinocytosis during the uptake of nanoparticles [297]. The tomography segmentation data suggest that macropinocytosis is less abundant in A549 than in HCT-116, as the total number of intracellular aggregates decreases upon incubation with pre-aggregated gold nanoparticles.

According to previous discussions, macropinocytosis is not a prioritized uptake mechanism by A549 cells [84], which explains the decrement of intracellular gold nanoparticles structures in these cells upon incubation with pre-aggregated gold nanoparticles.

Regardless of the number of internalized aggregates, in both cell culture media and both cell lines, the total number of internalized nanoparticles is higher in the case of incubation with pre-aggregated gold nanoparticles than with non-aggregated nanoparticles. Therefore, the experiments with pre-aggregated gold nanoparticles serve as a model for higher particle uptake, and differential data can be extracted corresponding to the effects of gold nanoparticles on cells.

9.4. XTT cell proliferation studies of gold nanoparticle cytotoxicity

The XRT data suggest a difference in the cell viability in the different culture media when incubated with single and pre-aggregated gold nanoparticles, respectively. To assess the question of changes induced by gold nanoparticles in cell viability, proliferation tests were performed for each incubation condition with a commercial XTT cell proliferation assay (Cayman Chemical, Michigan, USA). The experimental details were described in Section 4.22. As seen in the XRT results (Figures 9.1-9.6) and the analysis of the intracellular aggregates (Figure 9.7), the incubation with pre-aggregated gold nanoparticles resulted in a higher amount of intracellular gold nanoparticles and it induced stronger cellular stress than the incubation with non-aggregated nanoparticles.

The XTT results are shown in Figure 9.8. Cells grown in different culture media show opposite tendencies: while a decreasing tendency was found in the viability of both cell lines in McCoy-FBS, it was reversed in DMEM-FBS. The tendencies in viability in McCoy-FBS are in agreement with the tendencies inferred based on the XRT results. In HCT-116 (compare Figures 9.2B and 9.3B with the red bars in Figure 9.8A), the administration of non-aggregated gold nanoparticles lowered the viability to 91%, while the strong cellular stress induced by the uptake of pre-aggregated gold nanoparticles resulted in a relative viability of 64%. In contrast, the viability of A549 cells did not change after incubation with non-aggregated gold nanoparticles, and it only decreased to 85% after the administration of pre-aggregated gold nanoparticles. These results indicate

that HCT-116 cells are more sensitive to the presence of internalized gold nanoparticles than A549 cells. The sensitivity of HCT-116 to gold nanoparticles could be explained by the lack of vimentin in the hard corona due to the different processing of the nanoparticles than in A549 (Tables S9.1 and S9.2), as vimentin reduces oxidative stress, the primary reason of mitochondrial and ribosomal damage [296]. Therefore, the high abundance of proteins originated from mitochondria and ribosomes in the hard corona formed in HCT-116, as discussed in Section 9.1 and Table S9.1, can be explained by the generation of reactive oxygen species and the resulting oxidative stress, which is better suppressed in A549 by the presence of vimentin.

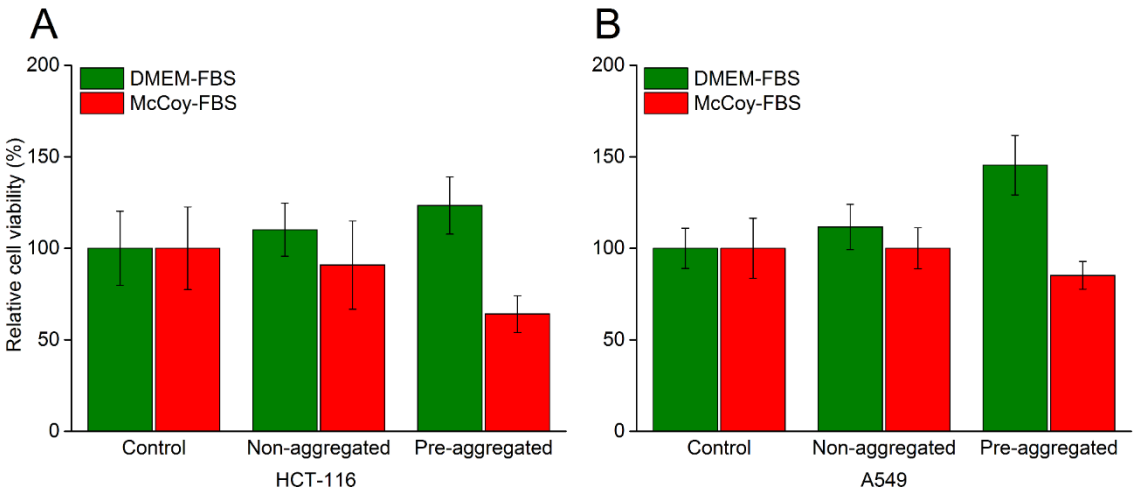

Figure 9.8. XTT viability studies of HCT-116 cells (A) and A549 cells (B) in DMEM- and in McCoy's 5A-based culture media, respectively. Opposite tendencies are observed in different culture media. The error bars represent the distribution of the measured cell viability based on t-test.

Based on the XRT experiments and preliminary light microscopic observations of the cultures, it is evident that the cell viability does not increase to values over 100% (Figure 9.8 green bars). The individual culture media and gold nanoparticles were investigated as control samples, which proved that they do not influence the results; therefore, the increasing tendency must come from intracellular processes that – at least seemingly – increase the signal of viability. The XTT dye is transformed into its measured form in the mitochondria [298], thus, the higher viability with increasing nanoparticle uptake is possibly the result of a higher number of functioning mitochondria in DMEM-FBS (see Figure 9.2A and Figure 9.5A) due to the induced cellular stress upon nanoparticle internalization. When A549 cells were incubated with non-aggregated gold

nanoparticles (Figure 9.8B, green bars), only a mild increment in the number of mitochondria was seen in DMEM-FBS compared to the sample incubated in McCoy-FBS (Figure 9.5A and Figure 9.6A). This mild increment is reflected in the viability results in the two media, rendering the nominal viability of A549 cells slightly higher in DMEM-FBS. The difference is larger in the case of incubation with pre-aggregated gold nanoparticles, as the viability in McCoy-FBS drops while that in DMEM-FBS seems to increase (Figure 9.8B). This increment can be attributed to the mitochondrial fission observed in Figure 9.5B, as discussed above. In the case of HCT-116 (Figures 9.2, 9.3, and the green bars in Figure 9.8A), the increasing tendency in the nominal viability in DMEM-FBS is less steep than in A549, which is probably due to the faster drop in the number of viable cells.

9.5. SERS studies of HCT-116 and A549 cells

SERS studies were performed with both cell lines in both cell culture media with single- and pre-aggregated gold nanoparticles as well to reveal the interactions of the identified proteins and the gold nanoparticle surface. Figure 9.9 shows the average spectra from five cells under each incubation condition for both cell lines. The tentative band assignments are listed in Table 9.1.

The average spectra differ based on whether the cells were incubated with non-aggregated or pre-aggregated gold nanoparticles, but they are independent of the cell line or the chosen culture medium. It can be observed that the 1130 cm^{-1}/1565 cm^{-1} band ratio assigned to C-C and C-N stretching versus vibrations of tryptophan, tyrosine, amide II, and COO^- and the 500 cm^{-1}/655 cm^{-1} band ratio assigned to S-S stretching versus C-S stretching vibrations are higher in the spectra of cells incubated with non-aggregated gold nanoparticles (see tentative assignments in Table 9.1). At the same time, the 1350 cm^{-1}/1315 cm^{-1} band ratio assigned to vibrations of tryptophan and guanine versus an amide III mode (Table 9.1) is higher in the average spectra of cells with pre-aggregated nanoparticles.

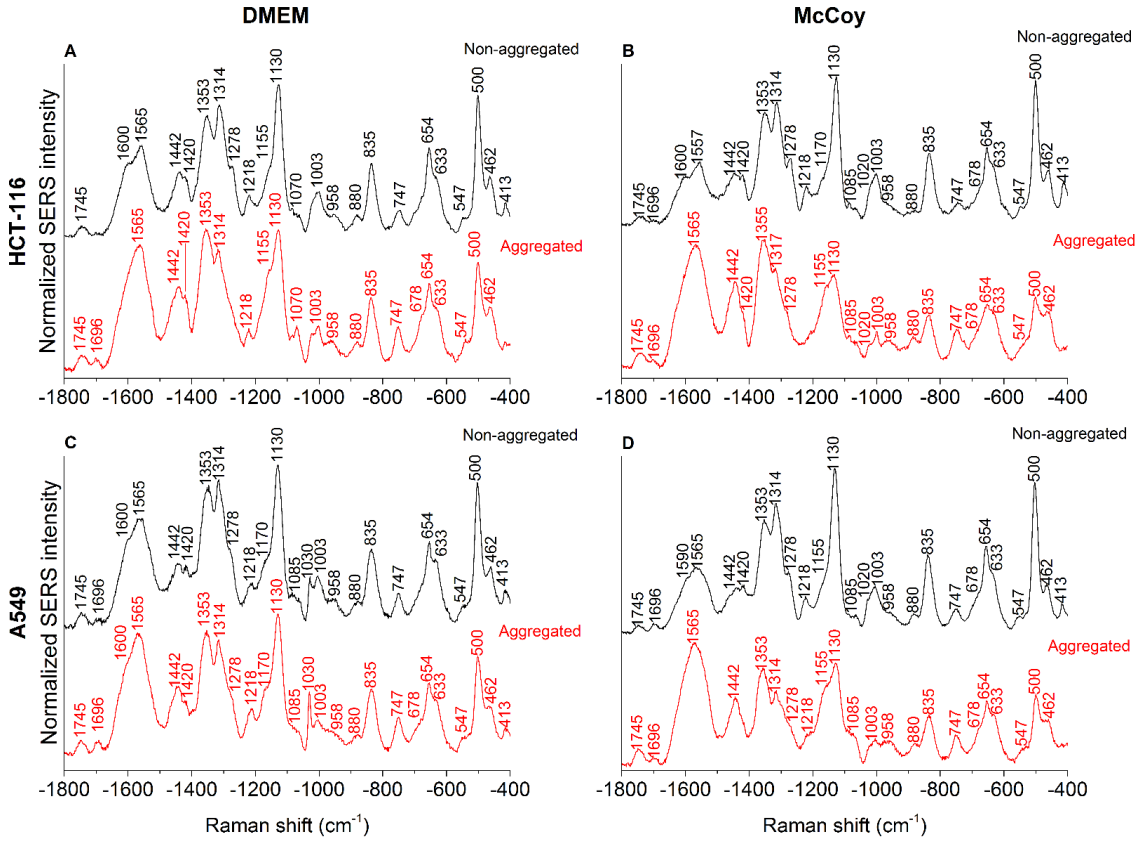

Figure 9.9. Average SERS spectra of five respective HCT-116 cells grown in DMEM-based (A) and McCoy's 5A-based culture medium (B), and of five respective A549 cells grown in DMEM-FBS (C) and McCoy-FBS (D). 24 h incubation, excitation wavelength: 785 nm, acquisition time: 1 s, excitation intensity: 2.3×10^5 W/cm^2. The spectra were stacked for clarity.

The pre-aggregation of gold nanoparticles was induced by the addition of NaCl. As it has been discussed previously [23], the addition of saline to gold nanoparticles decreases their absolute zeta potential. The zeta potential determines the magnitude of the electrostatic interactions of the gold nanoparticles [299], *i.e.,* the lower the absolute zeta potential, the lower the affinity to electrostatic interactions. It has been shown that the interaction between proteins and nanoparticles is the combination of different effects, among them, electrostatic and hydrophobic interactions [299]. While due to the decreased absolute zeta potential, the electrostatic component of the protein-nanoparticle interactions becomes weaker, the increased hydrophobicity of the gold nanoparticles [23] pushes the equilibrium of interactions more towards the hydrophobic component. Therefore, when gold nanoparticles are pre-aggregated with NaCl, the aggregates already possess a low absolute zeta potential at the moment of their addition to the culture medium.

Table 9.1. Raman shifts and their tentative assignments in Figure 9.9. *v* stretching, *δ* deformation, *symm* symmetric, *wag* wagging, *br* breathing, *R* benzene ring, *r* pyrrole ring. Band assignments were based on refs. [40, 104, 171, 172, 215, 219, 253].

Raman shift (cm^{-1})	Tentative assignment
1745	ν(C=O)
1696	Amide I
1600	Tyr, Phe ν(R), Amide I
1590	ν(C=C), COO^-
1565	Amide II, Trp, Tyr, ν(COO^-)
1557	Amide II, Trp, Tyr, ν(COO^-)
1442	δ(CH_2)
1420	A, G, CH_3CH_2 twisting
1353	Trp, G
1314	G, δ(C-H), Amide III
1278	Amide III, CH_2 wag, DNA/RNA
1218	Amide III, T, A, ν(PO_2,C-N)
1170	C, G, Tyr C-H bend, lipids
1155	ν(C-C, C-N)
1130	ν(C-C, C-N)
1085	ν(C-C, C-N)
1070	ν(C-C), ν(PO_2) of DNA/RNA, Pro
1030	Phe, ν(C-C)
1020	ν(C-O) of ribose
1003	R br
958	ν(C-C) of Pro and Val
880	ν(C-C) of Pro and Val
835	$\nu(O\text{-}P\text{-}O)_{asymm}$, Tyr, Pro
747	T, ν(C-S,C-C), Pro, Trp symm br
678	ν(C-S), G, T
654	ν(C-S), C-C twisting of Tyr, Phe
633	ν(C-S), C-C twisting of Tyr, Phe
547	ν(S-S), cholesterol
500	ν(S-S)
462	ν(C-S)
413	Trp

This affects the formation of the primary corona, resulting in protein adsorption based more on hydrophobic than electrostatic interactions, which appears in the average SERS signal of cells incubated with pre-aggregated gold nanoparticles. The possibility of such interactions between proteins and nanoparticles was discussed in Chapter 6. When the nanoparticles were not pre-aggregated, the interactions in the rapidly formed primary protein corona could rely more on electrostatic interactions, while the proteins partially

shield the surface of the nanoparticles from the higher ion concentration of the culture medium or the intracellular environment that could potentially lower their zeta potential. Since the protein corona forms a multi-layer coverage on the gold nanoparticles, the exchange of the proteins directly interacting with the nanoparticles occurs in a protected environment that at least partially prevents the exposure of the nanoparticle surface to the environment with higher ionic strength. These phenomena explain the lower signal of nonpolar group vibrations in the cells incubated with non-aggregated particles compared to those incubated with pre-aggregated nanoparticles.

To further analyze the nanoparticle-protein interactions in cells, the band occurrences and co-occurrences were evaluated in the whole datasets. Figure 9.10 displays the band occurrence curves of all the SERS data of the incubated cells. The datasets consisted of 661 and 602 (HCT-116 and A549, respectively, in DMEM-FBS incubated with non-aggregated nanoparticles), 627 and 823 (HCT-116 and A549, respectively, in DMEM-FBS incubated with pre-aggregated nanoparticles), 402 and 909 (HCT-116 and A549, respectively, in McCoy-FBS incubated with non-aggregated nanoparticles), and 705 and 604 spectra (HCT-116 and A549, respectively, in McCoy-FBS incubated with pre-aggregated nanoparticles). The band at 1130 cm^{-1} is present in the majority of the spectra, which is the C-C and C-N stretching vibrational contribution of the peptide backbone (Table 9.1). The previously described tendencies of the 500 cm^{-1}, 654 cm^{-1}, 1130 cm^{-1}, 1314 cm^{-1}, 1353 cm^{-1}, and 1565 cm^{-1} bands (see tentative band assignments in Table 9.1) were found in the relative band occurrence curves as well (Figure 9.10). To support the in-depth discussion of nanoparticle-side chain interactions, the co-occurrences of the most abundant spectral bands were evaluated. In DMEM-FBS, the 1353 cm^{-1} vibrational band assigned to tryptophan and guanine vibrations is mostly independent from the 1314 cm^{-1} and 500 cm^{-1} vibrational bands, assigned to vibrations of amide III and S-S stretching, respectively, while in McCoy-FBS the majority of spectra from cells incubated with non-aggregated particles exhibiting the 1314 cm^{-1} band showed the 1353 cm^{-1} band as well (see Table 9.1 for tentative band asignments). Therefore, it could seem that the 1353 cm^{-1} band co-occurs with the 500 cm^{-1} band. To evaluate their co-dependency, the spectra exhibiting the 1353 cm^{-1} vibrational band but not the 1314 cm^{-1} band were analyzed.

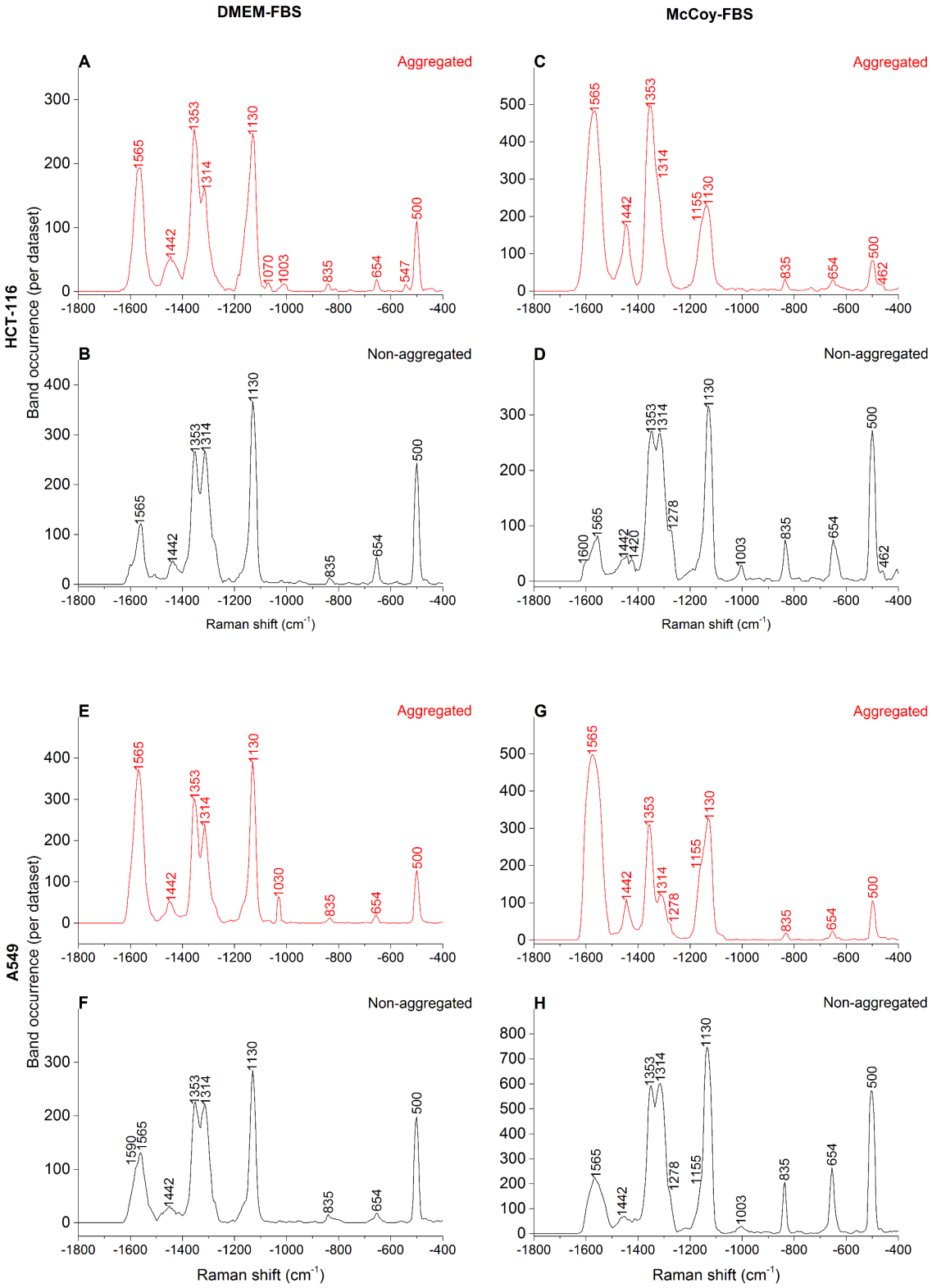

Figure 9.10. Results of the analysis of band occurrence in the complete SERS data of HCT-116 cells grown in DMEM-based medium (A, B) and McCoy's 5A-based medium (C, D), and of A549 cells grown in DMEM-based medium (E, F) and McCoy's 5A-based medium (G, H).

It was found that in this case, the occurrence of the vibration at 500 cm^{-1} decreased to only a fraction of its original abundance. Therefore, the data suggest that the 1314 cm^{-1} band co-occurs with the 500 cm^{-1} band and they are not related directly to the vibration at 1354 cm^{-1}. The co-occurrence of the 1314 cm^{-1} and the 500 cm^{-1} bands indicates intact structural elements in the secondary structure of proteins composing the corona since the role of disulfide bonds is to stabilize them (see tentative band assignments in Table 9.1). Besides the amide III vibrations, bands attributed to aromatic side-chain vibrations, *e.g.,* at 1565 cm^{-1} and 1353 cm^{-1}, often co-occur with the 500 cm^{-1} band attributed to S-S stretching vibration (Table 9.1) due to the concentration of aromatic residues around disulfides in proteins as shown before [260]. The band at 654 cm^{-1} assigned to a C-S stretching vibration of cystine (Table 9.1) appears nearly exclusively with an S-S stretching vibration, which indicates the presence of intact disulfide bonds. Therefore, the co-occurrence of these bands can suggest the interaction of the gold nanoparticle surface with one of the sulfur atoms in a disulfide bridge, which can take place *via* a nonbonding electron pair of the sulfur atom. Such interactions have been proposed previously [300].

The band at 1565 cm^{-1}, assigned to vibrations of tryptophan, tyrosine, amide II, and COO^- often appears together with the 1353 cm^{-1} band assigned to tryptophan and guanine vibrations in cells (Table 9.1). Since a portion of these spectra exhibits the vibration at 500 cm^{-1} characteristic to proteins, it is most likely that the co-occurrence of the 1565 cm^{-1} and 1353 cm^{-1} bands comes from the interaction of gold nanoparticles with tryptophan residues rather than with nucleic acids.

The vibration at 1070 cm^{-1} appears mostly in the SERS data of HCT-116 cells grown in DMEM-FBS and incubated with pre-aggregated gold nanoparticles. This band appears together with the bands at 1110 cm^{-1} assigned to C-C stretching of carbohydrates, lipids, proteins [253], 1190 cm^{-1} assigned to cytosine, guanine, adenine, antisymmetric phosphate vibration [253], and 1470 cm^{-1} assigned to C=N deformation of nucleobases and lipids [253]. The co-occurrence of these bands was not observed in the other datasets, and it suggests the interaction of gold nanoparticles with nucleic acids. Based on the mass spectrometric, XRT, and cell viability results, it is probable that the stronger contribution of nucleic acids to the SERS signal in this sample compared to the others is the result of the significant cellular damage caused by the internalized gold nanoparticles.

9.6. Summary

Here, the different aspects of studying the protein-nanoparticle interactions presented in Chapters 5-8 are brought together. In this chapter, the potential of the combined proteomics, XRT, and SERS analysis was demonstrated in the study of the hard protein corona formed in living cells. The proteomic results provide qualitative information of the hard corona composition, the XRT results carry ultrastructural information, while the SERS data indicate the interactions of the gold nanoparticles with the hard protein corona *in situ*.

The tentative functional analysis of the hard corona proteome of internalized gold nanoparticles yields information about the processing of the nanoparticles. It was found that several bovine proteins deriving from the culture medium remain in the hard protein corona, which suggests their high affinity to the gold nanoparticle surface. However, the most abundant serum protein, bovine serum albumin, was not found in the hard protein corona above the significance threshold, which suggests its low affinity to the gold nanoparticle surface, as proposed in Chapter 6 as well. The hard corona composition reveals essential events in the cellular processing of the gold nanoparticles, such as their interaction with the outer surface of the cell, their clathrin-mediated endocytosis, and it also indicates the induced cellular response mechanisms.

The XRT studies suggest that the internalized gold nanoparticles induce cellular stress in both HCT-116 and A549 cells. However, A549 was more robust and showed severe cellular damage under the least optimal conditions, *i.e.,* in the case of incubation with pre-aggregated gold nanoparticles. This could be explained by the presence of the protein vimentin in the hard corona proteome extracted from A549 cells, which has been shown to reduce oxidative stress [296]. The effects of vimentin show in the aggregate morphologies as well. The number of intracellular nanoparticles and their aggregates was evaluated after the segmentation of the tomograms, and in combination with the proteomics data, they revealed different uptake mechanisms and intracellular nanoparticle processing in the two cell lines, which can further account for the difference in the cytotoxicity observed in the XTT studies.

The nanoparticle-protein interactions were analyzed by SERS. While significant ultrastructural differences were observed in the XRT results, the protein-nanoparticle

surface interactions appeared to be independent of the cell line or the choice of culture medium. The average SERS spectra showed that in the cells incubated with pre-aggregated gold nanoparticles, the surface interactions rely more on hydrophobic than electrostatic effects. This allowed for the conclusion that only by increasing the ionic strength, different surface interactions can be expected due to changes in the zeta potential of the gold nanoparticles. The band occurrences and co-occurrences revealed that in the case of each incubation condition, the secondary structure of the adsorbed protein remains at least partially intact. The stronger contribution of the nonpolar group vibrations, *e.g.,* the vibrations of tryptophan at 1565 cm^{-1} and 1353 cm^{-1} further support the preference of hydrophobic interactions over electrostatic interactions due to the decreased absolute zeta potential. The signs of cellular damage indicated by the XRT results were also evident in the SERS dataset of HCT-116 cells incubated with pre-aggregated gold nanoparticles in DMEM-FBS, where an increased contribution of vibrations from nucleic acids was observed.

As presented in this chapter, the combination of SDS-PAGE, HPLC-ESI-Q-TOF-MS, XRT, and SERS provide valuable insight into the interaction of the gold nanoparticles from the moment they are introduced into the culture medium until cell lysis. The results illustrate that these analytical techniques complement each other, and by their combination, a new analytical approach has been proposed for the investigation of the protein corona of nanoparticles in living cells.

Chapter 10

Summary and outlook

The knowledge about the protein corona is of crucial importance to the pharmaceutical, medical, and environmental research fields, among others. The focus of this thesis was the investigation of the protein corona composition in living cells and the nanoparticle-protein surface interactions responsible for the cellular response mechanisms observed upon gold nanoparticle uptake. This thesis was meant to approach these phenomena at different biological organizational levels: in simple protein solutions, an *in vitro* enzymatic reaction model, isolated cytosol, and in living cells.

First, the pure solution of bovine serum albumin (BSA) was studied with surface-enhanced Raman scattering (SERS) as discussed in Chapter 5. For this purpose, a sample preparation approach was presented, which is based on the agglomeration of gold nanoparticles in the presence of protein molecules. Therefore, the acquired SERS data with a signal enhancement of up to 10^8 were suitable for the comparison with the SERS data of biological systems, where the active processing of the gold nanoparticles by the biomolecular environment results in SERS-active aggregates. Different signals at different concentrations allowed for the conclusion of distinct aggregation mechanisms and the data proved that the live cell SERS signals of high enhancement are the result of the positioning of the intracellularly formed gold nanoparticle aggregates rather than only the crowded biomolecular environment. In Chapter 6, BSA and human serum albumin

(HSA) were studied under identical experimental conditions. The results suggested differences in the interactions of the two proteins with the gold nanoparticles: indirect interactions based on the electrostatic attraction of the citrate ions adsorbed on the nanoparticles and the lysine groups on the surface of the protein molecules, and in the case of HSA, the direct interaction of the gold surface with a specific protein segment. These findings contributed to the discussion of the nature of nanoparticle-protein interactions, which are often debated in the literature.

In Chapter 7, a combination of soft cell lysis, electrophoresis, liquid chromatography, and mass spectrometry was developed for the proteomic analysis of the hard corona, that is, the layer of proteins with the highest affinity to the nanoparticles' surface. In contrast to other discussions in the literature where the whole corona complex or labeled corona proteins are analyzed, this analytical method reveals only those proteins that directly interact with the surface of the gold nanoparticles without chemical modifications. This analytical approach was robust to the natural heterogeneity of the samples. The results presented in Chapter 7 and 9 with four different cell lines showed that the hard corona proteome is typical for each cell line. Moreover, the extraction of the hard protein corona after different incubation times and its subsequent analysis suggested that the hard protein corona of gold nanoparticles formed in J774 mouse macrophage cells did not change over time in the range of 1.5-24 h. Since the protein corona is extracted before its analysis, the source of the sample does not affect the success of the hard corona analysis, and the proposed analytical approach is expected to be suitable for the proteomic analysis of the hard corona formed in more complex samples, such as *ex vivo* or *in vivo* tissues.

In the analysis of the time-dependent composition of the hard corona, a band in the electropherograms indicated the presence of low-mass peptide species. To learn whether those small polypeptides originate from proteolysis, the SERS data of live J774 cells and those of the isolated J774 cytoplasm after 1.5 h incubation with gold nanoparticles were collected. The results revealed spectral features that can indicate protein fragmentation in the live cell SERS spectra, such as the higher abundance of nonpolar group vibrations and the lower abundance of amide bands. To identify these differences as the spectral features of protein cleavage, SERS data were acquired from the solutions of BSA, bovine trypsin, and trypsinized BSA, respectively. The comparison of the datasets revealed identical differences in the SERS spectra of trypsinized BSA to those found in the live cell SERS

spectra, confirming the presence of protein fragments in the hard protein corona. Due to the lower signal of the corresponding vibrations in the SERS data of the isolated cytoplasm, it was concluded that the proteins were cleaved after, rather than prior to their adsorption on the nanoparticles, which indicates the active intracellular processing of the gold nanoparticles. The comparison of the SERS spectra of BSA and trypsin allowed for the discussion of some secondary structural elements in the probed volume, thus extending the discussion of citrate stabilized gold nanoparticle-protein interactions presented in Chapters 5 and 6.

The findings presented in Chapters 5-8 confirm the possibility of the more comprehensive analysis of the intracellular protein-nanoparticle surface interactions and the composition of the hard corona based on SERS and proteomics. Therefore, in Chapter 9, SERS and proteomics are brought together in combination with cryo soft X-ray nanotomography (XRT) for the extensive analysis of the intracellular hard protein corona and the processing of gold nanoparticles. The experiments were performed with two human cell lines: HCT-116 from colorectal carcinoma and A549 lung carcinoma in DMEM-FBS and McCoy-FBS media, respectively. The tentative functional assignment of the identified hard corona proteins indicated cellular mechanisms induced by gold nanoparticles, such as their internalization by clathrin-mediated endocytosis in HCT-116 cells, or those in A549 aimed at reducing cellular stress. Histones were abundant in both hard corona proteomes indicating the possibility of the direction of internalized nanoparticles into cellular compartments targeted for exocytosis. The ultrastructural information revealed by XRT indicated that HCT-116 cells are more sensitive to the presence of gold nanoparticles and the suboptimal conditions of incubation, *e.g.,* culture medium with fewer nutrients. It was found that the higher nanoparticle uptake during the incubation with pre-aggregated gold nanoparticles can easier result in induced apoptosis in HCT-116 cells than in A549 cells. The intracellular gold nanoparticle aggregate morphologies suggested that macropinocytosis is a less favored uptake mechanism by A549 cells and that HCT-116 cells process the nanoparticles differently and in some sense more than A549 cells, which can result in higher sensitivity to their presence. In A549 cells, gold nanoparticles are grouped into homogeneously formed gold nanoparticle agglomerates, which can be explained by the high abundance of vimentin in the hard corona proteome. Even though strong differences were found in the hard corona proteome and the cellular

ultrastructure in different cell lines, the SERS data revealed that the nanoparticle-protein surface interactions mostly depend only on the aggregation state of the nanoparticles. The larger contribution of nonpolar group vibrations to the SERS spectra was observed in the datasets of samples incubated with pre-aggregated gold nanoparticles than in those of samples incubated with non-aggregated gold nanoparticles, which suggest the higher abundance of nonpolar residues, such as tryptophan, in the close proximity of the nanoparticles' surface. This was explained by the lower absolute zeta potential of the gold nanoparticles pre-aggregated with NaCl solution, which was shown to enhance their hydrophobicity. The co-occurrence of specific spectral bands in the SERS spectra at 500 cm^{-1} and 655 cm^{-1} assigned to S-S and C-S stretching vibrations, respectively, indicated that intact secondary structural elements are present in the close proximity of the nanoparticles' surface and that the sulfur atoms participating in disulfide bonds can interact with the gold nanoparticle *via* their lone-pair electrons. In HCT-116 cells incubated with pre-aggregated gold nanoparticles in DMEM-FBS, under which conditions this cell line showed the most excessive cellular stress, signs of nucleic acids interacting with the gold nanoparticles were found, indicating the severe cellular damage observed in XRT experiments.

As a conclusion, in this thesis, different analytical approaches were proposed for the analysis of nanoparticle-protein interactions and the protein corona that forms around nanoparticles in living cells. The results address key questions in the literature by confirming the presence of both the direct and indirect interactions between proteins and nanoparticles, as well as the unchanged composition of the hard corona proteome over time. As summarized above, the combined proteomics, XRT, and SERS studies related the hard corona composition to ultrastructural changes and nanoparticle-protein interactions with unprecedented details.

The presented results identify several connected aspects of the protein-nanoparticle interactions and, more generally, the nanoparticle-biosystem interactions that must be discussed further. Some of these aspects are listed below as a possible outlook of the work summarized above.

As it was shown in Chapter 8, the SERS data of model systems and isolated body fluids can be related after the proper data analysis is performed. The SERS data of the

interactions of proteins with distinct structures and differently engineered nanoparticles have to be collected, which can elucidate the behavior of *in vivo* nanoparticles administered for medical applications. The adsorption on the surface of nanoparticles can result in conformational changes in proteins, which can change enzyme activity. The proposed data analytical approaches were demonstrated to reveal structural information of the adsorbed enzymes and their substrates, and the spectral signatures of the enzymatic process were identified. Therefore, biomolecular processes can be monitored based on the findings mentioned in this thesis, which can reveal so-far unknown information of the interactions in the presence of plasmonic nanoparticles. Based on a recent discovery [144] and the results of the Chapters 8 and 9, SERS can be used to monitor changes in the biochemical environment of intracellular plasmonic nanoparticles. This could be beneficial for the understanding of how nanoparticles can alter enzymatic processes once inside a cell, and it can provide more comprehensive knowledge of enzyme-substrate interactions.

The protein corona composition was shown to strongly depend on the cell line with which the nanoparticles interact. The hard corona formed in different cell lines has to be analyzed to learn more about the intracellular processing of nanoparticles, based on the analytical approach described in Chapter 7. It is possible that recent improvements in the involved analytical techniques [248, 301] can contribute to the efficiency of identifying constituents in the protein corona, and it is possible that the approaches can be tuned towards a more quantitative direction as well.

The proposed experimental approaches, if necessary after optimization to the sample, are expected to reveal information about the nanoparticle processing and its protein corona in other, more complex biological systems as well, such as *ex vivo* tissues. The comparison of *in vitro* protein coronas formed in body fluids and those formed in two-dimensional cell lines and on nanoparticles administered *in vivo* can greatly contribute to our understanding of protein-nanoparticle interactions and the formation of the protein corona.

Tables of identified hard corona proteins

Table S7.1. The protein accession number (ID), name, recovered number of residues with respect to total chain length (# vs. total), MASCOT score (Score), and molecular weight (Mw) in Da of the identified proteins in the hard protein corona formed in MCF-7 cells. Bovine proteins are marked with italic font. The identified peptides, their charge, and their m/z values are not shown here.

ID	Name	# vs. total	Score	Mw (Da)
Q00610	Clathrin heavy chain 1	380/1675	839	191467
Q9UHD8	Septin-9	176/586	618	65361
P42166	Lamina-associated polypeptide 2, isoform alpha	233/694	520	75446
Q96CN7	Isochorismatase domain-containing protein 1	127/298	413	32216
P42167	Lamina-associated polypeptide 2, isoforms beta/gamma	134/454	378	50639
Q9NVA2	Septin-11	93/429	361	49367
Q15019	Septin-2	106/361	344	41461
Q92599	Septin-8	139/483	284	55721
P26641	Elongation factor 1-gamma	68/437	245	50087
P32969	60S ribosomal protein L9	51/192	239	21850
P02545	Prelamin-A/C	126/664	238	74095
P62805	Histone H4	37/103	220	11360
Q16181	Septin-7	118/437	211	50648
P02081	*Hemoglobin fetal subunit beta (Bos taurus)*	*69/145*	*200*	*15849*
P50402	Emerin	88/254	178	28976
P09874	Poly [ADP-ribose] polymerase 1	89/1014	168	113012
P60709	Actin, cytoplasmic 1	58/375	167	41710
P62241	40S ribosomal protein S8	44/208	163	24190
P62917	60S ribosomal protein L8	34/257	152	28007
P62424	60S ribosomal protein L7a	33/266	135	29977
P62081	40S ribosomal protein S7	70/194	135	22113
Q07020	60S ribosomal protein L18	37/188	135	21621
P11142	Heat shock cognate 71 kDa protein	90/646	133	70854
Q02543	60S ribosomal protein L18a	17/176	133	20749
P62899	60S ribosomal protein L31	23/125	131	14454
P11940	Polyadenylate-binding protein 1	68/636	128	70626
P05141	ADP/ATP translocase 2	41/298	115	32831
P46781	40S ribosomal protein S9	25/194	115	22578
P62807	Histone H2B type 1-C/E/F/G/I	39/126	113	13944
P39019	40S ribosomal protein S19	19/145	107	16051
P08865	40S ribosomal protein SA	38/295	105	32833

ID	Name	# vs. total	Score	Mw (Da)
P62701	40S ribosomal protein S4, X isoform	29/263	98	29579
P68363	Tubulin alpha-1B chain	37/451	95	50120
P60866	40S ribosomal protein S20	11/119	93	13364
P68104	Elongation factor 1-alpha 1	35/462	92	50109
P67809	Nuclease-sensitive element-binding protein 1	19/324	92	35903
P61026	Ras-related protein Rab-10	33/200	92	22527
O75531	Barrier-to-autointegration factor	43/89	91	10052
P04908	Histone H2A type 1-B/E	35/130	87	14127
Q13283	Ras GTPase-activating protein-binding protein 1	37/466	86	52132
P22626	Heterogeneous nuclear ribonucleoproteins A2/B1	10/353	86	37407
P63010	AP-2 complex subunit beta	25/937	85	104486
P04792	Heat shock protein beta-1	19/205	85	22768
P62847	40S ribosomal protein S24	12/133	85	15413
P61353	60S ribosomal protein L27	17/136	84	15788
P02769	*Serum albumin (Bos taurus)*	*14/607*	*83*	*69248*
P46776	60S ribosomal protein L27a	11/148	82	16551
P62753	40S ribosomal protein S6	20/249	80	28663
P19338	Nucleolin	30/710	79	76568
P09651	Heterogeneous nuclear ribonucleoprotein A1	26/372	78	38723
P18124	60S ribosomal protein L7	31/248	78	29207
P62269	40S ribosomal protein S18	40/152	77	17708
Q6NXT2	Histone H3.3C	7/135	77	15204
P39023	60S ribosomal protein L3	27/403	75	46080
Q8NC56	LEM domain-containing protein 2	24/503	74	56940
P62277	40S ribosomal protein S13	44/151	73	17212
P49448	Glutamate dehydrogenase 2, mitochondrial	45/558	72	91395
P24534	Elongation factor 1-beta	35/225	71	24748
P18621	60S ribosomal protein L17	16/184	71	21383
P62249	40S ribosomal protein S16	10/146	71	16435
P15880	40S ribosomal protein S2	19/293	70	31305
Q13885	Tubulin beta-2A chain	18/445	69	49875
P50914	60S ribosomal protein L14	12/215	66	23417
Q14444	Caprin-1	34/709	65	78318
Q9UBS4	DnaJ homolog subfamily B member 11	19/358	65	40489
P62244	40S ribosomal protein S15a	17/130	65	14830
P05386	60S acidic ribosomal protein P1	16/114	65	11507
P17844	Probable ATP-dependent RNA helicase DDX5	23/614	64	69105
Q9HCE1	Helicase MOV-10	20/1003	62	113599
P35030	Trypsin-3	13/304	60	32508
P23396	40S ribosomal protein S3	39/243	60	26671
P46783	40S ribosomal protein S10	24/165	59	18886
P46779	60S ribosomal protein L28	11/137	59	15738
Q15233	Non-POU domain-containing octamer-binding protein	8/471	58	54197

ID	Name	# vs. total	Score	Mw (Da)
P01966	*Hemoglobin subunit alpha (Bos taurus)*	*27/142*	*58*	*15175*
P41361	*Antithrombin-III (Bos taurus)*	*13/465*	*56*	*52314*
P36578	60S ribosomal protein L4	23/427	56	47667
O95782	AP-2 complex subunit alpha-1	10/977	55	107478
P26373	60S ribosomal protein L13	24/211	55	24247
P60842	Eukaryotic initiation factor 4A-I	21/406	53	46125
P62906	60S ribosomal protein L10a	20/217	52	24816
P62851	40S ribosomal protein S25	28/125	52	13734
Q2KIL1	Uncharacterized protein C1orf141 homolog	7/430	51	49689
P26599	Polypyrimidine tract-binding protein 1	23/531	49	57186
Q99986	Serine/threonine-protein kinase VRK1	70/396	49	45447
P05387	60S acidic ribosomal protein P2	12/115	49	11658
P22492	Histone H1t	11/207	48	22006
Q3ZBS7	*Vitronectin (Bos taurus)*	*15/484*	*47*	*54065*
P09496	Clathrin light chain A	9/248	47	27060
P15170	Eukaryotic peptide chain release factor GTP-binding subunit ERF3A	8/499	45	55720
P38405	Guanine nucleotide-binding protein G(olf) subunit alpha	11/381	45	44280
Q9UN81	LINE-1 retrotransposable element ORF1 protein	13/338	45	40031
Q02241	Kinesin-like protein KIF23	18/960	44	109990
P83111	Serine beta-lactamase-like protein LACTB, mitochondrial	7/547	44	60655
P51114	Fragile X mental retardation syndrome-related protein 1	8/621	43	69678
Q00325	Phosphate carrier protein, mitochondrial	9/362	43	40069
Q29RV1	*Protein disulfide-isomerase A4 (Bos taurus)*	*8/643*	*42*	*72481*
Q8N554	Zinc finger protein 276	7/614	42	67176
P62873	Guanine nucleotide-binding protein G(I)/G(S)/G(T) subunit beta-1	10/340	42	37353
Q16698	2,4-dienoyl-CoA reductase, mitochondrial	10/335	42	36045
P35268	60S ribosomal protein L22	11/128	42	14778
Q8TF72	Protein Shroom3	9/1996	41	216724
P13010	X-ray repair cross-complementing protein 5	10/732	41	82652
P63244	Receptor of activated protein C kinase 1	11/317	41	35055
Q96M66	Putative uncharacterized protein FLJ32790	12/194	41	20680
P17096	High mobility group protein HMG-I/HMG-Y	24/107	41	11669
Q9Y2K5	R3H domain-containing protein 2	20/976	40	106932
O15347	High mobility group protein B3	13/200	40	22965

Table S7.2. The protein identification number (ID), name, recovered number of residues with respect to total chain length (# vs. total), MASCOT score (Score), and molecular weight (Mw) in Da of the identified proteins in the hard protein corona formed in J774 cells. Bovine proteins are marked with italic font. The identified peptides, their charge, and their m/z values are not shown here.

ID	Name	# vs. total	Score	Mw (Da)
P20152	Vimentin	157/466	470	53655
P60710	Actin, cytoplasmic 1	76/375	269	41710
C0HKE1	Histone H2A type 1-B	71/130	269	14127
P62806	Histone H4	63/103	228	11360
Q64475	Histone H2B type 1-B	40/126	124	13944
O88569	Heterogeneous nuclear ribonucleoproteins A2/B1	26/353	94	37380
P02301	Histone H3.3C	16/136	61	15306
P15864	Histone H1.2	32/212	58	21254
Q8CFK6	DENN domain-containing protein 1C	19/786	57	86635
Q8VDG6	Mitogen-activated protein kinase kinase kinase 21	7/1002	47	110042
P01966	*Hemoglobin subunit alpha (Bos taurus)*	*15/142*	*41*	*15175*

Table S9.1. The protein identification number (ID), name, recovered number of residues with respect to total chain length (# vs. total), MASCOT score (Score), and molecular weight (Mw) in Da of the identified proteins in the hard protein corona formed in HCT-116 cells. Bovine proteins are marked with italic font. The identified peptides, their charge, and their m/z values are not shown here.

ID	Name	# vs. total	Score	Mw (Da)
Q9UHD8	Septin-9	218/586	1164	65361
E1BNR0	*Similar to apolipoprotein B, partial (Bos taurus)*	*486/3618*	*899*	*409608*
Q9NVA2	Septin-11	148/429	835	48961
Q02878	60S ribosomal protein L6	112/288	769	32708
P07355	Annexin A2	137/339	683	38580
P42166	Lamina-associated polypeptide 2, isoform alpha	304/694	664	75446
P46781	40S ribosomal protein S9	78/194	662	22578
Q09666	Neuroblast differentiation-associated protein AHNAK	249/5890	559	628699
Q00610	Clathrin heavy chain 1	256/1675	539	191493
P51114	Fragile X mental retardation syndrome-related protein 1	170/621	517	69678
P15311	Ezrin	195/586	503	69370
P61247	40S ribosomal protein S3a	93/264	483	29926
P62701	40S ribosomal protein S4, X isoform	89/263	473	29579
Q96CN7	Isochorismatase domain-containing protein 1	115/298	460	32216
Q8NC51	Plasminogen activator inhibitor 1 RNA-binding protein	93/408	455	44938
P13010	X-ray repair cross-complementing protein 5	196/732	434	82652
P15880	40S ribosomal protein S2	88/293	433	31305
P46783	40S ribosomal protein S10	69/165	418	18886
P11940	Polyadenylate-binding protein 1	206/636	413	70626
P40227	T-complex protein 1 subunit zeta	110/531	388	57988
P12956	X-ray repair cross-complementing protein 6	196/609	359	69799
P21796	Voltage-dependent anion-selective channel protein 1	133/283	359	30754
P68104	Elongation factor 1-alpha 1	98/462	356	50109
Q7KZF4	Staphylococcal nuclease domain-containing protein 1	179/910	354	101934
P50990	T-complex protein 1 subunit theta	125/548	350	59583
Q13765	Nascent polypeptide-associated complex subunit alpha	70/215	347	23370
P63241	Eukaryotic translation initiation factor 5A-1	44/154	344	16821
P11142	Heat shock cognate 71 kDa protein	159/646	340	70854
P02545	Prelamin-A/C	206/664	338	74095
P05388	60S acidic ribosomal protein P0	110/317	334	34252
P78371	T-complex protein 1 subunit beta	158/535	331	57452
Q13283	Ras GTPase-activating protein-binding protein 1	181/466	328	52132
P62424	60S ribosomal protein L7a	69/266	316	29977
P08865	40S ribosomal protein SA	129/295	310	32833
P06748	Nucleophosmin	85/294	310	32555

ID	Name	# vs. total	Score	Mw (Da)
P61978	Heterogeneous nuclear ribonucleoprotein K	130/463	308	50944
P23396	40S ribosomal protein S3	120/243	295	26671
P62753	40S ribosomal protein S6	53/249	289	28663
P26599	Polypyrimidine tract-binding protein 1	120/531	288	57186
P63244	Receptor of activated protein C kinase 1	88/317	287	35055
P32969	60S ribosomal protein L9	94/192	287	21850
P05198	Eukaryotic translation initiation factor 2 subunit 1	84/315	286	36089
P46777	60S ribosomal protein L5	75/297	283	34341
P62841	40S ribosomal protein S15	53/145	280	17029
Q13347	Eukaryotic translation initiation factor 3 subunit I	59/325	272	36479
P02081	*Hemoglobin fetal subunit beta (Bos taurus)*	*63/145*	*270*	*15849*
Q9UBS4	DnaJ homolog subfamily B member 11	114/358	268	40489
P62081	40S ribosomal protein S7	70/194	267	22113
Q14444	Caprin-1	99/709	266	78318
P47914	60S ribosomal protein L29	23/159	264	17741
P62249	40S ribosomal protein S16	52/146	264	16435
P62269	40S ribosomal protein S18	73/152	262	17708
P05387	60S acidic ribosomal protein P2	55/115	256	11658
Q9NVI7	ATPase family AAA domain-containing protein 3A	69/634	255	71325
P00367	Glutamate dehydrogenase 1, mitochondrial	161/558	255	61359
P60842	Eukaryotic initiation factor 4A-I	157/406	253	46125
P19338	Nucleolin	160/710	249	76568
P39019	40S ribosomal protein S19	53/145	246	16051
P46782	40S ribosomal protein S5	66/204	243	22862
O60506	Heterogeneous nuclear ribonucleoprotein Q	101/623	241	69560
P48643	T-complex protein 1 subunit epsilon	61/541	240	59633
Q04637	Eukaryotic translation initiation factor 4 gamma 1	128/1599	236	175382
P36578	60S ribosomal protein L4	71/427	234	47667
P17987	T-complex protein 1 subunit alpha	106/556	230	60306
P12532	Creatine kinase U-type, mitochondrial	88/417	228	47007
Q12905	Interleukin enhancer-binding factor 2	94/390	227	43035
P62750	60S ribosomal protein L23a	47/156	227	17684
O00425	Insulin-like growth factor 2 mRNA-binding protein 3	96/576	224	63666
O15479	Melanoma-associated antigen B2	80/319	224	35255
P18124	60S ribosomal protein L7	75/248	221	29207
P78527	DNA-dependent protein kinase catalytic subunit	162/4128	215	468788
P26373	60S ribosomal protein L13	67/211	213	24247
Q15149	Plectin	204/4684	212	531466
Q02543	60S ribosomal protein L18a	17/176	212	20749
Q99832	T-complex protein 1 subunit eta	107/543	211	59329
P27694	Replication protein A 70 kDa DNA-binding subunit	133/616	209	68095
P62263	40S ribosomal protein S14	55/151	209	16263
Q16698	2,4-dienoyl-CoA reductase, mitochondrial	81/335	203	36045

ID	Name	# vs. total	Score	Mw (Da)
Q9Y262	Eukaryotic translation initiation factor 3 subunit L	88/564	201	66684
O75489	NADH dehydrogenase [ubiquinone] iron-sulfur protein 3, mitochondrial	39/264	200	30223
P49368	T-complex protein 1 subunit gamma	56/545	199	60495
P61313	60S ribosomal protein L15	49/204	199	24131
P50991	T-complex protein 1 subunit delta	123/539	198	57888
P31943	Heterogeneous nuclear ribonucleoprotein H	59/449	198	49198
Q00688	Peptidyl-prolyl cis-trans isomerase FKBP3	62/224	198	25161
P22626	Heterogeneous nuclear ribonucleoproteins A2/B1	92/353	196	37407
P67809	Nuclease-sensitive element-binding protein 1	70/324	192	35903
Q14152	Eukaryotic translation initiation factor 3 subunit A	111/1382	191	166468
O00571	ATP-dependent RNA helicase DDX3X	101/662	190	73198
P09651	Heterogeneous nuclear ribonucleoprotein A1	70/372	189	38723
P60228	Eukaryotic translation initiation factor 3 subunit E	79/445	188	52187
P62851	40S ribosomal protein S25	35/125	183	13734
P62241	40S ribosomal protein S8	68/208	179	24190
Q14694	Ubiquitin carboxyl-terminal hydrolase 10	82/798	177	87080
P09874	Poly [ADP-ribose] polymerase 1	93/1014	172	113012
Q9BXJ9	N-alpha-acetyltransferase 15, NatA auxiliary subunit	78/866	171	101208
O00303	Eukaryotic translation initiation factor 3 subunit F	86/357	170	37540
O60841	Eukaryotic translation initiation factor 5B	115/1220	166	138742
P83731	60S ribosomal protein L24	45/157	166	17768
P04843	Dolichyl-diphosphooligosaccharide--protein glycosyltransferase subunit 1	82/607	165	68527
Q99623	Prohibitin-2	77/299	163	33276
P50914	60S ribosomal protein L14	24/215	163	23417
P62244	40S ribosomal protein S15a	49/130	162	14830
P45880	Voltage-dependent anion-selective channel protein 2	74/294	159	31547
P62899	60S ribosomal protein L31	42/125	159	14454
Q99613	Eukaryotic translation initiation factor 3 subunit C	69/913	158	105278
P60709	Actin, cytoplasmic 1	69/375	156	41710
Q07020	60S ribosomal protein L18	37/188	155	21621
Q15717	ELAV-like protein 1	45/326	154	36069
Q92945	Far upstream element-binding protein 2	112/711	152	73070
Q9UQ80	Proliferation-associated protein 2G4	72/394	152	43759
Q9Y295	Developmentally-regulated GTP-binding protein 1	51/367	152	40517
Q99988	Growth/differentiation factor 15	61/308	152	34119
P62913	60S ribosomal protein L11	52/178	151	20240
P62807	Histone H2B type 1-C/E/F/G/I	39/126	149	13898
P39023	60S ribosomal protein L3	89/403	148	46080
P18621	60S ribosomal protein L17	49/184	147	21383
Q00839	Heterogeneous nuclear ribonucleoprotein U	72/825	146	90528
P62906	60S ribosomal protein L10a	62/217	146	24816
P04908	Histone H2A type 1-B/E	71/130	145	14127

ID	Name	# vs. total	Score	Mw (Da)
Q16181	Septin-7	79/437	144	50648
P63220	40S ribosomal protein S21	24/83	144	9106
P62857	40S ribosomal protein S28	21/69	143	7836
P62917	60S ribosomal protein L8	34/257	140	28007
P23284	Peptidyl-prolyl cis-trans isomerase B	73/216	139	23728
P61353	60S ribosomal protein L27	36/136	136	15788
P62873	Guanine nucleotide-binding protein G(I)/G(S)/G(T) subunit beta-1	21/340	135	37353
Q96AG4	Leucine-rich repeat-containing protein 59	68/307	134	34909
Q9UN86	Ras GTPase-activating protein-binding protein 2	39/482	131	54088
P62805	Histone H4	44/103	131	11360
P26368	Splicing factor U2AF 65 kDa subunit	39/475	130	53467
P04844	Dolichyl-diphosphooligosaccharide--protein glycosyltransferase subunit 2	67/631	123	69241
P41091	Eukaryotic translation initiation factor 2 subunit 3	94/472	123	51077
P62280	40S ribosomal protein S11	19/158	122	18419
P40429	60S ribosomal protein L13a	26/203	121	23562
Q96HS1	Serine/threonine-protein phosphatase PGAM5, mitochondrial	26/289	120	31985
Q92499	ATP-dependent RNA helicase DDX1	58/740	119	82380
P46779	60S ribosomal protein L28	18/137	116	15738
Q9P0L0	Vesicle-associated membrane protein-associated protein A	42/249	115	27875
P17844	Probable ATP-dependent RNA helicase DDX5	67/614	113	69105
P68363	Tubulin alpha-1B chain	48/451	113	50120
P41227	N-alpha-acetyltransferase 10	51/235	112	26442
Q08211	ATP-dependent RNA helicase A	70/1270	107	140869
P30419	Glycylpeptide N-tetradecanoyltransferase 1	40/496	107	56770
P20042	Eukaryotic translation initiation factor 2 subunit 2	54/333	106	38364
P62847	40S ribosomal protein S24	27/133	106	15413
P37108	Signal recognition particle 14 kDa protein	22/136	106	14561
P39656	Dolichyl-diphosphooligosaccharide--protein glycosyltransferase 48 kDa subunit	33/456	105	50769
P07437	Tubulin beta chain	30/444	105	49639
P22695	Cytochrome b-c1 complex subunit 2, mitochondrial	52/453	105	48413
P29692	Elongation factor 1-delta	70/281	105	31103
P62277	40S ribosomal protein S13	45/151	105	17212
Q16795	NADH dehydrogenase [ubiquinone] 1 alpha subcomplex subunit 9, mitochondrial	61/377	104	42483
P63173	60S ribosomal protein L38	22/70	104	8213
Q3ZBS7	*Vitronectin (Bos taurus)*	*27/484*	*100*	*54065*
P32322	Pyrroline-5-carboxylate reductase 1, mitochondrial	45/319	100	33340
Q9NSD9	Phenylalanine-tRNA ligase beta subunit	56/589	96	66074
P55884	Eukaryotic translation initiation factor 3 subunit B	61/814	95	92424
O75531	Barrier-to-autointegration factor	43/89	95	10052
Q14157	Ubiquitin-associated protein 2-like	132/1087	94	114465

ID	Name	# vs. total	Score	Mw (Da)
Q9UG63	ATP-binding cassette sub-family F member 2	55/623	94	71245
Q07955	Serine/arginine-rich splicing factor 1	27/248	93	27728
Q01130	Serine/arginine-rich splicing factor 2	15/221	93	25461
P35268	60S ribosomal protein L22	24/128	92	14778
O75821	Eukaryotic translation initiation factor 3 subunit G	22/320	91	35589
O15371	Eukaryotic translation initiation factor 3 subunit D	33/548	90	63932
P30050	60S ribosomal protein L12	24/165	90	17808
O75477	Erlin-1	24/346	89	38901
P61026	Ras-related protein Rab-10	22/200	89	22527
Q7L2E3	ATP-dependent RNA helicase DHX30	30/1194	87	133854
P09471	Guanine nucleotide-binding protein G(o) subunit alpha	23/354	87	40025
P35232	Prohibitin	88/272	87	29786
Q9Y3U8	60S ribosomal protein L36	20/105	87	12246
Q92900	Regulator of nonsense transcripts 1	50/1129	86	124267
P26641	Elongation factor 1-gamma	47/437	86	50087
P07910	Heterogeneous nuclear ribonucleoproteins C1/C2	21/306	86	33650
P24534	Elongation factor 1-beta	35/225	86	24748
P16403	Histone H1.2	41/213	86	21352
Q8WU90	Zinc finger CCCH domain-containing protein 15	24/426	85	48573
Q9HCN8	Stromal cell-derived factor 2-like protein 1	74/221	85	23584
P62854	40S ribosomal protein S26	31/115	85	13007
P62273	40S ribosomal protein S29	11/56	85	6672
Q9NQW6	Anillin	91/1124	84	124122
P51659	Peroxisomal multifunctional enzyme type 2	49/736	84	79636
P61513	60S ribosomal protein L37a	18/92	82	10268
P42766	60S ribosomal protein L35	10/123	81	14543
Q12931	Heat shock protein 75 kDa, mitochondrial	14/704	79	80060
Q07021	Complement component 1 Q subcomponent-binding protein, mitochondrial	41/282	77	31343
P20674	Cytochrome c oxidase subunit 5A, mitochondrial	24/150	77	16752
Q96N67	Dedicator of cytokinesis protein 7	58/2140	76	242407
P01966	*Hemoglobin subunit alpha (Bos taurus)*	*36/142*	*76*	*15175*
Q99470	Stromal cell-derived factor 2	24/211	75	23011
P46776	60S ribosomal protein L27a	11/148	75	16551
P20290	Transcription factor BTF3	44/206	74	22154
P60866	40S ribosomal protein S20	23/119	74	13364
Q9GZZ1	N-alpha-acetyltransferase 50	9/169	73	19386
P27635	60S ribosomal protein L10	24/214	72	24588
P12236	ADP/ATP translocase 3	45/298	71	32845
P00403	Cytochrome c oxidase subunit 2	33/227	71	25548
P46778	60S ribosomal protein L21	15/160	71	18553
P14406	Cytochrome c oxidase subunit 7A2, mitochondrial	23/83	71	9390
P47985	Cytochrome b-c1 complex subunit Rieske, mitochondrial	15/274	69	29649

ID	Name	# vs. total	Score	Mw (Da)
P83881	60S ribosomal protein L36a	16/106	69	12433
Q9Y224	RNA transcription, translation and transport factor protein	24/244	68	28051
P35244	Replication protein A 14 kDa subunit	27/121	67	13560
O95782	AP-2 complex subunit alpha-1	19/977	66	107478
P35637	RNA-binding protein FUS	25/526	66	53394
P08708	40S ribosomal protein S17	43/135	66	15540
P19525	Interferon-induced, double-stranded RNA-activated protein kinase	12/551	65	62056
P31930	Cytochrome b-c1 complex subunit 1, mitochondrial	61/480	65	52612
Q14103	Heterogeneous nuclear ribonucleoprotein D0	34/355	65	38410
P84098	60S ribosomal protein L19	26/196	65	23451
Q15233	Non-POU domain-containing octamer-binding protein	31/471	64	54197
P04792	Heat shock protein beta-1	10/205	64	22768
Q86V81	THO complex subunit 4	37/257	63	26872
P00403	Cytochrome c oxidase subunit 2	53/227	63	25548
Q9UH03	Neuronal-specific septin-3	19/358	62	40678
O95816	BAG family molecular chaperone regulator 2	20/211	62	23757
O60869	Endothelial differentiation-related factor 1	15/148	62	16359
P06730	Eukaryotic translation initiation factor 4E	14/217	61	25082
Q15365	Poly(rC)-binding protein 1	21/356	60	37474
Q96FQ6	Protein S100-A16	11/103	60	11794
P51116	Fragile X mental retardation syndrome-related protein 2	36/673	59	74178
Q9Y285	Phenylalanine--tRNA ligase alpha subunit	15/508	59	57528
Q9H3Q1	Cdc42 effector protein 4	19/356	59	37957
P49207	60S ribosomal protein L34	16/117	59	13284
Q9P258	Protein RCC2	15/522	58	56049
Q9HAN9	Nicotinamide/nicotinic acid mononucleotide adenylyltransferase 1	48/279	58	31913
P09496	Clathrin light chain A	9/248	58	27060
P42677	40S ribosomal protein S27	12/84	58	9455
Q9Y5B9	FACT complex subunit SPT16	11/1047	57	119838
O96008	Mitochondrial import receptor subunit TOM40 homolog	17/361	57	37869
Q6NXT2	Histone H3.3C	7/135	57	15204
P81605	Dermcidin	22/110	57	11277
Q08170	Serine/arginine-rich splicing factor 4	9/494	56	56645
P62888	60S ribosomal protein L30	19/115	56	12776
O96000	NADH dehydrogenase [ubiquinone] 1 beta subcomplex subunit 10	24/172	55	20763
P62266	40S ribosomal protein S23	11/143	55	15798
Q6PKG0	La-related protein 1	8/1096	54	123434
Q07065	Cytoskeleton-associated protein 4	62/602	54	65983
P31689	DnaJ homolog subfamily A member 1	44/397	54	44839
Q8TD26	Chromodomain-helicase-DNA-binding protein 6	11/2715	53	305220

ID	Name	# vs. total	Score	Mw (Da)
P28288	ATP-binding cassette sub-family D member 3	49/659	53	75428
P40222	Alpha-taxilin	18/546	53	61853
O14979	Heterogeneous nuclear ribonucleoprotein D-like	24/420	53	46409
P26196	Probable ATP-dependent RNA helicase DDX6	44/483	52	54382
Q15019	Septin-2	18/361	52	41461
Q12906	Interleukin enhancer-binding factor 3	23/894	51	95279
Q8NI51	Transcriptional repressor CTCFL	7/663	50	75698
Q15366	Poly(rC)-binding protein 2	22/365	50	38556
P04406	Glyceraldehyde-3-phosphate dehydrogenase	50/335	50	36030
P51571	Translocon-associated protein subunit delta	30/173	50	18987
P38646	Stress-70 protein, mitochondrial	12/679	49	73635
Q9UHB9	Signal recognition particle subunit SRP68	22/627	49	70686
P26583	High mobility group protein B2	13/209	49	24019
Q04837	Single-stranded DNA-binding protein, mitochondrial	23/148	49	17249
P47813	Eukaryotic translation initiation factor 1A, X-chromosomal	17/144	49	16450
P60468	Protein transport protein Sec61 subunit beta	10/96	49	9968
O14880	Microsomal glutathione S-transferase 3	27/152	48	16506
P62829	60S ribosomal protein L23	10/140	48	14856
P10809	60 kDa heat shock protein, mitochondrial	9/573	47	61016
P55010	Eukaryotic translation initiation factor 5	19/431	47	49192
Q09161	Nuclear cap-binding protein subunit 1	12/790	46	91781
P49902	Cytosolic purine 5'-nucleotidase	7/561	46	64928
Q5JU67	Cilia- and flagella-associated protein 157	12/520	46	60496
O00515	Ladinin-1	7/517	46	57097
Q12824	SWI/SNF-related matrix-associated actin-dependent regulator of chromatin subfamily B member 1	7/385	46	44113
P31946	14-3-3 protein beta/alpha	10/246	46	28065
P84103	Serine/arginine-rich splicing factor 3	8/164	46	19318
P25398	40S ribosomal protein S12	10/132	46	14505
Q5VT25	Serine/threonine-protein kinase MRCK alpha	7/1732	45	197182
P15170	Eukaryotic peptide chain release factor GTP-binding subunit ERF3A	8/499	45	55720
Q9NX58	Cell growth-regulating nucleolar protein	25/379	45	43588
Q8NGZ3	Olfactory receptor 13G1	7/307	45	34649
P61254	60S ribosomal protein L26	23/145	45	17248
P49458	Signal recognition particle 9 kDa protein	8/86	45	10105
Q8TF72	Protein Shroom3	9/1996	44	216724
Q7Z7K6	Centromere protein V	13/275	44	29927
P50402	Emerin	33/254	44	28976
E9PRG8	Uncharacterized protein C11orf98	13/122	44	13790
Q6ZSZ5	Rho guanine nucleotide exchange factor 18	10/1361	43	151549
P28331	NADH-ubiquinone oxidoreductase 75 kDa subunit, mitochondrial	27/727	43	79417
Q9NVA2	Septin-11	24/429	43	49367

ID	Name	# vs. total	Score	Mw (Da)
Q9UJZ1	Stomatin-like protein 2, mitochondrial	25/356	43	38510
P09669	Cytochrome c oxidase subunit 6C	8/75	43	8776
P78344	Eukaryotic translation initiation factor 4 gamma 2	11/907	42	102297
Q8TCS8	Polyribonucleotide nucleotidyltransferase 1, mitochondrial	8/783	42	85897
O76094	Signal recognition particle subunit SRP72	21/671	42	74560
P49821	NADH dehydrogenase [ubiquinone] flavoprotein 1, mitochondrial	10/464	42	50785
P19404	NADH dehydrogenase [ubiquinone] flavoprotein 2, mitochondrial	10/249	42	27374
Q9UBQ5	Eukaryotic translation initiation factor 3 subunit K	32/218	42	25043
P61927	60S ribosomal protein L37	9/97	42	11071
Q86YZ3	Hornerin	16/2850	41	282228
Q9UKX3	Myosin-13	19/1938	41	223465
Q8IV33	Uncharacterized protein KIAA0825	8/1275	41	147640
Q13724	Mannosyl-oligosaccharide glucosidase	12/837	41	91861
P23246	Splicing factor, proline- and glutamine-rich	31/707	41	76102
P08574	Cytochrome c1, heme protein, mitochondrial	11/325	41	35399
P43307	Translocon-associated protein subunit alpha	23/286	41	32215
B2RXH8	Heterogeneous nuclear ribonucleoprotein C-like 1	8/293	41	32053
Q13151	Heterogeneous nuclear ribonucleoprotein A0	36/305	41	30822
P15531	Nucleoside diphosphate kinase A	12/152	41	17138
P62495	Eukaryotic peptide chain release factor subunit 1	27/437	40	49000

Table S9.2. The protein identification number (ID), name, recovered number of residues with respect to total chain length (# vs. total), MASCOT score (Score), and molecular weight (Mw) in Da of the identified proteins in the hard protein corona formed in A549 cells. Bovine proteins are marked with italic font. The identified peptides, their charge, and their m/z values are not shown here.

ID	Name	# vs. total	Score	Mw (Da)
P08670	Vimentin	245/466	678	53619
P48594	Serpin B4	143/390	342	44825
P31947	14-3-3 protein sigma	47/248	256	27757
P06702	Protein S100-A9	51/114	221	13234
P62807	Histone H2B type 1-C/E/F/G/I	33/126	214	13898
P29508	Serpin B3	115/390	204	44537
P33778	Histone H2B type 1-B	33/126	193	13942
P60709	Actin, cytoplasmic 1	87/375	188	41710
Q9NZT1	Calmodulin-like protein 5	82/146	185	15883
P04908	Histone H2A type 1-B/E	35/130	157	14127
P47929	Galectin-7	60/136	141	15066
P02545	Prelamin-A/C	74/664	140	74095
P10599	Thioredoxin	13/105	110	11730
Q01469	Fatty acid-binding protein 5	9/135	108	15155
Q13501	Sequestosome-1	29/440	93	47657
P05109	Protein S100-A8	18/93	77	10828
P68104	Elongation factor 1-alpha 1	47/462	73	50109
P62937	Peptidyl-prolyl cis-trans isomerase A	27/165	71	18001
P01859	Immunoglobulin heavy constant gamma 2	16/326	70	35878
Q96QV6	Histone H2A type 1-A	39/131	70	14225
Q13885	Tubulin beta-2A chain	18/445	67	49875
P01966	*Hemoglobin subunit alpha (Bos taurus)*	*36/142*	*66*	*15175*
P62805	Histone H4	30/103	65	11360
P62979	Ubiquitin-40S ribosomal protein S27a	16/156	64	17953
P0DP23	Calmodulin-1	8/149	64	16827
P68431	Histone H3.1	14/136	63	15394
P04792	Heat shock protein beta-1	62/205	62	22768
P68363	Tubulin alpha-1B chain	23/451	60	50120
P06733	Alpha-enolase	46/434	59	47139
Q3ZBS7	*Vitronectin (Bos taurus)*	*27/484*	*57*	*54065*
P04406	Glyceraldehyde-3-phosphate dehydrogenase	14/335	57	36030
Q71UI9	Histone H2A.V	19/128	57	13501
Q96A08	Histone H2B type 1-A	7/127	56	14159
P11142	Heat shock cognate 71 kDa protein	37/646	55	70854
P07355	Annexin A2	26/339	55	38580
P00338	L-lactate dehydrogenase A chain	34/332	54	36665
P31949	Protein S100-A11	9/105	51	11733
Q15233	Non-POU domain-containing octamer-binding protein	8/471	46	54197

ID	Name	# vs. total	Score	Mw (Da)
Q53RT3	Retroviral-like aspartic protease 1	13/343	46	36968
P62277	40S ribosomal protein S13	7/151	46	17212
Q7RTR8	Taste receptor type 2 member 42	7/314	45	36171
P29762	Cellular retinoic acid-binding protein 1	7/137	45	15556
P31151	Protein S100-A7	30/101	45	11464
P0DOY2	Immunoglobulin lambda constant 2	25/106	45	11287
P05387	60S acidic ribosomal protein P2	12/115	44	11658
P13639	Elongation factor 2	11/858	43	95277
Q8TF72	Protein Shroom3	9/1996	42	216724
P14923	Junction plakoglobin	18/745	42	81693
P05121	Plasminogen activator inhibitor 1	10/402	42	45031
P22626	Heterogeneous nuclear ribonucleoproteins A2/B1	10/353	41	37407
O75531	Barrier-to-autointegration factor	36/89	41	10052
P04083	Annexin A1	15/346	40	38690
P31944	Caspase-14	11/242	40	27662
P23528	Cofilin-1	11/166	40	18491

Bibliography

[1] M. Bundschuh, J. Filser, S. Luderwald, M.S. McKee, G. Metreveli, G.E. Schaumann, R. Schulz, S. Wagner, *Nanoparticles in the environment: where do we come from, where do we go to?*, Environ. Sci. Eur. 30(1) (2018) 6.

[2] C. Buzea, I.I. Pacheco, K. Robbie, *Nanomaterials and nanoparticles: Sources and toxicity*, Biointerphases 2(4) (2007) MR17-MR71.

[3] L.A. DeLouise, *Applications of nanotechnology in dermatology*, J. Invest. Dermatol. 132(3 Pt 2) (2012) 964-75.

[4] P.R. Lockman, R.J. Mumper, M.A. Khan, D.D. Allen, *Nanoparticle technology for drug delivery across the blood-brain barrier*, Drug. Dev. Ind. Pharm. 28(1) (2002) 1-13.

[5] X. Qian, X.H. Peng, D.O. Ansari, Q. Yin-Goen, G.Z. Chen, D.M. Shin, L. Yang, A.N. Young, M.D. Wang, S. Nie, *In vivo tumor targeting and spectroscopic detection with surface-enhanced Raman nanoparticle tags*, Nat. Biotechnol. 26(1) (2008) 83-90.

[6] S. Wohlfart, S. Gelperina, J. Kreuter, *Transport of drugs across the blood-brain barrier by nanoparticles*, J. Control. Release 161(2) (2012) 264-73.

[7] Y. Zhang, X. Zhan, J. Xiong, S. Peng, W. Huang, R. Joshi, Y. Cai, Y. Liu, R. Li, K. Yuan, N. Zhou, W. Min, *Temperature-dependent cell death patterns induced by functionalized gold nanoparticle photothermal therapy in melanoma cells*, Sci. Rep. 8(1) (2018) 8720.

[8] K. Yang, L. Hu, X. Ma, S. Ye, L. Cheng, X. Shi, C. Li, Y. Li, Z. Liu, *Multimodal imaging guided photothermal therapy using functionalized graphene nanosheets anchored with magnetic nanoparticles*, Adv. Mater. 24(14) (2012) 1868-72.

[9] P.L. Gourley, J.K. Hendricks, A.E. McDonald, R.G. Copeland, K.E. Barrett, C.R. Gourley, K.K. Singh, R.K. Naviaux, *Mitochondrial correlation microscopy and nanolaser spectroscopy - new tools for biophotonic detection of cancer in single cells*, Technol. Cancer. Res. Treat. 4(6) (2005) 585-92.

[10] Y.P. Bao, T.F. Wei, P.A. Lefebvre, H. An, L. He, G.T. Kunkel, U.R. Muller, *Detection of protein analytes via nanoparticle-based bio bar code technology*, Anal. Chem. 78(6) (2006) 2055-9.

[11] Z. Heiner, M. Guhlke, V. Zivanovic, F. Madzharova, J. Kneipp, *Surface-enhanced hyper Raman hyperspectral imaging and probing in animal cells*, Nanoscale 9(23) (2017) 8024-8032.

[12] M.P. Monopoli, C. Aberg, A. Salvati, K.A. Dawson, *Biomolecular coronas provide the biological identity of nanosized materials*, Nat. Nanotechnol. 7(12) (2012) 779-86.

[13] T. Cedervall, I. Lynch, S. Lindman, T. Berggard, E. Thulin, H. Nilsson, K.A. Dawson, S. Linse, *Understanding the nanoparticle-protein corona using methods to quantify exchange rates and affinities of proteins for nanoparticles*, Proc. Natl. Acad. Sci. U S A 104(7) (2007) 2050-5.

[14] P.C. Ke, S. Lin, W.J. Parak, T.P. Davis, F. Caruso, *A Decade of the Protein Corona*, ACS Nano 11(12) (2017) 11773-11776.

[15] V.P. Zhdanov, N.J. Cho, *Kinetics of the formation of a protein corona around nanoparticles*, Math. Biosci. 282 (2016) 82-90.

[16] P.A. Cuypers, G.M. Willems, H.C. Hemker, W.T. Hermens, *Adsorption kinetics of protein mixtures. A tentative explanation of the Vroman effect*, Ann. N. Y. Acad. Sci. 516 (1987) 244-52.

[17] L. Vroman, A.L. Adams, G.C. fischer, P.C. Munoz, *Interaction of high molecular weight kininogen, factor XII, and fibrinogen in plasma at interfaces*, Blood 55 (1980) 156-159.

[18] D. Docter, D. Westmeier, M. Markiewicz, S. Stolte, S.K. Knauer, R.H. Stauber, *The nanoparticle biomolecule corona: lessons learned - challenge accepted?*, Chem. Soc. Rev. 44(17) (2015) 6094-121.

[19] D. Walczyk, F.B. Bombelli, M.P. Monopoli, I. Lynch, K.A. Dawson, *What the Cell "Sees" in Bionanoscience*, J. Am. Chem. Soc. 132(16) (2010) 5761-5768.

[20] C.D. Walkey, W.C. Chan, *Understanding and controlling the interaction of nanomaterials with proteins in a physiological environment*, Chem. Soc. Rev. 41(7) (2012) 2780-99.

[21] M. Lundqvist, J. Stigler, T. Cedervall, T. Berggard, M.B. Flanagan, I. Lynch, G. Elia, K. Dawson, *The evolution of the protein corona around nanoparticles: a test study*, ACS Nano 5(9) (2011) 7503-9.

[22] D.H. Tsai, F.W. DelRio, A.M. Keene, K.M. Tyner, R.I. MacCuspie, T.J. Cho, M.R. Zachariah, V.A. Hackley, *Adsorption and conformation of serum albumin protein on gold nanoparticles investigated using dimensional measurements and in situ spectroscopic methods*, Langmuir 27(6) (2011) 2464-77.

[23] S. Dominguez-Medina, J. Blankenburg, J. Olson, C.F. Landes, S. Link, *Adsorption of a Protein Monolayer via Hydrophobic Interactions Prevents Nanoparticle Aggregation under Harsh Environmental Conditions*, ACS Sustain. Chem. Eng. 1(7) (2013) 833-842.

[24] A. Wang, Y.R. Perera, M.B. Davidson, N.C. Fitzkee, *Electrostatic Interactions and Protein Competition Reveal a Dynamic Surface in Gold Nanoparticle-Protein Adsorption*, J. Phys. Chem. C Nanomater. Interfaces 120(42) (2016) 24231-24239.

[25] S.H. Brewer, W.R. Glomm, M.C. Johnson, M.K. Knag, S. Franzen, *Probing BSA binding to citrate-coated gold nanoparticles and surfaces*, Langmuir 21(20) (2005) 9303-7.

[26] B. Fazio, C. D'Andrea, A. Foti, E. Messina, A. Irrera, M.G. Donato, V. Villari, N. Micali, O.M. Marago, P.G. Gucciardi, *SERS detection of biomolecules at physiological pH via aggregation of gold nanorods mediated by optical forces and plasmonic heating*, Sci. Rep. 6 (2016) 26952.

[27] X.X. Han, G.G. Huang, B. Zhao, Y. Ozaki, Label-Free *Highly Sensitive Detection of Proteins in Aqueous Solutions Using Surface-Enhanced Raman Scattering*, Anal. Chem. 81(9) (2009) 3329-3333.

[28] T. Brulé, A. Bouhelier, A. Dereux, E. Finot, *Discrimination between Single Protein Conformations Using Dynamic SERS*, ACS Sensors 1(6) (2016) 676-680.

[29] J.E. Clement, A. Leray, A. Bouhelier, E. Finot, *Spectral pointillism of enhanced Raman scattering for accessing structural and conformational information on single protein*, Phys. Chem. Chem. Phys. 19(1) (2016) 458-466.

[30] L.J. Xu, C. Zong, X.S. Zheng, P. Hu, J.M. Feng, B. Ren, *Label-free detection of native proteins by surface-enhanced Raman spectroscopy using iodide-modified nanoparticles*, Anal. Chem. 86(4) (2014) 2238-45.

[31] N. Fernandez-Iglesias, J. Bettmer, *Synthesis, purification and mass spectrometric characterisation of a fluorescent Au9@BSA nanocluster and its enzymatic digestion by trypsin*, Nanoscale 6(2) (2014) 716-21.

[32] S. Tenzer, D. Docter, J. Kuharev, A. Musyanovych, V. Fetz, R. Hecht, F. Schlenk, D. Fischer, K. Kiouptsi, C. Reinhardt, K. Landfester, H. Schild, M. Maskos, S.K. Knauer, R.H. *Stauber, Rapid formation of plasma protein corona critically affects nanoparticle pathophysiology*, Nat. Nanotechnol. 8(10) (2013) 772-81.

[33] C.D. Walkey, J.B. Olsen, H. Guo, A. Emili, W.C. Chan, *Nanoparticle size and surface chemistry determine serum protein adsorption and macrophage uptake*, J. Am. Chem. Soc. 134(4) (2012) 2139-47.

[34] R.R. Arvizo, K. Giri, D. Moyano, O.R. Miranda, B. Madden, D.J. McCormick, R. Bhattacharya, V.M. Rotello, J.P. Kocher, P. Mukherjee, *Identifying new therapeutic targets via modulation of protein corona formation by engineered nanoparticles*, PLoS One 7(3) (2012) e33650.

[35] N. Fernandez-Iglesias, J. Bettmer, *Complementary mass spectrometric techniques for the quantification of the protein corona: a case study on gold nanoparticles and human serum proteins*, Nanoscale 7(34) (2015) 14324-31.

[36] Y. Yue, R. Behra, L. Sigg, M.J.F. Suter, S. Pillai, K. Schirmer, *Silver nanoparticle–protein interactions in intact rainbow trout gill cells*, Environ. Sci. Nano 3(5) (2016) 1174-1185.

[37] M. Nicoletti, C. Capodanno, C. Gambarotti, E. Fasoli, *Proteomic investigation on bio-corona of functionalized multi-walled carbon nanotubes*, Biochim. Biophys. Acta Gen. Subj. 1862(10) (2018) 2293-2303.

[38] K. Giri, K. Shameer, M.T. Zimmermann, S. Saha, P.K. Chakraborty, A. Sharma, R.R. Arvizo, B.J. Madden, D.J. McCormick, J.P. Kocher, R. Bhattacharya, P. Mukherjee, *Understanding protein-nanoparticle interaction: a new gateway to disease therapeutics*, Bioconjug. Chem. 25(6) (2014) 1078-90.

[39] D. Drescher, P. Guttmann, T. Buchner, S. Werner, G. Laube, A. Hornemann, B. Tarek, G. Schneider, J. Kneipp, *Specific biomolecule corona is associated with ring-shaped organization of silver nanoparticles in cells*, Nanoscale 5(19) (2013) 9193-8.

[40] D. Drescher, T. Buchner, D. McNaughton, J. Kneipp, *SERS reveals the specific interaction of silver and gold nanoparticles with hemoglobin and red blood cell components*, Phys. Chem. Chem. Phys. 15(15) (2013) 5364-73.

[41] M.A. Dobrovolskaia, A.K. Patri, J. Zheng, J.D. Clogston, N. Ayub, P. Aggarwal, B.W. Neun, J.B. Hall, S.E. McNeil, *Interaction of colloidal gold nanoparticles with human blood: effects on particle size and analysis of plasma protein binding profiles*, Nanomedicine 5(2) (2009) 106-17.

[42] J. Kneipp, H. Kneipp, M. McLaughlin, D. Brown, K. Kneipp, *In vivo molecular probing of cellular compartments with gold nanoparticles and nanoaggregates*, Nano Lett. 6(10) (2006) 2225-31.

[43] K. Kneipp, H. Kneipp, R. Manoharan, E.B. Hanlon, I. Itzkan, R.R. Dasari, M.S. Feld, *Extremely large enhancement factors in surface-enhanced Raman scattering for molecules on colloidal gold clusters*, Appl. Spec. 52(12) (1998) 1493-1497.

[44] V. Joseph, A. Matschulat, J. Polte, S. Rolf, F. Emmerling, J. Kneipp, *SERS enhancement of gold nanospheres of defined size*, J. Raman Spectrosc. 42(9) (2011) 1736-1742.

[45] P.J. Thul, L. Akesson, M. Wiking, D. Mahdessian, A. Geladaki, H. Ait Blal, T. Alm, A. Asplund, L. Bjork, L.M. Breckels, A. Backstrom, F. Danielsson, L. Fagerberg, J. Fall, L. Gatto, C. Gnann, S. Hober, M. Hjelmare, F. Johansson, S. Lee, C. Lindskog, J. Mulder, C.M. Mulvey, P. Nilsson, P. Oksvold, J. Rockberg, R. Schutten, J.M. Schwenk, A. Sivertsson, E. Sjostedt, M. Skogs, C. Stadler, D.P. Sullivan, H. Tegel, C. Winsnes, C. Zhang, M. Zwahlen, A. Mardinoglu, F. Ponten, K. von Feilitzen, K.S. Lilley, M. Uhlen, E. Lundberg, *A subcellular map of the human proteome*, Science 356(6340) (2017).

[46] V. Ádám, *Orvosi biokémia*, 4th ed., Semmelweis Kiadó és Multimédia Stúdió, Budapest, 2016.

[47] B. Kalinowska, M. Banach, Z. Wisniowski, L. Konieczny, I. Roterman, *Is the hydrophobic core a universal structural element in proteins?*, J. Mol. Model. 23(7) (2017) 205.

[48] K. Landsteiner, R. Uhlirz, *Ueber die Adsorption von Eiweißkörpern*, Zeitschrift für Chemie und Industrie der Kolloide 2(11) (1908) 337-337.

[49] H. Neurath, H.B. Bull, *The Surface Activity of Proteins*, Chem. Rev. 23(3) (1938) 391-435.

[50] L. Vroman, *Effect of adsorbed proteins on the wettability of hydrophilic and hydrophobic solids*, Nature 196(4853) (1962) 476-477.

[51] V. Hlady, J. Buijs, *Protein adsorption on solid surfaces*, Curr. Opin. Biotechnol. 7(1) (1996) 72-77.

[52] V.P. Zhdanov, *Formation of a protein corona around nanoparticles*, Curr. Opin. Colloid Interface Sci. 41 (2019) 95-103.

[53] P. Roach, D. Farrar, C.C. Perry, *Interpretation of protein adsorption: surface-induced conformational changes*, J. Am. Chem. Soc. 127(22) (2005) 8168-73.

[54] M. Rabe, D. Verdes, M. Rankl, G.R. Artus, S. Seeger, *A comprehensive study of concepts and phenomena of the nonspecific adsorption of beta-lactoglobulin*, Chemphyschem. 8(6) (2007) 862-72.

[55] C. Calonder, P.R. Van Tassel, *Kinetic Regimes of Protein Adsorption*, Langmuir 17(14) (2001) 4392-4395.

[56] A. Tsuda, N.K. Venkata, *The role of natural processes and surface energy of inhaled engineered nanoparticles on aggregation and corona formation*, NanoImpact 2 (2016) 38-44.

[57] A. Lesniak, A. Salvati, M.J. Santos-Martinez, M.W. Radomski, K.A. Dawson, C. Aberg, *Nanoparticle adhesion to the cell membrane and its effect on nanoparticle uptake efficiency*, J. Am. Chem. Soc. 135(4) (2013) 1438-44.

[58] A. Lesniak, F. Fenaroli, M.P. Monopoli, C. Aberg, K.A. Dawson, A. Salvati, *Effects of the presence or absence of a protein corona on silica nanoparticle uptake and impact on cells*, ACS Nano 6(7) (2012) 5845-57.

[59] J. Mosquera, I. García, M. Henriksen-Lacey, G. González-Rubio, L.M. Liz-Marzán, *Reducing Protein Corona Formation and Enhancing Colloidal Stability of Gold Nanoparticles by Capping with Silica Monolayers*, Chem. Mater. 31(1) (2018) 57-61.

[60] M. Lundqvist, I. Sethson, B.H. Jonsson, *Protein adsorption onto silica nanoparticles: conformational changes depend on the particles' curvature and the protein stability*, Langmuir 20(24) (2004) 10639-47.

[61] H.S. Mandal, H.B. Kraatz, *Effect of the surface curvature on the secondary structure of peptides adsorbed on nanoparticles*, J. Am. Chem. Soc. 129(20) (2007) 6356-7.

[62] X. Wu, G. Narsimhan, *Characterization of secondary and tertiary conformational changes of beta-lactoglobulin adsorbed on silica nanoparticle surfaces*, Langmuir 24(9) (2008) 4989-98.

[63] S. Dominguez-Medina, S. McDonough, P. Swanglap, C.F. Landes, S. Link, *In situ measurement of bovine serum albumin interaction with gold nanospheres*, Langmuir 28(24) (2012) 9131-9.

[64] M. Lundqvist, J. Stigler, G. Elia, I. Lynch, T. Cedervall, K.A. Dawson, *Nanoparticle size and surface properties determine the protein corona with possible implications for biological impacts*, Proc. Natl. Acad. Sci. U S A 105(38) (2008) 14265-70.

[65] A. Bonifacio, S. Dalla Marta, R. Spizzo, S. Cervo, A. Steffan, A. Colombatti, V. Sergo, *Surface-enhanced Raman spectroscopy of blood plasma and serum using Ag and Au nanoparticles: a systematic study*, Anal. Bioanal. Chem. 406(9-10) (2014) 2355-65.

[66] M. Hassoun, W.S. I, T. Tolstik, S.E. Stanca, C. Krafft, J. Popp, *Surface-enhanced Raman spectroscopy of cell lysates mixed with silver nanoparticles for tumor classification*, Beilstein J. Nanotechnol. 8 (2017) 1183-1190.

[67] M.P. Monopoli, D. Walczyk, A. Campbell, G. Elia, I. Lynch, F.B. Bombelli, K.A. Dawson, *Physical-chemical aspects of protein corona: relevance to in vitro and in vivo biological impacts of nanoparticles*, J. Am. Chem. Soc. 133(8) (2011) 2525-34.

[68] E. Casals, T. Pfaller, A. Duschl, G.J. Oostingh, V. Puntes, *Time evolution of the nanoparticle protein corona*, ACS Nano 4(7) (2010) 3623-32.

[69] F. Bertoli, D. Garry, M.P. Monopoli, A. Salvati, K.A. Dawson, *The intracellular destiny of the protein corona: A study on its cellular internalization and evolution*, ACS Nano 10(11) (2016) 10471-10479.

[70] M. Kokkinopoulou, J. Simon, K. Landfester, V. Mailander, I. Lieberwirth, *Visualization of the protein corona: towards a biomolecular understanding of nanoparticle-cell-interactions*, Nanoscale 9(25) (2017) 8858-8870.

[71] C.C. Fleischer, C.K. Payne, *Secondary structure of corona proteins determines the cell surface receptors used by nanoparticles*, J. Phys. Chem. B 118(49) (2014) 14017-26.

[72] D. Chen, S. Ganesh, W. Wang, M. Amiji, *Plasma protein adsorption and biological identity of systemically administered nanoparticles*, Nanomedicine (Lond) 12(17) (2017) 2113-2135.

[73] D. Docter, C. Bantz, D. Westmeier, H.J. Galla, Q. Wang, J.C. Kirkpatrick, P. Nielsen, M. Maskos, R.H. Stauber, *The protein corona protects against size- and dose-dependent toxicity of amorphous silica nanoparticles*, Beilstein J. Nanotechnol. 5 (2014) 1380-92.

[74] I. Persaud, J.H. Shannahan, A.J. Raghavendra, N.B. Alsaleh, R. Podila, J.M. Brown, *Biocorona formation contributes to silver nanoparticle induced endoplasmic reticulum stress*, Ecotoxicol. Environ. Saf. 170 (2019) 77-86.

[75] M.A. Dobrovolskaia, B.W. Neun, S. Man, X. Ye, M. Hansen, A.K. Patri, R.M. Crist, S.E. McNeil, *Protein corona composition does not accurately predict hematocompatibility of colloidal gold nanoparticles*, Nanomedicine 10(7) (2014) 1453-63.

[76] T. Wang, J. Bai, X. Jiang, G.U. Nienhaus, *Cellular uptake of nanoparticles by membrane penetration: a study combining confocal microscopy with FTIR spectroelectrochemistry*, ACS Nano 6(2) (2012) 1251-9.

[77] K. Kostarelos, L. Lacerda, G. Pastorin, W. Wu, S. Wieckowski, J. Luangsivilay, S. Godefroy, D. Pantarotto, J.P. Briand, S. Muller, M. Prato, A. Bianco, *Cellular uptake of functionalized carbon nanotubes is independent of functional group and cell type*, Nat. Nanotechnol. 2(2) (2007) 108-13.

[78] B.M. Rothen-Rutishauser, S. Schurch, B. Haenni, N. Kapp, P. Gehr, *Interaction of fine particles and nanoparticles with red blood cells visualized with advanced microscopic techniques*, Environ. Sci. Technol. 40(14) (2006) 4353-9.

[79] Y. Cheng, W. Boll, T. Kirchhausen, S.C. Harrison, T. Walz, *Cryo-electron tomography of clathrin-coated vesicles: structural implications for coat assembly*, J. Mol. Biol. 365(3) (2007) 892-9.

[80] H.T. McMahon, E. Boucrot, *Molecular mechanism and physiological functions of clathrin-mediated endocytosis*, Nat. Rev. Mol. Cell. Biol. 12(8) (2011) 517-33.

[81] C.J. Merrifield, M. Kaksonen, *Endocytic accessory factors and regulation of clathrin-mediated endocytosis*, Cold Spring Harb. Perspect. Biol. 6(11) (2014) a016733.

[82] M. Desjardins, J.E. Celis, G. Van Meer, H. Dieplinger, A. Jahraus, G. Griffiths, L.A. Huber, *Molecular characterization of phagosomes*, J. Biol. Chem. 269(51) (1994) 32194-32200.

[83] J. Garin, R. Diez, S. Kieffer, J.F. Dermine, S. Duclos, E. Gagnon, R. Sadoul, C. Rondeau, M. Desjardins, *The phagosome proteome: insight into phagosome functions*, J. Cell. Biol. 152(1) (2001) 165-80.

[84] D.A. Kuhn, D. Vanhecke, B. Michen, F. Blank, P. Gehr, A. Petri-Fink, B. Rothen-Rutishauser, *Different endocytotic uptake mechanisms for nanoparticles in epithelial cells and macrophages*, Beilstein J. Nanotechnol. 5 (2014) 1625-36.

[85] B.D. Chithrani, W.C. Chan, *Elucidating the mechanism of cellular uptake and removal of protein-coated gold nanoparticles of different sizes and shapes*, Nano Lett. 7(6) (2007) 1542-50.

[86] S.E. Gratton, P.A. Ropp, P.D. Pohlhaus, J.C. Luft, V.J. Madden, M.E. Napier, J.M. DeSimone, *The effect of particle design on cellular internalization pathways*, Proc. Natl. Acad. Sci. U S A 105(33) (2008) 11613-8.

[87] X. Xie, J. Liao, X. Shao, Q. Li, Y. Lin, *The effect of shape on cellular uptake of gold nanoparticles in the forms of stars, rods, and rriangles*, Sci. Rep. 7(1) (2017) 3827.

[88] C. He, Y. Hu, L. Yin, C. Tang, C. Yin, *Effects of particle size and surface charge on cellular uptake and biodistribution of polymeric nanoparticles*, Biomaterials 31(13) (2010) 3657-66.

[89] O. Harush-Frenkel, N. Debotton, S. Benita, Y. Altschuler, *Targeting of nanoparticles to the clathrin-mediated endocytic pathway*, Biochem. Biophys. Res. Commun. 353(1) (2007) 26-32.

[90] C.T. Ng, F.M. Tang, J.J. Li, C. Ong, L.L. Yung, B.H. Bay, *Clathrin-mediated endocytosis of gold nanoparticles in vitro*, Anat. Rec. (Hoboken) 298(2) (2015) 418-27.

[91] E. Panzarini, S. Mariano, E. Carata, F. Mura, M. Rossi, L. Dini, *Intracellular transport of silver and gold nanoparticles and biological responses: An update*, Int. J. Mol. Sci. 19(5) (2018) 1305.

[92] M. Kaksonen, A. Roux, *Mechanisms of clathrin-mediated endocytosis*, Nat. Rev. Mol. Cell. Biol. 19(5) (2018) 313-326.

[93] J. Huotari, A. Helenius, *Endosome maturation*, EMBO J. 30(17) (2011) 3481-500.

[94] G. Raposo, W. Stoorvogel, *Extracellular vesicles: exosomes, microvesicles, and friends*, J. Cell Biol. 200(4) (2013) 373-83.

[95] C. Théry, A. Regnault, J. Garin, J. Wolfers, L. Zitvogel, P. Ricciardi-Castagnoli, G. Raposo, S. Amigorena, *Molecular characterization of dendritic cell-derived exosomes*, J. Cell Biol. 147(3) (1999) 599-610.

[96] C. Thery, M. Boussac, P. Veron, P. Ricciardi-Castagnoli, G. Raposo, J. Garin, S. Amigorena, *Proteomic analysis of dendritic cell-derived exosomes: A secreted subcellular compartment distinct from apoptotic vesicles*, J. Immunol. 166(12) (2001) 7309-7318.

[97] J. Xu, R. Camfield, S.M. Gorski, *The interplay between exosomes and autophagy - partners in crime*, J. Cell Sci. 131(15) (2018).

[98] A. Smekal, *Zur Quantentheorie der Dispersion*, Die Naturwissenschaften 11(43) (1923) 873-875.

[99] C.V. Raman, K.S. Krishnan, *A new radiation*, Indian J. Phys. 2(1928) 387-398.

[100] C.V. Raman, K.S. Krishnan, *A new type of secondary radiation*, Nature 121(3048) (1928) 501-502.

[101] G. Landsberg, L. Mandelstam, *Eine neue Erscheinung bei der Lichtzerstreuung in Krystallen*, Die Naturwissenschaften 16(28) (1928) 557-558.

[102] J.T. Edsall, *Raman spectra of amino acids and related compounds I. The ionization of the carboxyl group*, J. Chem. Phys. 4(1) (1936) 1-8.

[103] J.T. Edsall, J.W. Otvos, A. Rich, *Raman spectra of amino acids and related compounds. VII. Glycylglycine, cysteine, cystine and other amino acids 1*, J. Am. Chem. Soc. 72(1) (1950) 474-477.

[104] V.J. Lin, J.L. Koenig, *Raman studies of bovine serum albumin*, Biopolymers 15(1) (1976) 203-18.

[105] A. Rygula, K. Majzner, K.M. Marzec, A. Kaczor, M. Pilarczyk, M. Baranska, *Raman spectroscopy of proteins: a review*, J. Raman Spectrosc. 44(8) (2013) 1061-1076.

[106] W.L. Peticolas, *Raman spectroscopy of DNA and proteins*, Methods Enzymol. 246(1995) 389-416.

[107] T.G. Spiro, T.C. Strekas, *Resonance Raman spectra of heme proteins. Effects of oxidation and spin state*, J. Am. Chem. Soc. 96(2) (1974) 338-345.

[108] J. Bandekar, *Amide modes and protein conformation*, Biochim. Biophys. Acta, Protein Struct. Mol. Enzymol. 1120(2) (1992) 123-143.

[109] R.S. Jakubek, J. Handen, S.E. White, S.A. Asher, I.K. Lednev, *Ultraviolet resonance Raman spectroscopic markers for protein structure and dynamics*, Trends Anal. Chem. 103 (2018) 223-229.

[110] G.J. Puppels, F.F. de Mul, C. Otto, J. Greve, M. Robert-Nicoud, D.J. Arndt-Jovin, T.M. Jovin, *Studying single living cells and chromosomes by confocal Raman microspectroscopy*, Nature 347(6290) (1990) 301-3.

[111] G.J. Puppels, C. Otto, J. Greve, M. Robert-Nicoud, D.J. Arndt-Jovin, T.M. Jovin, *Raman microspectroscopic study of low-pH-induced changes in DNA structure of polytene chromosomes*, Biochemistry 33(11) (1994) 3386-95.

[112] A.F. Palonpon, M. Sodeoka, K. Fujita, *Molecular imaging of live cells by Raman microscopy*, Curr. Opin. Chem. Biol. 17(4) (2013) 708-15.

[113] R. Smith, K.L. Wright, L. Ashton, *Raman spectroscopy: an evolving technique for live cell studies*, Analyst 141(12) (2016) 3590-600.

[114] M. Fleischmann, P.J. Hendra, A.J. McQuillan, *Raman spectra of pyridine adsorbed at a silver electrode*, Chem. Phys. Lett. 26(2) (1974) 163-166.

[115] J.A. Creighton, C.G. Blatchford, M.G. Albrecht, *Plasma resonance enhancement of Raman scattering by pyridine adsorbed on silver or gold sol particles of size comparable to the excitation wavelength*, J. Chem. Soc., Faraday Trans. 2 75 (1979) 790.

[116] M.G. Albrecht, J.A. Creighton, A*nomalously intense Raman spectra of pyridine at a silver electrode*, J. Am. Chem. Soc. 99(15) (1977) 5215-5217.

[117] M. Moskovits, *Surface roughness and the enhanced intensity of Raman scattering by molecules adsorbed on metals*, J. Chem. Phys. 69(9) (1978) 4159-4161.

[118] M. Moskovits, *Surface-Enhanced Spectroscopy*, Rev. Mod. Phys. 57(3) (1985) 783-826.

[119] D.L. Jeanmaire, R.P. Van Duyne, *Surface Raman spectroelectrochemistry*, J. Electroanal. Chem. Interf. Electrochem. 84(1) (1977) 1-20.

[120] M.R. Philpott, *Effect of surface plasmons on transitions in molecules*, J. Chem. Phys. 62(5) (1975) 1812-1817.

[121] K. Kneipp, H. Kneipp, I. Itzkan, R.R. Dasari, M.S. Feld, *Surface-enhanced Raman scattering and biophysics*, J. Phys. Condens. Mat. 14(18) (2002) R597-R624.

[122] A. Campion, J.E. Ivanecky, C.M. Child, M. Foster, *On the Mechanism of Chemical Enhancement in Surface-Enhanced Raman Scattering*, J. Am. Chem. Soc. 117(47) (1995) 11807-11808.

[123] N.S. Chong, K. Donthula, R.A. Davies, W.H. Ilsley, B.G. Ooi, *Significance of chemical enhancement effects in surface-enhanced Raman scattering (SERS) signals of aniline and aminobiphenyl isomers*, Vibr. Spectrosc. 81 (2015) 22-31.

[124] V.A. Markel, V.M. Shalaev, P. Zhang, W. Huynh, L. Tay, T.L. Haslett, M. Moskovits, *Near-field optical spectroscopy of individual surface-plasmon modes in colloid clusters*, Phys. Rev. B 59(16) (1999) 10903 - 10909.

[125] K. Kneipp, Y. Wang, H. Kneipp, L.T. Perelman, I. Itzkan, R.R. Dasari, M.S. Feld, *Single molecule detection using surface-enhanced Raman scattering (SERS)*, Phys. Rev. Lett. 78(9) (1997) 1667-1670.

[126] K. Kneipp, H. Kneipp, P. Corio, S.D. Brown, K. Shafer, J. Motz, L.T. Perelman, E.B. Hanlon, A. Marucci, G. Dresselhaus, M.S. Dresselhaus, *Surface-enhanced and normal stokes and anti-stokes Raman spectroscopy of single-walled carbon nanotubes*, Phys. Rev. Lett. 84(15) (2000) 3470-3.

[127] C.G. Blatchford, J.R. Campbell, J.A. Creighton, *Plasma resonance — enhanced raman scattering by absorbates on gold colloids: The effects of aggregation*, Surf. Sci. 120(2) (1982) 435-455.

[128] J. McMahon, A.-I. Henry, K. Wustholz, M. Natan, R. Freeman, R. Van Duyne, G. Schatz, *Gold nanoparticle dimer plasmonics: finite element method calculations of the electromagnetic enhancement to surface-enhanced Raman spectroscopy*, Anal. Bioanal. Chem. 394(7) (2009) 1819-1825.

[129] M.I. Stockman, *Nanoplasmonics: past, present, and glimpse into future*, Optics Exp. 19(22) (2011) 22029.

[130] V.P. Drachev, M.D. Thoreson, V. Nashine, E.N. Khaliullin, D. Ben-Amotz, V.J. Davisson, V.M. Shalaev, *Adaptive silver films for surface-enhanced Raman spectroscopy of biomolecules*, J. Raman Spectrosc. 36(6-7) (2005) 648-656.

[131] S. Han, S. Hong, X. Li, *Effects of cations and anions as aggregating agents on SERS detection of cotinine (COT) and trans-3'-hydroxycotinine (3HC)*, J. Colloid Inter. Sci. 410 (2013) 74-80.

[132] N.R. Yaffe, E.W. Blanch, Effects and anomalies that can occur in SERS spectra of biological molecules when using a wide range of aggregating agents for hydroxylamine-reduced and citrate-reduced silver colloids, Vibrational Spectroscopy 48(2) (2008) 196-201.

[133] S. Sánchez-Cortés, J.V. García-Ramos, G. Morcillo, *Morphological study of metal colloids employed as substrate in the SERS spectroscopy*, J. Colloid Inter. Sci. 167(2) (1994) 428-436.

[134] P.F. Liao, M.B. Stern, *Surface-enhanced Raman scattering on gold and aluminum particle arrays*, Optics Lett. 7(10) (1982) 483-485.

[135] G.C. Schatz, R.P. Van Duyne, P.R. Griffiths, *Electromagnetic mechanism of surface-enhanced spectroscopy*, in: K. Kneipp, M. Moskovits, H. Kneipp: Surface-Enhanced Raman Scattering: Physics and Applications. Berlin, Heidelberg: Springer (2006) 19-45.

[136] F. Madzharova, Z. Heiner, J. Simke, S. Selve, J. Kneipp, *Gold nanostructures for plasmonic enhancement of hyper-Raman scattering*, J. Phys. Chem. C 122(5) (2018) 2931-2940.

[137] A.M. Anger, J.P. Armache, O. Berninghausen, M. Habeck, M. Subklewe, D.N. Wilson, R. Beckmann, *Structures of the human and Drosophila 80S ribosome*, Nature 497(7447) (2013) 80-5.

[138] T. Ali, P. Coles, T.J. Stevens, K. Stott, J.O. Thomas, *Two homologous domains of similar structure but different stability in the yeast linker histone, Hho1p*, J. Mol. Biol. 338(1) (2004) 139-48.

[139] G.R. Andersen, L. Valente, L. Pedersen, T.G. Kinzy, J. Nyborg, *Crystal structures of nucleotide exchange intermediates in the eEF1A-eEF1Balpha complex*, Nat. Struct. Biol. 8(6) (2001) 531-4.

[140] M. Iosin, V. Canpean, S. Astilean, *Spectroscopic studies on pH- and thermally induced conformational changes of Bovine Serum Albumin adsorbed onto gold nanoparticles*, J. Photochem. Photobiol. A 217(2-3) (2011) 395-401.

[141] J.M. Connolly, K. Davies, A. Kazakeviciute, A.M. Wheatley, P. Dockery, I. Keogh, M. Olivo, *Non-invasive and label-free detection of oral squamous cell carcinoma using saliva surface-enhanced Raman spectroscopy and multivariate analysis*, Nanomed. Nanotechnol. Biol. Med. 12(6) (2016) 1593-1601.

[142] C.V. Di Anibal, L.F. Marsal, M.P. Callao, I. Ruisánchez, *Surface Enhanced Raman Spectroscopy (SERS) and multivariate analysis as a screening tool for detecting Sudan I dye in culinary spices*, Spectrochim. Acta A Mol. Biomol. Spectrosc. 87 (2012) 135-141.

[143] M. Altunbek, D. Cetin, Z. Suludere, M. Culha, *Surface-enhanced Raman spectroscopy based 3D spheroid culture for drug discovery studies*, Talanta 191 (2019) 390-399.

[144] V. Zivanovic, S. Seifert, D. Drescher, P. Schrade, S. Werner, P. Guttmann, G.P. Szekeres, S. Bachmann, G. Schneider, C. Arenz, J. Kneipp, *Optical nanosensing of lipid accumulation due to enzyme inhibition in live cells*, ACS Nano (2019).

[145] T. Buchner, D. Drescher, H. Traub, P. Schrade, S. Bachmann, N. Jakubowski, J. Kneipp, *Relating surface-enhanced Raman scattering signals of cells to gold nanoparticle aggregation as determined by LA-ICP-MS micromapping*, Anal. Bioanal. Chem. 406(27) (2014) 7003-7014.

[146] C.A.R. Auchinvole, P. Richardson, C. McGuinnes, V. Mallikarjun, K. Donaldson, H. McNab, C.J. Campbell, *Monitoring intracellular redox potential changes using SERS nanosensors*, ACS Nano 6(1) (2012) 888-896.

[147] J. Kneipp, H. Kneipp, B. Wittig, K. Kneipp, *One- and two-photon excited optical pH probing for cells using surface-enhanced Raman and hyper-Raman nanosensors*, Nano Lett. 7(9) (2007) 2819-2823.

[148] M. Gühlke, Z. Heiner, J. Kneipp, *Combined near-infrared excited SEHRS and SERS spectra of pH sensors using silver nanostructures*, Phys. Chem. Chem. Phys. 17(39) (2015) 26093-26100.

[149] R. Peng, Y. Si, T. Deng, J. Zheng, J. Li, R. Yang, W. Tan, *A novel SERS nanoprobe for the ratiometric imaging of hydrogen peroxide in living cells*, Chem. Comm. 52(55) (2016) 8553-8556.

[150] B. Kang, L.A. Austin, M.A. El-Sayed, *Observing real-time molecular event dynamics of apoptosis in living cancer cells using nuclear-targeted plasmonically enhanced Raman nanoprobes*, ACS Nano 8(5) (2014) 4883-4892.

[151] J. Ando, K. Fujita, N.I. Smith, S. Kawata, *Dynamic SERS imaging of cellular transport pathways with endocytosed gold nanoparticles*, Nano Lett. 11(12) (2011) 5344-5348.

[152] D. Lu, J. Xia, Z. Deng, X. Cao, *Detection of squamous cell carcinoma antigen in cervical cancer by surface-enhanced Raman scattering-based immunoassay*, Anal. Met. 11(21) (2019) 2809-2818.

[153] M. Aioub, M.A. El-Sayed, *A real-time surface enhanced Raman spectroscopy study of plasmonic photothermal cell death using targeted gold nanoparticles*, J. Am. Chem. Soc. 138(4) (2016) 1258-1264.

[154] T. Buchner, D. Drescher, V. Merk, H. Traub, P. Guttmann, S. Werner, N. Jakubowski, G. Schneider, J. Kneipp, *Biomolecular environment, quantification, and intracellular interaction of multifunctional magnetic SERS nanoprobes*, Analyst 141(17) (2016) 5096-106.

[155] D. Drescher, H. Traub, T. Buchner, N. Jakubowski, J. Kneipp, *Properties of in situ generated gold nanoparticles in the cellular context*, Nanoscale 9(32) (2017) 11647-11656.

[156] X. Jin, B.N. Khlebtsov, V.A. Khanadeev, N.G. Khlebtsov, J. Ye, *Rational design of ultrabright SERS probes with embedded reporters for bioimaging and photothermal therapy*, ACS Appl. Mater. Inter. 9(36) (2017) 30387-30397.

[157] V. Zivanovic, G. Semini, M. Laue, D. Drescher, T. Aebischer, J. Kneipp, *Chemical mapping of Leishmania infection in live cells by SERS microscopy*, Anal Chem 90(13) (2018) 8154-8161.

[158] D. Drescher, C. Giesen, H. Traub, U. Panne, J. Kneipp, N. Jakubowski, *Quantitative imaging of gold and silver nanoparticles in single eukaryotic cells by laser ablation ICP-MS*, Anal. Chem. 84(22) (2012) 9684-8.

[159] P.B. Grosshans, A.G. Marshall, *General theory of excitation in ion cyclotron resonance mass spectrometry*, Anal. Chem. 63(18) (1991) 2057-2061.

[160] S.S. Rubakhin, J.V. Sweedler, *A mass spectrometry primer for mass spectrometry imaging*, in: S.S. Rubakhin, J.V. Sweedler (Eds.), Mass Spectrometry Imaging: Principles and Protocols, Humana Press, Totowa, NJ, 2010, pp. 21-49.

[161] A. Cox, P. Andreozzi, R. Dal Magro, F. Fiordaliso, A. Corbelli, L. Talamini, C. Chinello, F. Raimondo, F. Magni, M. Tringali, S. Krol, P. Jacob Silva, F. Stellacci, M. Masserini, F. Re, *Evolution of nanoparticle protein corona across the blood-brain barrier*, ACS Nano 12(7) (2018) 7292-7300.

[162] T. Zhang, M.J. Gaffrey, B.D. Thrall, W.J. Qian, *Mass spectrometry-based proteomics for system-level characterization of biological responses to engineered nanomaterials*, Anal. Bioanal. Chem. 410(24) (2018) 6067-6077.

[163] S. Tenzer, D. Docter, S. Rosfa, A. Wlodarski, J. Kuharev, A. Rekik, S.K. Knauer, C. Bantz, T. Nawroth, C. Bier, J. Sirirattanapan, W. Mann, L. Treuel, R. Zellner, M. Maskos, H. Schild, R.H. Stauber, *Nanoparticle size is a critical physicochemical determinant of the human blood plasma corona: a comprehensive quantitative proteomic analysis*, ACS Nano 5(9) (2011) 7155-67.

[164] G. Schneider, P. Guttmann, S. Heim, S. Rehbein, F. Mueller, K. Nagashima, J.B. Heymann, W.G. Muller, J.G. McNally, *Three-dimensional cellular ultrastructure resolved by X-ray microscopy*, Nat. Met. 7(12) (2010) 985-7.

[165] E.M. Duke, M. Razi, A. Weston, P. Guttmann, S. Werner, K. Henzler, G. Schneider, S.A. Tooze, L.M. Collinson, *Imaging endosomes and autophagosomes in whole mammalian cells using correlative cryo-fluorescence and cryo-soft X-ray microscopy (cryo-CLXM)*, Ultramicroscopy 143 (2014) 77-87.

[166] C. Hagen, K.C. Dent, T. Zeev-Ben-Mordehai, M. Grange, J.B. Bosse, C. Whittle, B.G. Klupp, C.A. Siebert, D. Vasishtan, F.J. Bauerlein, J. Cheleski, S. Werner, P. Guttmann, S. Rehbein, K. Henzler, J. Demmerle, B. Adler, U. Koszinowski, L. Schermelleh, G. Schneider, L.W. Enquist, J.M. Plitzko, T.C. Mettenleiter, K. Grunewald, *Structural basis of vesicle formation at the inner nuclear membrane*, Cell 163(7) (2015) 1692-701.

[167] M. Chiappi, J.J. Conesa, E. Pereiro, C.O. Sorzano, M.J. Rodriguez, K. Henzler, G. Schneider, F.J. Chichon, J.L. Carrascosa, *Cryo-soft X-ray tomography as a quantitative three-dimensional tool to model nanoparticle:cell interaction*, J. Nanobiotechnol. 14 (2016) 15.

[168] D. Drescher, T. Büchner, P. Guttmann, S. Werner, G. Schneider, J. Kneipp, *X-ray tomography shows the varying three-dimensional morphology of gold nanoaggregates in the cellular ultrastructure*, Nanoscale Adv. (2019).

[169] W.G. Muller, J.B. Heymann, K. Nagashima, P. Guttmann, S. Werner, S. Rehbein, G. Schneider, J.G. McNally, *Towards an atlas of mammalian cell ultrastructure by cryo soft X-ray tomography*, J. Struct. Biol. 177(2) (2012) 179-92.

[170] P.C. Lee, D. Meisel, *Adsorption and surface-enhanced Raman of dyes on silver and gold sols*, J. Phys. Chem. 86(17) (1982) 3391-3395.

[171] G.P. Szekeres, J. Kneipp, *SERS probing of proteins in gold nanoparticle agglomerates*, Front. Chem. 7 (2019) 30.

[172] G.P. Szekeres, J. Kneipp, *Different binding sites of serum albumins in the protein corona of gold nanoparticles*, Analyst 143(24) (2018) 6061-6068.

[173] R. Milo, *What is the total number of protein molecules per cell volume? A call to rethink some published values*, Bioessays 35(12) (2013) 1050-5.

[174] D. Alberghina, C. Giannetto, I. Vazzana, V. Ferrantelli, G. Piccione, *Reference intervals for total protein concentration, serum protein fractions, and albumin/globulin ratios in clinically healthy dairy cows*, J. Vet. Diagnost. Invest. 23(1) (2011) 111-4.

[175] J.T. Busher, Serum Albumin and Globulin, in: H.K. Walker, W.D. Hall, J.W. Hurst (Eds.), *Clinical methods: The history, physical, and laboratory examinations*, Butterworths, Boston, 1990, pp. 497-499.

[176] P.H.C. Eilers, *A perfect smoother*, Anal. Chem. 75(14) (2003) 3631-3636.

[177] P. Lasch, *Spectral pre-processing for biomedical vibrational spectroscopy and microspectroscopic imaging*, Chemom. Intell. Lab. Syst. 117 (2012) 100-114.

[178] A. Savitzky, M.J.E. Golay, *Smoothing and differentiation of data by simplified least squares procedures*, Anal. Chem. 36(8) (1964) 1627-1639.

[179] H.M. Berman, J. Westbrook, Z. Feng, G. Gilliland, T.N. Bhat, H. Weissig, I.N. Shindyalov, P.E. Bourne, *The Protein Data Bank*, Nucl. Acids Res. 28(1) (2000) 235-42.

[180] A. Bujacz, K. Zielinski, B. Sekula, *Structural studies of bovine, equine, and leporine serum albumin complexes with naproxen*, Proteins 82(9) (2014) 2199-208.

[181] B. Sekula, A. Ciesielska, P. Rytczak, M. Koziolkiewicz, A. Bujacz, *Structural evidence of the species-dependent albumin binding of the modified cyclic phosphatidic acid with cytotoxic properties*, Biosci. Rep. 36(3) (2016).

[182] W. Humphrey, A. Dalke, K. Schulten, *VMD: visual molecular dynamics*, J. Mol. Graph. 14(1) (1996) 33-8, 27-8.

[183] D. Jia, J. Hamilton, L.M. Zaman, A. Goonewardene, *The time, size, viscosity, and temperature dependence of the Brownian motion of polystyrene microspheres*, Am. J. Phys. 75(2) (2007) 111-115.

[184] S. Yadav, S.J. Shire, D.S. Kalonia, *Viscosity analysis of high concentration bovine serum albumin aqueous solutions*, Pharm. Res. 28(8) (2011) 1973-83.

[185] M.A. Abdelhalim, M.M. Mady, M.M. Ghannam, *Rheological and dielectric properties of different gold nanoparticle sizes*, Lipids Health. Dis. 10 (2011) 208.

[186] C. Tanford, J.G. Buzzell, *The viscosity of aqueous solutions of bovine serum albumin between pH 4.3 and 10.5*, J. Phys. Chem. 60(2) (1956) 225-231.

[187] D. Docter, U. Distler, W. Storck, J. Kuharev, D. Wunsch, A. Hahlbrock, S.K. Knauer, S. Tenzer, R.H. Stauber, *Quantitative profiling of the protein coronas that form around nanoparticles*, Nat. Protoc. 9(9) (2014) 2030-44.

[188] Y.P. See, P.M. Olley, G. Jackowski, *The effects of high salt concentrations in the samples on molecular weight determination in sodium dodecyl sulfate polyacrylamide gel electrophoresis*, Electrophoresis 6(8) (1985) 382-387.

[189] R. van Furth, I. Elzenga-Claasen, M. van Schadewijk-Nieuwstad, M.M. Diesselhoff-den Dulk, H. Toivonen, T. Rytömaa, *Cell kinetic analysis of a murine macrophage cell line*, Eur. J. Cell. Biol. 44(1) (1987) 93-96.

[190] N. Fernández-Iglesias, *Caracterización de conjugados de proteínas y nanopartículas metálicas mediante el empleo de técnicas complementarias de espectrometría de masas y de microscopía*, Departamento de Química Física y Analítica, Universidad de Oviedo, Oviedo, Spain, 2017, p. 337.

[191] J.P.D. Goldring, *The roles of acetic acid and methanol during fixing and staining proteins in an SDS–polyacrylamide electrophoresis Gel*, in: B.T. Kurien, R.H. Scofield (Eds.), Protein Gel Detection and Imaging: Methods and Protocols, Springer New York, New York, NY, 2018, pp. 15-18.

[192] G. Steck, P. Leuthard, R.R. Bürk, *Detection of basic proteins and low molecular weight peptides in polyacrylamide gels by formaldehyde fixation*, Anal. Biochem. 107(1) (1980) 21-24.

[193] B.W. Sutherland, J. Toews, J. Kast, *Utility of formaldehyde cross-linking and mass spectrometry in the study of protein-protein interactions*, J. Mass Spectrom. 43(6) (2008) 699-715.

[194] L.A. Echan, D.W. Speicher, *Protein detection in gels using fixation*, Curr. Protoc. Protein Sci. Chapter 10 (2002) Unit 10 5.

[195] D.N. Perkins, D.J.C. Pappin, D.M. Creasy, J.S. Cottrell, *Probability-based protein identification by searching sequence databases using mass spectrometry data*, Electrophoresis 20(18) (1999) 3551-3567.

[196] Matrix Science, MS/MS Results Interpretation. http://www.matrixscience.com/help/interpretation_help.html, 2016 (accessed 2019.).

[197] K. Kneipp, J. Flemming, *Surface enhanced Raman scattering (SERS) of nucleic acids adsrobed on colloidal silver particles*, J. Mol. Struct. 145(1-2) (1986) 173-179.

[198] A. Barhoumi, N.J. Halas, *Label-free detection of DNA hybridization using surface enhanced Raman spectroscopy*, J. Am. Chem. Soc. 132(37) (2010) 12792-3.

[199] C. Blum, T. Schmid, L. Opilik, S. Weidmann, S.R. Fagerer, R. Zenobi, *Understanding tip-enhanced Raman spectra of biological molecules: a combined Raman, SERS and TERS study*, J. Raman Spectrosc. 43(12) (2012) 1895-1904.

[200] J.M. McMahon, S.K. Gray, G.C. Schatz, *Fundamental behavior of electric field enhancements in the gaps between closely spaced nanostructures*, Phys. Rev. B 83(11) (2011).

[201] S. Reymond-Laruinaz, L. Saviot, V. Potin, M.d.C. Marco de Lucas, *Protein–nanoparticle interaction in bioconjugated silver nanoparticles: A transmission electron microscopy and surface enhanced Raman spectroscopy study*, Appl. Surf. Sci. 389 (2016) 17-24.

[202] H.X. Xu, E.J. Bjerneld, M. Kall, L. Borjesson, *Spectroscopy of single hemoglobin molecules by surface enhanced Raman scattering*, Phys. Rev. Lett. 83(21) (1999) 4357-4360.

[203] D.S. Wang, M. Kerker, *Enhanced Raman scattering by molecules adsorbed at the surface of colloidal spheroids*, Phys. Rev. B 24(4) (1981) 1777.

[204] R.A. Alvarez-Puebla, A. Agarwal, P. Manna, B.P. Khanal, P. Aldeanueva-Potel, E. Carbo-Argibay, N. Pazos-Perez, L. Vigderman, E.R. Zubarev, N.A. Kotov, L.M. Liz-Marzan, *Gold nanorods 3D-supercrystals as surface enhanced Raman scattering spectroscopy substrates for the rapid detection of scrambled prions*, Proc. Natl. Acad. Sci. U S A 108(20) (2011) 8157-61.

[205] N.P. Ivleva, M. Wagner, A. Szkola, H. Horn, R. Niessner, C. Haisch, *Label-free in situ SERS imaging of biofilms*, J. Phys. Chem. B 114(31) (2010) 10184-94.

[206] C. Fasolato, S. Giantulli, I. Silvestri, F. Mazzarda, Y. Toumia, F. Ripanti, F. Mura, F. Luongo, F. Costantini, F. Bordi, P. Postorino, F. Domenici, *Folate-based single cell screening using surface enhanced Raman microimaging*, Nanoscale 8(39) (2016) 17304-17313.

[207] H. Kneipp, N. Møbjerg, A. Jørgensen, H.G. Bohr, C. Hélix-Nielsen, J. Kneipp, K. Kneipp, *Surface enhanced Raman scattering on Tardigrada - towards monitoring and imaging molecular structures in live cryptobiotic organisms*, J. Biophotonics 6(10) (2012) 759-764.

[208] S. Charan, F.-C. Chien, N. Singh, C.-W. Kuo, P. Chen, *Development of lipid targeting Raman probes for in vivo imaging of Caenorhabditis elegans*, Chem. Eur. J. 17(18) (2011) 5165-5170.

[209] K. Ma, J.M. Yuen, N.C. Shah, J.T. Walsh, Jr., M.R. Glucksberg, R.P. Van Duyne, *In vivo, transcutaneous glucose sensing using surface-enhanced spatially offset Raman spectroscopy: multiple rats, improved hypoglycemic accuracy, low incident power, and continuous monitoring for greater than 17 days*, Anal. Chem. 83(23) (2011) 9146-52.

[210] J. Kneipp, *Interrogating cells, tissues, and live animals with new generations of surface-enhanced Raman scattering probes and labels*, ACS Nano 11(2) (2017) 1136-1141.

[211] G.C. Brown, *Total cell protein concentration as an evolutionary constraint on the metabolic control distribution in cells*, J. Theor. Biol. 153(2) (1991) 195-203.

[212] D.M. Zhang, O. Neumann, H. Wang, V.M. Yuwono, A. Barhoumi, M. Perham, J.D. Hartgerink, P. Wittung-Stafshede, N.J. Halas, *Gold nanoparticles can induce the formation of protein-based aggregates at physiological pH*, Nano Lett. 9(2) (2009) 666-671.

[213] B. Bharti, J. Meissner, G.H. Findenegg, *Aggregation of silica nanoparticles directed by adsorption of lysozyme*, Langmuir 27(16) (2011) 9823-33.

[214] S.T. Moerz, A. Kraegeloh, M. Chanana, T. Kraus, *Formation mechanism for stable hybrid clusters of proteins and nanoparticles*, ACS Nano 9(7) (2015) 6696-705.

[215] A. Hornemann, D. Drescher, S. Flemig, J. Kneipp, *Intracellular SERS hybrid probes using BSA-reporter conjugates*, Anal. Bioanal. Chem. 405(19) (2013) 6209-6222.

[216] J. Kneipp, H. Kneipp, B. Wittig, K. Kneipp, *Novel optical nanosensors for probing and imaging live cells*, Nanomedicine 6(2) (2010) 214-26.

[217] K. Czamara, K. Majzner, M.Z. Pacia, K. Kochan, A. Kaczor, M. Baranska, *Raman spectroscopy of lipids: a review*, J. Raman Spectrosc. 46(1) (2015) 4-20.

[218] F. Madzharova, Z. Heiner, M. Guhlke, J. Kneipp, *Surface-enhanced hyper-Raman spectra of adenine, guanine, cytosine, thymine, and uracil*, J. Phys. Chem. C Nanomater. Inter. 120(28) (2016) 15415-15423.

[219] F. Madzharova, Z. Heiner, J. Kneipp, *Surface enhanced hyper-Raman scattering of the amino acids tryptophan, histidine, phenylalanine, and tyrosine*, J. Phys. Chem. C 121(2) (2017) 1235-1242.

[220] D.A. Weitz, S. Garoff, T.J. Gramila, *Excitation spectra of surface-enhanced Raman scattering on silver-island films*, Opt. Lett. 7(4) (1982) 168-170.

[221] D. Liu, G.J. Szulczewski, L.D. Kispert, A. Primak, T.A. Moore, A.L. Moore, D. Gust, *A thiol-substituted carotenoid self-assembles on gold surfaces*, J. Phys. Chem. B 106(11) (2002) 2933-2936.

[222] T.E. Creighton, *The biophysical chemistry of nucleic acids and proteins*, Helvetian Press, York, United Kingdom, 2010.

[223] T. Huser, C.A. Orme, C.W. Hollars, M.H. Corzett, R. Balhorn, *Raman spectroscopy of DNA packaging in individual human sperm cells distinguishes normal from abnormal cells*, J. Biophotonics 2(5) (2009) 322-32.

[224] E.W. Small, W.L. Peticolas, *Conformational dependence of the Raman scattering intensities from polynucleotides. 3. Order-disorder changes in helical structures*, Biopolymers 10(8) (1971) 1377-418.

[225] R. An, Y. Jia, B. Wan, Y. Zhang, P. Dong, J. Li, X. Liang, *Non-enzymatic depurination of nucleic acids: factors and mechanisms*, PLoS One 9(12) (2014) e115950.

[226] S.C. Erfurth, P.J. Bond, W.L. Peticolas, *Characterization of the A in equilibrium B transition of DNA in fibers and gels by laser Raman spectroscopy*, Biopolymers 14(6) (1975) 1245-57.

[227] Y.H. Choi, H.K. Han, *Nanomedicines: current status and future perspectives in aspect of drug delivery and pharmacokinetics*, J. Pharm. Investig. 48(1) (2018) 43-60.

[228] P. Aggarwal, J.B. Hall, C.B. McLeland, M.A. Dobrovolskaia, S.E. McNeil, *Nanoparticle interaction with plasma proteins as it relates to particle biodistribution, biocompatibility and therapeutic efficacy*, Adv. Drug. Deliv. Rev. 61(6) (2009) 428-37.

[229] J.L. Koenig, *Raman spectroscopy of biological molecules: A review*, J. Polym. Sci. Macromol. Rev. 6(1) (1972) 59-177.

[230] J.M. Benevides, S.A. Overman, G.J. Thomas, Jr., *Raman spectroscopy of proteins*, Curr. Protoc. Protein Sci. Chapter 17 (2004) Unit 17 8.

[231] E. Gasteiger, *ExPASy: the proteomics server for in-depth protein knowledge and analysis*, Nucl. Acids Res. 31(13) (2003) 3784-3788.

[232] P.J. Sadler, A. Tucker, *pH-induced structural transitions of bovine serum albumin. Histidine pKa values and unfolding of the N-terminus during the N to F transition*, Eur. J. Biochem. 212(3) (1993) 811-7.

[233] M. Iosin, F. Toderas, P.L. Baldeck, S. Astilean, *Study of protein–gold nanoparticle conjugates by fluorescence and surface-enhanced Raman scattering*, J. Mol. Struct. 924-926 (2009) 196-200.

[234] G. Das, F. Mecarini, F. Gentile, F. De Angelis, H. Mohan Kumar, P. Candeloro, C. Liberale, G. Cuda, E. Di Fabrizio, *Nano-patterned SERS substrate: application for protein analysis vs. temperature*, Biosens. Bioelectron. 24(6) (2009) 1693-9.

[235] T. Watanabe, H. Maeda, *Adsorption-controlled redox activity. Surface-enhanced Raman investigation of cystine versus cysteine on silver electrodes*, J. Phys. Chem. 93(8) (1989) 3258-3260.

[236] X. Shi, D. Li, J. Xie, S. Wang, Z. Wu, H. Chen, *Spectroscopic investigation of the interactions between gold nanoparticles and bovine serum albumin*, Ch. Sci. Bull. 57(10) (2012) 1109-1115.

[237] A.I. Ivanov, R.G. Zhbankov, E.A. Korolenko, E.V. Korolik, L.A. Meleshchenko, M. Marchewka, H. Ratajczak, *Infrared and Raman spectroscopic studies of the structure of human serum albumin under various ligand loads*, J. Appl. Spectrosc. 60 (1994) 305-309.

[238] N.C. Dingari, G.L. Horowitz, J.W. Kang, R.R. Dasari, I. Barman, *Raman spectroscopy provides a powerful diagnostic tool for accurate determination of albumin glycation*, PLoS One 7(2) (2012) e32406.

[239] H. Al-Johani, E. Abou-Hamad, A. Jedidi, C.M. Widdifield, J. Viger-Gravel, S.S. Sangaru, D. Gajan, D.H. Anjum, S. Ould-Chikh, M.N. Hedhili, A. Gurinov, M.J. Kelly, M. El Eter, L. Cavallo, L. Emsley, J.M. Basset, *The structure and binding mode of citrate in the stabilization of gold nanoparticles*, Nat. Chem. 9(9) (2017) 890-895.

[240] S.K. Kim, M.S. Kim, S.W. Suh, *Surface-enhanced Raman scattering (SERS) of aromatic amino acids and their glycyl dipeptides in silver sol*, J. Raman Spectrosc. 18(3) (1987) 171-175.

[241] S.M. Liao, Q.S. Du, J.Z. Meng, Z.W. Pang, R.B. Huang, *The multiple roles of histidine in protein interactions*, Chem. Cent. J. 7(1) (2013) 44.

[242] F.Y. Oliva, L.B. Avalle, O.R. Cámara, C.P. De Pauli, *Adsorption of human serum albumin (HSA) onto colloidal TiO2 particles, Part I*, J. Colloid Inter. Sci. 261(2) (2003) 299-311.

[243] A. Kudelski, *Raman studies of rhodamine 6G and crystal violet sub-monolayers on electrochemically roughened silver substrates: Do dye molecules adsorb preferentially on highly SERS-active sites?*, Chem. Phys. Lett. 414(4-6) (2005) 271-275.

[244] U. Kreibig, L. Genzel, *Optical absorption of small metallic particles*, Surf. Sci. 156(Part 2) (1985) 678-700.

[245] N.C. Fitzkee, G.D. Rose, *Reassessing random-coil statistics in unfolded proteins*, Proc. Natl. Acad. Sci. U S A 101(34) (2004) 12497-502.

[246] A. Kuriata, A.M. Gierut, T. Oleniecki, M.P. Ciemny, A. Kolinski, M. Kurcinski, S. Kmiecik, *CABS-flex 2.0: a web server for fast simulations of flexibility of protein structures*, Nucl. Acids Res. 46(W1) (2018) W338-W343.

[247] B. Dalzon, C. Aude-Garcia, V. Collin-Faure, H. Diemer, D. Beal, F. Dussert, D. Fenel, G. Schoehn, S. Cianferani, M. Carriere, T. Rabilloud, *Differential proteomics highlights macrophage-specific responses to amorphous silica nanoparticles*, Nanoscale 9(27) (2017) 9641-9658.

[248] M. Zarei, J. Aalaie, *Profiling of nanoparticle-protein interactions by electrophoresis techniques*, Anal. Bioanal. Chem. 411(1) (2019) 79-96.

[249] T.J. Anchordoquy, Y. Barenholz, D. Boraschi, M. Chorny, P. Decuzzi, M.A. Dobrovolskaia, Z.S. Farhangrazi, D. Farrell, A. Gabizon, H. Ghandehari, B. Godin, N.M. La-Beck, J. Ljubimova, S.M. Moghimi, L. Pagliaro, J.H. Park, D. Peer, E. Ruoslahti, N.J. Serkova, D. Simberg, *Mechanisms and barriers in cancer nanomedicine: addressing challenges, looking for solutions*, ACS Nano 11(1) (2017) 12-18.

[250] S.M. Moghimi, D. Peer, R. Langer, *Reshaping the future of nanopharmaceuticals: ad iudicium*, ACS Nano 5(11) (2011) 8454-8.

[251] T. dos Santos, J. Varela, I. Lynch, A. Salvati, K.A. Dawson, *Quantitative assessment of the comparative nanoparticle-uptake efficiency of a range of cell lines*, Small 7(23) (2011) 3341-9.

[252] H.H. Gustafson, D. Holt-Casper, D.W. Grainger, H. Ghandehari, *Nanoparticle uptake: The phagocyte problem*, Nano Today 10(4) (2015) 487-510.

[253] Z. Movasaghi, S. Rehman, I.U. Rehman, *Raman spectroscopy of biological tissues*, Appl. Spectrosc. Rev. 42(5) (2007) 493-541.

[254] J.M. Thornton, *Disulphide bridges in globular proteins*, J. Mol. Biol. 151(2) (1981) 261-287.

[255] T.E. Creighton, *Disulphide bonds and protein stability*, Bioessays 8(2) (1988) 57-63.

[256] L. Marino-Ramirez, M.G. Kann, B.A. Shoemaker, D. Landsman, *Histone structure and nucleosome stability*, Expert Rev. Proteom. 2(5) (2005) 719-29.

[257] B. Dorigo, T. Schalch, A. Kulangara, S. Duda, R.R. Schroeder, T.J. Richmond, *Nucleosome arrays reveal the two-start organization of the chromatin fiber*, Science 306(5701) (2004) 1571-3.

[258] B. Dorigo, T. Schalch, K. Bystricky, T.J. Richmond, *Chromatin Fiber Folding: Requirement for the Histone H4 N-terminal Tail*, J. Mol. Biol. 327(1) (2003) 85-96.

[259] N. Karna, A. Legowska, S. Malicki, D. Debowski, P. Golik, A. Gitlin, P. Grudnik, B. Wladyka, K. Brzozowski, G. Dubin, K. Rolka, *Investigation of serine-proteinase-catalyzed peptide splicing in analogues of sunflower trypsin inhibitor 1 (SFTI-1)*, Chembiochem. 16(14) (2015) 2036-45.

[260] J.R. Marques, R.R. da Fonseca, B. Drury, A. Melo, *Amino acid patterns around disulfide bonds*, Int. J. Mol. Sci. 11(11) (2010) 4673-86.

[261] M. Jackson, H.H. Mantsch, T*he use and misuse of FTIR spectroscopy in the determination of protein structure*, Crit. Rev. Biochem. Mol. Biol. 30(2) (1995) 95-120.

[262] J. Alvarez, D. Lee, S. Baldwin, D. Chapman, *Fourier transform infrared spectroscopic study of the structure and conformational changes of the human erythrocyte glucose transporter*, J. Biol. Chem. 262(8) (1987) 3502-3509.

[263] J. Kong, S. Yu, *Fourier transform infrared spectroscopic analysis of protein secondary structures*, Acta Biochim. Biophys. Sin. (Shanghai) 39(8) (2007) 549-59.

[264] A. Ghosh, J.S. Ostrander, M.T. Zanni, *Watching proteins wiggle: Mapping structures with two-dimensional infrared spectroscopy*, Chem. Rev. 117(16) (2017) 10726-10759.

[265] A. Remorino, I.V. Korendovych, Y. Wu, W.F. DeGrado, R.M. Hochstrasser, *Residue-specific vibrational echoes yield 3D structures of a transmembrane helix dimer*, Science 332(6034) (2011) 1206-9.

[266] S. Beychok, *Circular dichroism of biological macromolecules*, Science 154(3754) (1966) 1288-99.

[267] B. Rost, C. Sander, *Prediction of protein secondary structure at better than 70% accuracy*, J. Mol. Biol. 232(2) (1993) 584-99.

[268] N. Sreerama, R.W. Woody, *Estimation of protein secondary structure from circular dichroism spectra: comparison of CONTIN, SELCON, and CDSSTR methods with an expanded reference set*, Anal. Biochem. 287(2) (2000) 252-60.

[269] A. Borgia, M.B. Borgia, K. Bugge, V.M. Kissling, P.O. Heidarsson, C.B. Fernandes, A. Sottini, A. Soranno, K.J. Buholzer, D. Nettels, B.B. Kragelund, R.B. Best, B. Schuler, *Extreme disorder in an ultrahigh-affinity protein complex*, Nature 555(7694) (2018) 61-66.

[270] M. Gniadecka, O. Faurskov Nielsen, D.H. Christensen, H.C. Wulf, *Structure of water, proteins, and lipids in intact human skin, hair, and nail*, J. Invest. Dermatol. 110(4) (1998) 393-8.

[271] G. Sekar, S. Sugumar, A. Mukherjee, N. Chandrasekaran, *Multiple spectroscopic studies of the structural conformational changes of human serum albumin—Essential oil based nanoemulsions conjugates*, J. Luminesc. 161 (2015) 187-197.

[272] C.-H. Wang, C.-C. Huang, L.-L. Lin, W. Chen, *The effect of disulfide bonds on protein folding, unfolding, and misfolding investigated by FT-Raman spectroscopy*, J. Raman Spectrosc. 47(8) (2016) 940-947.

[273] A.V. Mikhonin, Z. Ahmed, A. Ianoul, S.A. Asher, *Assignments and conformational dependencies of the amide III peptide backbone UV resonance Raman bands*, J. Phys. Chem. B 108(49) (2004) 19020-19028.

[274] K. Kneipp, H. Kneipp, J. Kneipp, *Surface-enhanced Raman scattering in local optical fields of silver and gold nanoaggregates-from single-molecule Raman spectroscopy to ultrasensitive probing in live cells*, Acc. Chem. Res. 39(7) (2006) 443-50.

[275] D. Szklarczyk, A. Franceschini, S. Wyder, K. Forslund, D. Heller, J. Huerta-Cepas, M. Simonovic, A. Roth, A. Santos, K.P. Tsafou, M. Kuhn, P. Bork, L.J. Jensen, C. von Mering, *STRING v10: protein-protein interaction networks, integrated over the tree of life*, Nucl. Acids Res. 43(Database issue) (2015) D447-52.

[276] U. Rescher, V. Gerke, *Annexins-unique membrane binding proteins with diverse functions*, J. Cell Sci. 117(13) (2004) 2631-9.

[277] M. Klobucar, M. Sedic, P. Gehrig, J. Grossmann, M. Bilic, L. Kovac-Bilic, K. Pavelic, S. Kraljevic Pavelic, *Basement membrane protein ladinin-1 and the MIF-CD44-beta1 integrin signaling axis are implicated in laryngeal cancer metastasis*, Biochim. Biophys. Acta 1862(10) (2016) 1938-54.

[278] B.J. Galletta, O.L. Mooren, J.A. Cooper, *Actin dynamics and endocytosis in yeast and mammals*, Curr. Opin. Biotechnol. 21(5) (2010) 604-10.

[279] S.M. Smith, M. Baker, M. Halebian, C.J. Smith, *Weak molecular interactions in clathrin-mediated endocytosis*, Front. Mol. Biosci. 4 (2017) 72.

[280] S.L. Schmid, *Clathrin-coated vesicle formation and protein sorting: an integrated process*, Annu. Rev. Biochem. 66 (1997) 511-48.

[281] J.A. Johnston, C.L. Ward, R.R. Kopito, *Aggresomes: A cellular response to misfolded proteins*, J. Cell Biol. 143(7) (1998) 1883-1898.

[282] F. Ding, Y. Li, J. Liu, L. Liu, W. Yu, Z. Wang, H. Ni, B. Liu, P. Chen, *Overendocytosis of gold nanoparticles increases autophagy and apoptosis in hypoxic human renal proximal tubular cells*, Int. J. Nanomed. 9 (2014) 4317-30.

[283] K. Kai, O. Nagano, E. Sugihara, Y. Arima, O. Sampetrean, T. Ishimoto, M. Nakanishi, N.T. Ueno, H. Iwase, H. Saya, *Maintenance of HCT116 colon cancer cell line conforms to a stochastic model but not a cancer stem cell model*, Cancer Sci. 100(12) (2009) 2275-82.

[284] S.N. Saldanha, R. Kala, T.O. Tollefsbol, *Molecular mechanisms for inhibition of colon cancer cells by combined epigenetic-modulating epigallocatechin gallate and sodium butyrate*, Exp. Cell. Res. 324(1) (2014) 40-53.

[285] M.R. Bhonde, M.L. Hanski, J. Budczies, M. Cao, B. Gillissen, D. Moorthy, F. Simonetta, H. Scherubl, M. Truss, C. Hagemeier, H.W. Mewes, P.T. Daniel, M. Zeitz, C. Hanski, *DNA damage-induced expression of p53 suppresses mitotic checkpoint kinase hMps1: the lack of this suppression in p53MUT cells contributes to apoptosis*, J. Biol. Chem. 281(13) (2006) 8675-85.

[286] Z. Yang, H.-R. Xiong, *Culture conditions and types of growth media for mammalian cells*, in: Luca Ceccherini-Nelli and Barbara Matteoli: Biomedical Tissue Culture, (2012).

[287] M.K. Sakamoto, S. Mima, T. Kihara, T. Tanimura, *Sequential morphological changes of erythrocyte apoptosis in Xenopus larvae exposed to 2,3,7,8-tetrachlorodibenzo-p-dioxin (TCDD)*, Anat. Rec. A Discov. Mol. Cell. Evol. Biol. 279(1) (2004) 652-63.

[288] E. Falcieri, P. Gobbi, A. Cataldi, L. Zamai, I. Faenza, M. Vitale, *Nuclear pores in the apoptotic cell*, Histochem. J. 26(9) (1994) 754-763.

[289] S.B. Berman, F.J. Pineda, J.M. Hardwick, *Mitochondrial fission and fusion dynamics: the long and short of it*, Cell Death Differ. 15(7) (2008) 1147-52.

[290] R.J. Youle, M. Karbowski, *Mitochondrial fission in apoptosis*, Nat. Rev. Mol. Cell Biol. 6(8) (2005) 657-63.

[291] C.L. Yen, M.H. Mar, C.N. Craciunescu, L.J. Edwards, S.H. Zeisel, *Deficiency in methionine, tryptophan, isoleucine, or choline induces apoptosis in cultured cells*, J. Nutr. 132(7) (2002) 1840-7.

[292] A.S. Rambold, B. Kostelecky, N. Elia, J. Lippincott-Schwartz, *Tubular network formation protects mitochondria from autophagosomal degradation during nutrient starvation*, Proc. Natl. Acad. Sci. U S A 108(25) (2011) 10190-5.

[293] W.J. Lee, M.H. Chien, J.M. Chow, J.L. Chang, Y.C. Wen, Y.W. Lin, C.W. Cheng, G.M. Lai, M. Hsiao, L.M. Lee, *Nonautophagic cytoplasmic vacuolation death induction in human PC-3M prostate cancer by curcumin through reactive oxygen species -mediated endoplasmic reticulum stress*, Sci. Rep. 5 (2015) 10420.

[294] C. Wu, C. Wang, J. Zheng, C. Luo, Y. Li, S. Guo, J. Zhang, *Vacuolization in cytoplasm and cell membrane permeability enhancement triggered by micrometer-sized graphene oxide*, ACS Nano 9(8) (2015) 7913-24.

[295] S. Elmore, *Apoptosis: a review of programmed cell death*, Toxicol. Pathol. 35(4) (2007) 495-516.

[296] L. Haversen, J.P. Sundelin, A. Mardinoglu, M. Rutberg, M. Stahlman, U. Wilhelmsson, L.M. Hulten, M. Pekny, P. Fogelstrand, J.F. Bentzon, M. Levin, J. Boren, *Vimentin deficiency in macrophages induces increased oxidative stress and vascular inflammation but attenuates atherosclerosis in mice*, Sci. Rep. 8(1) (2018) 16973.

[297] S. Palvai, M.M. Kuman, P. Sengupta, S. Basu, *Hyaluronic acid layered chimeric nanoparticles: targeting MAPK-PI3K signaling nub in colon cancer cells*, ACS Omega 2(11) (2017) 7868-7880.

[298] F.P. Altman, *Tetrazolium salts and formazans*, Prog. Histochem. Cytochem. 9(3) (1976) III-51.

[299] S. Salgin, U. Salgin, S. Bahadir, *Zeta potentials and isoelectric points of biomolecules: The effects of ion types and ionic strengths*, Int. J. Electrochem. Sci. 7(12) (2012) 12404-12414.

[300] R. Srivastava, *Interaction of cysteine with Au_n (n=8, 10, 12) even neutral clusters: A theoretical study*, ChemistrySelect 2(9) (2017) 2789-2796.

[301] P. Xiang, Y. Yang, Z. Zhao, A. Chen, S. Liu, *Experimentally validating open tubular liquid chromatography for a peak capacity of 2000 in 3 h*, Anal. Chem. (2019).

List of Figures

List of Tables

List of Abbreviations

APS:	Ammonium persulfate
ASLS:	Asymmetric least squares
BSA:	Bovine serum albumin
DAVID:	Database for Annotation, Visualization and Integrated Discovery
DMEM:	Dulbecco's Modified Eagle Medium
DMEM-FBS:	Dulbecco's Modified Eagle Medium with 10% fetal bovine serum
DNA:	Deoxyribonucleic acid
FBS:	Fetal bovine serum
FDTD:	Finite-difference time-domain
FTIR:	Fourier-transform infrared spectroscopy
HPLC:	High-performance liquid chromatography
HPLC-ESI-Q-TOF-MS:	High-performance liquid chromatography-coupled electrospray ionization-quadrupole-time-of-flight mass spectrometry
HSA:	Human serum albumin
ICP:	Inductively coupled plasma
ICP-MS:	Inductively coupled plasma-mass spectrometry
LA-ICP-MS:	Laser ablation-inductively coupled plasma-mass spectrometry
LSPR:	Localized surface plasmon resonance
MALDI:	Matrix-assisted laser desorption/ionization
McCoy:	McCoy's Modified 5A Medium
McCoy-FBS:	McCoy's Modified 5A Medium with 10% fetal bovine serum
MS/MS:	Tandem mass spectrometry
PBS:	Phophate buffered saline
PCA:	Principal component analysis
PCn:	n^{th} Principal component
PDB:	Protein Database
***p*MBA:**	*para*-mercaptobenzoicacid
RNA:	Ribonucleic acid
SDS:	Sodium dodecyl sulphate
SDS-PAGE:	Sodium dodecyl sulfate-polyacrylamide gel electrophoresis
SERS:	Surface-enhanced Raman scattering
TEMED:	Tetramethylenediamine
Tris:	Tris(hydroxymethyl)aminomethane
VMD:	Visual Molecular Dynamics
XRT:	Cryo soft X-ray nanotomography

Amino acids were referred to as their conventional three-letter code, while nucleobases were marked with their conventional one-letter code.

Declaration

I declare that I have completed the thesis independently using only the aids and tools specified. I have not applied for a doctor's degree in the doctoral subject elsewhere and do not hold a corresponding doctor's degree. I have taken due note of the Faculty of Mathematics and Natural Sciences PhD Regulations, published in the Official Gazette of Humboldt-Universität zu Berlin no. 42/2018 on 11/07/2018.

…….

Berlin, 08.08.2019